TP 13263E

CROSS-POLARIZED RADAR PROCESSING

PREPARED BY: SICOM SYSTEMS LTD.

DATE: April 1998

PREPARED FOR: TRANSPORTATION DEVELOPMENT CENTRE
SAFETY AND SECURITY
TRANSPORT CANADA

Sicom Systems Ltd.
www.sicom.on.ca

71 Millbridge Cr.
Fonthill, Ontario
L0S 1E1

TP 13263E

CROSS-POLARIZED RADAR PROCESSING

PREPARED BY: SICOM SYSTEMS LTD.
Tarun K. Bhattacharya
Tim J. Nohara
Al Premji
Peter Weber
Brian Currie (McMaster University)
Joseph Ryan (Sigma Engineering Ltd.)

DATE: April 1998

Sicom Systems Ltd.
www.sicom.on.ca

71 Millbridge Cr.
Fonthill, Ontario
L0S 1E1

NOTICES

This report reflects the views of the authors and not necessarily those of the Transportation Development Centre.

The Transportation Development Centre does not endorse products or manufacturers. Trade or manufacturers' names appear in this report only because they are essential to its objectives.

Un sommaire français se trouve avant la table des matières.

Transport Canada / Transports Canada

PUBLICATION DATA FORM

1. Transport Canada Publication No.	2. Project No.	3. Recipient's Catalogue No.
TP 13263E	9079	

4. Title and Subtitle	5. Publication Date
Cross-Polarized Radar Processing	April 1998
	6. Performing Organization Document No.

7. Author(s)	8. Transport Canada File No.
T.K. Bhattacharya, T.J. Nohara, A. Premji, P. Weber, B. Currie, and J. Ryan	ZCD-1460-367

9. Performing Organization Name and Address	10. PWGSC File No.
Sicom Systems Ltd. 71 Millbridge Cr. Fonthill, Ontario L0S 1E1	XSD-6-01572
	11. PWGSC or Transport Canada Contract No. T8200-6-6533

12. Sponsoring Agency Name and Address	13. Type of Publication and Period Covered
Transportation Development Centre (TDC) 800 René Lévesque Blvd. West 6th Floor Montreal, Quebec H3B 1X9	Final
	14. Project Officer C. Gautier

15. Supplementary Notes (Funding programs, titles of related publications, etc.)

Co-sponsored by the Program of Energy Research and Development (PERD)

16. Abstract

This study examined the feasibility of developing an improved and affordable ice navigation radar for vessels that must navigate through ice-infested waters. Such a radar would be able to distinguish between hazardous (e.g. icebergs and multi-year ice) and nonhazardous (e.g. first-year) ice, using non-coherent, cross-polarized radar processing. Two key issues were investigated. First, it was determined whether useful polarimetric information can be retained and exploited when using uncalibrated radars for polarimetric processing. Second, the use of non-specialized, non-collocated radars to provide the polarimetric information was considered.

The first issue is of interest because conventional marine radars are not absolutely calibrated, and therefore cross-polarized ratios cannot be directly measured from two radars. Data-dependent processing offers one way to self-calibrate the signals so that meaningful ratios between the like- and cross-polarized returns could be obtained. Data sets selected from the November 1995 MV *Arctic* field trials were analysed to develop the required techniques. After the HH and HV channels were matched, polarimetric algorithms (developed in this study) were applied to the matched channel data. To test the ability of these algorithms to discriminate between hazardous and non-hazardous ice, several data files were selected and multi-year ice features were identified by ice recognition experts (who manually compared HH and HV radar images). The polarimetric algorithms were tested on these images, and they performed quite well in discriminating the identified hazardous ice features. The second issue arises because specialized cross-polarized radar antennas are expensive. Dual-channel rotary joints and dual waveguide runs also increase sensor cost. An alternative is to use two, non-collocated, conventional marine radars (horizontally polarized) and alter the polarization of the second to provide vertical polarization. The second radar would be set to receive-only and synchronized to the transmitting radar in rotation, frequency, and pulse timing.

A literature review found that polarizer lenses appear able to transform a horizontally polarized antenna to vertical. The study also derived synchronization and timing requirements for slaving the second radar to the first. The economic feasibility of this non-collocated radar concept remains to be examined.

17. Key Words	18. Distribution Statement
Ice navigation, cross-polarized radar, hazardous ice detection, ice classification, marine radar, horizontal polarization, vertical polarization, Arctic navigation, radar navigation, radar calibration	Limited number of copies available from the Transportation Development Centre

19. Security Classification (of this publication)	20. Security Classification (of this page)	21. Declassification (date)	22. No. of Pages	23. Price
Unclassified	Unclassified	—	xviii, 208, app.	—

Transports Canada Transport Canada

FORMULE DE DONNÉES POUR PUBLICATION

1. N° de la publication de Transports Canada	2. N° de l'étude	3. N° de catalogue du destinataire
TP 13263E	9079	

4. Titre et sous-titre	5. Date de la publication
Cross-Polarized Radar Processing	Avril 1998
	6. N° de document de l'organisme exécutant

7. Auteur(s)	8. N° de dossier - Transports Canada
T.K. Bhattacharya, T.J. Nohara, A. Premji, P. Weber, B. Currie, et J. Ryan	ZCD-1460-367

9. Nom et adresse de l'organisme exécutant	10. N° de dossier - TPSGC
Sicom Systems Ltd. 71 Millbridge Cr. Fonthill, Ontario L0S 1E1	XSD-6-01572
	11. N° de contrat - TPSGC ou Transports Canada T8200-6-6533

12. Nom et adresse de l'organisme parrain	13. Genre de publication et période visée
Centre de développement des transports (CDT) 800, boul. René-Lévesque Ouest 6e étage Montréal (Québec) H3B 1X9	Final
	14. Agent de projet C. Gautier

15. Remarques additionnelles (programmes de financement, titres de publications connexes, etc.)

Coparrainée par le Programme de recherche et développement énergétiques (PRDE)

16. Résumé

Cette recherche a porté sur la faisabilité d'un radar amélioré et peu coûteux pour la navigation dans des eaux chargées de glaces. Ce radar serait en mesure de discriminer entre les glaces dangereuses (les icebergs et les glaces pluriannuelles, p. ex.) et celles qui sont plutôt inoffensives (les glaces de première année), grâce au traitement de signaux non cohérents à polarisation croisée. Deux grandes questions ont été étudiées. Premièrement, on s'est interrogé sur la possibilité de dériver une information polarimétrique utile de l'utilisation de radars non calibrés pour le traitement polarimétrique. On a ensuite examiné l'opportunité d'utiliser des radars non spécialisés et non adjacents pour l'obtention d'information polarimétrique.

La première question est d'un grand intérêt, car les radars marins classiques n'étant pas calibrés par rapport à un repère fixe, il est impossible d'établir directement des rapports entre les signaux à polarisation croisée obtenus à l'aide de radars distincts. Le traitement dépendant des données est une façon de calibrer les canaux l'un par rapport à l'autre, qui débouche sur des rapports significatifs entre les signaux à polarisation parallèle et croisée. Les données recueillies au cours des essais réalisés en novembre 1995 à bord du NM *Arctic* ont été analysées pour la mise au point des techniques de calibrage nécessaires. Après le calibrage des canaux HH et HV, des algorithmes polarimétriques (mis au point en marge de la présente étude) ont été appliqués aux données provenant de ces canaux calibrés. Pour vérifier la capacité de ces algorithmes de discriminer entre les glaces dangereuses et inoffensives, des fichiers de données choisis ont été soumis à des spécialistes en reconnaissance des glaces, qui ont établi les caractéristiques des glaces pluriannuelles (en comparant visuellement les images radar HH et HV). Les algorithmes ainsi mis à l'essai ont démontré une bonne capacité de discerner les caractéristiques des glaces dangereuses telles qu'établies par les experts. La deuxième question naît du coût élevé des antennes utilisées dans les systèmes à polarisation croisée. Les joints tournants à deux canaux et les deux guides d'ondes alourdissent encore le coût de ces systèmes. Une solution de rechange consiste à utiliser deux radars marins classiques (à polarisation horizontale) non adjacents et à modifier la polarisation du second pour qu'elle soit verticale. Ce dernier est alors réglé pour la réception seule et il est asservi au radar actif par la vitesse de rotation de son antenne, sa fréquence et la cadence de ses impulsions.

Une recherche documentaire laisse penser que les lentilles polarisantes sont capables de transformer d'horizontale à verticale la polarisation d'une antenne. L'étude a également permis d'établir les paramètres de synchronisation pour l'asservissement du deuxième radar au premier. Il reste à étudier la faisabilité économique de l'exploitation de radars non adjacents.

17. Mots clés	18. Diffusion
Navigation dans les glaces, radar à polarisation croisée, détection de glaces dangereuses, classification des glaces, radar marin, polarisation horizontale, polarisation verticale, navigation dans l'Arctique, navigation radar, calibrage radar	Le Centre de développement des transports dispose d'un nombre limité d'exemplaires.

19. Classification de sécurité (de cette publication)	20. Classification de sécurité (de cette page)	21. Déclassification (date)	22. Nombre de pages	23. Prix
Non classifiée	Non classifiée	—	xviii, 208, ann.	—

Executive Summary

This study examines the feasibility of developing an improved ice navigation radar for vessels that must navigate through ice-infested waters. Such a radar would be able to distinguish between hazardous (e.g. icebergs and multi-year ice) and nonhazardous (e.g. first-year) ice. The use of cross-polarized radar has been demonstrated to offer improved detection and classification of ice features. With a cross-polarized system that uses non-coherent radar signals, the relevant signal features are the like- and cross-polarized amplitudes, both in absolute levels and their ratio. The stronger the radar return amplitude, the more significant is the ice feature in terms of its impediment to navigation. However, using only like-polarized radar amplitudes, rough first-year ice features cannot be reliably distinguished from features containing multi-year or glacial (iceberg) ice. Since the latter two ice types represent a much greater mechanical impediment to navigation and safety, it is highly desirable to separately identify them. Earlier research has indicated that the cross-polarized radar signal undergoes volume scattering within the ice feature, returning a much stronger signal from the fresher multi-year ice and iceberg ice as opposed to the more saline first-year ice.

This study is intended to add to previous research by demonstrating the feasibility of developing an affordable ice hazard detection system that would be of great importance to Arctic navigation. The polarimetric algorithms developed during this project were motivated by, and tested on polarimetric data collected during the 1995 MV *Arctic* field trials during the first week of November 1995. HH and HV marine radar PPI data were captured as the vessel navigated through Lancaster Sound, along the south shore of Devon Island. Both hazardous and non-hazardous ice were present. This study is the first to involve a detailed examination of the radar data collected during the aforementioned field trials.

Two key issues were investigated during this project:

Can polarimetric information be retained and exploited when using uncalibrated radars for polarimetric processing?

Can non-specialized, non-collocated radars provide the polarimetric information?

The first issue arises because conventional marine radars are not absolutely calibrated and therefore estimating absolute signal strengths (and consequently the like-polarized to cross-polarized ratios) is not directly possible. Data-dependent processing offers one way to self-calibrate the signals so that meaningful ratios between the like- and cross-polarized returns could be obtained. Selected 1995 MV *Arctic* data sets were analysed to develop the required techniques.

The statistics of the recorded data were analysed, and it was determined that the median return versus range was quite stable over the 1-2 minute sequences examined. The median versus range profile was used to calibrate gain versus range variations between the HH and HV channel. A relative gain was then computed using additional data-derived statistics to balance the HH channel with respect to the HV channel. The HH to HV matching process developed was shown to work quite well.

Once the HH and HV channels were matched, polarimetric algorithms were developed and applied to the matched channel data. To test the ability of these algorithms to discriminate between hazardous and non-hazardous ice, several data files were selected and multi-year ice features were identified by ice recognition experts (who manually compared HH and HV radar images). The polarimetric algorithms were tested on these images, and performed quite well in discriminating the identified hazardous ice features. The results are very encouraging because they suggest sufficient polarimetric information survived the image matching process. As only a small sample of the MV *Arctic* data was analysed, future efforts should refine and validate these results using as much of the available data as possible. Airborne SAR data, which became available only near the end of this project, should be used more extensively for ground truthing.

The second issue arises because specialized cross-polarized radar antennas are expensive. Dual-channel rotary joints and dual waveguide runs increase the sensor's cost. An alternative is to use two, low-cost, conventional marine radars (horizontally polarized) and alter the polarization of the second to provide vertical polarization. The second radar would be set to receive-only and synchronized to the transmitting radar in rotation, frequency, and pulse timing. The ability to economically modify conventional marine antennas to give vertical polarization, and to develop and integrate the appropriate timing hardware will determine the viability of this approach. A literature review found that polarizer lenses can twist a horizontally polarized antenna to vertical polarization. It must be determined whether such lenses can be economically applied to produce a vertically polarized marine radar antenna.

Requirements for synchronizing the timing of two distinct radars were derived. It was determined that the horizontal displacement between two antennas should be minimized. Ideally they should be mounted directly above one another. If this is not feasible, the horizontal displacement should not exceed 3.75 m. This will keep both the range and angular errors below acceptable limits. There are no simple solutions to removing these errors once they have been introduced into the system. In the future, prototype control hardware should be developed to demonstrate the feasibility of synchronizing two independent radars for cross-polarized processing.

The results presented in this report demonstrate the potential for an economical, cross-polarimetric ice navigation system that effectively discriminates between hazardous and non-hazardous ice.

Sommaire

Cette recherche examine la faisabilité d'un radar amélioré et peu coûteux pour la navigation dans des eaux chargées de glaces. Ce radar serait en mesure de discriminer entre les glaces dangereuses (les icebergs et les glaces pluriannuelles, p. ex.) et celles qui sont plutôt inoffensives (les glaces de première année). Le radar à polarisation croisée s'est révélé offrir une plus grande qualité de détection et de caractérisation des glaces. Dans un système à polarisation croisée mettant en jeu des signaux non cohérents, la caractéristique utile des signaux à polarisation parallèle et croisée est l'amplitude absolue ou relative de ces derniers. Plus l'amplitude de l'écho radar est grande, plus les glaces détectées sont assimilées à un obstacle à la navigation. Mais à elle seule, l'amplitude de signaux radar à polarisation parallèle ne permet pas de distinguer de façon fiable les glaces de première année des glaces pluriannuelles ou des icebergs. Comme ces deux derniers types de glaces représentent une menace et un obstacle beaucoup plus importants à la navigation, il est grandement souhaitable de pouvoir les distinguer des glaces de première année, plutôt inoffensives. Des études antérieures ont montré que les signaux radar à polarisation croisée se diffusent dans la glace, renvoyant un écho beaucoup plus puissant des glaces pluriannuelles et des icebergs, composés d'eau relativement douce, que des glaces de première année, davantage salines.

Cette étude, qui se veut un complément aux recherches antérieures, vise à démontrer la faisabilité d'un système peu coûteux de détection des glaces, qui serait un atout majeur pour la navigation dans l'Arctique. Les algorithmes polarimétriques mis au point et essayés au cours de ce projet avaient pour but de mettre à profit les données polarimétriques colligées lors des essais en mer réalisés à bord du NM *Arctic*, pendant la première semaine de novembre 1995. Les données HH et HV obtenues à l'aide de radars marins PPI ont été acquises alors que le navire naviguait dans le détroit de Lancaster, le long de la côte sud de l'île Devon, en présence de glaces, certaines dangereuses, d'autres non. Cette étude est inédite en ce qu'elle comporte un examen approfondi des données radar colligées pendant les essais en mer susmentionnés.

Deux grandes questions ont été étudiées au cours de ce projet :

Est-il possible de dériver une information polarimétrique utile de l'utilisation de radars non calibrés pour le traitement polarimétrique?

Des radars non spécialisés et non adjacents peuvent-ils fournir une information polarimétrique?

La première question se pose parce que les radars marins classiques n'étant pas calibrés par rapport à un repère fixe, il est impossible d'apprécier directement l'amplitude absolue des signaux (et, partant, les rapports d'amplitude entre les signaux à polarisation parallèle et croisée). Le traitement dépendant des données est une façon de calibrer les canaux l'un par rapport à l'autre, qui débouche sur des rapports significatifs entre les échos à polarisation parallèle et croisée. L'analyse d'ensembles de données colligées à bord du NM *Arctic* a permis la mise au point des techniques de calibrage nécessaires.

L'analyse statistique des données enregistrées a révélé une relative stabilité des valeurs médianes des échos en fonction de la portée au cours des séquences de 1 à 2 minutes examinées. La courbe des médianes par rapport à la portée a été utilisée pour calibrer les variations de gain en fonction de la portée entre les canaux HH et HV. Un gain relatif a alors été calculé, en faisant intervenir d'autres statistiques dérivées des données, pour équilibrer le canal HH par rapport au canal HV. La méthode de calibrage des canaux HH et HV ainsi mise au point s'est montrée relativement efficace.

Après le calibrage des canaux HH et HV, des algorithmes polarimétriques ont été mis au point et appliqués aux données de ces canaux calibrés. Pour vérifier la capacité des algorithmes de discriminer entre les glaces dangereuses et inoffensives, des fichiers de données choisis ont été soumis à des spécialistes en reconnaissance des glaces, qui ont établi les caractéristiques des glaces pluriannuelles (par comparaison visuelle des images HH et HV). Les algorithmes ainsi mis à l'essai ont démontré une bonne capacité de discerner les caractéristiques associées aux glaces dangereuses telles qu'établies par les experts. Les résultats sont très encourageants car ils donnent à penser qu'une information polarimétrique suffisante a survécu au calibrage des canaux. Comme seulement un faible échantillon des données du NM *Arctic* ont été analysées, d'autres travaux devraient être entrepris pour affiner et valider ces résultats au moyen de toutes les données possibles. Des données de radar à antenne latérale synthétique aéroporté n'ont été disponibles que vers la fin du présent projet : il y aurait lieu de les mettre davantage à profit pour une vérification au sol.

La deuxième question se pose en raison du coût élevé des antennes utilisées dans les systèmes à polarisation croisée. Les joints tournants à deux canaux et les deux guides d'ondes alourdissent encore le coût de ces systèmes. Une solution de rechange consiste à utiliser deux radars marins ordinaires (à polarisation horizontale) bon marché et à

modifier la polarisation du second pour qu'elle soit verticale. Ce dernier est alors réglé pour la réception seule et il est asservi au radar actif par la vitesse de rotation de son antenne, sa fréquence et la cadence de ses impulsions. La viabilité de cette démarche sera fonction de la capacité de modifier à faible coût la polarisation des antennes marines classiques, et de développer et intégrer le matériel approprié de synchronisation des impulsions. Une recherche documentaire laisse penser que les lentilles polarisantes sont capables de transformer d'horizontale à verticale la polarisation d'une antenne. Il reste à déterminer la viabilité économique du recours à de telles lentilles pour obtenir une antenne de radar marin à polarisation verticale.

Les paramètres de synchronisation des impulsions des deux radars ont été calculés. Il a été établi que l'espacement horizontal entre les deux antennes devait être minimal. Idéalement, les deux antennes devraient être montées dans le même axe vertical ou, à défaut, à au plus 3,75 m de distance dans le plan horizontal, afin que les erreurs de mesure angulaire et de mesure de la distance demeurent dans des limites acceptables. Il n'existe pas de solution simple pour éliminer ces erreurs une fois qu'elles ont été introduites dans le système. Il y aura lieu de mettre au point, dans l'avenir, un prototype d'instrument de contrôle afin de démontrer la possibilité de synchroniser deux radars indépendants pour le traitement radar à polarisation croisée.

Les résultats présentés dans ce rapport démontrent la faisabilité d'un système à polarisation croisée peu coûteux pour la navigation dans les glaces, capable de distinguer les glaces dangereuses de celles qui ne le sont pas.

TABLE OF CONTENTS

LIST OF TABLES

LIST OF FIGURES

ACRONYMS

A/D	Analog to Digital Converter
ASDE	Airport Surface Detection Equipment
CD	Compact Disk
CDF	Cumulative Density Function
CD-ROM	CD-Read Only Memory
CFAR	Constant False Alarm Rate
Co-Pol	Refers to two channels with same polarization
FP	Fractional Polarization
FY	First-year
GPS	Geo-Positioning System
HH	Horizontal-Horizontal
HPOL	Horizontal Polarization
HV	Horizontal-Vertical
JPL	Jet Propulsion Laboratory
LSL	Louis St. Laurent
MLP	Meanderline Polarizer
MRI	Modular Radar Interface
MY	Multi-year
PDF	Probability Density Function
PPI	Plan Position Indicator
RC	Resistor-Capacitor
RCS	Radar Cross Section
SAR	Synthetic Aperture Radar
SPAN	A measure of total power in scattered field
STC	Sensitivity Time Control
TE	Transverse Electric
TEM	Transverse ElectroMagnetic
VP	Vertical Polarization
VPOL	Vertical Polarization
VTS	Vessel Traffic Services

1 INTRODUCTION

1.1 Background

The use of cross-polarized radar has been demonstrated to offer improved detection and classification of ice features. With a cross-polarized system that uses non-coherent radar signals, the relevant signal features are the like- and cross-polarized amplitudes, both in absolute levels and their ratio. The stronger the radar return amplitude, the more significant is the ice feature in terms of its impediment to navigation. However, using only like-polarized radar amplitudes, rough first-year features cannot be reliably distinguished from features containing multi-year or glacial (iceberg) ice. Since the latter two ice types represent a much greater mechanical impediment to navigation and safety, it is highly desirable to separately identify these ice types. Earlier research has indicated that the cross-polarized radar signal undergoes volume scattering within the ice feature, returning a much stronger signal from the fresher multi-year ice and iceberg ice as opposed to the more saline first-year ice.

The current study is intended to add on to previous research by demonstrating the feasibility of developing an affordable, ice hazard detection system, which would be of great importance to Arctic navigation. The polarimetric algorithms developed during this project were motivated by, and tested on polarimetric data collected during the 1995 MV Arctic Field Trials during the first week in November 1995. HH and HV marine radar PPI data were captured as the vessel navigated through Lancaster Sound, along the south shore of Devon Island. Both hazardous and non-hazardous ice were present. This study is the first that has examined in detail the radar data collected during the aforementioned field trials.

Two key issues were investigated during this project are:

1. Can polarimetric information be retained and exploited when using uncalibrated radars for polarimetric processing, and

2. Can non-specialized, non-collocated radars provide the polarimetric information.

Conventional marine radars are not absolutely calibrated and therefore estimating absolute signal strengths (and consequently the like to cross polarized ratios) is not directly feasible. Data-dependent processing offers one possible way to self-calibrate the signals so that meaningful ratios between the like- and cross-polarized returns could be obtained.

Having a specialized cross-polarized radar antenna is an expensive proposition. Dual-channel rotary joints and and dual waveguide runs can add to the cost. A possible alternative would be to use two distinct radars with orthogonal polarizations. The second radar would be set to receive-only and synchronized to the transmitting radar in rotation, frequency, and pulse timing. The ability to economically modify conventional marine antennas to achieve vertical polarization is a key to this concept.

The next section provides some of the conclusions reached during this project.

1.2 Main Findings

The statistics of the recorded data, more specifically the median return versus range, appeared quite stable over the 1-2 minute sequences examined herein. The calculation of the relative gain to balance the HH channel (with respect to the HV) was also reasonably stable over the data sequences, at ranges for which unclipped data was available.

The HH to HV matching process that was developed in this study worked reasonably well despite all vagaries and shortcomings of the recorded data. It is expected with the inclusion of MRI-controlled gain and bias adjustments, the problems related to the current data base will be largely mitigated, and the algorithms should work well.

Once the HH and HV channels were matched, polarimetric algorithms were developed and applied to the matched channel data. In order to test the ability of these algorithms to discriminate between hazardous and non-hazardous ice, several data files were selected and multi-year ice features were identified by ice recognition experts by comparing HH and HV radar images. The polarimetric algorithms were tested on these images, and performed very well in discriminating these identified, hazardous ice features. These results are very encouraging as they suggest sufficient polarimetric information survived the image matching process.

The preferred configuration for positioning the two antennae will minimize the horizontal displacement. Ideally they should be mounted directly above one another. If this is not feasible, the horizontal displacement should not exceed 3.75 m. This would keep both the range and angular errors below acceptable limits. There are no simple solutions to removing these errors once they have been introduced to the system.

Apart from the vertically polarized slotted waveguide antennas that are commercially available, a number of technically feasible solutions were found in the literature to convert the polarization of an existing antenna using external polarizers. Although the use of polarizers to convert from horizontal to vertical polarization has been rather limited, it is possible to do so, both technically and from an engineering point of view.

A large literature database has been collected that specifically deals with detection and classification of sea ice using cross-polarization. This literature, will be valuable for any future studies.

In conclusion, the results presented in this report do show potential and can be used for a better ice navigation system that discriminates between hazardous and non-hazardous ice. Such a system is believed to be both technically feasible and economically viable. As this project was only a feasibility study, a number of issues still need to be investigated in greater detail, to better characterize the possible improvements, and to demonstrate the technical and economic viability of a cross-polarized ice hazard radar. These issues are pointed out as suggestions for future directions, in Section 6 of this Report.

1.3 Organization of the Report

In Section 2, the results of the literature review are presented. Section 3 provides a detailed presentation of the HH and HV radar balancing algorithms, and the calculation of the polarimetric radar display that discriminates between hazardous and non-hazardous ice. In Section 4, the technical feasibility of implementing a cross-polarized marine radar using two existing marine radars is examined. This approach is of interest because many large vessels have a second marine radar on-board. Section 5 presents analysis of the recorded data to study the effectiveness of the developed techniques for non-collocated radars. Section 6 describes the availability of SAR data in support of studies performed in Section 3. Conclusions and future directions are presented in Section 7. Finally,

Appendix A provides STAR-1 SAR flight line images that map the ice conditions in Lancaster Sound, during the November 1995 MV Arctic Field Trials.

2 LITERATURE REVIEW

2.1 Introduction

In this section, the results of a literature review are presented. The literature review examines papers dealing with the properties of dual polarized radars both for linear (horizontal and vertical) and circular polarizations (e.g. left and right), and also with the use of polarimetry for discrimination between ice types. In Section 2.2, an overview of the findings of the literature review is presented. Then, in Section 2.3, a detailed list of references is presented, along with the abstracts from key papers.

2.2 Overview of Findings

Active radar returns from sea ice are determined by the electromagnetic fields scattered from the snow surface, the ice surface and from the volume of the snow-ice medium. It must be noted that from electromagnetic theory we know that in cases when the penetration depth of the medium exceeds one wavelength and when there is an abundance of scattering elements with scale dimensions longer than the wavelength, the radar return from such media would have significant volume scattering component. This property by itself can be used to explain the bulk electromagnetic scattering behaviour of sea ice, based on our knowledge of the physical attributes. Cold old ice fits the scattering medium description provided above and thus leads to volume scattering at microwave frequencies. However, first-year ice is smooth and hence scattering is predominantly surface

scattering. Dry snow also has significant skin depth and is not a smooth surface, thus leading to volume scattering. Moreover, dry snow cover over sea ice has a significant penetration depth and if the snow cover is thinner than the penetration depth, contribution to scattering is also added by the bottom layer of ice. When the radar transmits and receives linear polarization, strong depolarization occurs for volume scattering and it is known that surface scattering leads to very weak depolarization.

The above conclusions are over-simplistic and the actual behaviour is additionally affected by other parameters such as incidence angle, ambient temperature, frequency of operation, etc. It is the aim of this section to summarize some of the earlier work in characterizing the radar signatures of ice. Care has been taken to limit our attention to amplitudes of like- and cross-polarized data only. Although, most of the work in sea ice remote sensing is using airborne radars, these have been included since a large number of them have reported results at larger incidence angles, albeit not as large as would be encountered in ship-based radars.

Sea ice backscatter measurements have also been made using ground based radars. In one such study, Carlstrom et al. [4] report results from various old ice floes and have shown that ice floe cross-polarisation backscattering is about 10 dB lower than the corresponding like-polarization at C-band. This trend has been observed to be consistent for a large range of incidence angles (20° to 60°). Currie et al. [6] have also reported results from surface based radar using X-band, with low grazing angles; and have reported higher cross-pol backscatter coefficients than like ones for icebergs.

2.2.1 Theoretical Basis of Microwave Signatures of Sea ice

There have been a number of studies which theoretically model the radar wave interaction and relate the backscatter to physical characteristics of sea ice. In general, the radar backscatter from snow-covered sea ice can be considered to be composed of surface scattering from the air-snow interface, snow volume scattering, surface scattering from the snow-ice interface, ice volume scattering and surface scattering from the ice-water interface, Kim et al. [8]. An additional effect is caused by the surface-volume scattering interaction. However this last effect is a second-order effect and is often ignored in the models. This section summarizes the salient points of some of these studies.

Ulander et al. [21] have compared actual C-band backscatter measurements with theoretical predictions based on surface and volume scattering models. Although the models they used included contributions from the snow surface, the snow volume, the ice surface, the ice volume, and the water interface, for the conditions encountered during actual data collections, they found that the scattering was dominated by ice surface scattering with small attenuation introduced by the snow cover. The ice surface scattering was modelled by either the Kirchoff model with the scaler approximation or the small perturbation model (Ulaby et al. [20]) depending on the surface parameters. They showed that the relatively simple model, which was driven by three parameters, namely ice surface rms height, autocorrelation function, and snow wetness, could accurately predict

the radar backscatter from snow-covered sea ice. These models would also be effective when the scattering is dominated by scattering from relatively smooth ice, like newer first-year ice.

Nghiem et al. [13] have presented a very detailed model for polarimetric signatures of sea ice that includes the thermodynamic phase distribution of sea ice components, wave speed modification, absorption and scattering losses in inhomogeneous media, and ellipsoidal inclusions for polarimetric volume scattering. Sea ice anisotropy, multiple wave interaction, and phase delays due to rough surface effects are also modelled. Additionally, explicit effect of hummock topography on both surface and volume scattering is accounted for. By comparing with actual measurements at C and L bands [13], they observed that the backscattering is dominated by the upper part of multi-year ice, which contains scatterers and surface features with less directional preference. It was also found that at large incidence angles, Hummocks significantly influence the signatures and size variations in the brine inclusions in multi-year ice is a main cause for large variations in signatures.

2.2.2 Polarimetric Classification of Sea Ice

In this section, several discriminants are introduced and previous results stated.

2.2.2.1 SPAN

Absolute calibration is not possible for many polarimetric data sets, owing to the absence of in-scene targets with known backscattering characteristics. Consequently, relative measures have to be derived. One such measure is SPAN which represents the total power in the scattered field.

$$SPAN = \langle S_{hh} S_{hh}^{*} \rangle + \langle S_{vv} S_{vv}^{*} \rangle + 2\langle S_{hv} S_{hv}^{*} \rangle$$

Where $\langle \cdots \rangle$ represents ensemble averaging of pixel values.

Israelsson and Askne [7] chose examples taken from JPL (Jet Propulsion Laboratory) polarimeter images of Beaufort Sea ice using 200 m^2 samples. They also contrasted the SPAN values for first-year and multi-year ice at three different frequencies and demonstrated the best discrimination at C-band with a separation of 10 dB. Typically, SPAN is greater for multi-year than first-year ice due to the fact that multi-year ice gives an additional depolarized component of backscatter along with the predominantly co-polarized returns from first-year ice of equivalent surface roughness. They also concluded that since the proportion of depolarized returns is significantly larger at C-band than at L and P bands, a significant component is derived from multiple scattering by bubbles and inhomogeneities present in the upper layers of old ice, in addition to second-order rough surface scattering and volume-surface interaction effects. Supporting evidence for

volume scattering was that the SPAN was relatively insensitive to incidence angles at C-band.

2.2.2.2 Power Ratios Between Channels

Heterogeneity of scattering mechanisms between pixels introduces a component of unpolarized or randomly polarized backscatter. This is manifested as a fraction of returns that exhibit diffuse scattering, characterized by rapidly varying polarizations from pixel to pixel (and thus widely differing covariance matrices in adjacent resolution elements). Generally, complex surfaces or anisotropic or multiple-scattering surface layers increase the unpolarized fraction of the backscatter. Another mechanism contributing to such an effect is the presence of system noise, which may occur at low backscatter. This circumstance is only really typical of situations of young smooth ice at far ranges.

A convenient method for using polarization combinations is by applying channel ratios which quantify the power differences and thus characterize the full polarimetric signatures. The various channel ratios which have been employed are

$$R_{hh/vv} = \frac{\langle S_{hh} S_{hh}^{*} \rangle}{\langle S_{vv} S_{vv}^{*} \rangle}$$

Similarly, the cross-pol ratio is

$$R_{hv/hh} = \frac{\langle S_{hv} S_{hv}^{*} \rangle}{\langle S_{hh} S_{hh}^{*} \rangle}$$

The depolarization ratio is defined as the ratio of cross-pol to both co-pol channels, i.e.

$$R_{depol} = \frac{2 \langle S_{hv} S_{hv}^{*} \rangle}{\langle S_{hh} S_{hh}^{*} \rangle + \langle S_{vv} S_{vv}^{*} \rangle}$$

Out of this, we are only interested in cross-pol ratio since the transmission is only using horizontal polarization. An increase in cross-pol ratio and second-order scattering effects generally implies anisotropy in the surface roughness or the dielectric structure of the first-year ice (e.g., as a consequence of brine-inclusion size and orientation), or air bubbles and inhomogeneities in multi-year ice. It has been found ([14] and [24]) that at X-band, the cross-pol ratio is higher for multi-year ice and decreases as salinity increases.

There are other discriminants employed but they need coherent reception and thus are of little use to us. A brief mention of these is made here for sake of completeness.

2.2.2.3 Co-Pol Correlation

$$\rho_{hhvv} = \left| \frac{\left\langle S_{hh} S_{vv}^{*} \right\rangle}{\sqrt{\left\langle S_{hh} S_{hh}^{*} \right\rangle \left\langle S_{vv} S_{vv}^{*} \right\rangle}} \right|$$

A condition for fully polarized radar backscattering from natural geophysical targets is that the cross-pol magnitude must be zero and HH and VV returns perfectly correlated (i.e., correlation coefficient of unity). In actual observations, multi-year ice was found to have a higher correlation than in higher salinity first-year ice.

2.2.2.4 Fractional Polarization

$$FP = \frac{P_{\max} - P_{\min}}{P_{\max} + P_{\min}}$$

The fractional polarization is calculated from a sample by synthetically varying the polarization state and by recording the maximum Pmax and minimum Pmin intensities as both transmission and reception polarization are varied. Thus, FP is a measure of the polarization purity of the return and a low value indicates larger unpolarized component and a lower correlation coefficient. An extensive experimental evaluation has been carried out by Drinkwater et al. [8] at different frequency bands namely C, L and P. It was found that FP is close to unity for both multi-year and first-year ice at L-band in direct contrast to other geophysical media such as forest vegetation where values of FP < 0.5 are typical. FP also shows a variation with wavelength with decreased values observed at C-band. The lowest FP value of 0.8 was observed for multi-year ice at C-band. This, together with low correlation coefficient indicates that the largest fraction of unpolarized returns occurs in lower salinity ice, and is probably due to multiple scattering from bubbles or air-filled inhomogeneities in the upper ice sheet.

2.2.2.5 Phase Difference

$$\phi_{hh-vv} = \tan^{-1}\left[\frac{\mathrm{Im}\left\langle S_{hh} S_{vv}^{*} \right\rangle}{\mathrm{Re}\left\langle S_{hh} S_{vv}^{*} \right\rangle} \right]$$

Relative differences in phase between channels are important because each scattering event, either at reflective horizons or from diffraction by particles in the medium,

transforms the relative phase of co-pol waves. The mean HH-VV phase difference is given by the equation above. Here Re(..) and Im(..) refer to the real and imaginary part. Normal incidence from a highly conductive material such as seawater results in $\rho_{hh\text{-}vv} = 0$ and extremely low variability in the individual pixel phase difference. More complex distributed and layered targets such as sea ice often produce multiple reflections and sometimes non-zero values for $\rho_{hh\text{-}vv}$. Once more, experimental results indicate variation of this parameter with frequency and incidence angle. However, a general trend seems to be that the mean value for multi-year ice is close to zero with negligible variance and is independent of incidence angle. Compared to this, the first-year measurements show significant variation both with frequency and incidence angle both in terms of mean and variance.

2.2.3 Ice Classification

Polarimetric image segmentation requires no a priori information about sea ice and is simply based on the statistical distribution of the data. Several parameters need to be selected prior to segmentation, e.g., the image classes in relation to the sea ice types that can be clearly identified, and the dimension and nature of the feature vector.

Selection of image classes can be done either in a supervised or unsupervised manner. In a supervised polarimetric selection scheme proposed by van Zyl [23], image classes, each corresponding to distinct polarimetric behaviour, were limited to single bounce, double bounce, and diffuse scattering. Supervised methods are known to provide better accuracy but suffer from the need for human interaction to determine classes and identify training regions. In contrast, unsupervised methods determine classes automatically but generally have limited ability to accurately determine division into classes. Rignot and Drinkwater [18] have proposed an unsupervised selection of image classes based on multidimensional cluster analysis of the polarimetric covariance matrix. This technique has been shown to be quite robust and can handle a high degree of noise effects. Furthermore, this method accounts for the distribution of each sample pixel into more than one image class.

Hara et al. [6] have reported the use of neural networks for the unsupervised classification of sea ice. The learning vector quantization (LVQ) is used to determine image classes. This is achieved in the LVQ by utilizing reference vectors in the feature space as training classes. Classification is accomplished by adjusting the reference vectors during training, such that boundaries determined by the minimum Euclidean distance from reference vectors separate the feature space into clustered regions [6].

Given distinct image classes and their polarimetric backscatter behaviour, various methods have been used to segment a radar image. These methods range from using single discriminants to complete polarimetric information (such as provided by the Meuller Matrix). A fully polarimetric maximum likelihood classifier was developed by Kong et al. [9] and extended by Lim [11] on the basis that polarimetric data are characterized by a multivariate Gaussian distribution. Both show from Monte Carlo

simulations and various images that the Bayes classifier produces better results than those obtained using single polarimetric discriminants. Van Zyl and Zebkar [23] used this method for the classification of ice in the Beufort sea. They found that no single frequency data could separate out multi-year and first-year ice reliably, with ridged first-year ice being confused with multi-year ice. The most reliable classification was obtained using data from three different frequencies (C, L and P-bands). The results obtained are noisy and unsatisfactory for most applications. However, an iterative procedure using LVQ and ML procedure [5] has recently shown improved performance.

Rignot and Chellapa [17] extended the ML approach to derive a MAP classifier, where image classes are not assumed to be equally probable and spatial context is used to improve the segmentation results. Using this technique, they extended the analysis of [22] to the delineation of five surface types compressed first-year ice, multi-year floes, first-year ridges and rubble, undeformed thick first-year ice, and thin ice. Though the best classification of these five ice types was obtained using C and L band fully polarimetric data together (> 90% classification accuracy), quite acceptable results were obtained using single frequency data as well (> 82 % classification accuracy). A MAP classifier for Surface based radar returns has been described by Murthy and Haykin [12], the approach is purely Bayesian and the a priori class probability densities are found in a supervised fashion using ground truth information. Also, all the classes are assumed to be equi-probable. The method independently classified like- and cross-pol images and logically combined the classified images to obtain final results.

2.2.4 Use of Circular Polarization for Ice Classification

Stewart [19] studied the statistical behaviour of cross-pol and co-pol returns for a variety of targets. This study also compared the relative bahaviour of linear and circular polarization. He found that for a variety of targets and clutter (not including sea ice, unfortunately), the cross-pol returns are higher than co-pol returns in the case of circular polarization whereas the effect was the opposite for linear polarization. Surprisingly, the correlation between the cross and the co-pol channels was found to be very low in the case of circular polarization, thereby indicating independence between the channels. This points to a increased feature space in the case of circular polarization.

The first reported use of circular polarization for ice studies was with Earth-based planetary radars in the 70s. It was observed that ice elsewhere in the solar system exhibited unique radar properties, namely, high radar reflectivity, circular polarization ratio $\mu_c > 1$, and linear polarization ratio $\mu_L < 0.5$. Circular polarization ratio is defined as RR/RL, LL/LR, or SS/OS. RL refers to echo power in left-circular (L) polarization. In general, μ_c is the ratio of the echo power in the same sense (SS) of circular polarization as transmitted to the echo power in the opposite sense (OS). Similarly, μ_L is HV/HH or VH/VV where H refers to horizontal polarization and V is vertical polarization. It must be noted that for most surfaces $\mu_c < 0.4$ and it is known that specular reflection from a smooth surface reverses the helicity of circular polarization but preserves the direction of linear polarization. Thus, both the ratios will tend to zero in the case of back-reflection

from a perfectly smooth dielectric interface. This is also indicated by the results of Stewart [19] reported earlier.

Recently, Rignot et al. [16] and Haldemann et al. [4] have found similar bahaviour from other terrestrial ice formations like ice on high mountainous regions at low lattitudes and the Greenland ice sheets. It has been found that though μ_c varies with wavelengths, these ice formations consistently indicate $\mu_c > 1$ for wavelengths up to 24 cm, with the ratio decreasing sharply at 68 cm wavelength. This has been observed to be true for a wide range of incidence angles (up to 70°), though it decreased significantly at incidence angles from about 50° to 18°. It was also noted that although the overall behaviour of the linear polarization ratio matched μ_c, the linear ratio was statistically more varying and had a smaller dynamic range (0 to 0.5 as opposed to 0 to 2).

They concluded that the fact that radar returns measured at 68 cm are significantly weaker and have lower polarization ratios than those at 5.6 and 24 cm, suggests that the discrete scatterers responsible for the radar echoes are typically less than a few tens of centimetres thick, similar to the scales of the solid-ice inclusions. The 68 cm echoes probably are dominated by single reflections from deeply buried layers of denser firns, whereas the lower wavelength echoes are probably dominated by multiple scattering from the ice layers and pipes in the most recent annual layer. The relatively sharp decrease in μ_c and μ_L for incidence angles below 50° perhaps reveals the presence of a strong, specular reflection component from the ice layers at small incidence angles, which is also corroborated by the dependence of radar reflectivity on incidence angles.

In a later paper, Rignot [16] presented a model wherein the icy inclusions were modelled as randomly oriented, discrete, noninteracting, dielectric cylinders embedded in a transparent snow medium. The model was able to correctly predict the actual radar observations described above. From studies of this model, they concluded that the large radar reflectivity and polarization ratios arise from internal reflections of the radar signals in the icy inclusions which external first-order reflection models fail to predict.

The discussion in this section has no direct results on sea ice but is nevertheless very interesting and it could be argued that the internal reflections from icy inclusions would be a major contributer to the radar echoes in multi-year ice too, whereas the first-year ice would be a more specular reflector. The rough nature of hummocks, etc. in multi-year ice could also lead to multiple bounce reflections which would increase μ_c. Another interesting fact which came out of the Stewart [19] study is the near zero correlation in the cross and co-pol components in the case of circular polarization. This clearly means that more information is contained in the two channels which could lead to better classification.

2.3 Reference Listings

[1] **C-band backscatter signatures of old sea ice in the central Arctic during freeze-up**

Authors Carlstrom, Anders and Ulander, Lars M. H.

Source IEEE Transactions on Geoscience and Remote Sensing, Vol. 31(4), 1993, pp. 819.

Abstract Radar backscatter signatures of old sea ice in the central Arctic have been measured and analysed. A ship-mounted scattermeter was used to acquire backscattering coefficients at 5.4 GHz in the four liner polarization states and at incidence angles between 20 degrees and 60 degrees. Detailed in situ characterizations of the snow and ice were also made to enable comparison with theoretical backscatter models. Freeze-up conditions were prevalent during the experiment period with air temperatures a few degrees below the freezing point and decreasing. The average backscattering coefficient was found to increase when the temperature of the ice surface layer decreased. The semi-empirical backscatter model is used to evaluate the measurements and shows that the backscatter increase is due to an increasing penetration depth causing the volume scattering to increase. In the paper, model predictions also show that both surface and volume scattering contribute significantly for the incidence angles of the ERS-1 SAR, i.e., 20 degrees to 26 degrees. At these incidence angles, the dominating scattering mechanism changes from surface to volume scattering as the ice surface temperature decreases during freeze-up.

[2] **Evaluation of dual-polarization in the surface-based radar detection of icebergs**

Authors Currie, B. W. and Lewis, E. O.

Source IEEE ELECTRONICOM ‘85 - Conference Proceedings, 1985, page 212

Abstract Ships and drillings platforms operating in Canadian waters need reliable radar detection of icebergs and other ice targets floating in open water. However, for surface-based radars very little quantitative performance measurement has been done. The Department of Fisheries and Oceans, together with the Communications Research Laboratory of McMaster University, conducted an Arctic field trip in September 1984 to record the surface-based radar returns of icebergs, and iceberg fragments. Based on results of previous work, emphasis was placed on the polarization properties of the return; in particular, comparison of horizontally and vertically polarized returns, as well as cross-polarized components. Physical measurements of the iceberg targets, sea surface, and meteorological conditions were taken. Results presented are values of the

normalized radar cross-section for both like-polarized and cross-polarized returns for a of ice targets. The effect of the various polarizations is discussed, and the nature of the returns shows that the use of cross polarization enhances the ice target detection performance of the radar.

[3] **Multifrequency polarimetric synthetic aperture radar observations of sea ice**

Authors Drinkwater, M. R.; Kwok, R; Winebrenner, D. P. and Rignot E.

Source Journal of geophysical research ©, Vol. 96(11), 1991, pp. 20679

[4] **High altitude ice fields searching for unique radar polarization properties**

Authors Haldemann A. F. C and Muhleman D. O.

Source 1996 Fall AGU Meeting Poster U42B-01

[5] **Application of neural networks for sea ice classification in polarimetric SAR images**

Authors Hara, Y.; Atkins, R. G.; Shin, R. T.; Kong, J. A.; Yueh, S. H. and Kwok, R.

Source IEEE Transactions on geoscience and remote sensing, Vol. 33(3), 1995, pp. 740.

[6] **Application of neural networks to radar image classification**

Authors Hara, Y.; Atkins, R. G.; Shin, R. T.; Kong, J. A.; Yueh, S. H. and Kwok, R.

Source IEEE Transactions on Geoscience and remote sensing, Vol. 32, 1994, pp. 100.

[7] **Analysis of polarimetric SAR observations of sea ice**

Authors Israelsson, H. and Askne, J.

Source Proceedings of IGARSS'91 symposium, Vol. 1, pp. 89.

[8] **Theoretical and experimental study of radar backscatter from sea ice**

Authors Kim, Y. S.; Moore, R. K.; and Onstott R. G.

Source RSL technical report RSL TR 331-37, Remote Sensing Laboratory, University of Kansas, 1984

[9] **Polarimetric remote sensing, progress in electromagnetic research**

Authors Kong, J. A. ed.

Source Elsevier Science Publishers, Vol. 3, 1990.

[10] **Theoretical models for active and passive remote sensing of sea ice**

Authors Lee, Yun Hee and Lee, Jay Kyoon

Source Proceedings of the 1995 International Geoscience and Remote Sensing Symposium, Vol. 2, pp. 1451.

Abstract We have developed the theoretical models for scattering and propagation of the electromagnetic wave in multi-layered anisotropic random media to study active and passive microwave remote sensing of sea ice. The theoretical results are used to interpret active and passive remote sensing data from multi-layered random media such as first-year and multi-year sea ices. The comparison between theoretical calculations and data matching with experiments illustrates the merits of theoretical models in understanding and interpreting radar and radiometric observation of various types of sea ice.

[11] **Classification of earth terrain using polarimetric synthetic aperture radar images**

Authors Lim, H. H.; Swartz, A. A.; Yueh, H. A.; Kong, J. A.; Shin, R. T. and van Zyl, J. J.

Source Journal of Geophysical research, Vol. 94, 1989, pp. 7049.

[12] **Bayesian classification of surface-based ice-radar images**

Authors Murthy, Hema A. and Haykin, Simon

Source IEEE Journal of Oceanic Engineering, Vol. 12(3), 1987, pp. 493.

Abstract The Bayes classification procedure has been used to discriminate types of sea ice based on images obtained from surface-based marine radars. The data sets were digitized images obtained from a dual-polarized Ku-band radar (16 GHz) and a like-polarized S-band radar (3 GHz) at a site located on the northern tip of Baffin Island, Canada. The images were range-compensated, and statistical properties of different ice types were determined. The observed histograms for different ice types were approximated by continuous density functions. The images were classified by maximizing the a posteriori probabilities obtained from Bayes' rule. The results suggest that there is sufficient information in the reflectivity to classify the different forms of ice using decision-theoretic pattern recognition techniques.

[13] **Polarimetric signatures of sea ice 1. Theoretical models and 2. Experimental observations**

Authors Nghiem, S. V.; Kwok, R.; Yueh, S. H. and Drinkwater, M. R.

Source Journal of Geophysical Research, Vol. 100(7), pp. 13665.

[14] **Active microwave measurements of artificial sea ice**

Authors Onstott, R. G. and Gaboury, S. H.

Source International Geoscience and Remote Sensing Symposium, Vol. 2, 1988, pp. 805.

Abstract During the winter of 1988, active microwave measurements were made of artificial sea ice using a 5-m multiplied by 15-m outdoor tank of 1.2-m depth filled with sea water. Polarimetric radar backscatter data were collected at 1.8, 5, and 10 GHz for incidence angles 0 degree to 60 degree. Observations commenced with open water and continued until 30 cm of sea ice were formed. Because the roughness of the ice surface is important in determining the general backscatter level for first-year ice, experiments were performed to study the change in backscatter with various roughness scales. Effects of freeze and thaw conditions were also examined. Absolute backscatter levels for new to grey ice are shown to be small, except for the large, coherent returns at vertical. The backscatter responses of new, grey, rough grey, and desalinated first- ice at linear polarization were found to be dissimilar. This was further demonstrated by examining their polarization signatures.

[15] **Polarimetric radar measurements of Arctic sea ice during the Coordinated Eastern Arctic Experiment**

Authors Onstott, Robert G.

Source 10th Annual International Geoscience and Remote Sensing Symposium, Vol. 2, 1990, pp. 1531.

Abstract During March 1989, the first fully polarimetric radar data of Arctic sea ice coordinated with detailed surface characterizations were obtained in the Greenland Sea and at frequencies of 1.8, 5, 10, and 35 GHz from the rail of a ship as part of the Coordinated Eastern Arctic Experiment (CEAREX). Observations were made of numerous ice forms, including multi ice, first- ice, and many stages of new ice, with the addition of the thinnest forms, very fine spicules of ice in suspension. Transits were made from open water through the ice edge and, after a significant opportunity when off-ice winds created a diffuse marginal ice zone (MIZ), to nearly 35 nm through the MIZ into the pack ice.

[16] **Unusual radar echoes from the greenland ice sheet**

Authors Rignot, E. J.; Ostro, S. J.; van Zyl, J. J. and Jezek, K. C.

Source Science, Vol. 261, 1993, pp. 1710.

[17] **Segmentation of polarimetric synthetic aperture radar data**

Authors Rignot, E. J. M. and Chellappa, R.

Source IEEE Transaction on Geoscience and remote sensing, Vol. 30(7), 1992.

[18] **On the application of polarimetric radar observations for sea ice classification**

Authors Rignot, E. J. M. and Drinkwater, M. R.

Source Proceedings of IGARSS'92 symposiumm 1992

[19] **Use of crosspolar returns to enhance target detectability**

Authors Stewart, N. A.

Source IEE Electromagn Waves Ser 20, Adv in Radar Tech. Publ by Peter Peregrinus Ltd, London, England, 1985, pp. 449.

Abstract An instrumental X-band radar has been used to measure the relative magnitudes of copolar and crosspolar returns from targets and clutter for linear and circular transmit polarizations. The data were analysed to see if the inclusion of a second receiver to make use of crosspolar information in the crosspolar signal can be justified. However, when circular polarization is transmitted, the inclusion of a second channel can enhance detections by 1-4 dB. The spectral returns of clutter were also measured, and it is shown that the spectra of copolar and crosspolar returns are identical.

[20] **Microwave remote sensing, Volume 2**

Authors Ulaby, F. T.; Moore, R. K. and Fung, A. K.

Source Reading, Massachusetts, Addison-Wesley, 1982

[21] **C-band radar backscatter of Baltic sea ice theoretical predictions compared with calibrated SAR measurements**

Authors Ulander, L. M. H.; Johansson, R. and Askne, J.

Source International Journal of Remote Sensing, Vol. 13(13), 1992, pp. 2447.

Abstract Airborne Synthetic Aperture Radar (SAR) data have been analysed together with in situ measurements of sea ice during the Bothnian Experiment in Preparation for ERS-1 (BEPERS) in March 1988. Based on the physical properties of the snow-covered level ice, a scattering

model is used to predict the C-band like-polarization backscattering coefficient in an experiment area. Both the average backscattering coefficient and the SAR image texture were found to be in good agreement with the scattering model predictions. The backscatter signature of the level ice was found to be dominated by the ice surface r.m.s. height and autocorrelation function. These parameters were determined from profiles of the ice surface height, which were measured using a laser profiler device with sub-mm accuracy. The present model is expected to be accurate when the backscattering is dominated by scattering from the cm-scale snow or ice surface roughness.

[22] **Unsupervised classification of scattering behaviour using radar polarimetry data**

Authors van Zyl, J. J.

Source IEEE Transactions on Geoscience and remote sensing, Vol. 27(1), 1989, pp. 36.

[23] **Imaging radar polarimetry, Polarimetric remote sensing**

Authors van Zyl, J.J. and Zebker H.A.

Source Progress in Electromagnetics research, edited by J.A. Kong, Elsevier Science Publishers, New York, 1990

[24] **Surface-based Radar: Noncoherent**

Authors Lewis, E. O.; Currie, B. W. and Haykin, S.

Source Remote Sensing of Sea Ice and Icebergs: Edited by: S. Haykin, E.O. Lewis, R. K. Raney and J. R. Rossiter, John Wiley and Sons Inc., New York, 1994.

2.4 Bibliography

[1] **Radar backscatter measurements from Arctic sea ice during the fall freeze-up**

Authors Beaven, Scott G. and Gogineni, S. Prasad

Source Proceedings of the 13th Annual International Geoscience and Remote Sensing Symposium, Volume 2, 1993, pp.850.

Abstract C-band radar backscatter from sea ice increases dramatically during the fall freeze-up. Measurements taken from a ship-borne scatterometer during the International Arctic Ocean Expedition IAOE'91 show that this increase is 15-20 dB at incidence angles from 25 degree to 35 degree. This increase in backscatter is shown to be due mainly to a transformation from primarily surface scattering to primarily volume

scattering through the use of simple scattering models. The re-freezing of moisture on or near the sea ice surface is believed to cause the increase in volume scatter. We applied a coherent noise reduction scheme to these data to improve the quality of the measurements and to remove systematic noise s that corrupt the measurements. This scheme reduces coherent noise s by 10 to 20 dB.

[2] **Comparison of measurements and theory for backscatter from bare and snow-covered saline ice**

Authors Bredow, Jonathan W. and Gogineni, Sivaprasad

Source IEEE Transactions on Geoscience and Remote Sensing, Vol. 28(4), 1969, pp. 456.

Abstract C-band radar backscatter measurements were made on artificially grown sea ice at the U.S. Army Cold Regions Research and Engineering Laboratory (CRREL) during the winters of 1987-1988 and 1988-1989. These measurements were made on smooth, rough, and snow-covered saline ice. The measured sigma degree (theta) of smooth saline ice (rms height less than 0.05 cm) disagreed with small perturbation method (SPM) surface scattering predictions. Using physical parameters of the ice in a simple layer model, we show that this discrepancy can be explained by scattering from beneath the surface. A thin (7-cm) dry snow cover had a significant influence on backscatter from the smooth ice sheet. This influence was due to scattering from particles within the snow, and can be predicted by a commonly used empirical layer model for snow. The results of backscatter measurements of a moderately rough saline ice sheet were found to agree with SPM predictions.

[3] **Radar backscattering from artificially grown sea ice**

Authors Bredow, Jonathan and Gogineni, Siva P.

Source IEEE Journal of Oceanic Engineering, Volume 14(3), 1969, pp. 259.

Abstract Fine-resolution X-band backscatter measurements from artificially grown sea ice were made at the U.S. Army Cold Region Research and Engineering Laboratory (CRREL) in January 1987. Backscatter data were collected from unmodified smooth ice and snow-covered ice, and from ice from which the snow had been removed (slightly roughened ice). The results indicate that vertically polarized returns were consistently higher than horizontally polarized echoes, from both the slightly roughened and snow-covered saline ice. A 6.5-cm-thick dry snow layer altered the sigma **0 of the original smooth-surfaced saline ice only slightly, but introduced a noticeable volume scattering component. It is shown that although substantial agreement exists between the bare first- ice measurements and commonly used surface-

scatter model predictions, a complete model of first- ice must include a volume-scatter contribution.

[4] **Active/passive microwave signatures of springtime Barents Sea ice**

Authors Collins, Michael J. and Ramseier, Rene O.

Source 10th Annual International Geoscience and Remote Sensing Symposium, Vol. 2, 1991, pp. 1517

Abstract Active and passive microwave signatures of young sea ice forms and complex snow covers encountered in the Barents Sea during the early summer of 1989 are presented. The data were collected during the ARKTIS VI-1 cruise of the FS Polarstern. The young ice was considered transient in that it had formed during the decreasing episodes of subzero weather and would melt or disappear altogether during the oncoming summer sun. The snow cover, which had suffered several freeze-melt cycles, was composed of many disparate layers of snow as well as scattered thin-ice lenses. These conditions, which are typical of early summer, are an important link to understanding the microwave signature of sea ice during this period. Backscatter data were collected with an X-band FM-CW radar. Emission data were collected with a 37-GHz radiometer. The major results from this study are summarized.

[5] **Frequency and polarization properties of the reflectivity from sea ice**

Authors Currie, N. C. and Odom, D. L.

Source IEEE 1985 International Radar Conference, 1985, pp. 247.

Abstract An experiment was performed in May 1983 to measure the reflectivity properties of first- and multi-year sea ice at frequencies of 3 GHz through 35 GHz. At several of the frequency bands, dual polarized measurements were performed as well (HH and HV polarizations). The primary motivation for the experiment was to develop discriminants for separating radar return, of multi-year ice from first-year ice. They describe the experiment and present some of the dual polarized data at 16 GHz for various ice features. Preliminary conclusions are presented concerning the usefulness of polarization as a sea ice discriminant, and an outline for future work is proposed.

[6] **Microwave remote sensing of sea ice**

Authors Carsey, Frank D.(Editor)

Source Geophysical Monograph Series, American Geophysical Union, Vol. 68, 1992.

[7] **Modeling interpretation of scattering from snow-covered sea ice**

Authors Fung, A. K.; Tjuatja, S. and Beaven, S.

Source Proceedings of the 1994 International Geoscience and Remote Sensing Symposium, Vol. 1, 1991, pp. 617.

Abstract Radar scattering measurements of saline ice at 5.3 and 13.4 GHz were collected during the 90 and 92 winter seasons at the U.S. Army Cold Regions Research and Engineering Laboratory (CRREL). Both like and cross polarizations were obtained from saline ice with and with out snow cover. The results of these measurements were examined with a radiative transfer model applied to inhomogeneous layers with densely populated discrete scatterers. It is found that bare saline ice has a low albedo and hence its like polarized backscattering is dominated by the irregular air-ice interface over 10 to 50 degrees. The effect of volume scattering is observable between 50 to 60 degrees. For cross-polarized scattering, volume scattering effect is also small compared with surface scattering. When there is snow cover, there is a general increase in scattering along nonspecular directions. This is attributed to the brine wicking effect which causes a higher concentration of brine along the interface region and a possible roughening of the snow-ice interface.

[8] **Time-domain and frequency-domain feature selection for reliable radar target identification.**

Authors Garber, Frederick D.; Chamberlain, Neil F. and Snorrason, Ogmundur

Source Proceedings of the 1988 IEEE National Radar Conference, pp. 79.

Abstract Techniques for selecting features that can be applied to time-domain or frequency-domain polarization-diverse radar scattering data are presented. A scheme for transforming broadband scattering matrix data in a horizontal-vertical polarization base, to a set of time-domain waveforms in a mixed linear/circular polarization base are described. The transient polarization impulse responses thus derived were shown to be closely related to target geometry. It was also shown that portions of this response could be parameterized in terms of elliptical features which, in turn, could be used to identify radar targets. The results presented indicate that polarization information alone is sufficient to allow reliable target identification performance at signal-to-noise ratios as low as 0 dB. In addition, a technique for selecting features directly from frequency-domain radar scattering data was presented. It is shown, using the results of simulation studies, that the technique is effective in selecting sets of frequencies that allow reliable target identification. These results also indicated trends in the characterization of the optimum feature sets and in the resulting performance relative to ranges of azimuth angle and the size of features.

[9] **Polarization diversity in radars**

Authors Giuli, Dino

Source Proceedings of the IEEE, Vol. 74(2), 1985, pp. 245.

[10] **Polarisation behaviour of ground clutter during dwell time**

Authors Giuli, D.; Fossi, M. and Gherardelli, M.

Source IEE Proceedings, Part F Radar and Signal Processing, Vol. 138(3), 1991, pp. 211.

Abstract The paper analyses the behaviour of ground clutter during dwell time in a low-resolution radar. The analysis is made with reference to measurements made through a pulse radar using right-handed circular polarisation at transmit and two orthogonally circularly polarised channels on reception. Symmetric and asymmetric distribution of polarisation with respect to its average is pointed out for two different types of ground clutter, the 'clustered clutter' and the 'distributed clutter'. Suitable parameters are defined and evaluated for statistical analysis of the experimental data to characterise and classify the observed phenomena. Frequent scan-to-scan stationarity of ground clutter polarisation is highlighted, which makes the statistical analysis meaningful for the application of suitable adaptive polarisation filtering techniques for ground clutter rejection.

[11] **Radar backscatter from sea ice**

Authors Gogineni, S. Prasad

Source Proceedings of the 1986 IEEE National Radar Conference, pp. 107.

Abstract Experiments have been conducted since 1977 to determine the optimum parameters for both satellite and aircraft imaging radars that can be used for ice mapping. The author summarizes the results of this research. A brief description of the system used in the measurement program is given. In order to acquaint the reader with the sea ice terminology, a brief review of physical properties is presented. The backscattering cross-sections of winter and summer ice are given. Finally, conclusions and future research directions are presented.

[12] **Experimental and theoretical investigation of radar backscattering from saline and desalinated ice**

Authors Gogineni, S.; Bredow, J.; Jezek, K. and Perovich, D.

Source 10th Annual International Geoscience and Remote Sensing Symposium, Vol. 3, 1990, pp. 1879.

Abstract An experiment was performed in May 1983 to measure the reflectivity properties of first- and multi sea ice at frequencies of 3 GHz through 35 GHz. At several of the frequency bands, dual polarized measurements were performed as well (HH and HV polarizations). The primary motivation for the experiment was to develop discriminants for separating radar return, of multi ice from first-year ice. They describe the experiment and presents some of the dual polarized data at 16 GHz for various ice features. Preliminary conclusions are presented concerning the usefulness of polarization as a sea ice discriminant, and an outline for future work is proposed.

[13] **Radar backscatter measurements over saline ice**

Authors Gogineni, S. and Moore, R. K.

Source International Journal of Remote Sensing, Vol. 11(4), 1990, pp. 603.

Abstract During the 1984 and 1985 winter seasons, radar backscatter measurements were performed on artificial sea ice at the U.S. Army Cold Regions Research and Engineering Laboratory (CRREL) at Hanover, New Hampshire. Radar data were collected at selected frequencies in the 4-17 GHz region for incidence angles from 0 to 60 degree with like and cross polarizations. These measurements were performed on smooth, rough, bare and snow-covered saline ice and open water. Backscattering from ice increased with its thickness until the ice was about 1 cm thick and then decreased gradually with further growth. Rough ice and snow-covered ice gave similar returns at 13.6 GHz, but the scattering coefficients of snow-covered ice were lower than that of rough ice at 9.6 GHz.

[14] **Multifrequency passive microwave observations of first-year sea ice grown in a tank**

Authors Grenfell, Thomas C.and Comiso, Josefino C.

Source IEEE Transactions on Geoscience and Remote Sensing, Vol. 24(6), 1986, pp. 826.

Abstract Microwave brightness temperatures were obtained for new, young, and optically opaque sea ice grown in a large tank. Dual-polarized observations were taken at frequencies of 10, 18, 37, and 90 GHz over a range of incidence angles, and the concurrent temperature and ice thickness were obtained. Bulk salinities as well as radar and dielectric properties were also measured concurrently by other investigators. Emissivity and degree of polarization were observed in detail during the early stages of ice growth and variations were found indicating that the ice became optically opaque at 10 GHz for ice thickness between 30 and 50 mm. The addition of a snow cover reduced the brightness temperature

at frequencies above 10 GHz. Artificial roughening of the surface reduced the degree of polarization considerably, but changed the emissivity at vertical polarization only slightly. Cluster plots of the data shown six distinguishable surface types optically opaque bare ice, thin ice (less than 15 mm), roughened ice, ridged ice, rotting wet ice, and open water.

[15] **On radar polarization mixed target state decomposition techniques**

Authors Holm, William A. and Barnes, Richard M.

Source Proceedings of the 1988 IEEE National Radar Conference, pp. 249.

Abstract The mathematical representations of mixed target states using Mueller, covariance, and density matrices are discussed, and the relationship between these matrices is shown. A decomposition technique due to J. R. Huynen (1970) is considered, and a simple algorithm for calculating it is demonstrated. It was shown that, in addition to the Huynen decomposition, exactly two other decompositions exist whose mixed-target-state components possess the same roll-invariant property as the distributed N-target mixed-target-state component in the Huynen decomposition. The mixed-target-state components of all three of these Huynen-type decompositions were shown to correspond to targets with circular polarization nulls. The characteristic decomposition was then discussed and applied to a simple example which demonstrated that its pure-state component provides the average target representation. It is noted that this decomposition may have applications to stationary target identification.

[16] **Comparison of radar backscatter from antarctic and arctic sea ice**

Authors Hosseinmostafa, A. R. and Lytle, V. I.

Source Journal of Electromagnetic Waves and Applications, vol. 9(3), 1995, 421.

Abstract Backscatter measurements at C band over sea ice in the Weddell Sea were made on First- (first-year) and Second- (SY) snow-covered sea ice at different incidence angles and detailed snow and ice characterizations were performed. The results showed that the presence of slush at the snow-ice interface effectively masked the distinction between first-year and SY ice. The results were compared with data collected over sea ice from the Arctic. Backscatter for first-year ice were similar in magnitude for both sites. Returns from the Arctic SY ice were about 3-7 dB higher than those from the Weddell Sea. This difference is believed to be due to the presence of a slush layer over the SY ice surface studied. The wet slush layer reduced the penetration depth into the ice, significantly reducing the volume scatter contribution from the ice.

[17] **Effect of a snow cover on microwave backscatter from sea ice**

Authors Kim, Young-Soo and Onstott, Robert G.

Source IEEE Journal of Oceanic Engineering, Vol. 9(5), 1984, pp. 383.

Abstract The effect of a snow cover on sea ice upon radar backscatter at microwave frequencies (X- and Ku-band) can be important. The effect of scattering from the snow cover on the SIGMA DEGREE of first- ice is shown to be severe (5 cm of dry snow can raise SIGMA DEGREE by 8 dB at 9 GHz), while that on SIGMA DEGREE of multi ice is shown to be smaller. The low thermal conductivity of snow compared to that of sea ice effectively raises the temperature of the upper surface of the ice, resulting in higher dielectric constants for the ice, thereby modifying the backscatter both from the ice surface and from the scattering volume. The temperature effect of a 10 cm snow cover on 3 m thick multi-year ice is to lower the SIGMA DEGREE by only about 0. 3 dB for air temperature of MINUS 20 DEGREE C.

[18] **Build a circularly polarized waveguide slot antenna**

Authors Kisliuk, M and Axelrod, A.

Source Microwaves & RF, Vol. 26(6), 1987, pp. 139.

Abstract The article provides design considerations and performance analysis of an antenna with nearly circular polarization, which incorporates a longitudinal and transverse resonant slot cut in the broad wall of a rectangular waveguide. The proposed antenna can be used as an element of phased arrays, imaging systems, or as a stand-alone circular polarized antenna.

[19] **Polarimetric backscattering characteristics of three-dimensional random targets multi-polarization scattering coefficients versus a modified Mueller matrix**

Authors Kobayashi, Osamu; Hirosawa, Haruto and Matsuzaka, Yukihiko

Source 10th Annual International Geoscience and Remote Sensing Symposium – IGARSS'90, pp. 49.

Abstract Full polarization signatures of backscatters from random media have been measured using a multipolarization power-measuring scatterometer in a laboratory. The targets are three-dimensional extended ones: coniferous trees and artificial random targets which imitate trees. The features of the polarization signatures and the polarizations with primary importance are discussed. For a target composed of needle- or rod-shaped scatterers, the ratios of the backscattering coefficients of linear copolarizations to those of linear cross-polarizations are quite small; and

the backscattering coefficients for circular copolarizations and cross-polarizations are roughly equal. For a target composed of flat scatterers, the ratios of the backscattering coefficients of linear copolarizations to those of linear cross-polarizations are large, and a difference is observed among the backscattering coefficients of circular copolarizations and cross-polarizations.

[20] **Identification of of terrain cover using the optimum polarimetric classifier**

Authors Kong, J. A.; Swartz A. A.; Yueh, H. A.; Novak, L. M. and Shin R. T.

Source Journal of Electromagnetic wave application, Vol. 2(2), 1988, pp. 171.

[21] **Active microwave remote sensing of an anisotropic random medium layer**

Authors Lee, Jay Kyoon and Kong, Jin Au

Source IEEE Transactions on Geoscience and Remote Sensing, Vol. 23(6), 1985, pp. 910.

Abstract A two-layer anisotropic random medium model has been developed to study the active remote sensing of the earth. The dyadic Green's function for a two-layer anisotropic medium is developed and used in conjunction with the first-order Born approximation to calculate the backscattering coefficients. It is shown that strong cross-polarization occurs in the single scattering process and is indispensable in the interpretation of radar measurements of sea ice at different frequencies, polarizations, and viewing angles. The effects of anisotropy on the angular responses of backscattering coefficients are also illustrated.

[22] **Effect of polarization on the marine radar detection of icebergs**

Authors Lewis, E. O.; Currie, B. W. and Haykin, S.

Source Record of the IEEE 1985 International Radar Conference, pp. 253.

Abstract Ships and drilling platforms operating in Canadian waters need reliable radar detection of icebergs and other ice targets floating in open water. A field trip made in September 1984 to record the surface-based radar returns of icebergs and iceberg fragments is discussed. Based on results of previous work, emphasis was placed on the polarization properties of the return, in particular, comparing horizontally and vertically polarized returns, as well as cross-polarized components. Physical measurements of the iceberg targets, sea surface, and meteorological conditions were taken. Results are presented as histograms of the normalized radar cross-section for both like- and cross-polarized returns for a of ice targets. The effect of the various polarizations is discussed and some preliminary conclusions drawn.

[23] **Detection of sea ice features using K//A-band radar**

Authors Lewis, E. O.; Haykin, S. and Currie, B. W.

Source Electronics Letters, Vol. 21(11), 1985, pp. 499.

Abstract Analysis of recorded radar data collected from a mixed field of Arctic ice shows that the K//a-band returns, more so than other frequencies, can be used to delineate targets that pose a threat or impediment to navigation. In particular, it is shown that the K//a-band returns highlight multi ice-floes, icebergs and first- ice pressure ridges.

[24] **Theoretical models for microwave remote sensing of snow-covered sea ice**

Authors Lin, F. C.; Kong, J. A. and Shin, R. T.

Source IGARSS'87. Remote Sensing Understanding the Earth as a System, 1987, pp. 1121.

Abstract The volume scattering effects of snow-covered sea ice are studied with a three-layer random-medium model for microwave remote sensing. The strong fluctuation theory and the bilocal approximation are applied to calculate the effective permittivities for snow and sea ice. The wave scattering theory in conjunction with the distorted Born approximation is then used to compute bistatic coefficients and Backscattering cross sections. Theoretical results are illustrated by matching experimental data for dry-snow-covered thick first- sea ice at Point Barrow. The radar backscattering cross sections are seen to increase with snow cover for snow-covered sea ice, due to the increased scattering effects in the snow layer. The results derived can also be applied to the passive remote sensing by calculating the emissivity from the bistatic scattering coefficients.

[25] **Effects of ice ridge properties on calculated surface backscattering in BEPERS-88**

Authors Manninen, A. T

Source International Journal of Remote Sensing, Vol. 13(13), 1992, pp. 2469.

Abstract The variation of the surface backscattering of ice ridges for frequency 5.3 GHz is examined with a three-dimensional geometrical model for ice ridges and small-scale perturbation theory. Multiple reflections are not included. The most important ridge properties for low salinity ice studied during the BEPERS experiment are the small scale surface roughness, the dielectric constant and the detailed ridge geometry parameters (like ice block orientations, etc.) in that order. The incidence angle distribution of an ice ridge is also affected by the minor facets of the ice blocks. For BEPERS ridges and radar parameters the contribution of single specular reflections to the backscattered intensity is not large.

[26] **Comparison of coherent and noncoherent polarimetric radar measurement techniques at 95 GHz**

Authors Mead, James B.; Pazmany, Andrew L.; Chang, Paul S. and McIntosh, Robert E.

Source Radio Science, Vol. 31(2), 1996, pp. 325.

[27] **Polarimetric observations and theory of millimeter-wave backscatter from snow cover**

Authors Mead, James B.; Chang, Paul S.; Lohmeier, Stephen P.; Langlois, Philip M. and McIntosh, Robert

Source IEEE Transactions on Antennas and Propagation, Vol. 41(1), 1993, pp. 38.

Abstract Polarimetric radar measurements carried out at 95 and 225 GHz are presented for fresh and refrozen snow cover. These data indicate that the Mueller matrix for snow cover consisting of spherical ice particles has a relatively simple form, with 10 of the 16 elements approximately zero. Measurements of new-fallen snow consisting of predominantly nonspherical snow crystals are also presented. The anisotropic structure of such snow cover results in a more complex Mueller matrix, fitting the general form for natural surfaces. An analytic expression for the Mueller matrix of isotropic snow cover is derived by computing the response of a semi-infinite layer of scatters that are insensitive to the orientation of the incident polarization. This matrix is shown to accurately predict the polarimetric response of the snow cover comprised of spherical ice particles based solely on co- and cross-polarized radar cross-section measurements. The model also correctly predicts that the correlation between S//h//h and S//v//v is independent of incidence angle and predicts that depolarization will decrease with increasing incidence angle.

[28] **Use of circular polarization in a marine radar positioning system**

Authors Michelson, D. G.; MacNeil, D. J.; Jull, E. V.; Lyall, R. G. and Lanziner, H. H.

Source IGARSS'89 - Twelfth Canadian Symposium on Remote Sensing, Vol. 2, 1989, pp. 932

Abstract There is a need for a simple, reliable vessel-positioning system for use by vessels navigating in coastal or inshore waters during periods of limited or restricted visibility. Existing aids to navigation either lack the accuracy required for use in narrow channels and harbors (e.g., loran-C or GPS), or are too expensive and require too much ongoing maintenance and support to be viable for general use (e.g., active

microwave transponders). A passive radar positioning system that uses a network of specially designed trihedral twist reflectors as landmarks and circular polarization for background clutter suppression is described. Field trials of the system have been conducted in Indian Arm, British Columbia and Port aux Basques, Newfoundland. Initial results have confirmed that use of circular polarization can suppress background clutter sufficiently to permit positive identification of the specially designed radar targets by an automated system.

[29] **Loop antenna with a branch wire for circular polarization**

Authors Nakamura, Takashi and Yokokawa, Senji

Source Electron Commun Jpn Part 1, Vol. 70(11), 1987, pp. 110.

Abstract Circular polarizations are used widely in radar, satellite communication and mobile communication. This paper reports on the analysis and design of a circularly polarized antenna consisting of a loop antenna with a branch wire of an appropriate length. The idea for developing this antenna derives from the fact that the branch wire has a characteristic as a transmission line coupled with a loop conductor. The present structure is a simple single-feed antenna operating equivalently as a two-point feed-loop antenna.

[30] **Radar backscatter signatures of thin sea ice in the central Arctic**

Authors ng

Source International Journal of Remote Sensing, Vol. 15(5), 1994, pp. 1149.

Abstract To investigate the ability of radars to map thin ice we performed radar backscatter measurements early in the fall freeze-up as part of the International Arctic Ocean Expedition '91 (IAOE'91). We collected data over the thin ice types of light nilas, dark nilas, and pancake/slush ice using a ship-based, C-band FM radar with all four linear polarizations. Our results indicate that radars must be able to measure sigma **0 as low as- 30 dB for VV polarization and -34 dB for HH polarization. The noise-equivalent sigma **0 for the ERS-1 Synthetic-Aperture Radar is -24 dB and for RADARSAT is -23 dB. This implies that these sensors are not capable of monitoring thin sea ice types such as dark niolas and grease ice but may be able to detect slightly thicker ice, such as light nilas and pancake ice, due to their higher backscatter.

[31] **Weibull-distributed radar clutter reflected from sea ice**

Authors Ogawa, Hiroshi and Sekine, Matsuo

Source Trans Inst Electron Inf Commun Eng Sect E, Vol. 70(2), 1987, pp. 116.

Abstract Sea ice clutter was measured using an X-band radar which is located at

Mombetsu in Hokkaido. The pulsewidth of the radar was 80 nsec. To sample by 40 nsec and record digitally, emitter coupled logic (ECL) was used as a high-speed IC. The sampled data were first transferred to 64 Kbyte dynamic memory board and next to a 5 inch floppy disk through an 8 bit microcomputer. These data were processed by a 16 bit microcomputer. As a result, it is shown that the amplitude of sea ice obeys a Weibull distribution with shape parameters of c = 0. 50 to 1. 65. Thus, the amplitude statistics deviate from the Rayleigh distribution of c = 2. 0, in which a logarithmic/constant false alarm rate (LOG/CFAR) circuit is useful. It is concluded that the new Weibull/CFAR should be considered to suppress sea ice clutter.

[32] **Detection of sea ice and ships in radar sea clutter**

Authors Oi, Masayuki and Ishikawa, Masao

Source Proceedings of the 1984 International Symposium, ISNCR-84, 1984, pp. 141.

Abstract Frequency analyses of the variations of radar return from sea ice were carried out to distinguish between sea ice and sea clutter. Based on these data, an experiment was executed to evaluate the effectiveness of the sea clutter suppression system to a sea ice observation.

[33] **Radar backscatter of sea ice during winter**

Authors Onstott, R. G. and Shuchman, R. A

Source IEEE IGARSS'88 - Remote Sensing Moving towards the 21st Century, 1988, pp. 1115

Abstract Active microwave measurements were made during the 1987 Marginal Ice Zone Experiment (MIZEX). Backscatter data were acquired at frequencies from 1.25 to 35 GHz, at incidence angles from 0 degree to 80 degree, and with linear antenna polarizations. The objective was to describe the scattering coefficients of the major ice types in the region and to study the winter conditions and their influence on the microwave response. Results show that multi and pancake ice produces strong backscatter, while returns from open water between floes and new ice are weak. First-year ice has a wide range of returns. When the surface is smooth, returns are weak; if the surface is roughened, i.e., like pancake ice, the returns increase substantially.

[34] **Theoretical and experimental study of the radar backscatter of Arctic sea ice**

Authors Onstott, Robert G.

Source International Geoscience and Remote Sensing Symposium (IGARSS) 1987, pp. 1121

Abstract A theory has been developed to model the backscatter from sea ice. This model has proven useful in interpreting the microwave signatures of the many ice forms. Results have also been used in providing direction in the measurement of physical and electrical properties in recent sea ice investigations. The parametric studies that have followed have allowed the examination of the sensitivity of the microwave signature to changes in key ice sheet parameters. These include salinity, temperature, brine volume, density, air bubble size, and surface roughness.

[35] **Real-time radar detection of iceberg shadows**

Authors Orlando, James R. and Haykin, Simon

Source IEEE Journal of Oceanic Engineering, Vol. 15(2), 1990

Abstract The Hough transform is used to estimate the radial direction of shadows cast by icebergs in surface-based marine radar returns using a Warp systolic computer. Automatically locating these shadows leads directly to automatically locating the icebergs casting the shadows. This is useful for the unattended navigation of a vessel through sea ice, as well as for improving the accuracy of a classified sea ice image. The results reported show that the Hough transform can successfully estimate the radial directions of the shadows cast by the icebergs, and that the implementation on the Warp computer is commensurate with a real-time requirement for shadow detection.

[36] **Classification of sea ice images using a dual-polarized radar**

Authors Orlando, James R.; Mann, Richard and Haykin, Simon

Source IEEE Journal of Oceanic Engineering, Vol. 15(3), 1990

Abstract The classification of the returns of a ship-borne like- and cross-polarized radar system into one of four categories, first-year ice, multilayer ice, icebergs, and shadows cast by icebergs is described. The data sets are digitized images obtained from a dual-polarized noncoherent Ku-band (16.5-GHz) radar used on the northern tip of Baffin Island, Canada. By using both the like- and cross-polarized radar inputs, classifier accuracy is improved compared to previous classifiers using only a single input. In particular, the use of both polarizations significantly improves the discrimination between icebergs and multilayer ice. In order to combine the like- and cross-polarized inputs, four classifiers are used a one-dimensional classifier using the composite image formed by fusing the two polarization inputs with principal components analysis; a two-dimensional Gaussian classifier; and two neural network classifiers (the multilayer perceptron and the Kohonen feature map classifier). The results are compared to the classification based on a single like- or cross-polarized input.

[37] **Radar cross-section analysis using theoretical and experimental signatures**

Authors Sampath, V.; Delisle, G. Y. and Raymond, J.

Source Canadian Journal of Electrical and computer engineering, Vol. 18(4), 1993, pp. 171.

[38] **Dual polarized ice surveillance radar antenna**

Authors Shafai, L. and Ittipiboon, A.

Source IEEE ELECTRONICOM '85 - Conference Proceedings, 1985.

Abstract The design and performance of a low-sidelobe, dual-polarized antenna is described. It consists of an offset parabolic cylindrical reflector having the aperture dimensions of 8. 8 ft X 1. 6 ft. The line- feed consists of two transverse and longitudinal half-wave dipole arrays over a ground plane, separately excited for simultaneous dual-polarized operation. The aperture illumination on the transverse plane of the longitudinal array is made identical to that of the transverse array by using two beam-forming rods located symmetrically and parallel to the arrays. The amplitude distributions of the arrays are tapered to provide the low-sidelobe requirement on the horizontal plane.

[39] **Sensitivities for two polarimetric backscattering models for sea ice to geophysical parameters**

Authors Winebrenner, Dale P.; Tsang, L.; Wen, B. and West, R.

Source W.M. Boerner (ed.) Direct and Inverse Methods in Radar Polarimetry, 1992.

2.5 Conclusions

The current study is limited to the use of only two channels, namely like- and cross-polarized ones. Therefore, the only quantity of interest is the cross polarization ratio defined earlier. Based on the theoretical models available in the literature ([13], [18], and [10]) it can be concluded that the main contribution to depolarization results from volume scattering and surface scattering has very little depolarization effect, the only contribution being because of surface roughness leading to multiple reflections [24]. Due to the inhomogeneous nature of multi-year ice, volume scattering is a dominent scattering component and thus it can be expected that the multi-year ice show a larger cross-polarization ratio than first-year ice.

A variety of experimental data is available in the literature, although very few studies have collected data at low grazing angles. A systematic study of polarization effects of sea ice using surface based radar has been reported in [24]. The results obtained are in

good agreement with the theoretical predictions and both at Ku band and X-band it was found that multi-year ice has higher cross-polarization ratios than moderately rough first-year ice.

Other results have also been reported at X, C and L-bands, these results however are for higher grazing angles ([21], [15], and [13]). It was generally observed that the depolarization differences between multi-year and first-year is more prominent at higher grazing angles, one possible explanation being the reduction of surface roughness of first-year ice at these angles, leading to even lower cross polarization ratios for smooth first-year ice.

We can therefore conclude that the cross-polarization ratio is a very important discriminant of the ice types and can be used to enhance the ice hazard detection capability of marine radars. Algorithms that exploit the cross-polarization ratio are described in the next section.

THIS PAGE IS INTENTIONALLY LEFT BLANK

3 RADAR IMAGE MATCHING

In the dual-polarized radar system used on the MV Arctic during the field experiment voyage in the fall of 1995, there were two receivers: one for the horizontal transmit - horizontal receive (HH) polarization signal and one for the horizontal transmit - vertical receive (HV) polarization signal. Each received signal was subject to its own receiver's gain and sensitivity time control (STC) settings. Each receiver's video out signal was connected to its own Modular Radar Interface (MRI), which processed the signal and produced a PPI (X-Y) radar image for display. At selected times, sequences of PPI images from successive scans of the HH and HV radars were captured to 8 mm tape, to provide a data base for post-experiment analysis.

This document describes the nature of the recorded data, selection of data sets for further study, issues and steps involved in matching the HH and HV images, and processing applied to the HH-HV image pairs in an attempt to provide a single informative image of greater use to the mariner.

3.1 Data Format

The data recorded by a given MRI for a single radar scan consisted of a PPI image, 1024 pixels by 1024 lines by 8 bits per pixel, and an information header. Both MRIs were

connected to a GPS (Global Positioning System) information system, which provided them with both position (latitude and longitude), and time. This GPS information was captured into the header.

Once data acquisition was initiated, both MRIs attempted to capture the image and associated header for each successive scan to tape until the process was manually interrupted. Each of these uninterrupted data collection runs is termed a sequence. Due to hardware/software limitations during the voyage, only a maximum of 9 sequences could be written to one tape. A compounding limitation was that the radar and MRI settings could only be changed with recording stopped; i.e., each change required the starting of a new sequence. The original intent was to vary radar settings as much as possible while in a given ice scenario, and record a sequence of scans for each setting. The above constraints limited the scope of the investigation.

The recorded data base consists of 19 8-mm tapes for each of the HH and HV radars. Typically there are 9 sequences on each tape, with about 25-50 scans per sequence, and with some change in settings between sequences. On a few tapes, a very long sequence was recorded.

3.2 Settings

There were a number of settings that could be changed in the radar/MRI system. For the radar itself, the operator could change the gain, STC, and range scale (to which pulse length was slaved). Both the gain and STC settings were analog rotary controls. During data collection, the approximate setting of each knob, relative to full rotation, was noted. The primary range scales of interest were 1.5, 3.0, and 6.0 nmi (nautical miles).

For the MRIs, there was also a gain and offset setting for the A/Ds. There were two filters available. The pulse filter used a double-pole recursive filter in azimuth to provide pulse-to-pulse filtering. This filter was on for nearly all the recordings. The constant false alarm rate (CFAR) filter, when selected, applied a sliding window in range over which the local background return level was estimated and subtracted from the return. This was in essence a high-pass filter operation, designed to remove extended areas of nearly constant return and highlight sudden signal variations.

3.3 Data Recovery

The data was recorded in a format proprietary to Titan, the MRI manufacturer. Titan was contracted to provide software to permit viewing of the recorded images, and to write selected images to disk for processing.

To facilitate subsequent processing, undertaken using Matlab 4.2, the Titan image extraction software configures each desired image and its corresponding small header into a separate

Matlab mat-file. The following file name convention is used, limited by the '8.3' DOS file name system. The file names are hhmmssSx.pnn, where hhmmss is 'hours-minutes-seconds' of the time stamp (associated with the first image quadrant) extracted from the recorded, S stands for Sequence, x is the sequence number on that tape (0 to 9), p is H or V indicating the received polarization, and nn is the tape number (01 to 19).

Each such file, after loading into Matlab, creates several matrices, as shown using the 'whos' command. The Matlab m-file *extrload.m* asks the user to interactively select a given mat-file, then loads it into memory. The following listing shows extrload being used to load a file, a whos listing, and display of the loaded variables.

```
»extrload

Tape number (e.g. 09): 09
load IMAGESEQ:TAPE09S0:142829S0.H09 -mat

»whos
Name              Size       Elements     Bytes    Density   Complex

ans              1 by 33           33       264       Full      No
cmd              1 by 40           40       320       Full      No
datafile         1 by 12           12        96       Full      No
datapath         1 by 18           18       144       Full      No
filter_parms     2 by 1             2        16       Full      No
gps_info         4 by 2             8        64       Full      No
radar_image   1024 by 1024    1048576   8388608     Full      No
range            1 by 1             1         8       Full      No
strng            1 by 23           23       184       Full      No
tapeid           1 by 2             2        16       Full      No
time             4 by 1             4        32       Full      No
titan_parms     10 by 1            10        80       Full      No


filter_parms =

     1
     0

gps_info =

   74.4828  -80.5360
   74.4828  -80.5360
   74.4827  -80.5363
   74.4827  -80.5363

range =

    0.0067

time =

   815322509
   815322509
   815322511
   815322511
```

```
titan_parms =

           5
           3
           5
           5
           2
           2
           2
           1
        1023
           0
```

The 1024x1024 matrix radar_image contains the 8-bit PPI radar image data. The first filter_parms value indicates the status of the pulse filter (0=off, 1=on), the second value is the CFAR filter status. The GPS values are latitude and longitude values in degrees. The range value indicates the distance in nautical miles represented by one image pixel. Therefore the image's maximum range is 512 x the 'range' value. Time is given as seconds since January 1, 1970, Microsoft's time stamp convention. The titan_parms array gives a number of values related to the Titan MRI system. One of main interest is titan_parms(8) which gives the number of scans integrated.

3.4 Data Review

To provide an overview of the available data base, a sample image pair was extracted from each sequence on each tape. The term pair is used only when the time-stamp (therefore the first 6 characters of the file names) are identical for both the HH and HV files. A Matlab m-file *printimg.m* was written to load a pair of HH and HV image files, and produce on a single page, a printed (Postscript) version with the HH image in the top half of the page, and the HV below. This provided the viewer a quick appreciation for the content of the images.

The collection of the printed images provided a quick-reference hardcopy catalogue of the available data.

The data files used for the catalogue were also written to CD, labelled IMAGECD2. The images are separated into separate directories based on the tape number.

3.5 Data Selection

It was desired to select a small subset of images for which to investigate various image enhancement techniques. The following criteria were used for image selection:

- Images which had been subject to as little pre-processing as possible would provide a good starting point.
- Consider only images for which the CFAR processing was off, so that images were as close to the original radar video output as possible.
- Ensure a variety of ice types and targets within the image, e.g. first-year ice, multi-year ice, and icebergs.
- Images for which the matching of the MRI A/D's digitization range to the variation in the input radar video was adequate to permit meaningful analysis, at least for a subset of the full radar coverage.
- Images for a variety of range scales of interest.

Keeping the above criteria in mind, the entire data catalogue was reviewed, and the recorded sets listed in Table 3-1. For each data set, the following extraction technique was used. For a given sequence (termed segment in the extraction software), all scans for that segment were extracted to disk. This was done for both the HH and HV tapes. Often there were a different number of scans captured from the HH tape compared to the HV tape for the same segment. As well, although both MRIs received the same GPS feed, there were slight differences in the time stamps (a second or two different). To ensure that radar scans from the same antenna rotation were being compared, it was decided to accept only those pairs of HH and HV scans which had identical time stamps. All other scans were deleted. The matched sequences were then written to CD, some on IMAGESEQ (CD 1), and the remainder on IMAGECD2 (CD 2), as listed in Table 3-1.

3.6 Data Processing

The following sections describe processing of the image data in order to facilitate HH to HV image intercomparison. Specific examples of intermediate products and data properties will be given using the image pair 132452S2.H16 and 132452S2.V16, unless otherwise indicated

Figure 3-1 and Figure 3-2 show the PPI radar images for the two files. The Matlab command 'axis equal' is used to ensure square pixels.

Tape	Seg-ment	CD	No. of scans	Range (nmi)	Pulse Filter	Scan-scan	HH Gain	HH STC	HV Gain	HV STC
9	0	1	50	3.48	on	1	.75	off	13	0
	1	1	26	1.74	on	1	.75	off	13	0
	3	1	23	1.74	on	1	.75	.50	13	7
	4	1	29	1.74	on	1	.75	.75	13	9
	7	1	35	3.48	on	1	.75	.50	13	7
	8	1	50	3.48	on	1	.75	off	13	0
10	1	2	25	6.91	on	1	.75	off	*13*	*0*
	2	2	30	6.91	on	1	.75	off	*13*	*0*
16	1	1	28	3.48	off	1	.50	.75	12	7
	2	1	26	3.48	on	1	.50	.75	12	7
17	1	2	39	3.48	on	1	.75	.50	11	6
18	7	2	20	1.74	on	4	.75	.50	13	0
	8	2	26	1.74	on	4	.75	.50	13	0

Table 3-1 List of image segments extracted and written to CD for further analysis.

CD 1 is IMAGESEQ, CD 2 is IMAGECD2. The number of scans indicates the number of HH/HV pairs. Range is 512 x the 'range' variable. Scan-scan is the number of scans integrated. For HH gain and STC, full on = 1.0. For HV gain and STC, full on = 14. The italicized entries indicate that these values were not explicitly listed in the experiment logs, but are deduced. CFAR was off for all scans. For both the HH and HV MRI, the gain setting was 140 and the offset setting was 128.

The radar signal naturally originates in a range-azimuth (R-θ) coordinate system, with a succession of sweeps of radar generated as the antenna rotates to successive azimuth angles. The radar may apply an operator-selected range-dependent variation in radar gain, i.e. sensitivity time control (STC). The MRI digitizes the radar video by sampling the sweep in range, and the MRI may apply some preprocessing in the R-θ domain, e.g. pulse-to-pulse filtering, CFAR processing. The MRI then scan-converts the R-θ data into a PPI image format. Multiple successive PPI images, suitably adjusted to allow for ship movement, can be combined to provide scan-to-scan averaging.

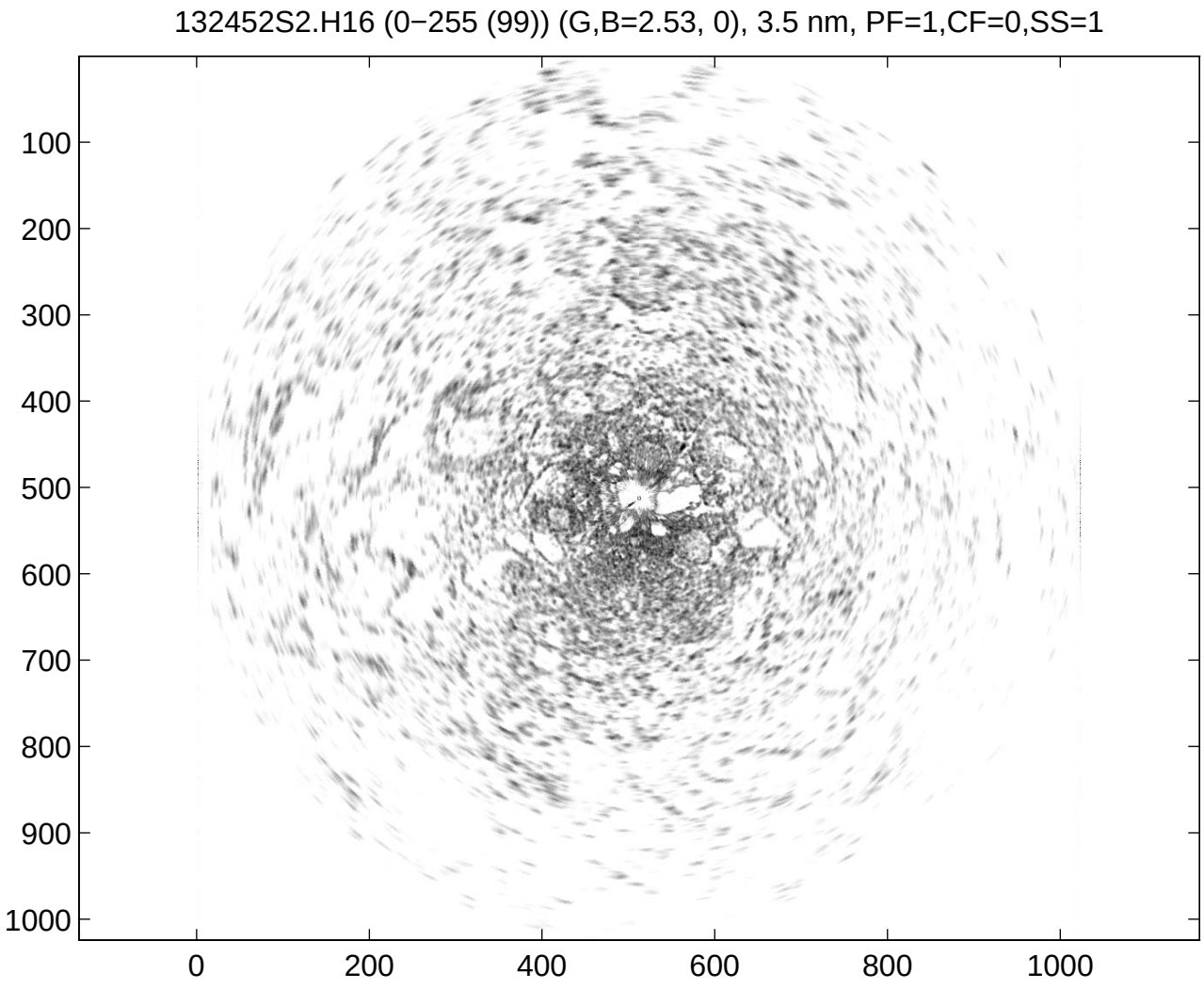

Figure 3-1 HH PPI image for file 132452S2.H16

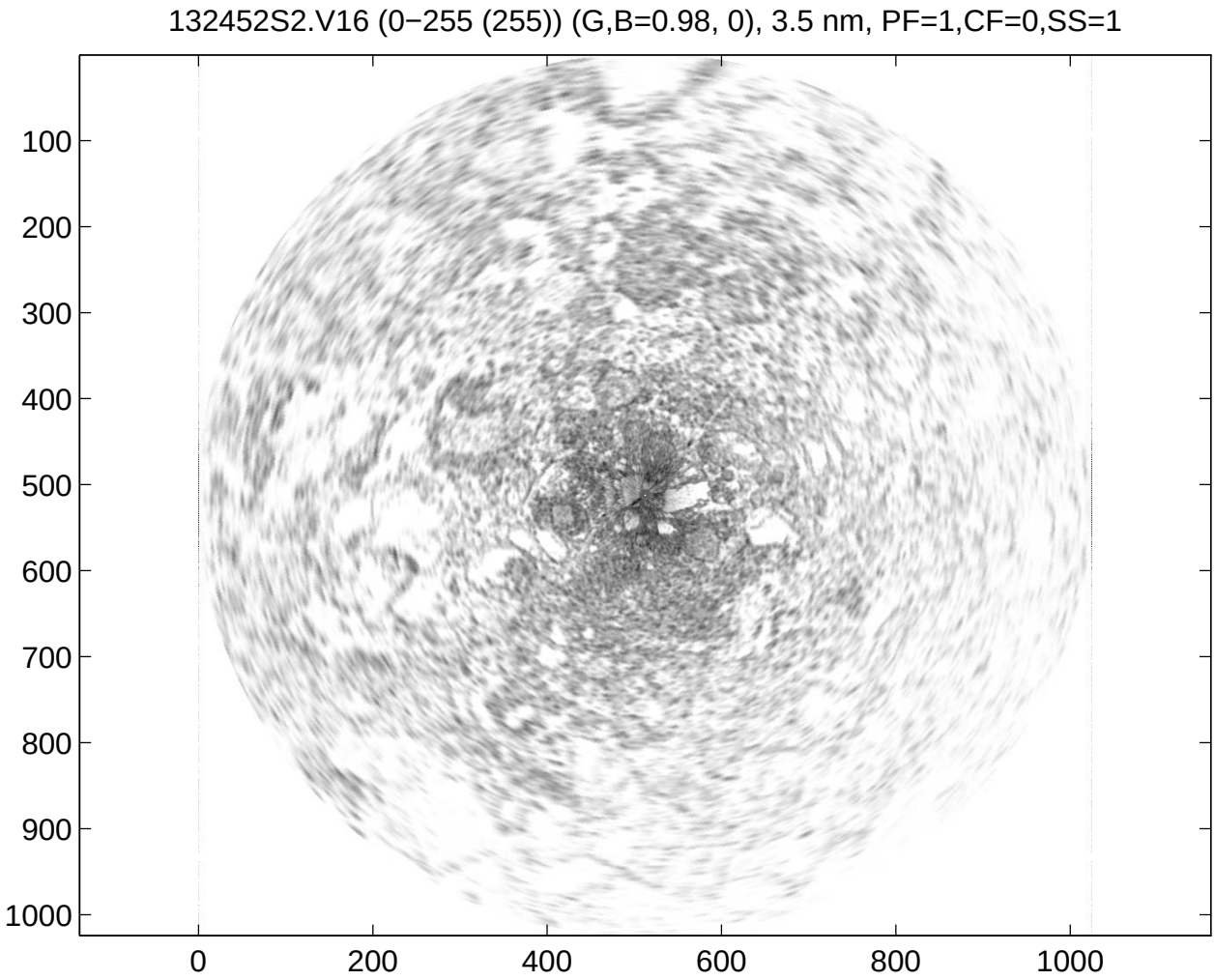

Figure 3-2 HV PPI image for file 132452S2.V16

To begin the balancing of the HH and HV images, it was first necessary to return the data to the R-θ domain in order to correct for differences that were a function of range only. Therefore the first step in the data processing was to create a B-scan (R-θ) image from the original PPI image, using m-file *mkbscana.m*. The centre pixel of the 1024x1024 PPI image was taken as 513,513. The routine creates an array for the values of sine and cosine for 2048 equally spaced angles around the 360 degree scan. Data for successive range rings are then extracted by stepping the range from 1 to 512, multiplying the range value times the sine and cosine arrays, and using the resulting values (rounded) as the X and Y indices into the PPI image, and extracting the corresponding pixel value. The result is a B-scan image of 512 pixels in range by 2048 azimuths. The data values are not altered during the process, they are simply copied from one coordinate system to another. The B-scan is saved to a new file, whose name is created by substituting a 'B' for the 'S' in the input file name. Figure 3-3 and Figure 3-4 show the first quadrant of the B-scan images for 132452B2.H16 and 132452B2.V16. With square pixels, the full B-scan image is 4 times longer (2048 azimuths) than wide (512 azimuths), making printing difficult.

Therefore only the first quadrant (512 azimuths = 90 degrees) is printed in the figure. Note how radial radar shadows show up as horizontal features in the B-scan.

The next step is to characterize the variation in range of each image set by measuring a number of statistical properties. M-file *bsnrmall.m* calculates the minimum, maximum, mean, median, and standard deviation of the 2048 azimuth values at each range index, from 1 to 512. The resulting range profiles are on the scale of 0 to 255, the dynamic range of the A/D. It is assumed that the statistical properties of all images in a data set will be fairly represented by those of a single image from that set. The various range profile statistics arrays are saved in a new file, whose name is created by substituting a 'Q' for the 'S' in the input file name. These statistical range profiles can be plotted using m-file *rprofplt.m*.

For example, Figure 3-5 and Figure 3-6 show the graph of the range profile information for image pair 132452S2.H16 and 132452S2.V16 as produced using *rprofplt.m*.

These profiles can indicate a number of conclusions about a data set. Clipping of the A/D converter can be seen from the minimum and maximum plots. Minimums of 0 indicate that the received power (at some azimuths) has gone an undetermined amount below the range of the A/D. Thus the A/D is not 'seeing' the noise floor of the radar. Similarly, maximum values of 255 show that the received power has exceeded the A/D range. In fact, the video actually clips at an A/D value of 251 (presumably an MRI hardware design property).

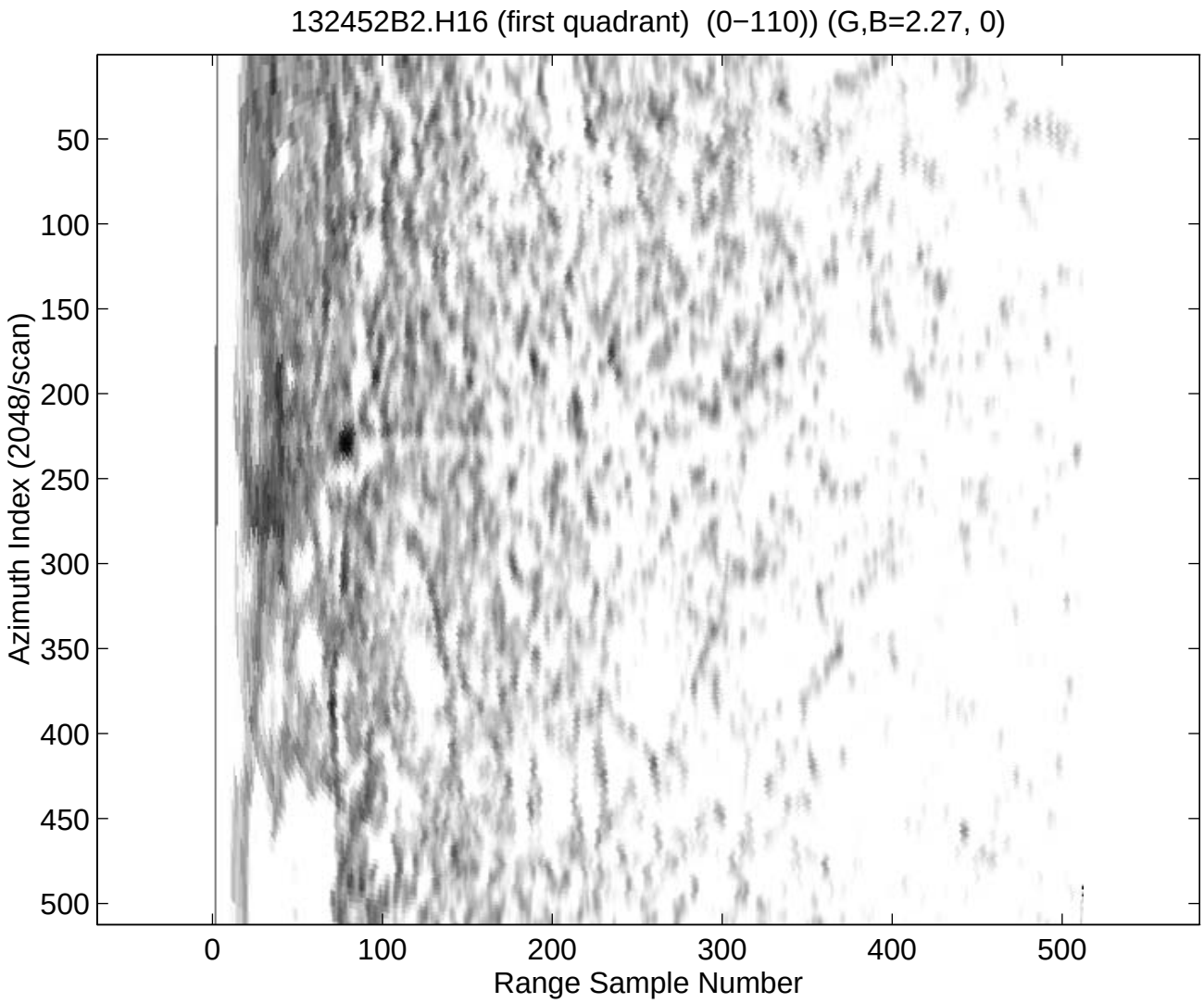

Figure 3-3 B-scan image for the upper right quadrant of HH PPI image in Figure 3-1

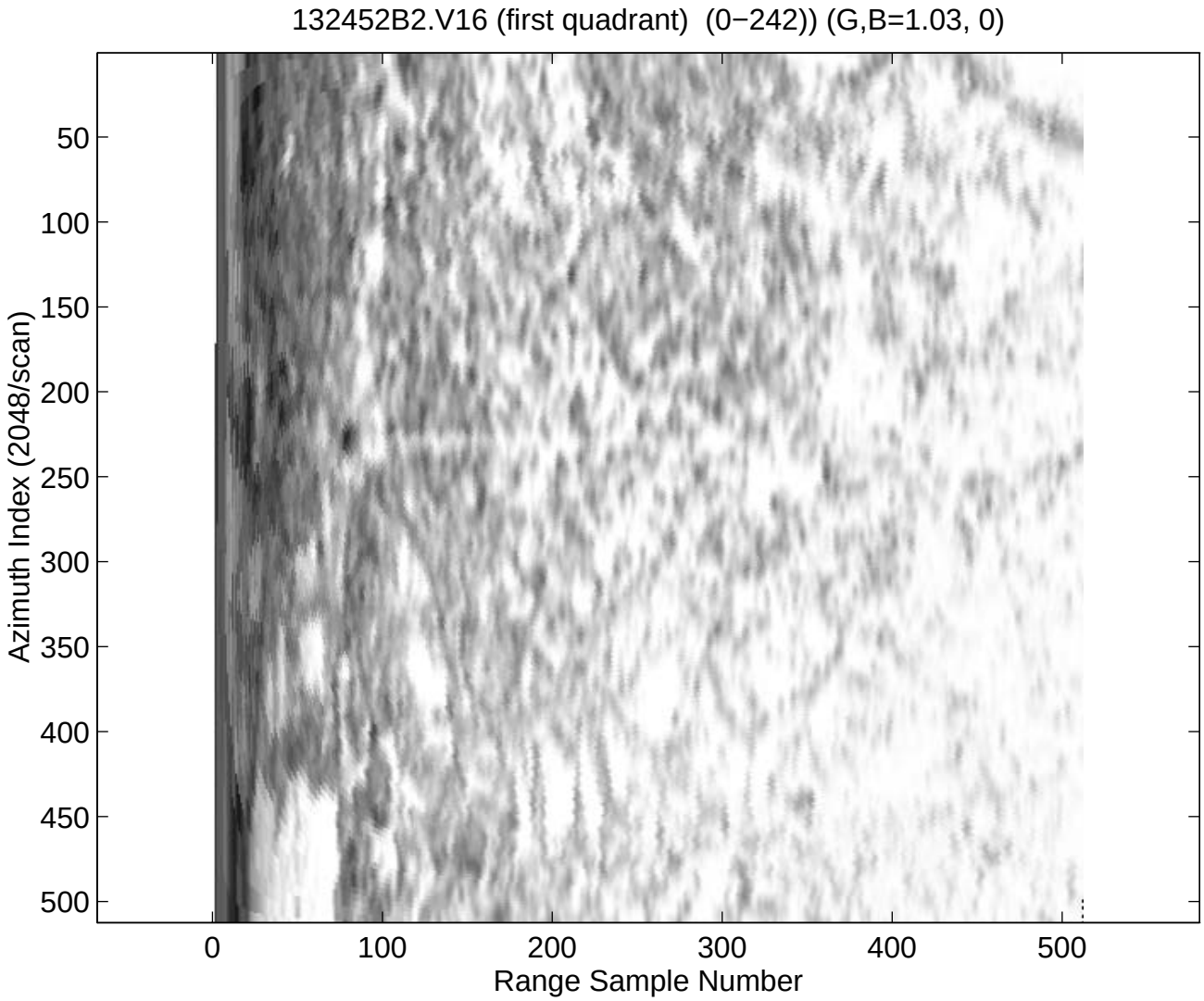

Figure 3-4 B-scan image for the upper right quadrant of HV PPI image in Figure 3-2

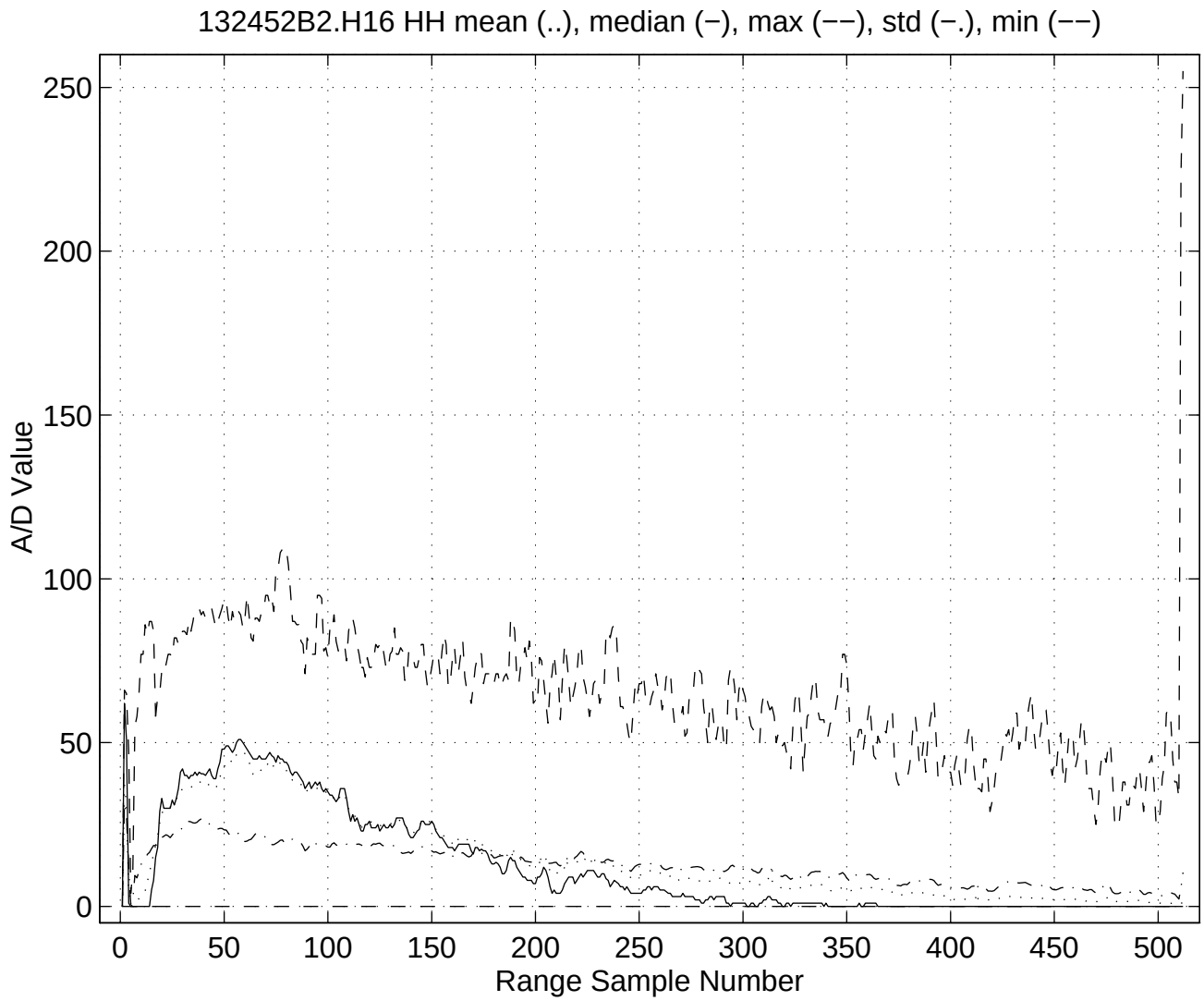

Figure 3-5 Plot of minimum, maximum, mean, median, and standard deviation vs. range for the HH B-scan data from file 132452S2.H16

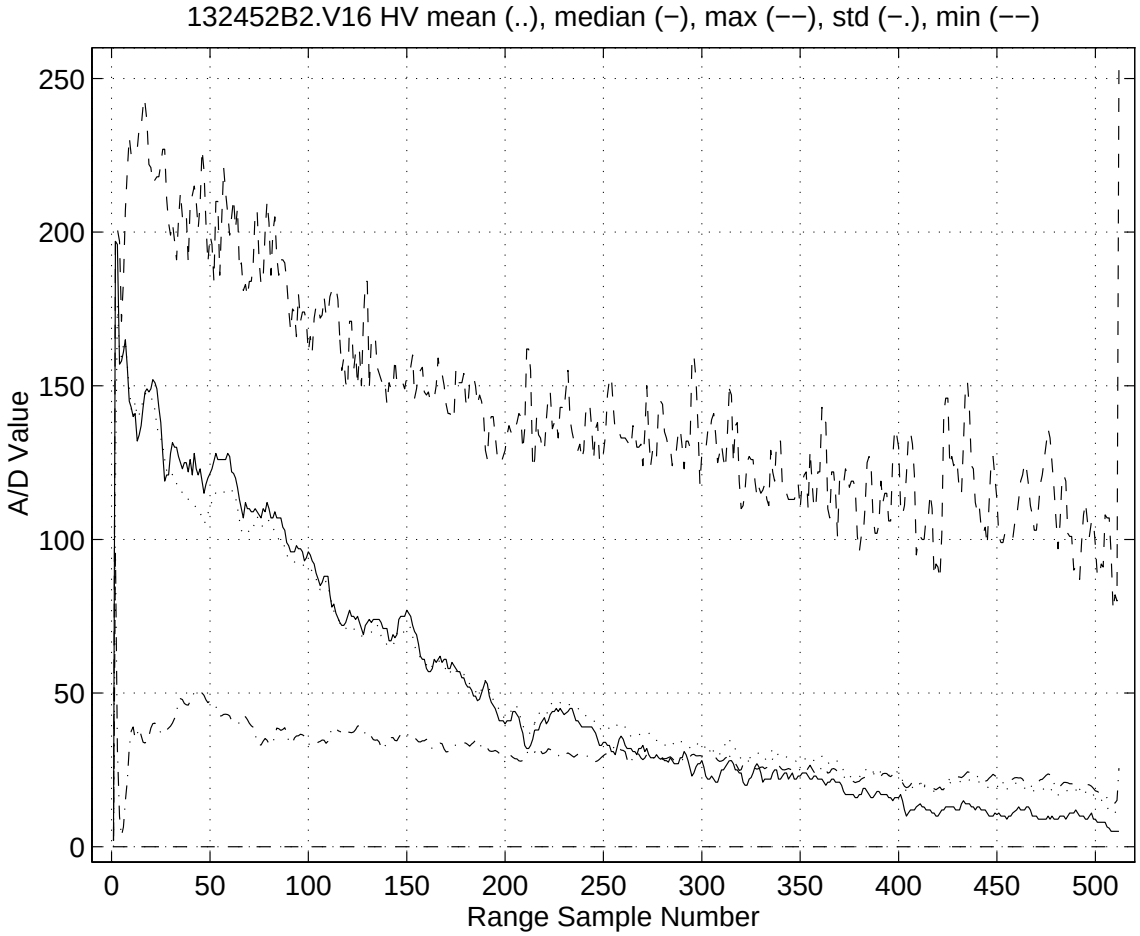

Figure 3-6 Plot of minimum, maximum, mean, median, and standard deviation vs. range for the HV B-scan data from file 132452S2.V16

The estimation of the mean value of the 'original' video is corrupted and biased by the presence of these clipped values. Therefore the mean value is only unbiased if the minimum and maximum values at that range are >0 and <251 respectively. Essentially, all the data sets have clipping at some ranges. Similarly the standard deviation, which measures data spread about the mean, is also biased by clipped data. However, it does give some feeling for the spread in the data values at each range, i.e. the number of A/D levels required indicates the dynamic range of the data.

One statistical technique that is more robust to sample clipping is the use of ranking. One such ranking measure is the median, which is the data value for which half the samples are smaller, and half are larger. Even though a sample may be clipped, it will still be counted as either larger or smaller than the median, and the median value will remain correct. However, as the median gets close to, or equals, either 0 or 251 it should be considered unreliable for processing, as a significant number of clipped samples are contributing to its calculation.

Range and Azimuth Offset

In comparing individual range sweeps in the HH and HV B-scan images it was noticed that there was a difference in the response of the HH and HV receivers, and an apparent offset in range. This is most clearly visible for an isolated (point) target return. Figure 3-7 shows the HH PPI image for 143123S1.H09. The Coast Guard vessel Louis St. Laurent (LSL) is in an area of open water/thin ice, range sample 283 at azimuth 865 (= bearing 152°), and represents an isolated target. Figure 3-8 shows a range profile, part of the HH and HV sweeps taken from the corresponding B-scan files 143123B1.H09 and 143123B1.V09, at the LSL's azimuth. The HV return is offset in range and is wider in response. Figure 3-9 similarly shows an azimuth profile, part of the HH and HV range rings at the centre range of the LSL return. A small offset in azimuth is visible. To permit HH - HV image overlay (i.e. combination), the spatial response of the radar returns must be aligned in range and azimuth. To estimate the offsets in range and bearing, sub-images of the HH and HV B-scan images were chosen, and the two-dimensional cross-correlation was calculated. Using an NxN sub-image, the cross-correlation image is 2N-1x2N-1. If the two sub-images are aligned, the cross-correlation peak should appear at index N,N. Using the sub-images of the LSL as shown in Figure 3-10 and Figure 3-11, the peak actually occurs offset in range by 5 samples and in azimuth by 1 sample. Figure 3-12 and Figure 3-13 show the HH and HV sweeps through the LSL after range and azimuth correction by appropriately shifting the HH image. Note that the wider response of the HV radar causes the HV return to seem larger relative to the HH return at the near- and far-range edges of the target as compared to the centre of the target. This will create some image artifacts when trying to combine the images, e.g. showing the difference HH-HV.

Similar offset evaluation using sub-images from 132452B2.H16 and 132452B2.V16 reveals a range offset of 2 and an azimuth offset of 0.

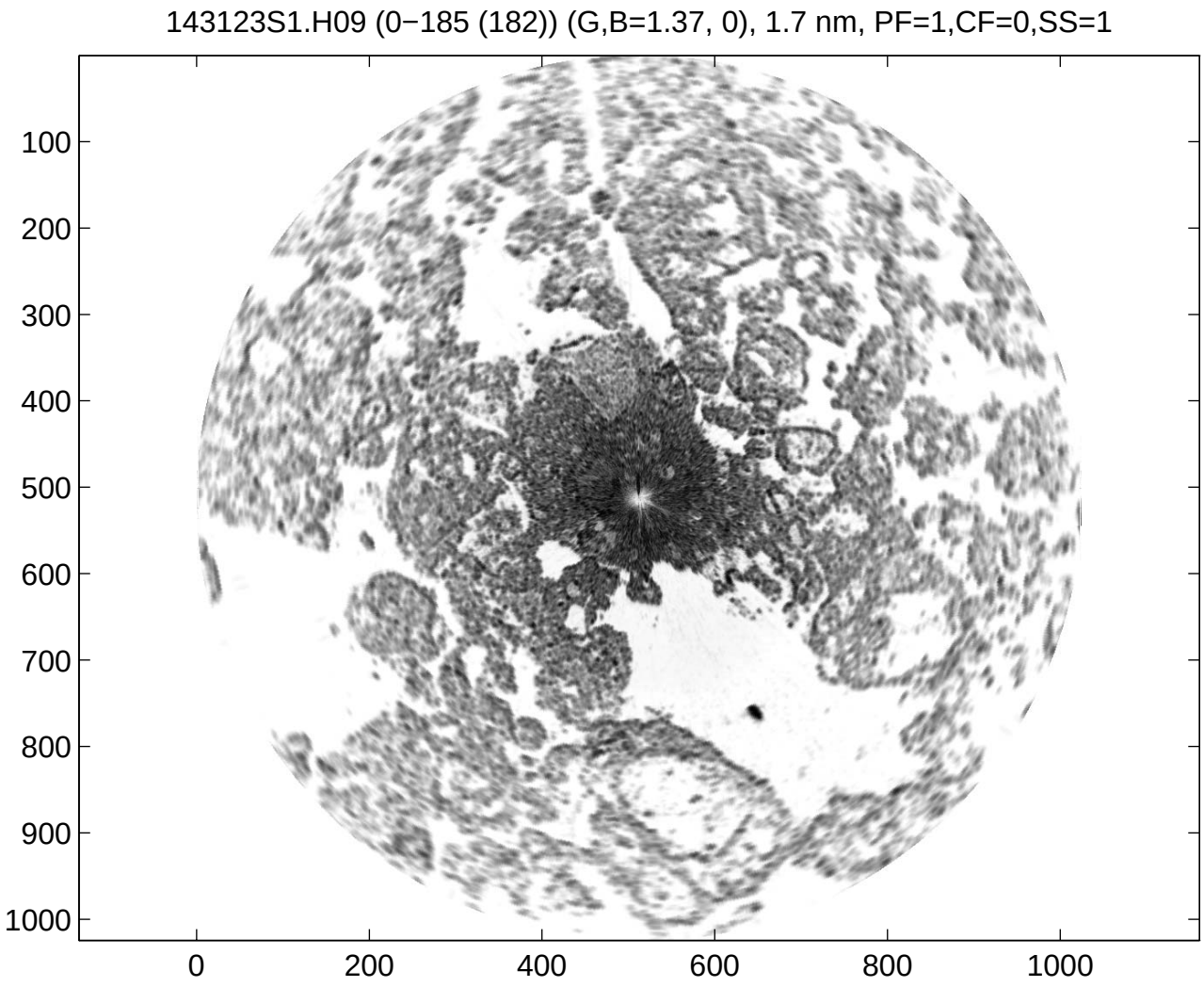

Figure 3-7 HH PPI image for file 143123S1.H09. Coast Guard vessel Louis St. Laurent is the dark spot in the large light area in the lower right

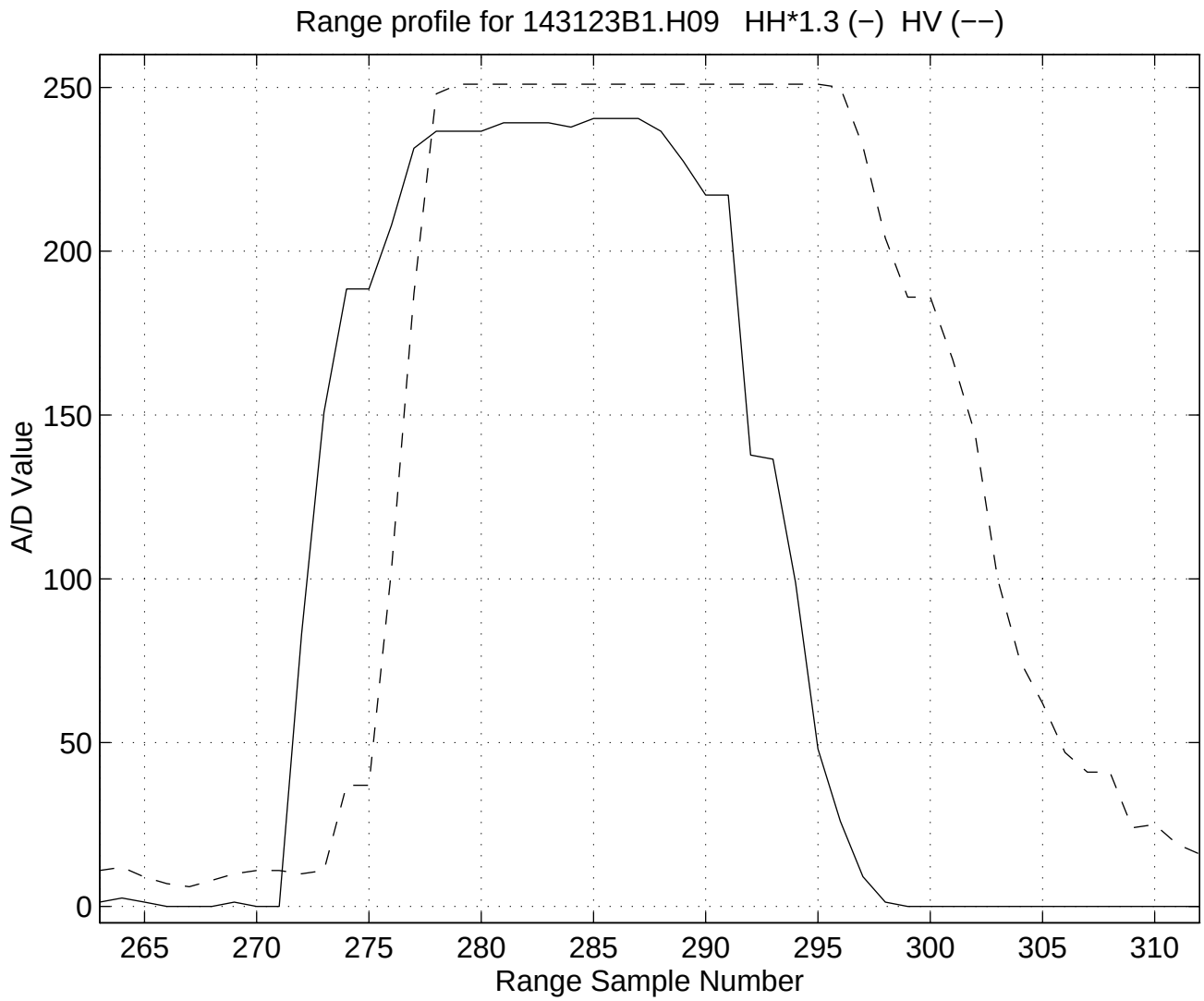

Figure 3-8 Range profile through radar return from the vessel Louis St. Laurent

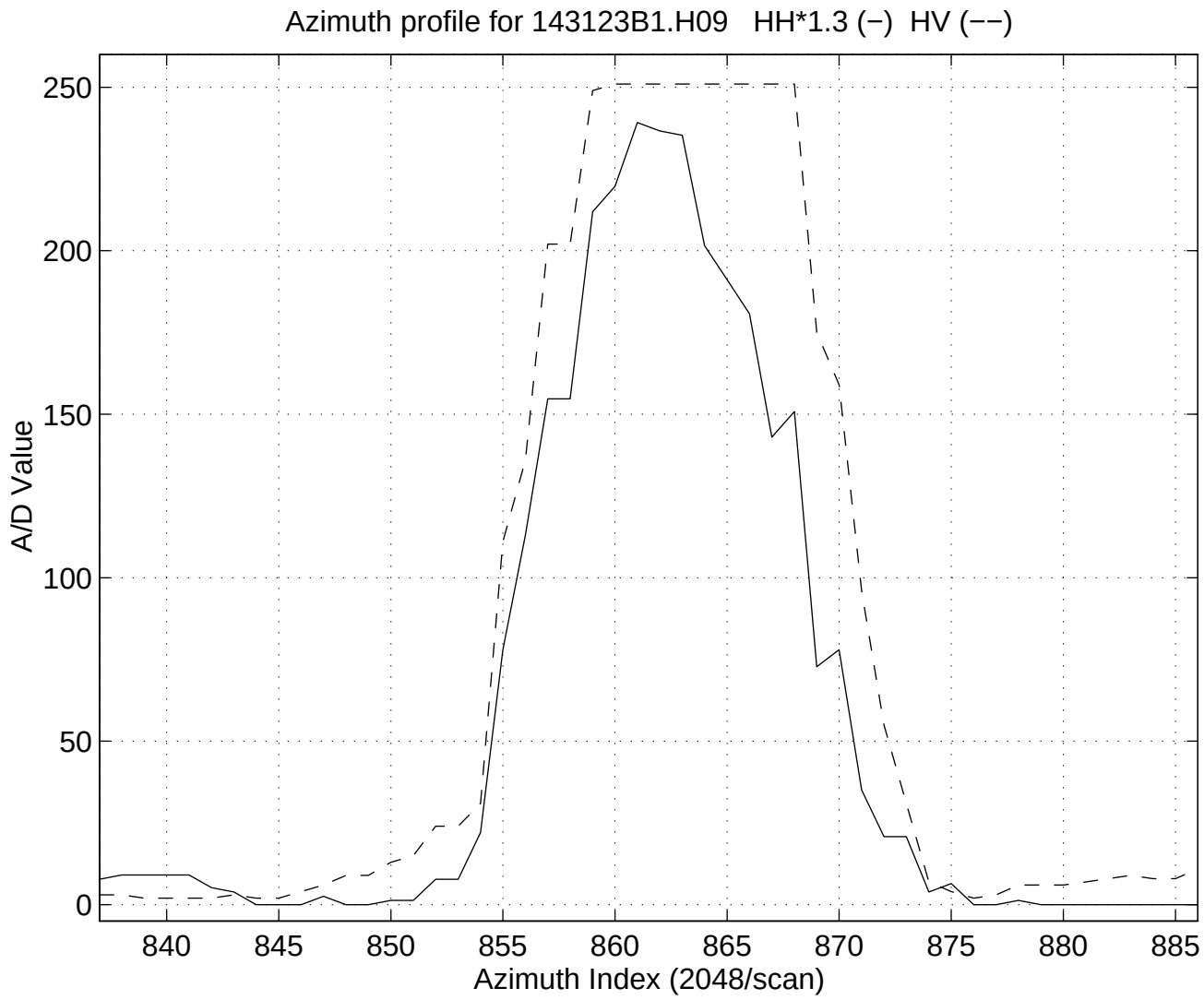

Figure 3-9 Azimuth profile through radar return from the vessel Louis St. Laurent

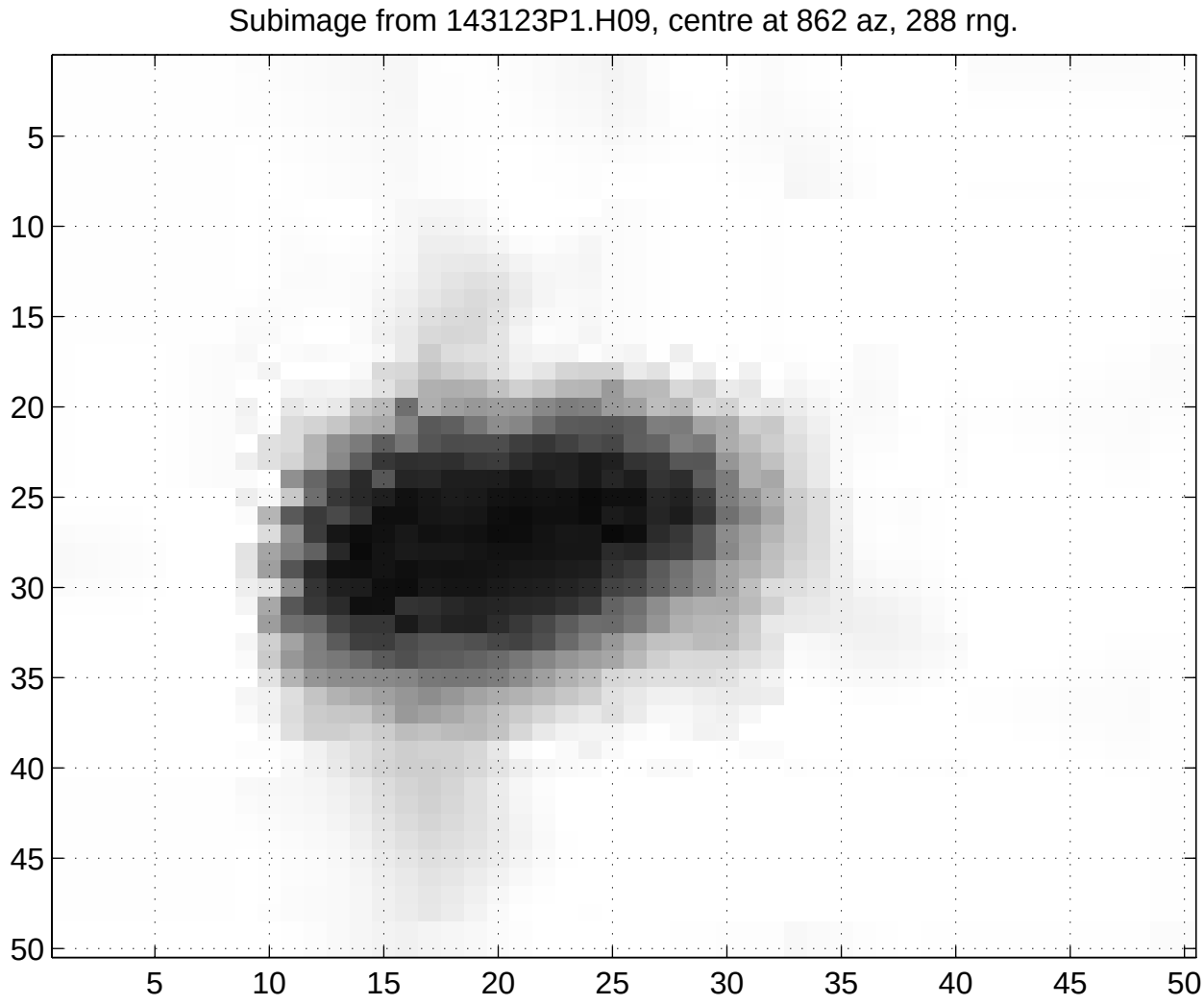

Figure 3-10 HH sub-image from file 143123B1.H09 showing the Louis St. Laurent return

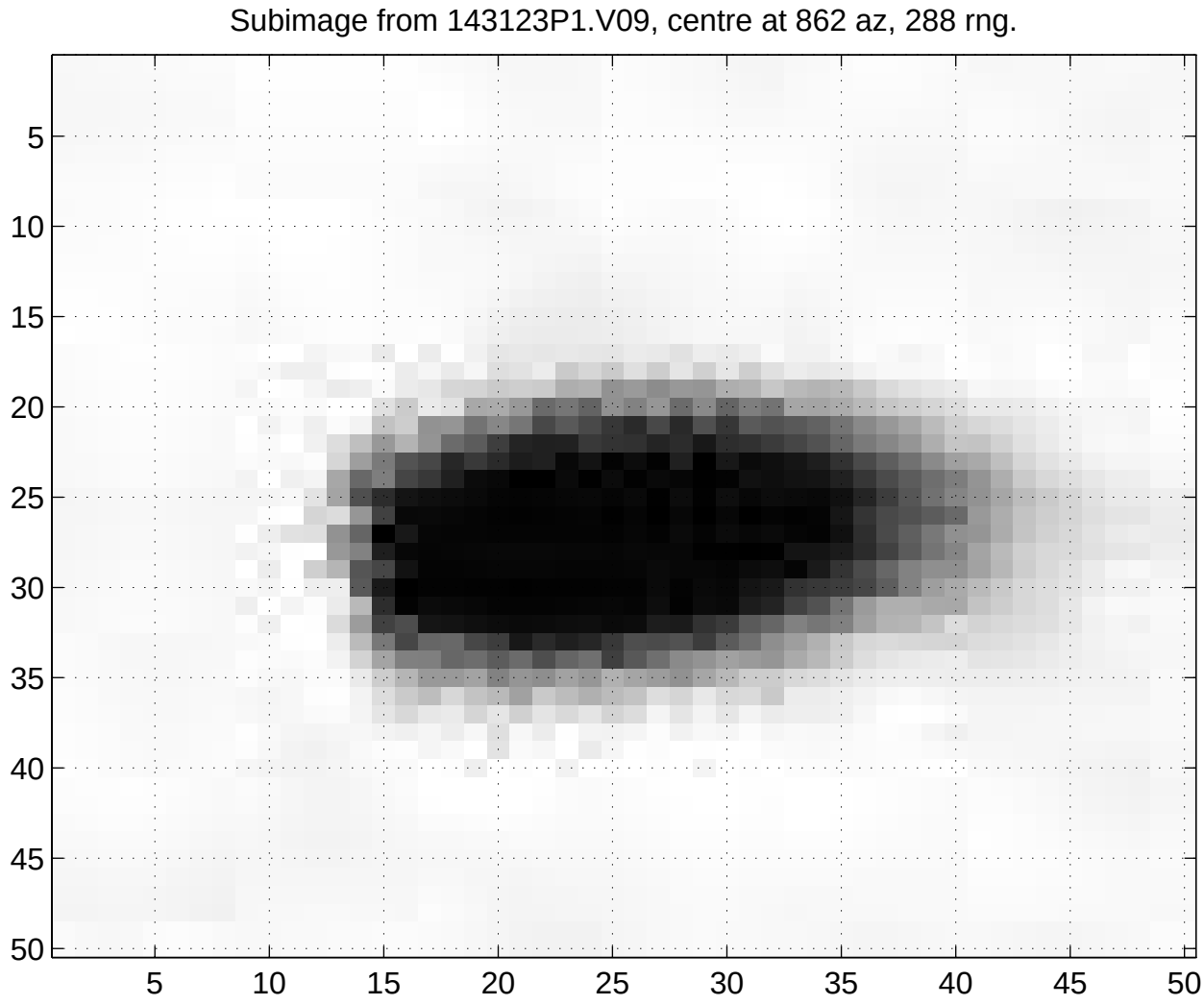

Figure 3-11 HV sub-image from file 143123B1.V09 showing the Louis St. Laurent return

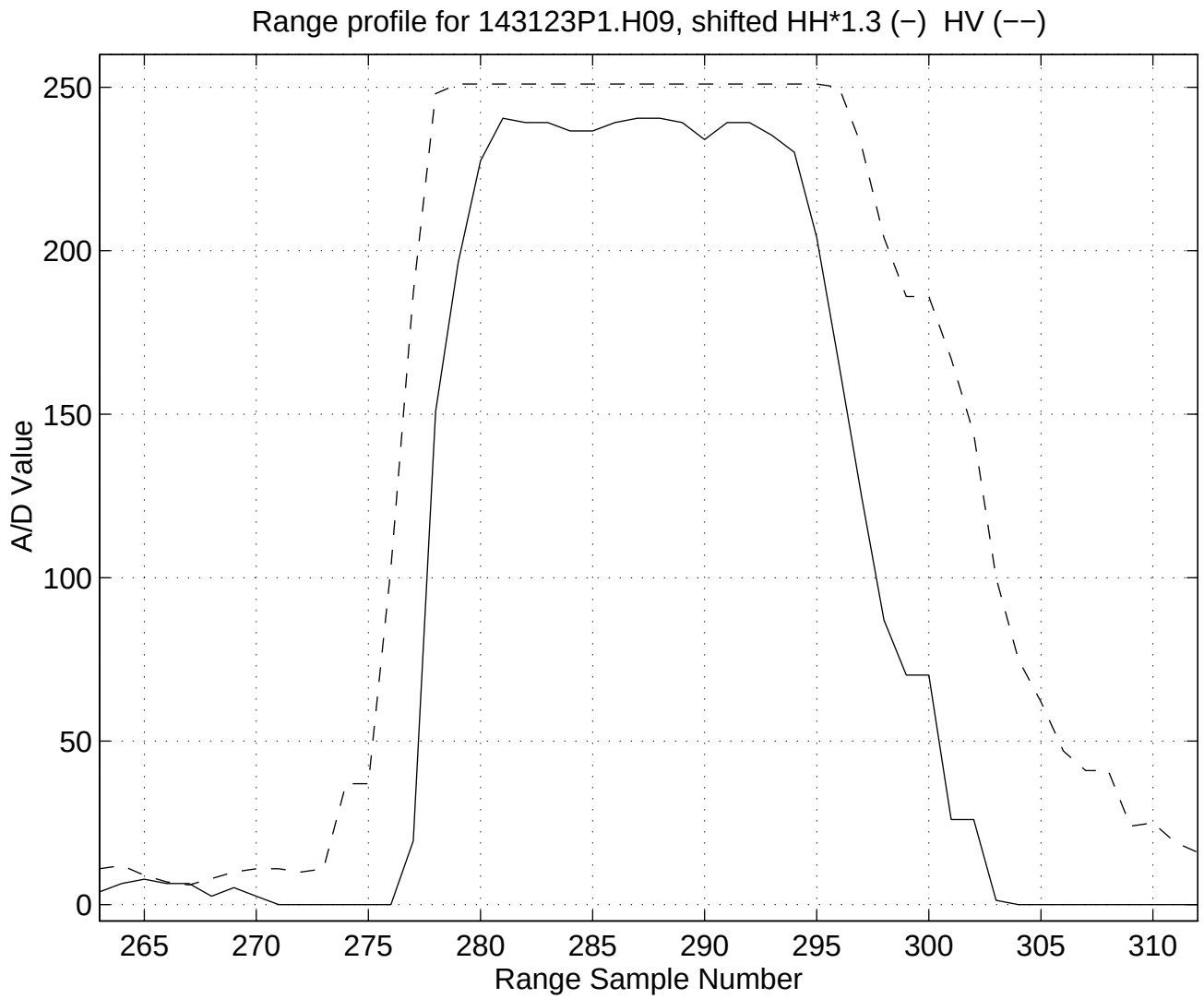

Figure 3-12 Range profile through radar return from the vessel Louis St. Laurent after shifting the HH return

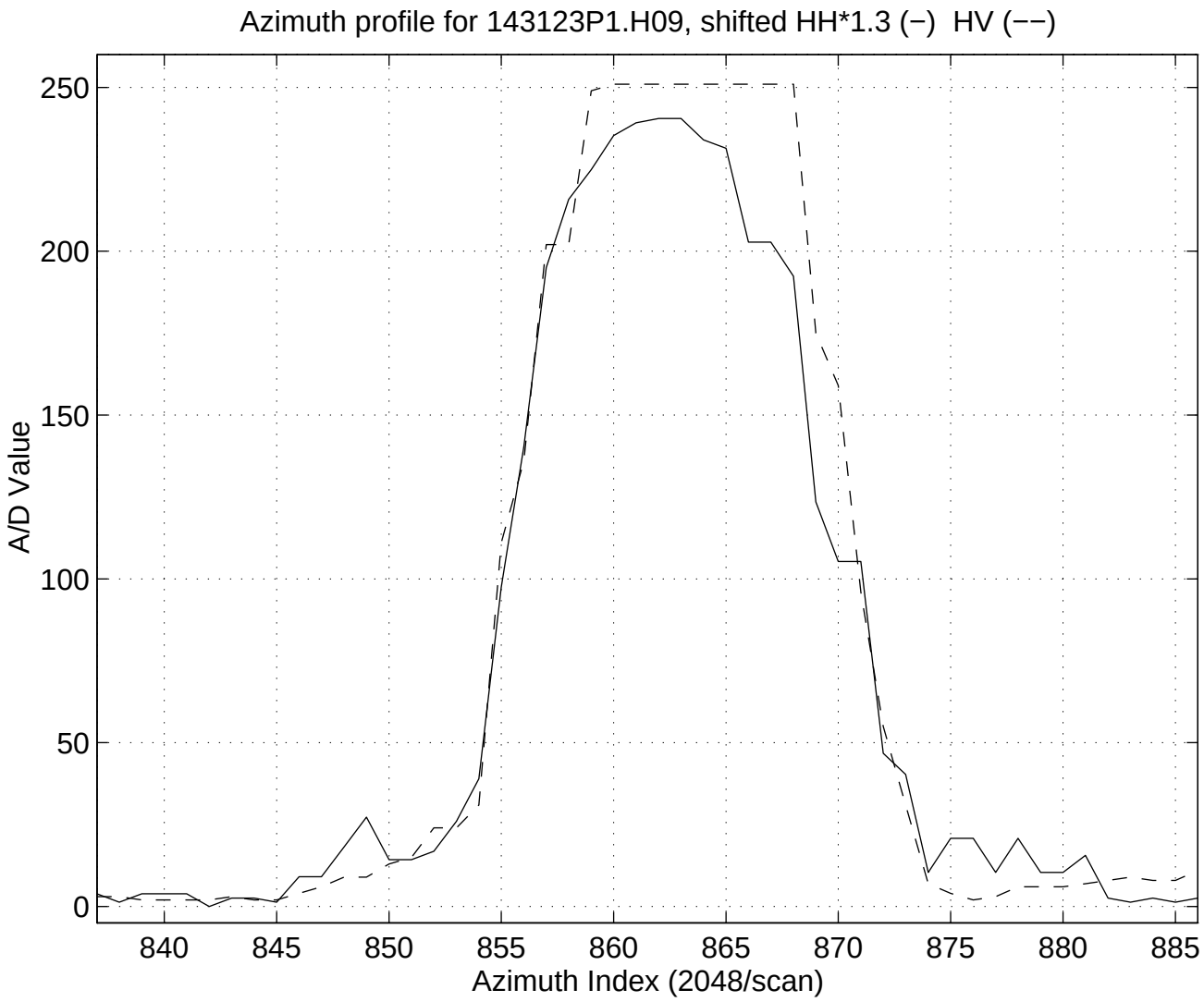

Figure 3-13 Azimuth profile through radar return from the vessel Louis St. Laurent after shifting the HH return

Received Power vs. Range

The basic radar equation used to predict the expected return power, ignoring losses, is

$$P_r = \frac{P_t G^2 \ ^2 \ _t}{(4\ )^3 \ R^4} \qquad (1)$$

where P_r = received power

P_t = transmitted power

G = antenna gain

λ = radar wavelength

R = range

σ_t = target radar cross-section (RCS)

For an area target such as the ice surface, the target cross-section σ_t is replaced by the product of the surface area of the radar resolution cell illuminated by the radar antenna times a per-unit-area reflectivity factor, termed the normalized radar cross-section, σ_o. That is,

$$_t = R \quad \frac{c}{2} \quad _o \qquad (2)$$

where θ = azimuthal antenna beamwidth

c = speed of light

τ = radar pulse length

Substituting (2) into (1) yields

$$P_r = \frac{P_t G^2 \quad ^2 \quad c \quad _o}{(4 \quad)^3 \; R^3 \quad 2} \qquad (3)$$

If one assumes a constant value of σ_o with range, then the received power should decrease as R^3. However, the value of σ_o decreases a function of decreasing grazing angle, which in turn decreases as a function of range. To provide a constant level return vs. range, the radar has a sensitivity time control (STC) function, which attempts to vary the radar gain with range to compensate for the R^{-3} power drop-off. The STC curve begins with fixed attenuation at near range, gradually permitting the gain to increase during the radar sweep to the level set by the radar gain control. The STC curve may be implemented using analog circuit components (e.g. resistor-capacitor pair), with an associated RC time constant. The effect of such an STC function is clearly apparent in the HH median plot of Figure 3-5, whereas there is much less STC in the HV plot of Figure 3-6. Note that each of these factors causes a smooth and relatively slowly-varying power reduction vs. range.

For each HH-HV pair, the initial desire is to adjust one radar image to make it look like the other so that intercomparisons can be made. There are two degrees of freedom that can be adjusted, which can be thought of as gain and bias. The bias seeks to balance the underlying 'long-term' image variation vs. range, while gain seeks to balance the 'short-term' variation in the data at each range index. The major complication is that each image has been subjected to different gain vs. range functions, and has differing underlying levels.

To provide a starting point in the image balancing, three basic assumptions had to be made:

1) The receiver output voltage vs. the input received power in dBm (i.e. a log receiver) is a linear function, and with the exception of clipping, this linear characteristic is preserved in the MRI data.

2) The spread in the variation in the received signal at each range should be similar for both the HH and the HV radar. Note that both radars are simultaneously viewing the same ice targets.

3) The underlying data variation vs. range should be similar for both the HH and HV radars.

Much effort was expended in attempting to identify the suitable measures for gain and bias, and how to determine and balance them satisfactorily. Many variations were tried in an effort to accommodate the variety of data conditions encountered in the test sets, and to overcome some of the effects of clipping, poor A/D settings, etc.

After much experimentation, the following method was chosen as being satisfactory for balancing the images, at least at the ranges permitted by the data. The method continues the use of ranking. The median is used as a measure of bias, i.e., the 'central' value of the data, while the gain is estimated from the spread of the data about its central value, and is determined from the histogram of the data values.

The balancing process needs to be applied at each range since there are range-dependent differences in the HH and HV images. Using the B-scan image as input, the data values from the 2048 azimuth values (at each range) are histogrammed into 256 bins (count of occurrence vs. A/D values 0 to 255). This produces a 256 bin x 512 range image of the data histograms vs. range. This processing was done with m-file *bshistim.m*. The histogram image array is saved in a new file, whose name is created by substituting a 'J' for the 'S' in the input file name.

Figure 3-14 and Figure 3-15 show the B-scan histogram images for image pair 132452B2.H16 and 132452B2.V16. Bins where the occurrence count is above 100 have been limited (clipped) for display purposes. The histogram image gives a quick appreciation for how well the radar video level was matched to the A/D range, i.e., how many A/D levels the data occupies, and the occurrence of clipping at the lower and upper range of the A/D. The HH image shows that the signal level was low, using only a small portion of the A/D input range, and the effect of STC at near-range is apparent. The HV image shows a more full use of the A/D range, but the dynamic range of the signal over the full sweep causes the signal to fall below the A/D input range toward the end of the sweeps. Both histograms reveal significant low-level clipping.

To balance the gain and bias of the radar images, the desire is to try to estimate only one adjustment parameter at a time. The easier parameter to initially estimate is the bias, taken as the median. Therefore, at each range, the histogram is shifted by the median value (i.e. median is subtracted from all the data for that range) so that the new median is standardized to a value of 0. This procedure is only performed for ranges at which the

original median value is valid (not 0 or 251). Other ranges are marked as invalid. To rank the shifted data, a cumulative sum procedure is used so that the cumulative sum is 0.0 at sample value 0 (the median of the shifted data), increasing to 1.0 by sample value 255. This creates a cumulative distribution function- (CDF-) like curve for the samples above the median, resulting in an image of this CDF vs. range. This procedure was applied at each range sample, yielding a CDF image from each B-scan histogram image. Examples for 132452J2.H16 and 132452J2.V16 are shown in Figure 3-16 and Figure 3-17. The CDF indicates the nature of the spread in the data above its median. This CDF processing was performed using m-file *cdfmatch.m*.

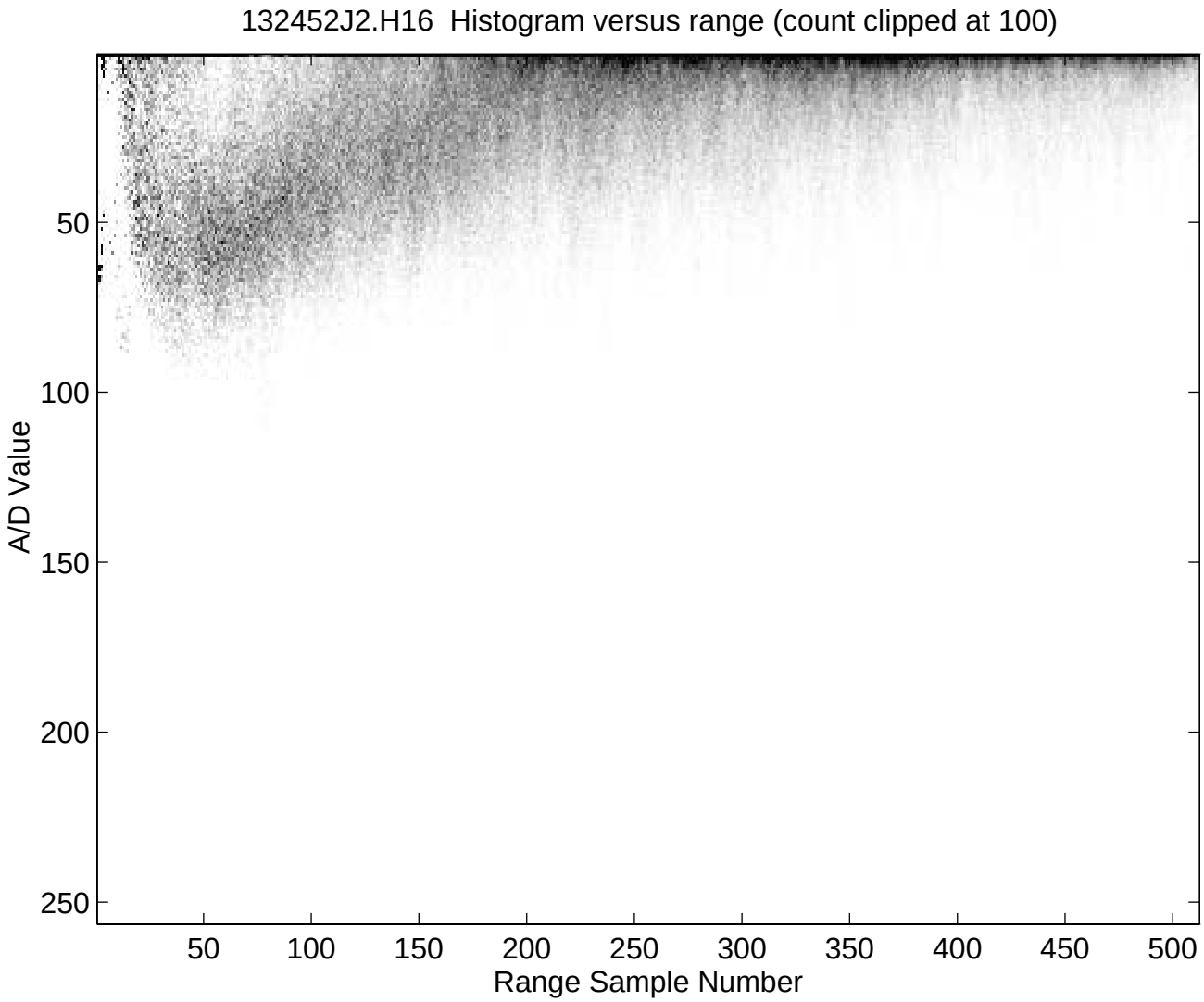

Figure 3-14 HH B-scan histogram based on data from file 132452B2.H16

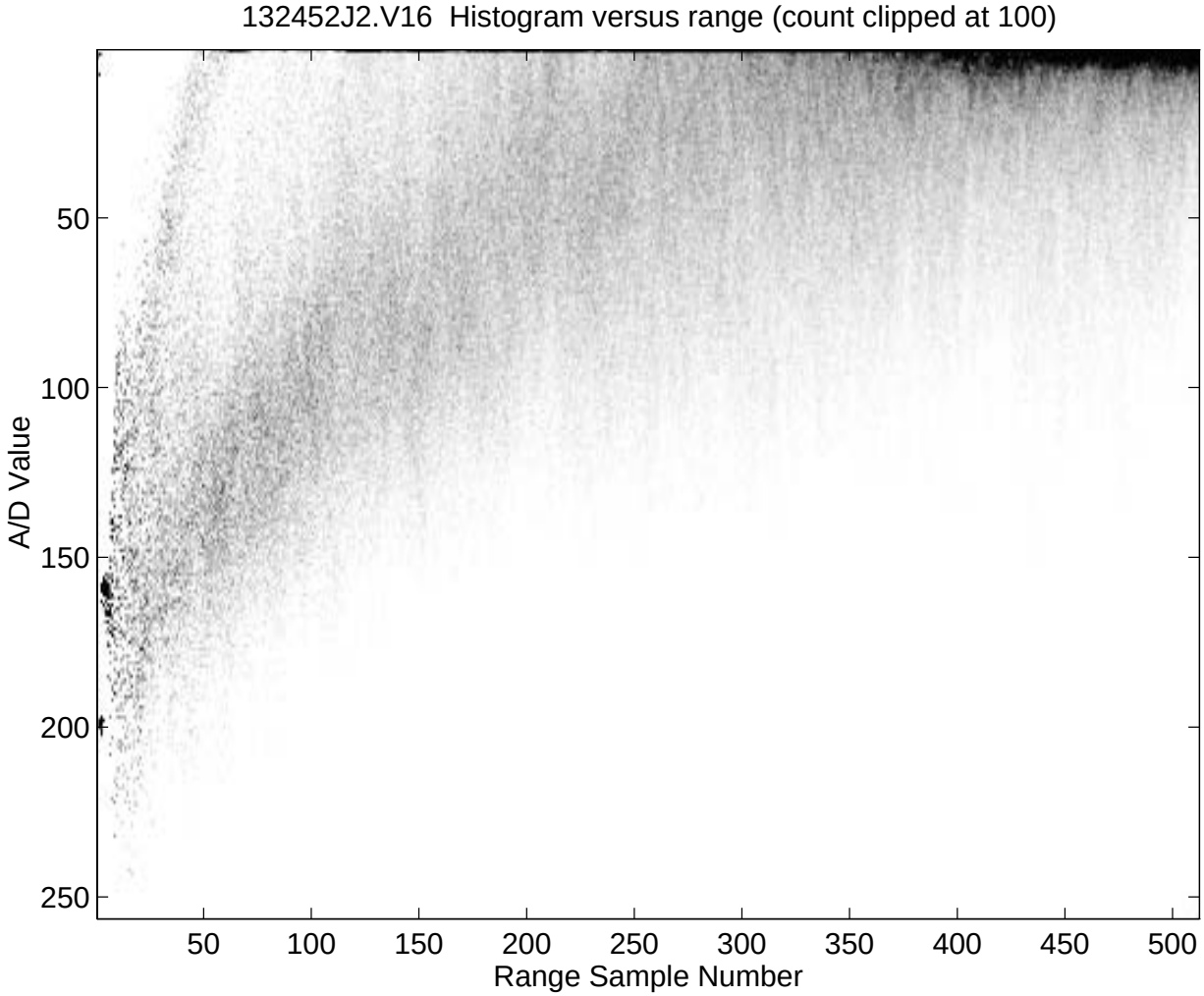

Figure 3-15 HV B-scan histogram based on data from file 132452B2.V16

Figure 3-18 shows the histogram for range sample index 50 from 132452J2.H16 after subtracting its median of 48, while Figure 3-19 shows histogram from 132452J2.V16, after subtracting its median of 121.5 (rounded to 122). The low level clipping of the HH data is apparent from the large peak at -48 after shifting, and the clipping prevents characterization of the histogram at low levels. The HV data with its higher median, permitted more of the low level distribution to be estimated. Figure 3-20 shows the two CDF curves for HH and HV generated using only the shifted samples above the median, i.e., only positive A/D values. The wider HV histogram yields a CDF that rolls off more slowly than the HH.

Balancing the gain of the two images amounts to matching the CDF image curves at each range. That is, we apply a multiplicative factor to one of the data sets in order to make the two CDF curves as close to each other as possible.

At first a minimization procedure was used to find the gain value that minimized the difference between the HV CDF curve and the gain*HH CDF curve. This procedure was somewhat slow and a simpler method was desired, more practical for implementation in a final system. The next approach was to match the points at which the CDF value equalled 0.5. (This is equivalent to the 75 percentile in the median-normalized data). The gain was determined as the HV CDF (0.5) / HH CDF (0.5). To try to make the procedure a bit more robust, the gain factor was estimated at a number of CDF matching levels: 0.5, 0.6, 0.7, 0.8, and 0.9. For example, Figure 3-21 shows the HV CDF curve, and the HH CDF curves matched at the various CDF levels. The associated gain factors are given in the legend, in order from matching at CDF (0.5) down to CDF (0.9). One may observe that the CDF curves are not particularly smooth, due to their being based on a relatively few number of samples. Each histogram uses data from 2048 azimuths, and the CDF is based on only the samples above the median, i.e., 1024 samples. Therefore the gain factors can vary significantly, depending upon which CDF level is used for matching. For example the HV curve has a left-ward dip at the CDF (0.6) level. Therefore the matching HH gain is only about 1.73, not the 1.9 value suggested by the other fits.

This variation in the fitted gains is even more pronounced when the median values are small, resulting in very narrow CDF curves. For example, Figure 3-22 shows the HH and HV CDFs for range sample 280 from the same data set as above. The HH median is 1, and the HV median is 29. The HH histogram is very narrow, resulting in a CDF that drops off quickly with a shape much different from the HV curve. As Figure 3-23 shows, trying to match these two curves of different shape at specific CDF levels yields a wide variation in gain factor estimation, from 1.8 to 3.0. Therefore, the quality of the gain factor estimation is directly governed by the strength of the returns, i.e., the median value. Gain factors calculated using low level data are much less reliable. To partially protect against this effect, matching was only calculated for CDF levels having a spread of at least 5 A/D levels.

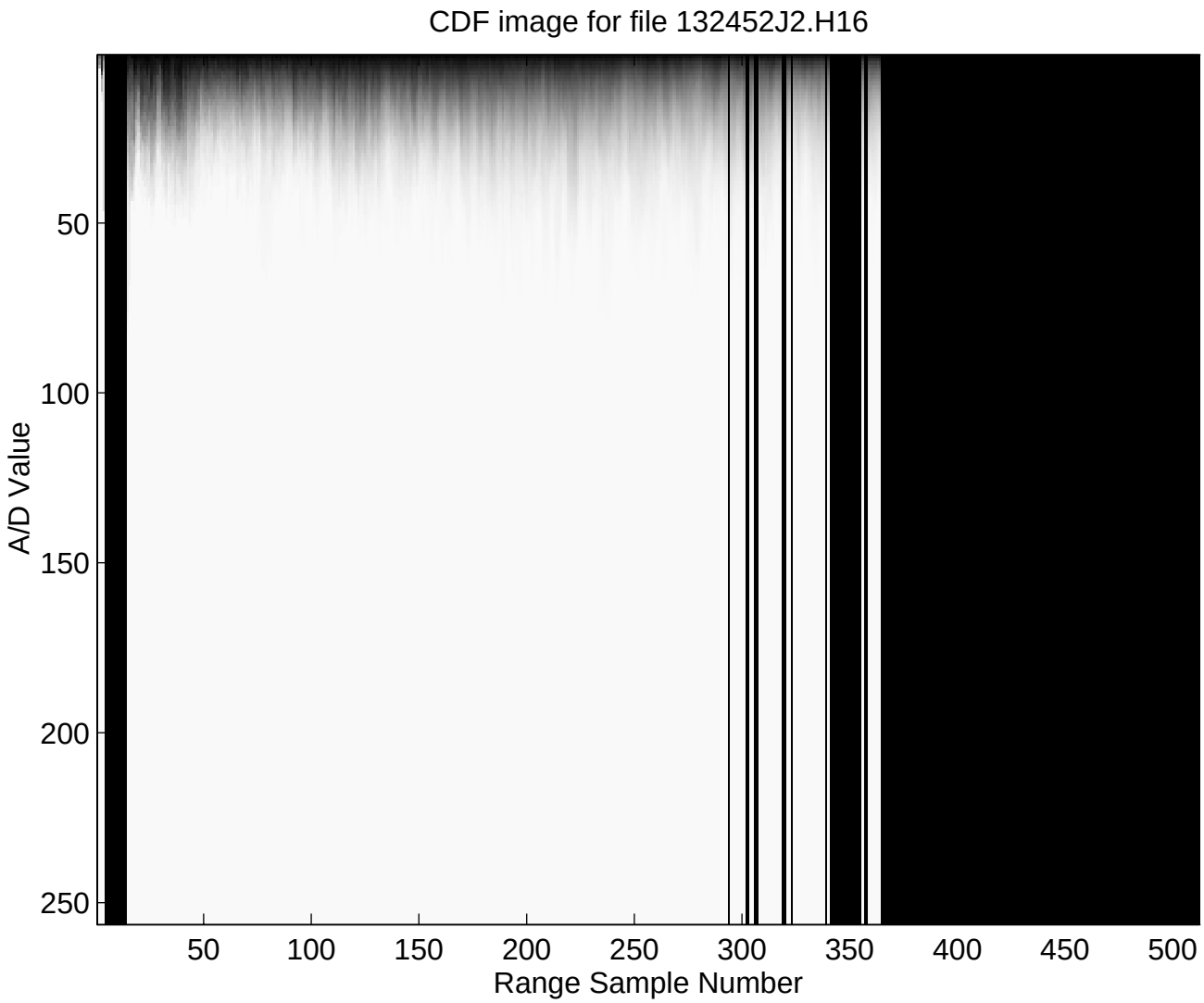

Figure 3-16 Cumulative distribution function (CDF) image for the data in file 132452J2.H16. The CDF curves are only generated for ranges having medians above 0

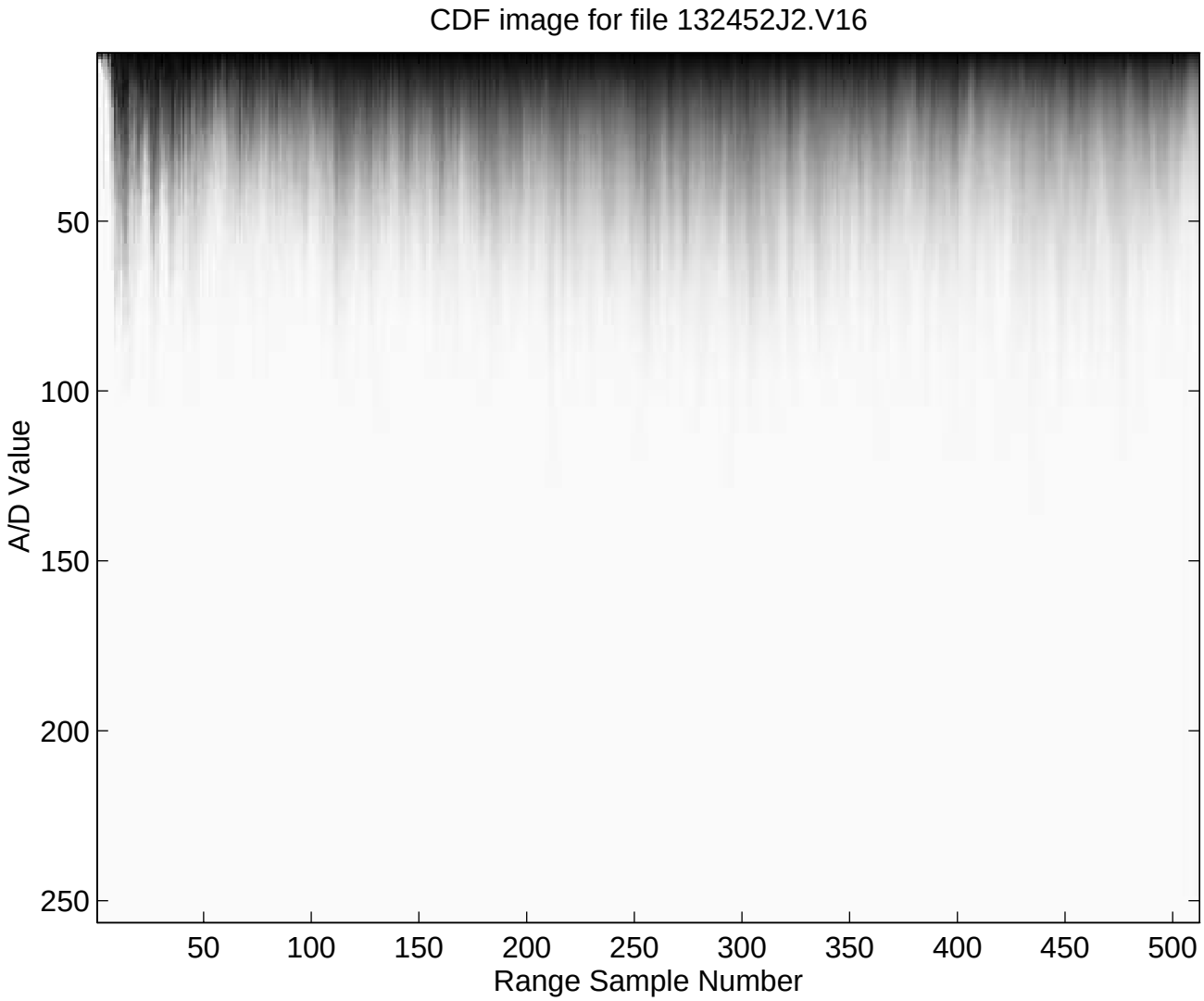

Figure 3-17 Cumulative distribution function (CDF) image for the data in file 132452J2.V16

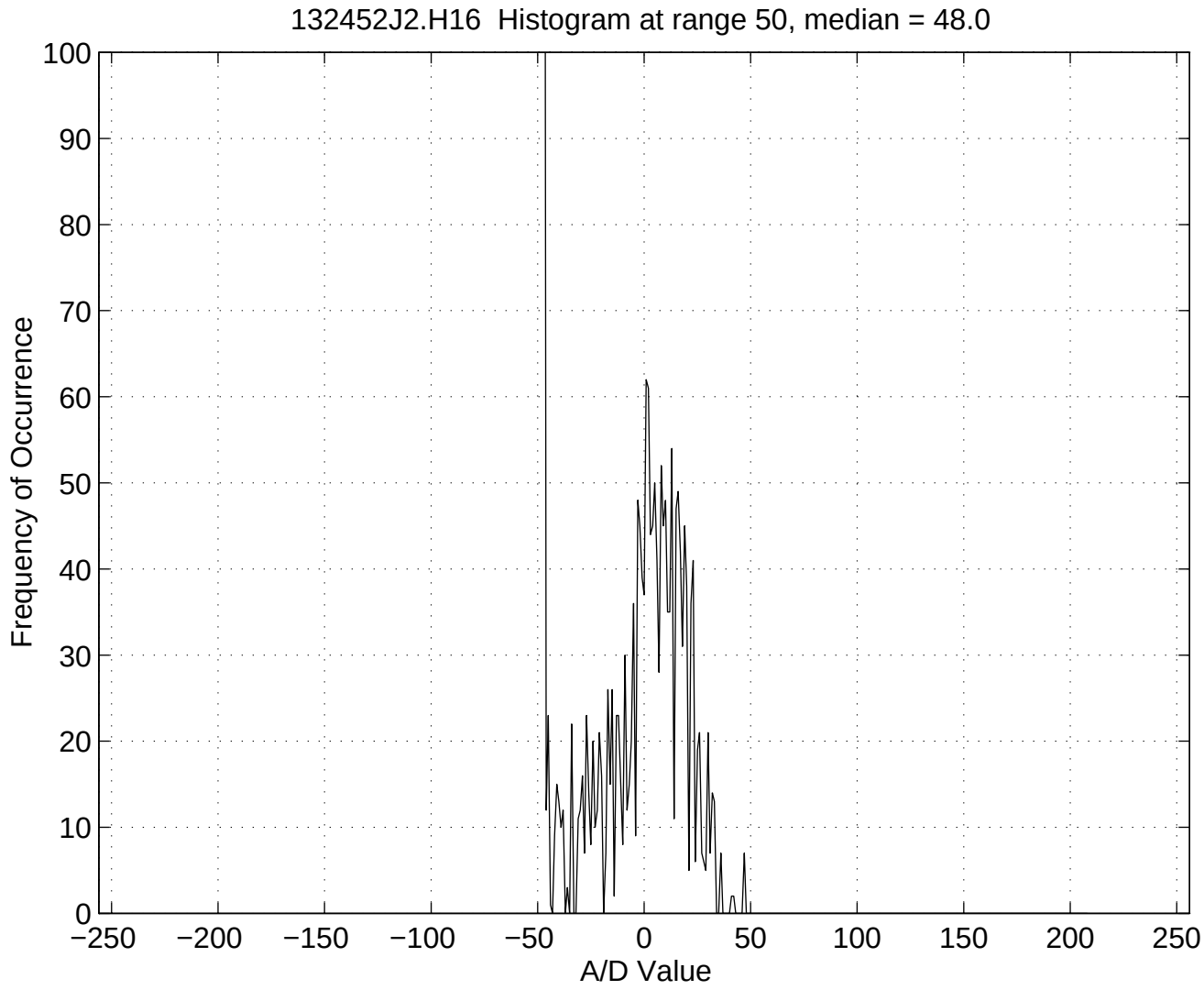

Figure 3-18 Histogram of HH data for range bin 50, after subtraction of median (=48)

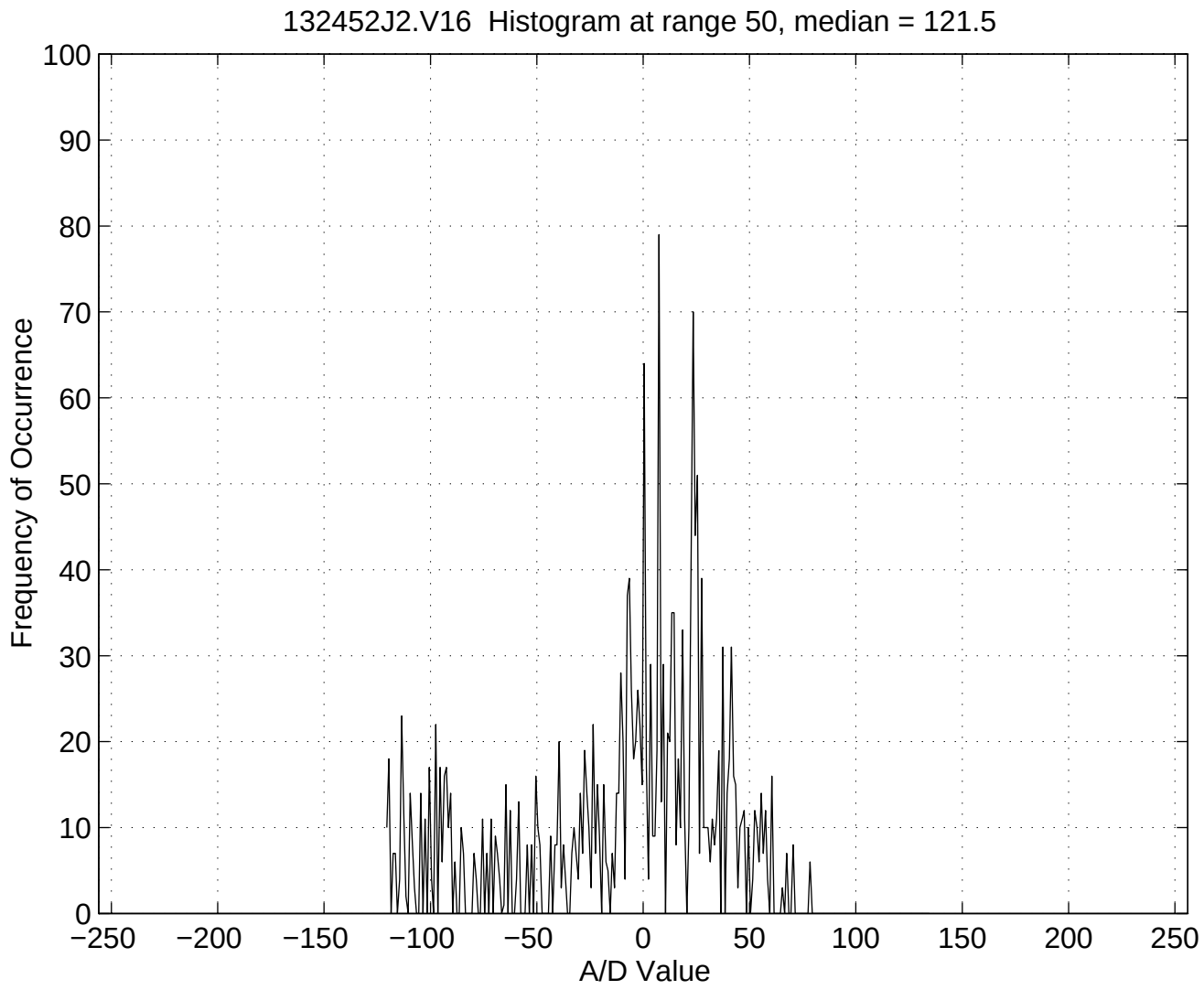

Figure 3-19 Histogram of HV data for range bin 50, after subtraction of median (=121.5)

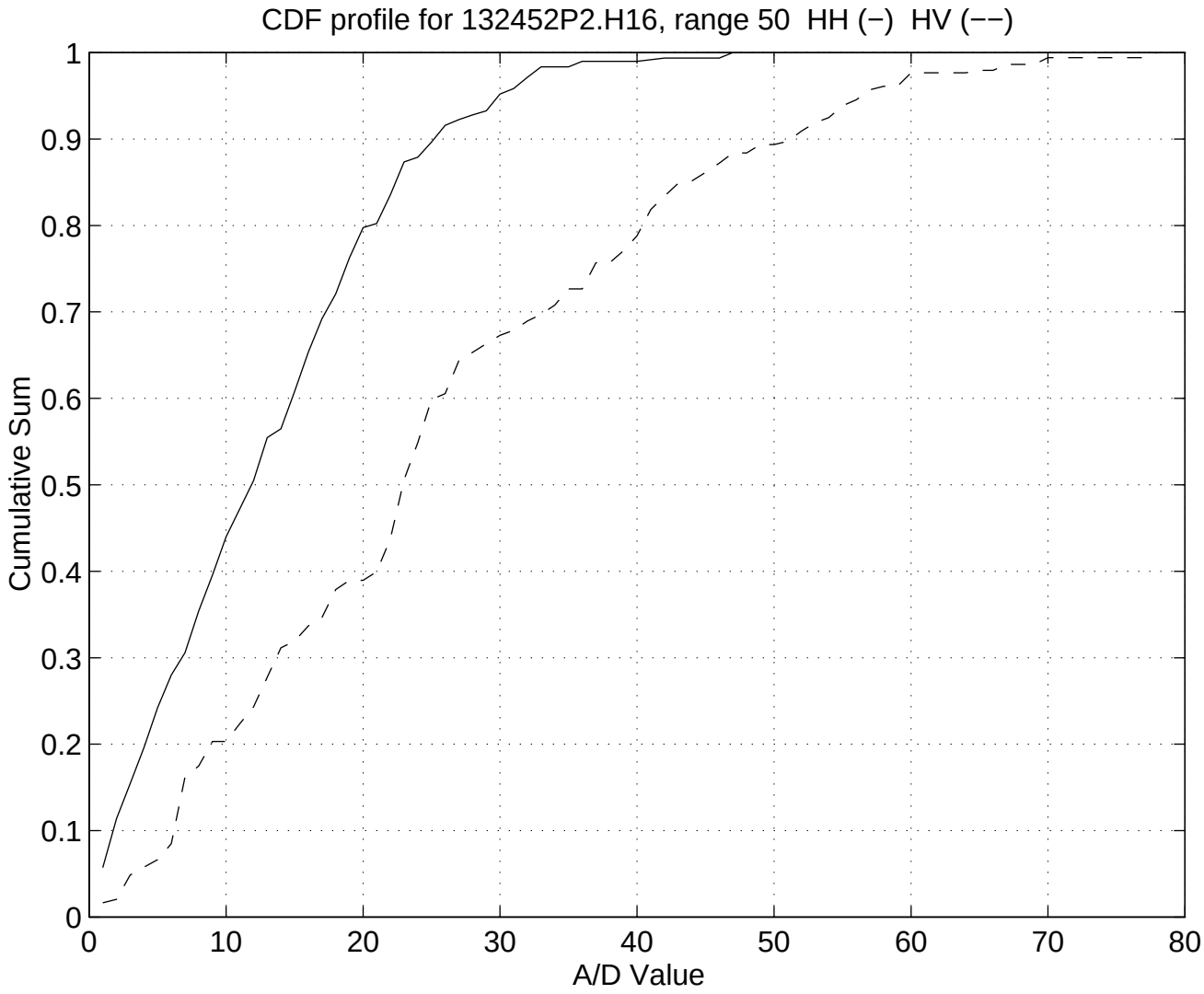

Figure 3-20 CDF curves based on data in Figure 3-18 and Figure 3-19

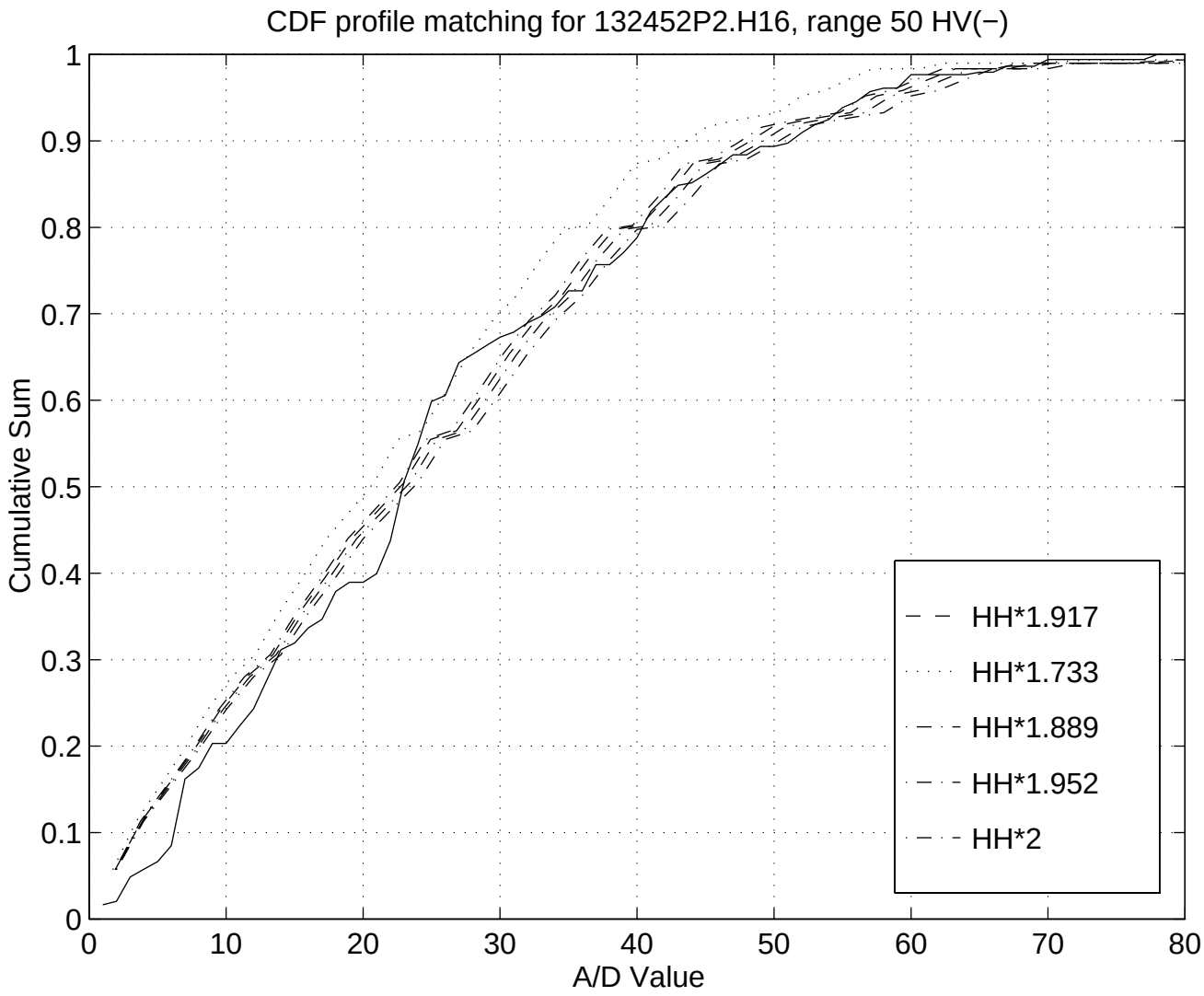

Figure 3-21 HH CDF curves matched to the HV CDF curve at various CDF levels

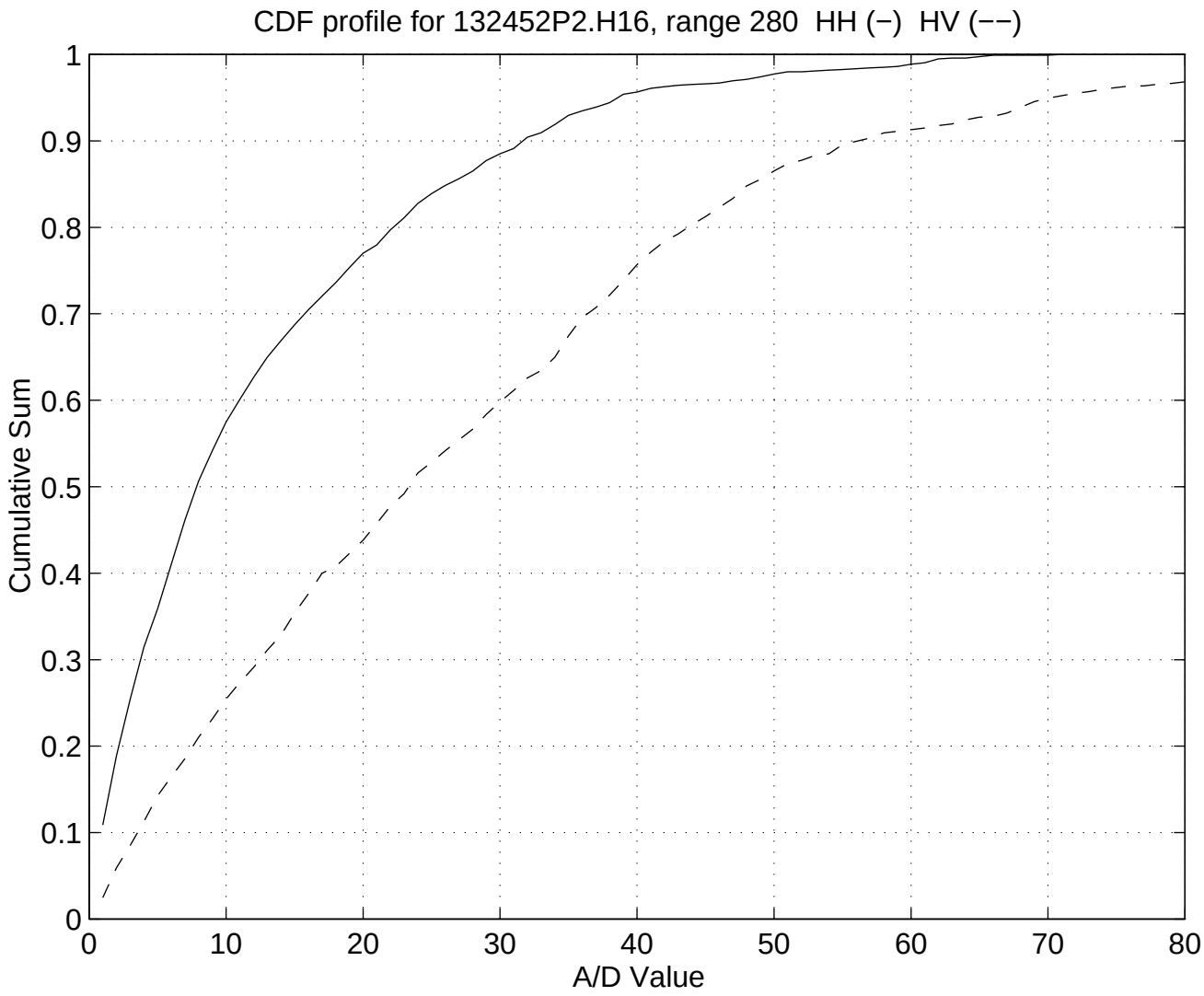

Figure 3-22 CDF curves for range sample 280. HH median was 1, HV median was 29

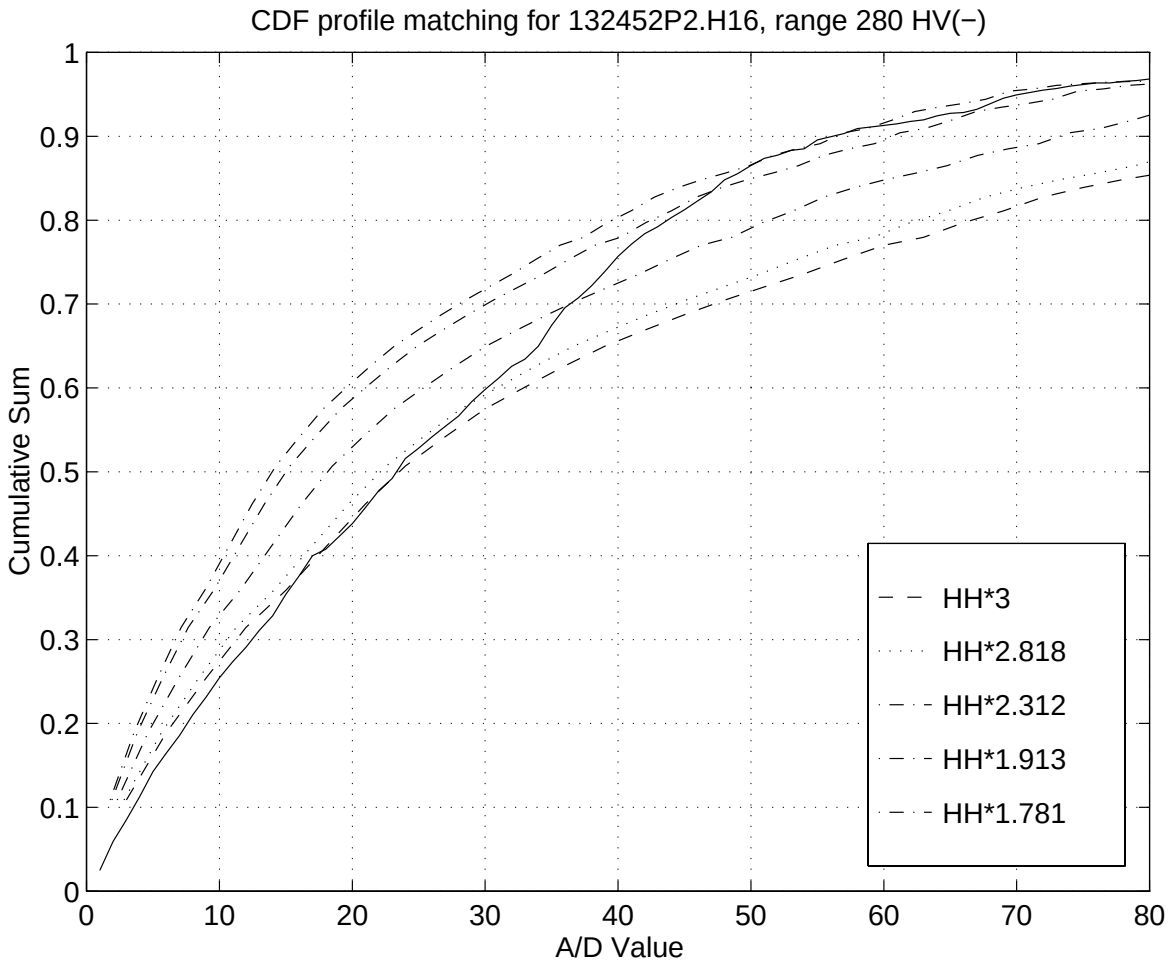

Figure 3-23 HH CDF curves matched to the HV CDF curve at various CDF levels for range sample 280.

A larger spread requirement should be used in future systems. Here it was relaxed to a low value to provide at least a rough estimate of the gain factor behaviour at as many ranges as possible. It was expected that grossly incorrect gain factors would be detectable and accommodated (e.g. through smoothing) at later stages.

The output of the above process was a gain multiplier vs. range to be applied to the HH image to match its data spread to that of the HV image. Separate arrays hold the gain factors based on 0.5, 0.6, 0.7, 0.8, and 0.9 CDF levels. These gain multiplier arrays were saved in a new file, whose name is created by substituting an 'F' for the 'S' in the input file name. Note that a gain value of 0 indicates a range marked as invalid for adjustment. Figure 3-24 shows the HH gain factor vs. range for the image pairs 132452B2.H16 and 132452B2.V16, as determined through matching at the various CDF levels. The figure shows that there can be quite a change in gain even from one range sample location to the

next. However, we expect in reality that the gain should vary quite slowly with range. Therefore the gain factors need to be sufficiently smoothed in range. Figure 3-25 shows the gain data from Figure 3-24, after smoothing using a 51-point median filter.

There is also the question of what gain factor to use for the ranges at which an estimate cannot be made, i.e., invalid ranges. Again this requires smooth extrapolation/interpolation based on a reasonable guess. In the case of Figure 3-25 it appears as if using a constant gain factor is appropriate over certain segments of range. Examining the median plot in Figure 3-5, the HH receiver seems to show strong STC effects, at least out to range sample 50. Therefore we would expect that the gain factor would be higher at the near ranges. However, the data does not permit a reliable estimate of the gain factor in this region. Therefore data within range index 50 may not be as well balanced. Similarly beyond range 200 the gain factor has been estimated using low-level data, with median values below 10. The apparent rise in gain factor may partly be due to the nature of the estimation procedure, and not be solely a function of the data. It is also not clear if the gain should continue to increase with range. In lieu of other information, it seems most prudent to simply extend the constant gain factor over the final range segment. Figure 3-26 shows a plot of the final gain curve determined for use with image file pair 132452B2.H16 and 132452B2.V16. The final output is a gain factor vs. range array, stored in a new file whose name is created by substituting an ‘E’ for the ‘S’ in the input file name.

The determination of the final gain factor behaviour vs. range is currently done by hand and eye, and represents a possible weakspot in the balancing procedure.

Range Normalizing

It is desirable to remove the range variation in received signal power to provide an image in which brightness (or colour) is related only to the radar reflectivity of the ice, regardless of range. This implies that the effects of STC and the spreading of the transmitted wave with range have both been normalized (i.e. removed). Both of these factors vary slowly between adjacent range cells.

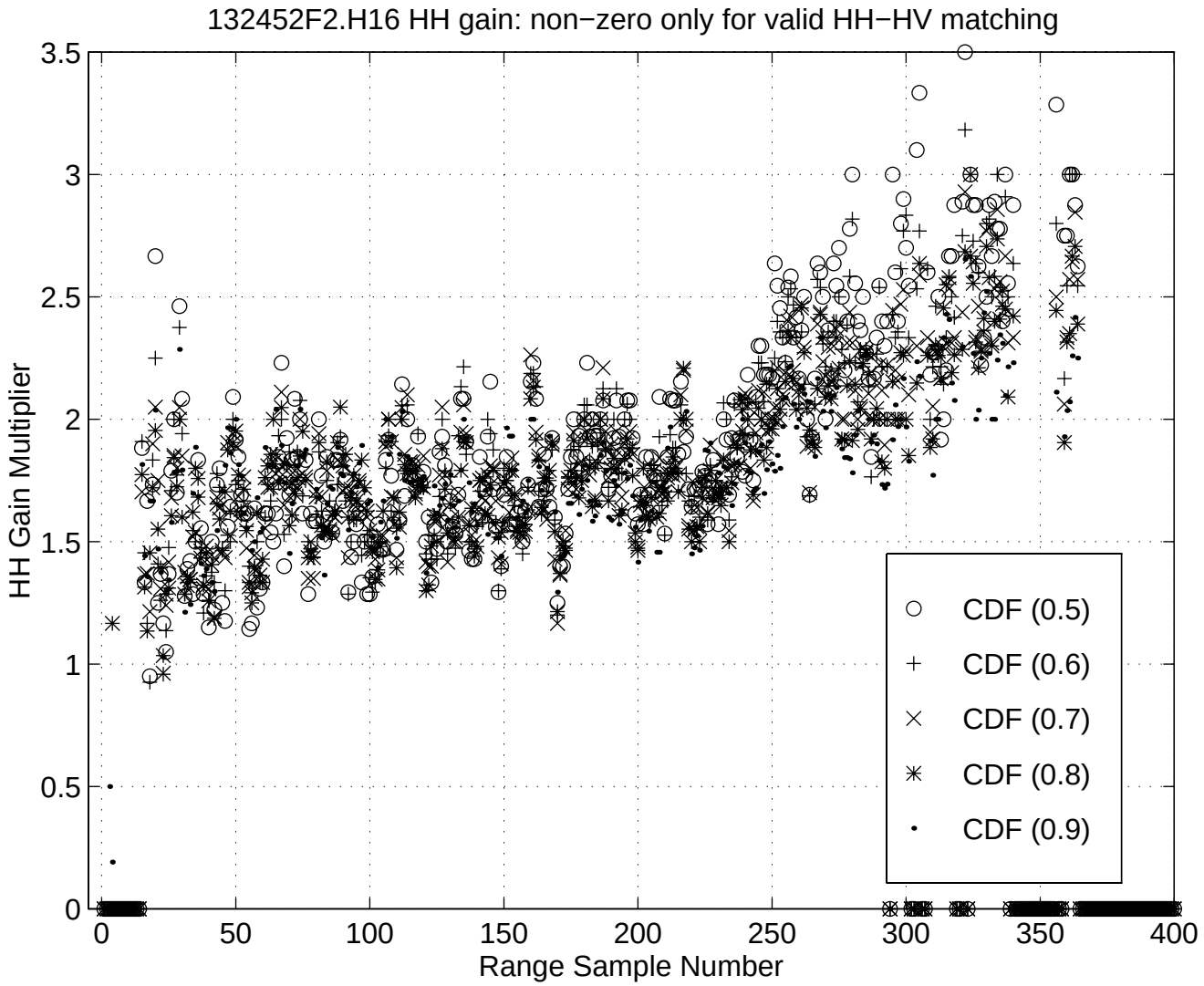

Figure 3-24 HH gain factor obtained by matching the CDF curves at various CDF levels.

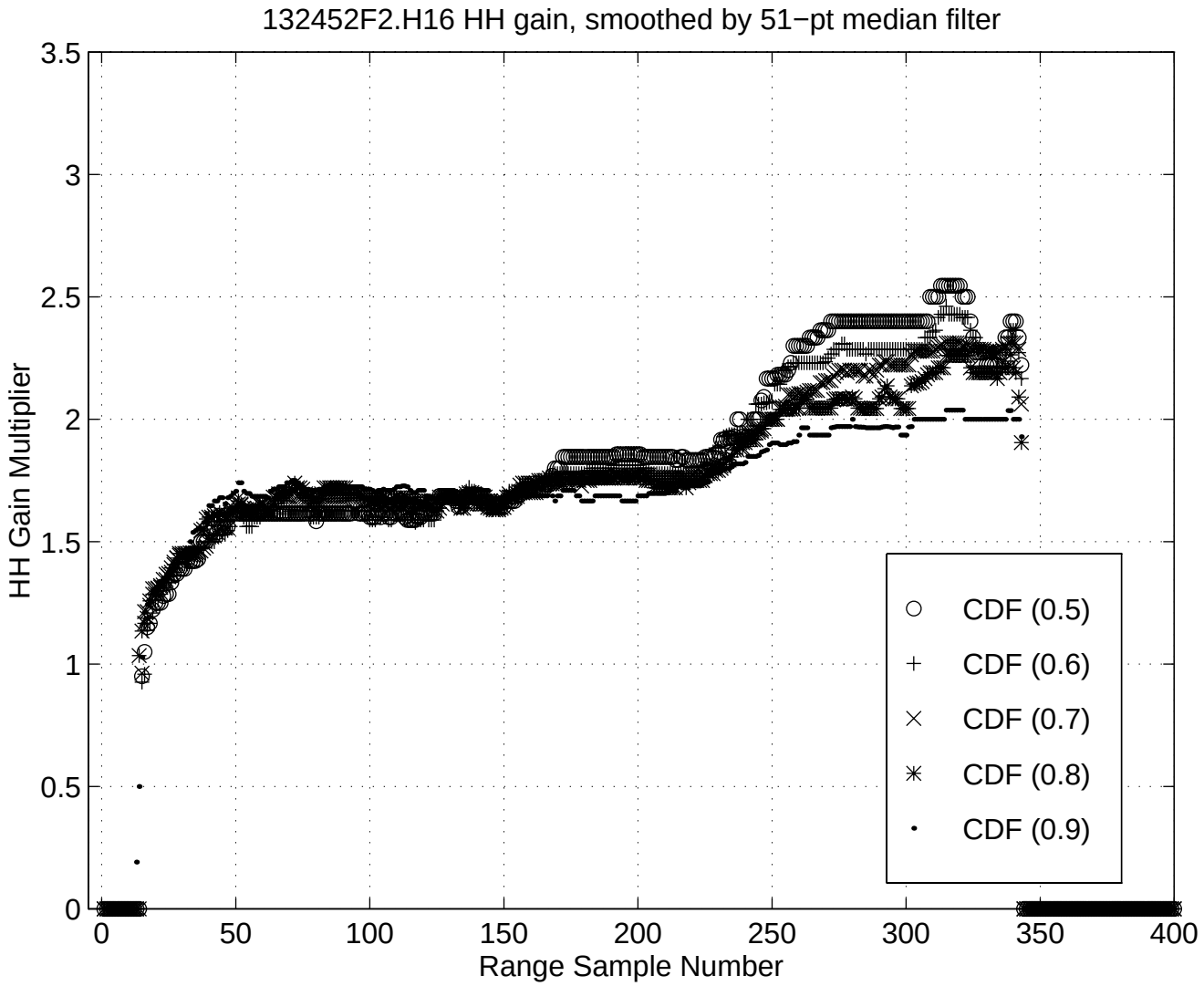

Figure 3-25 HH gain factors from Figure 3-24 after smoothing with a 51-point median filter.

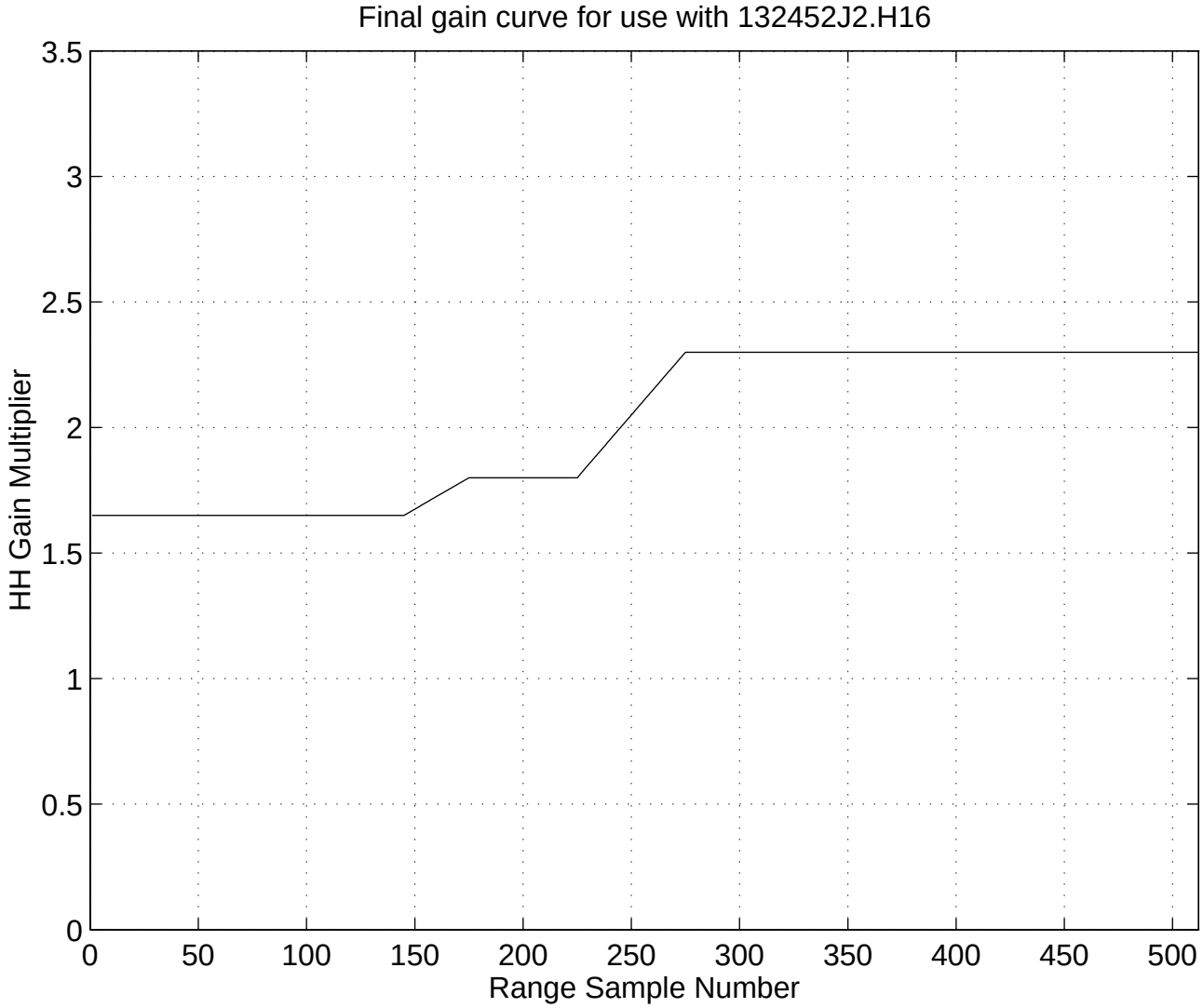

Figure 3-26 Final HH gain curve for use with file pair 132452B2.H16 and 132452B2.V16

We attempt to estimate their combined effect by fitting a smooth curve to the median range profile. The following basic technique is used. The HH median of Figure 3-5 is a typical case. The median value starts from a lower value at near range, quickly rising to a maximum, then decreasing more slowly with range. This curve is fit in two of three parts. The first part at near range, including slightly past the maximum, is fit visually and interactively with a 2nd or 3rd order polynomial. The longer range part is expected to fall off as some power of range. Thus the median is plotted vs. range on a log scale. The far-range portion of the curve is then fit with a straight line. Often the fitted curve must be extrapolated to try to estimate what the median would have been had the signal not fallen below the input range of the A/D, causing clipping at 0. There may be a third portion of the curve to be fit, smoothly joining the near and far range parts. Figure 3-27 to Figure

3-30 show the final result of the curve fitting process on both linear and log range scales, for image files 132452B2.H16 and 132452B2.V16. These smoothed estimated median curves are stored in a file whose name is created by substituting an ‘M’ for the ‘S’ in the input file name.

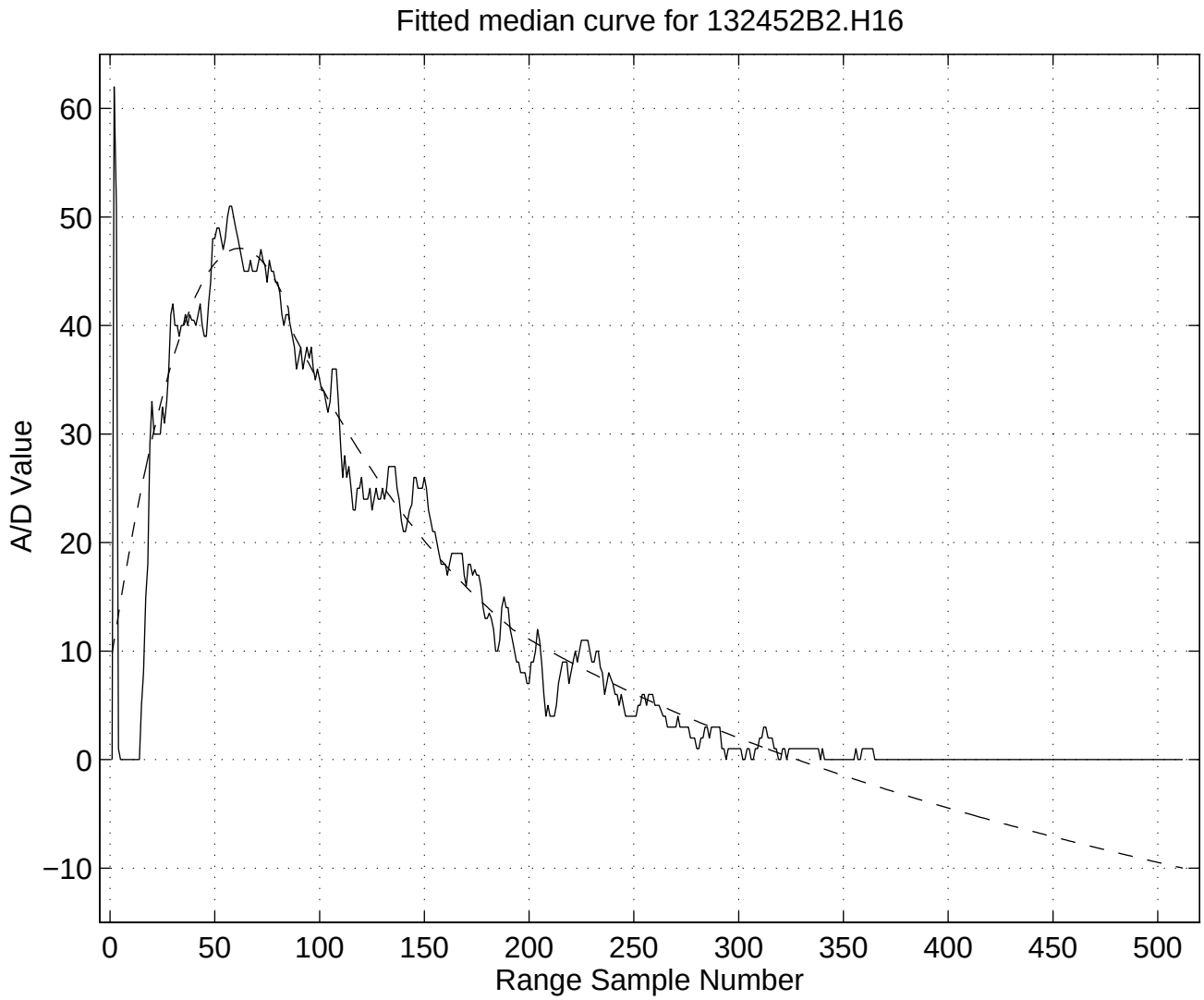

Figure 3-27 Median HH range profile and fitted curve for file 132452B2.H16, linear range scale

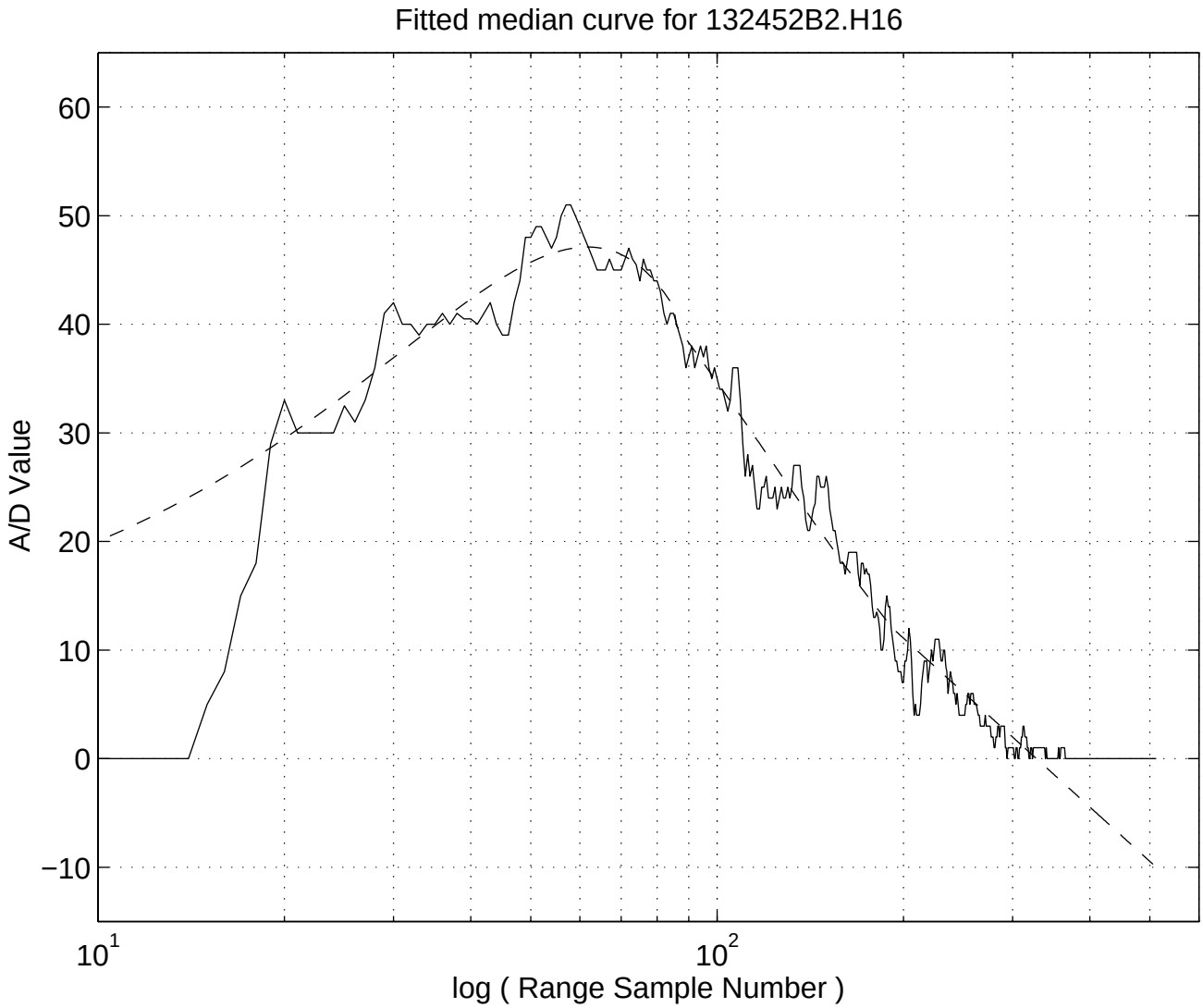

Figure 3-28 Median HH range profile and fitted curve for file 132452B2.H16, logarithmic range scale

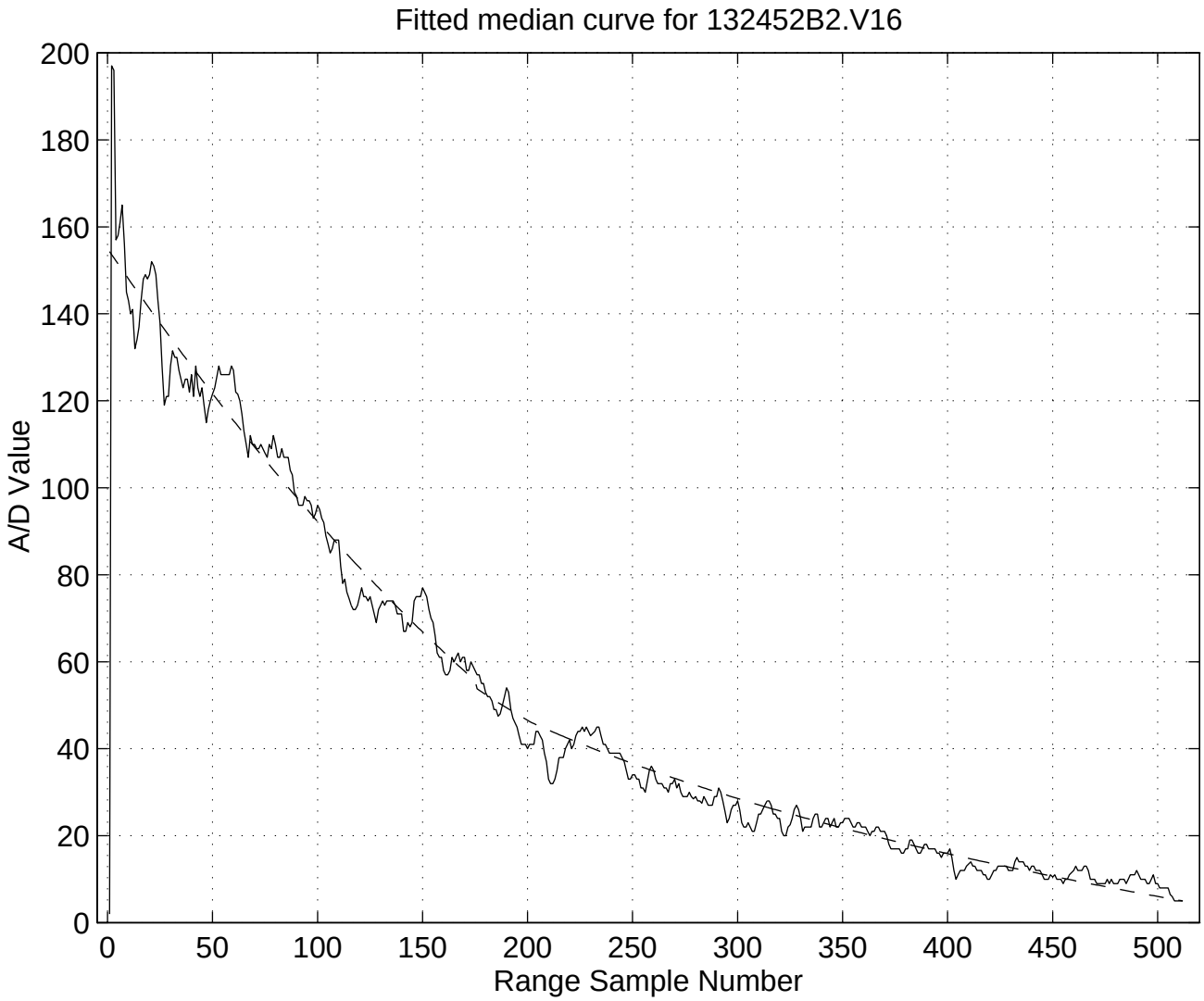

Figure 3-29 Median HV range profile and fitted curve for file 132452B2.V16, linear range scale

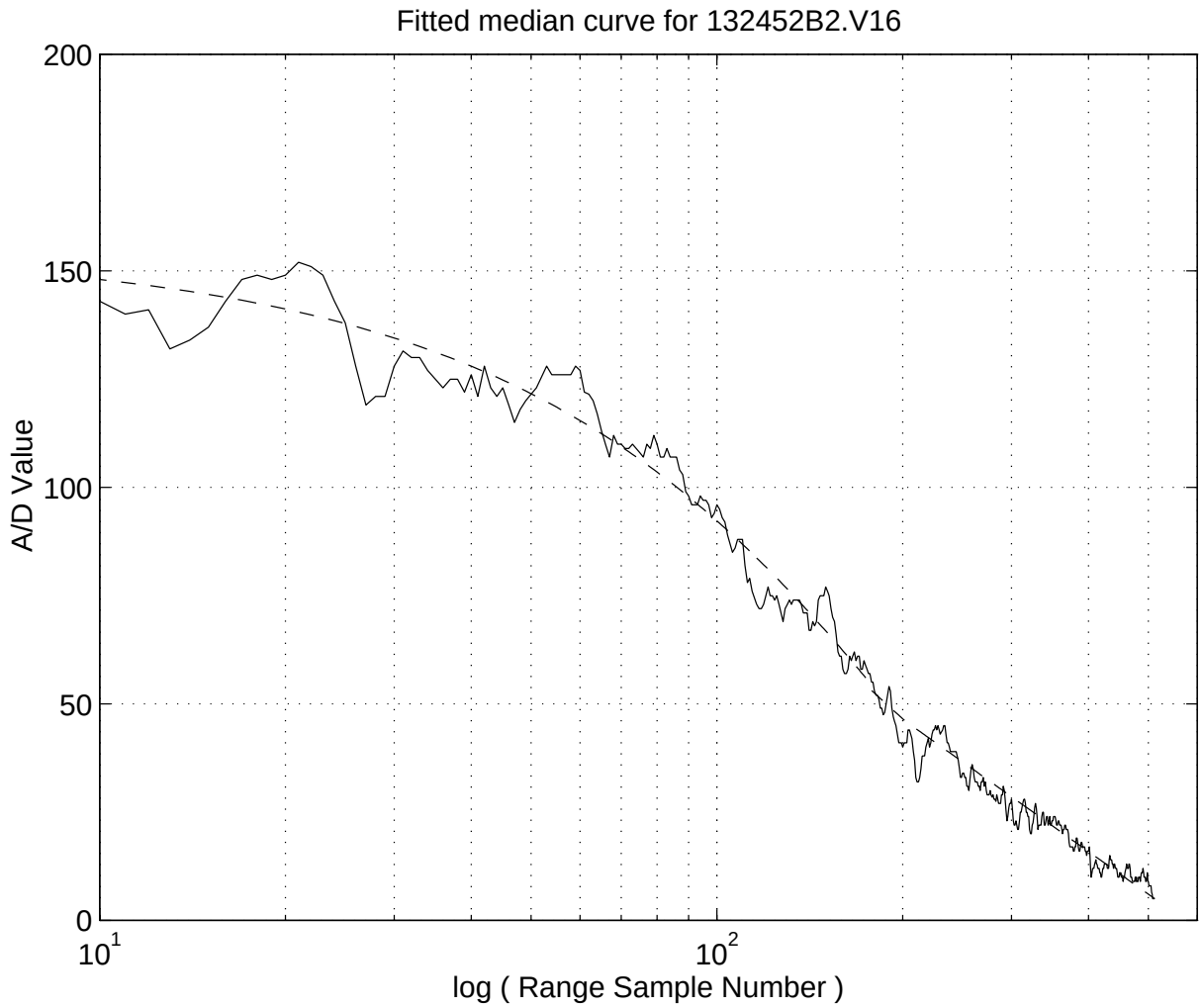

Figure 3-30 Median HV range profile and fitted curve for file 132452B2.V16, logarithmic range scale

The final procedure for preparing an image pair for intercomparison is the following. The smoothed median curve from the 'M' file is subtracted from each sweep of its corresponding B-scan, thereby normalizing the median value to zero at each range sample. (To avoid accenting 0 or very weak pixels, these pixels are separately marked for later adjustment.) Each sweep in the resulting HH B-scan is then multiplied by the gain factor vs. range curve obtained from the 'E' file. Finally, the HH B-scan is shifted in range and azimuth to correct for any offsets determined using the 2-D correlation discussed earlier. We now have a pair of B-scan images, both with a median of zero at all ranges, and matched data spreads (hopefully equal gains) at each range. Note that in further processing, range bins 511 and 512 are often ignored since they may contain wrong values, due to edge effects in the original PPI data. For example, vertical edges are visible on either side of the PPI image in Figure 3-2, which also accounts for the ‘maximum’ curves of Figure 3-5 and Figure 3-6 going toward 256 at range 512.

For display of range-normalized images, the image minimum and maximum values are calculated. Taking the greater of the absolute values of the minimum and maximum, the image is scaled (multiplied) by 127 / greater. Now the image values range from -127 to +127. A constant of +128 is added to the image to shift the data to 1 to 255 for display. Pixels marked as 'noise-only' are set to the desired level to make them non-distracting (e.g. set to the background level). If desired, the image can be scan-converted from the B-scan format to the PPI format. Figure 3-31 and Figure 3-32 show the final balanced HH and HV PPI images for files 132452B2.H16 and 132452B2.V16. The HH image contains values between 76 and 252, and the HV image is between 23 and 223. The same scale factor was used for both images.

Care must be taken in comparing the HH and HV images. The HV image shows more ice detail, particularly at longer ranges, since it suffered less low-level clipping than the HH image (evidenced by comparing the HH and HV medians in Figure 3-5 and Figure 3-6). The fair methods of comparison is to process only those image locations (pixels) for which both the HH and HV images are non-zero (i.e. not clipped). Figure 3-33 shows the HV image containing only those pixel locations for which the HH image is non-zero. Now the HH and HV images look very similar. This implies that the HH-HV differences that we are hoping to exploit to provide ice type discrimination may be relatively small quantitatively. We need to examine further the size of these differences in relation to the variance introduced through the median and gain estimation process.

Meanwhile the zero-median matched HH and HV images, both range normalized, are now available for intercomparison and combination. Earlier research has suggested that ice type can be determined by comparing the values of the HH and HV returns. For first-year (first-year) ice, the HH return is noticeably stronger larger than HV return, while for old ice (multi-year (multi-year) and iceberg (IB)) the HH and HV returns are much closer. This suggests that taking the difference between the images, i.e., HH-HV will show smaller values for old ice and larger values for first-year ice.

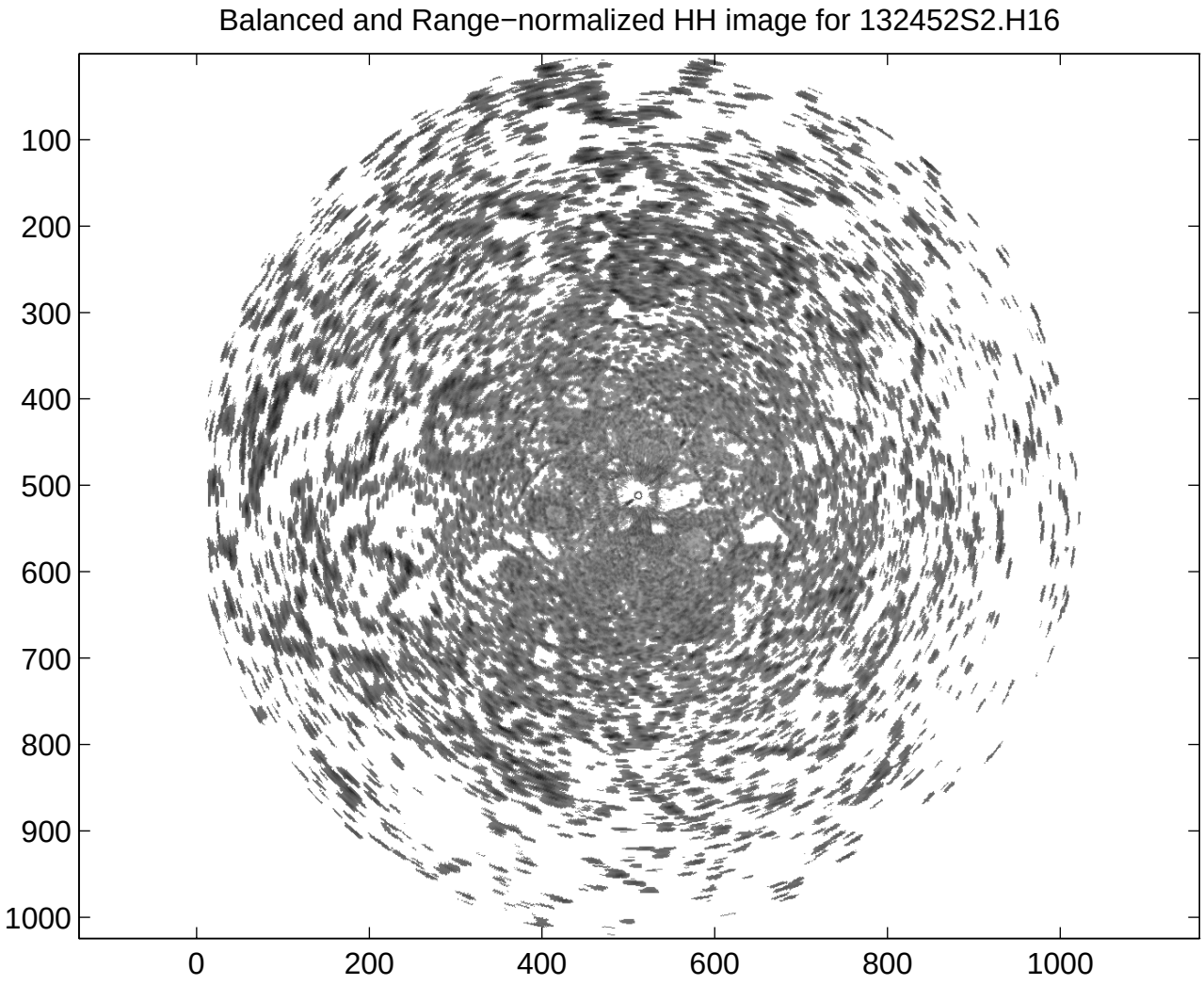

Figure 3-31 Final HH image, range normalized and balanced to match the HV image of Figure 3-32

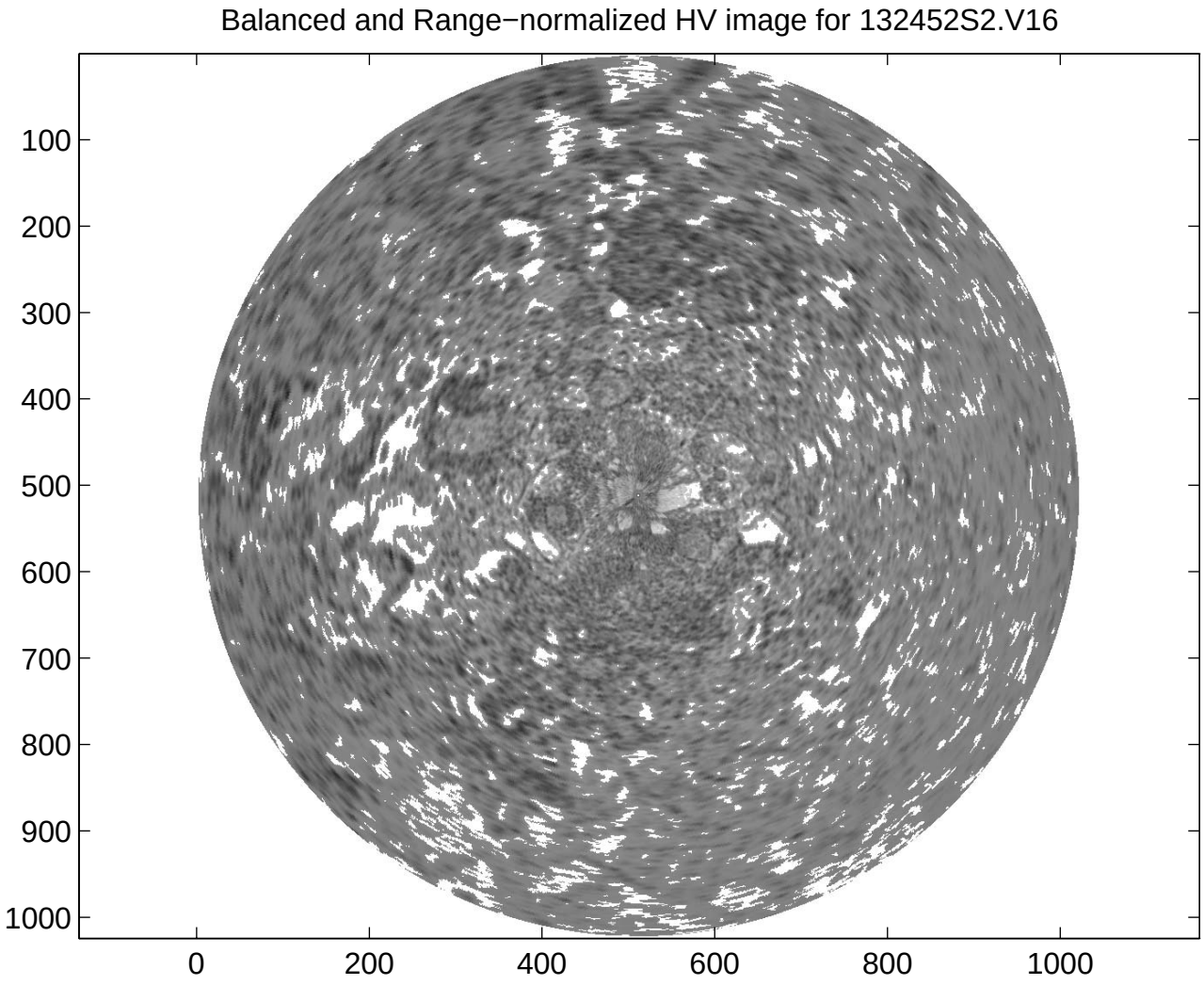

Figure 3-32 Final HV image, range normalized and balanced to match the HH image of Figure 3-31

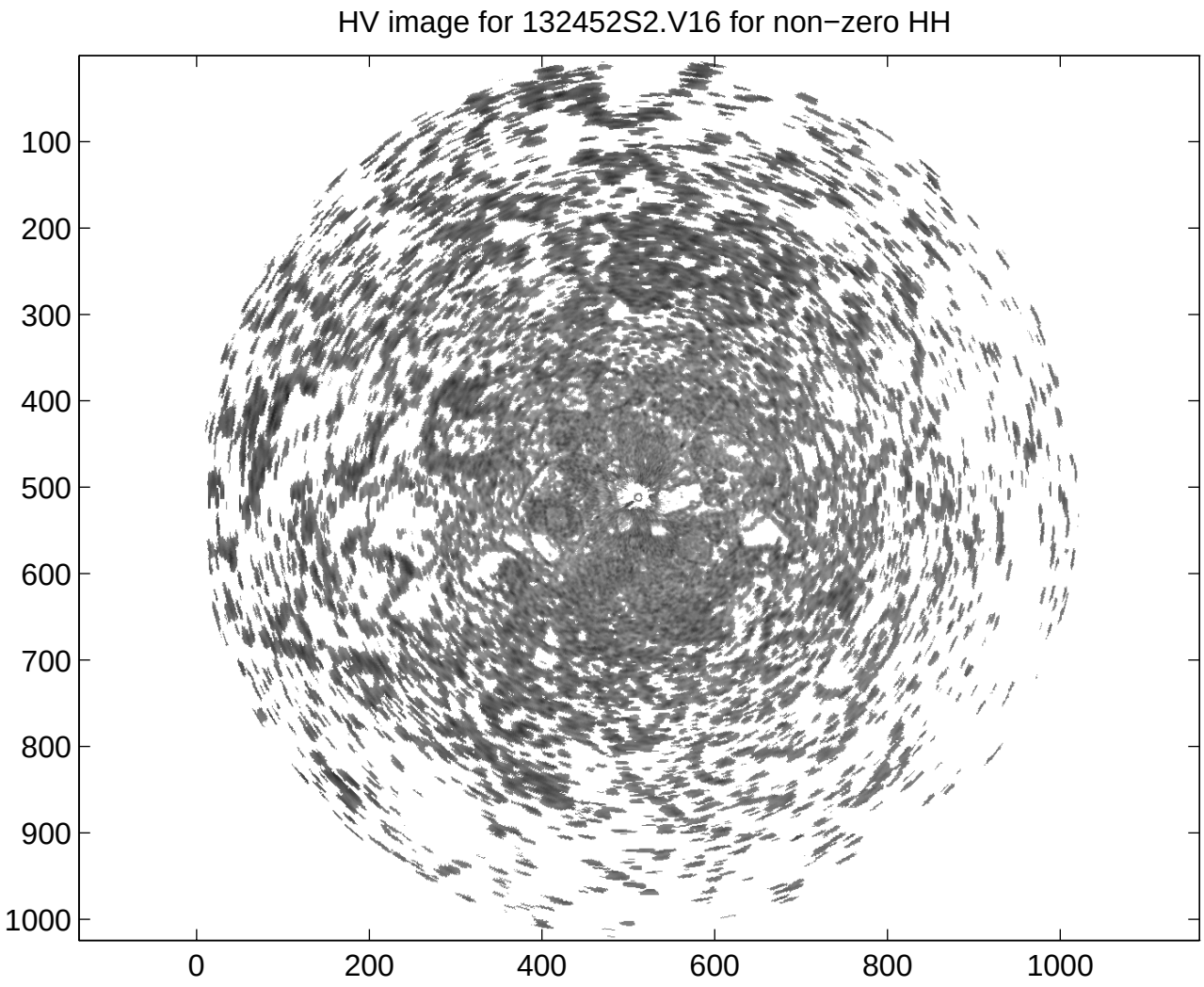

Figure 3-33 Final HV image, only for locations where the HH image is non-zero

There are, however, at least four caveats:

1) The ice type indication is of most interest for targets that show strong HH returns, indicating that they have significant size. However, a small HH-HV difference can arise from two very strong HH and HV signals, or two equally weak ones (of much less interest). Therefore the display of the HH-HV difference should include some indication of the strength of the HH and HV returns.

2) As discussed earlier, the response (video bandwidth) of the two radar/MRI systems seems to be different. The HH radar images look ‘crisper’ compared to the HV images. Overlaying the images will result in some vestiges of the HV returns around the narrower HH returns.

3) Some scan-to-scan variation in the HH or HV return from a given ice target is expected as the ship moves between scans, and the aspect of the target with respect to the radar changes slightly. Therefore the HH-HV difference may vary from scan to scan. (This effect is discussed later in the report)

4) The image balancing is based on some assumptions regarding the statistics of the HH and HV images, and the adjusting parameters are being estimated from a limited amount of data. Obviously there will be errors in the parameter determination. However, the goal here is simply to present the viewer with an image that will offer a quick and as accurate as possible impression of the ice conditions in a given area for the purposes of route selection. At this point, accurate information about the ice conditions within an arbitrary image pixel are not the focus; the larger picture is.

3.6.1 Combined Image Display

Given separate HH and HV images, the requirement is to display the pertinent information from both radars in one display. Two approaches have been considered, both based on the use of colour display.

Associated with the use of colour is the concept of a colour-space model. Two such models are RGB (red/green/blue) and HSV (hue/saturation/value). In each of these models, each of the three components can be varied independently; i.e., there are three degrees of freedom in each model.

Consider first the RGB model. Colours in a video display are created as mixtures of red, green, and blue, generated by controlling the intensity of the red, green, and blue guns of the display tube. Typically an 8-bit D/A converter (0 to 255) is used to control each gun. One display technique therefore is to use the value of the HH image data to control the red gun, the HV value to control the green gun, and keep the blue gun at 0. At each pixel the red due to the HH image will mix with the green due to the HV image, producing yellow (red+green) where both are strong, reddish where HH is stronger, and greenish where the HV is stronger. Other pairs of guns can be used.

Next consider the HSV model. Hue defines the colour. Saturation defines the strength of the colour. Value defines the intensity or brightness of the pixel. The average image data, taken as (HH+HV)/2, can be used to control the value. Areas of strong return will be brighter, weak returns will be dark. Setting full saturation, the HH-HV difference can be used to control the hue. Thus the colour will show the relative strengths of the HH and HV returns, while the brightness will show the strength of the average return, i.e., the importance of the underlying target. Figure 3-34 shows such a colour table. This is the scheme used to combine the two polarimetric channels into a single display. Two points to note are that apart from the loss of dynamic range of the display, the scheme in no way sacrifices the information available to the radar operator. Secondly, it is possible to reduce the loss in dynamic range by allocating lesser bits to code the colour (the example

shows a display when 4 bits are used to code both the intensity and the colour), thus providing the operator with an ability to selectively choose the colour overlay.

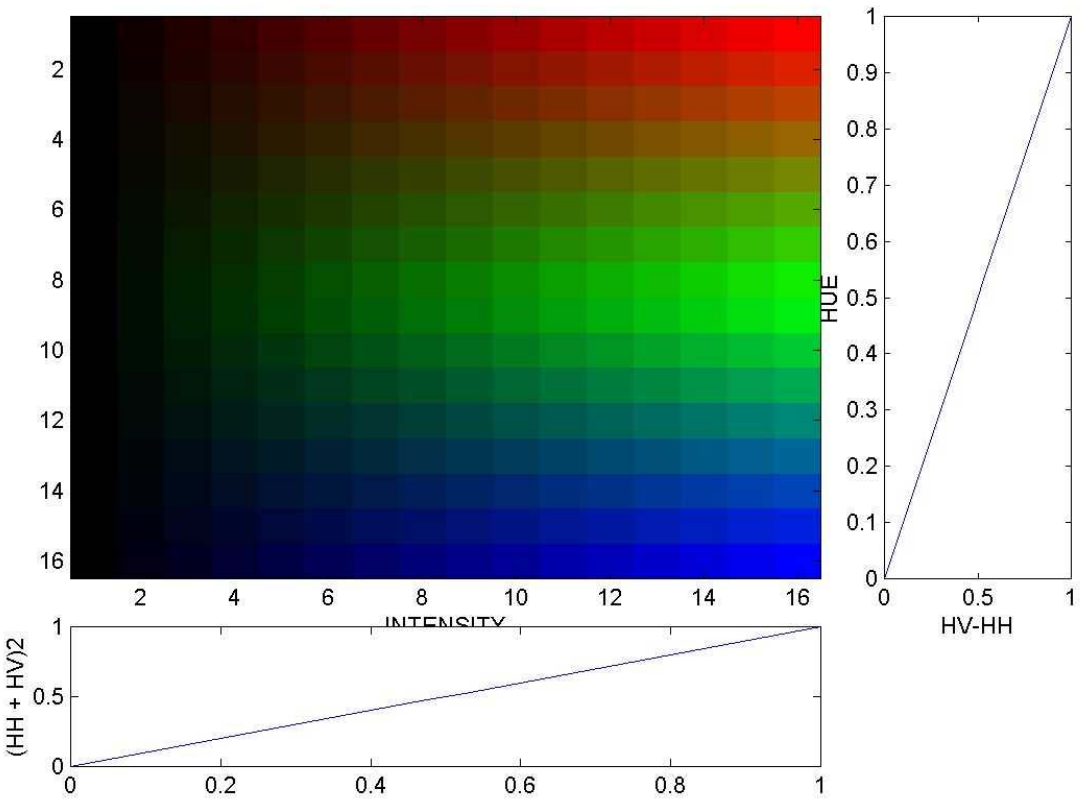

Figure 3-34 The HSV based colour mapping used to produce the composite images

Data Sequences

In total, five data sets were chosen for analysis. As described earlier, all scans within the selected segment on tape were extracted for each of the HH and HV tapes. The time stamps were then compared and only those HH-HV pairs that matched exactly were retained. Table 3-2 lists the resulting data sequences, the number of scans per sequence, the range scale represented by 512 samples, and the gain and STC settings.

Files	No. of scans	Range (nmi)	HH Gain	HH STC	HV Gain	HV STC
133113S1.H08 to 133312S1.H08	46	6.91	1.0	0.75	13	0
151301S1.H10 to 151430S1.H10	25	6.91	.75	off	13	0
132318S2.H16 to 132452S2.H16	26	3.48	.50	.75	12	7
185231S1.H18 to 185411S1.H18	40	6.91	.75	.25	13	0
190846S8.H18 to 191042S8.H18	26	1.74	.75	.50	13	0

Table 3-2 List of extracted and time-matched sequences. The pulse filter is on, CFAR is off for all sequences. The number of scans integrated is 1, except for S8.H18/V18 for which it is 4.

Initially, one pair of scans from each sequence, listed in Table 3-3, was chosen for processing. The results for pair S2.H16/V16 were presented above. The following sections report on similar processing applied to the remaining four pairs of scans.

File pairs (p=H or V)	Range scale factor (nmi/pixel)	Date collected	GPS latitude (^{O} N)	GPS longitude (^{O} W)
133126S1.p08	0.0135	Nov 2/95	74.4988	80.0293
151306S1.p10	0.0135	Nov 2/95	74.4505	80.9330
132452S2.p16	0.0068	Nov 3/95	74.5888	92.8357
185231S1.p18	0.0135	Nov 3/95	74.6193	94.7723
190854S8.p18	0.0034	Nov 3/95	74.6420	94.9818

Table 3-3 Five pairs of scans used for detailed processing

Figure 3-35 to Figure 3-42 show the various statistical profiles vs. range for the four data pairs.

Figure 3-35 shows that the HH data for S1H08 does not use the A/D range very effectively, and showing low returns with very small medians. This is partly a result of the relatively large STC setting, as listed in Table 3-2. The STC does accomplish the desired result of keeping the data faiirly constant level with range, based on observation of the maximum. On the other hand, the HV channel (Figure 3-36) used no STC, and the data makes good use of the A/D range. The reduction in return power with range is apparent.

The HH data for H1S10 (Figure 3-37) makes better use of the A/D, in this case using no STC. The setting for the HV channel (Figure 3-38) is unfortunately a little too strong, with clipping of the maximums up to a range of about 200 pixels. This clipping restricts the ability to quantifiably compare the HH and HV returns for strong targets, such as icebergs.

The HH and HV data for H1S18 (Figure 3-39 and Figure 3-40) is set slightly low, with low medians beyond the range of about 225 pixels, but is otherwise workable.The HH channel uses a small STC setting.

The HH and HV data for H8S18 (Figure 3-41 and Figure 3-42) shows similar settings, with slightly more HH STC. The curves for S8H18 are smoother than those for S1H18 as a result of the scan integration in the MRI, set at 4 for S8H18 and 1 for S1H18.

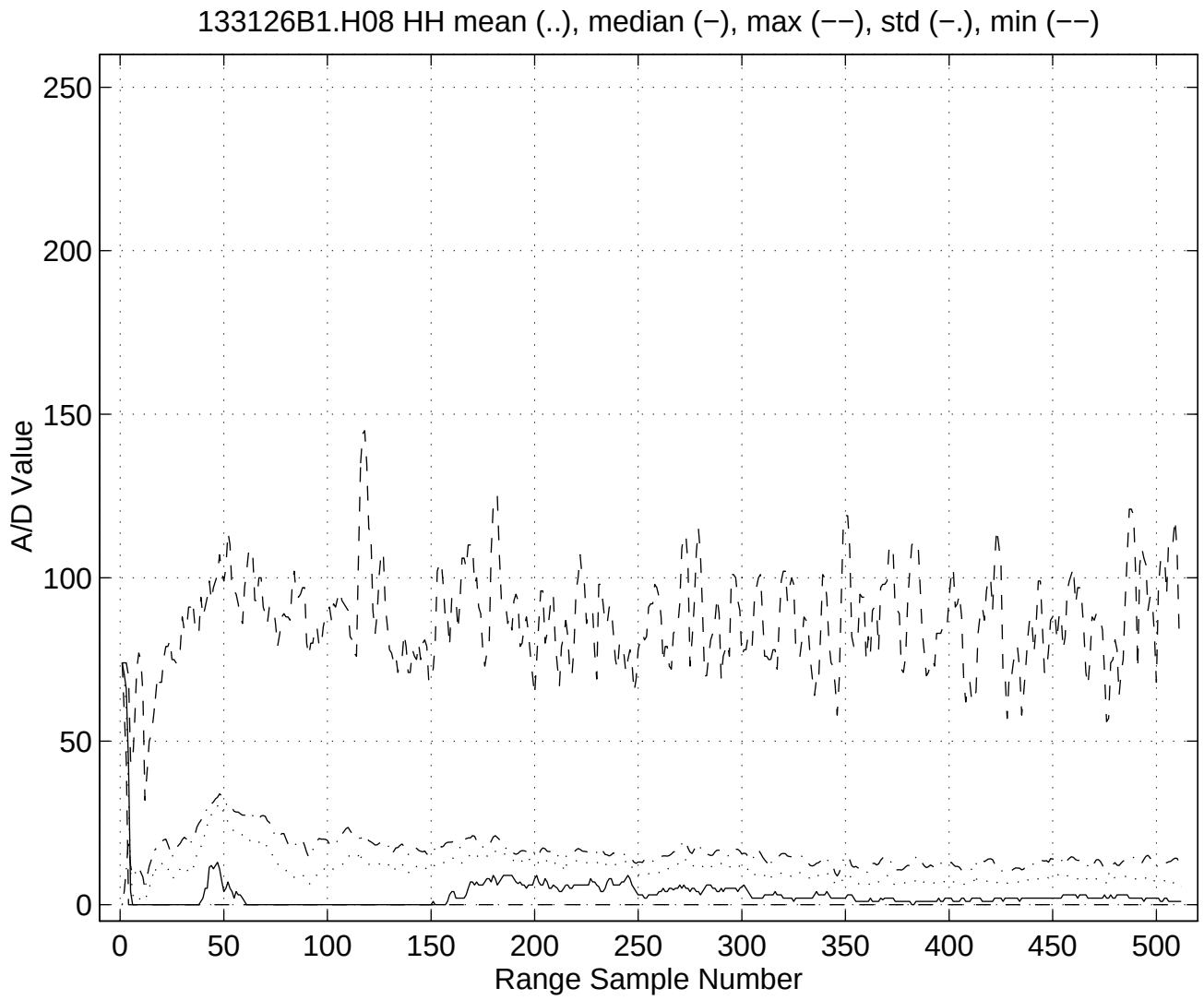

Figure 3-35 Plot of minimum, maximum, mean, median, and standard deviation vs. range for the HH B-scan data from file 133126S1.H08

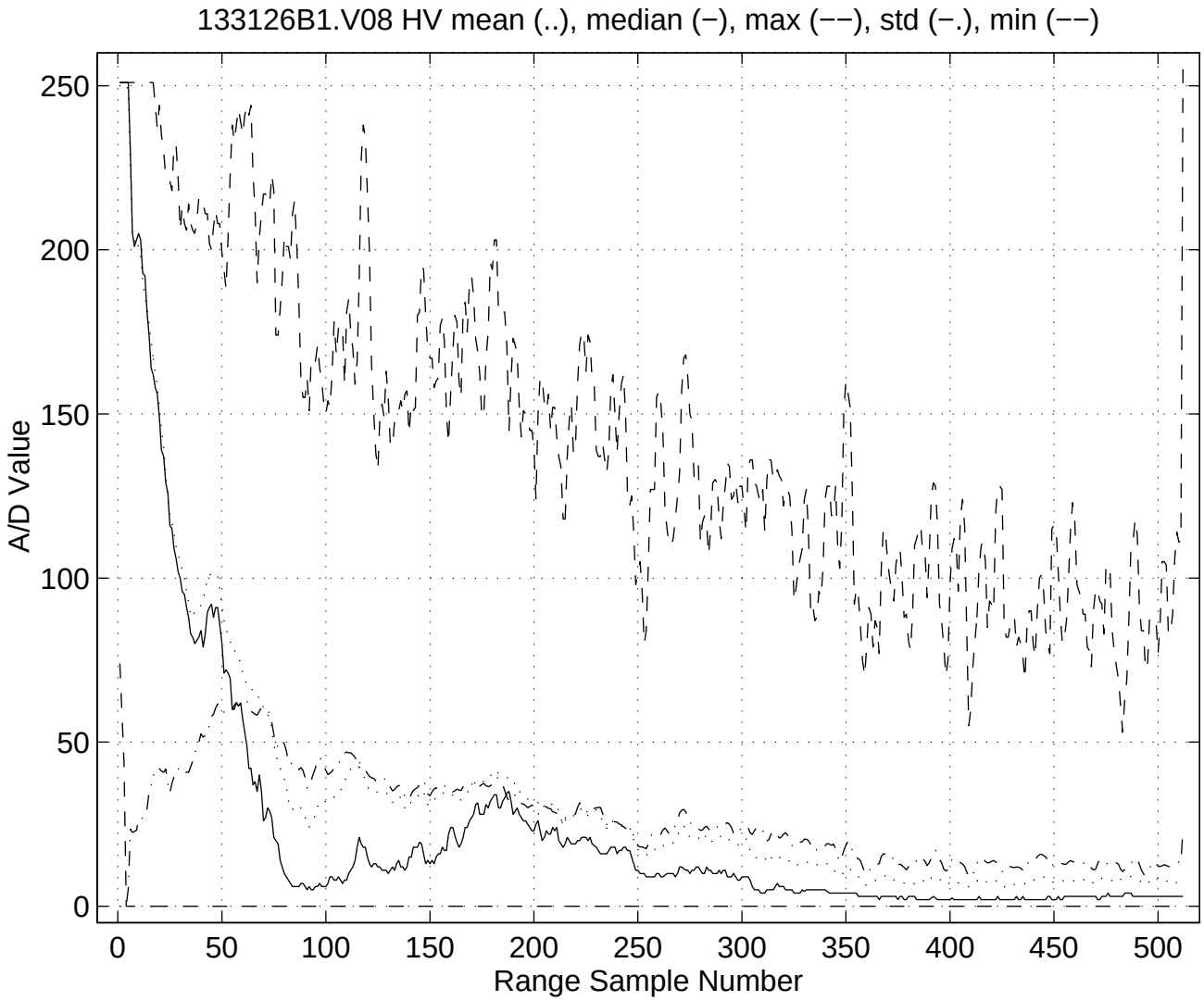

Figure 3-36 Plot of minimum, maximum, mean, median, and standard deviation vs. range for the HV B-scan data from file 133126S1.V08

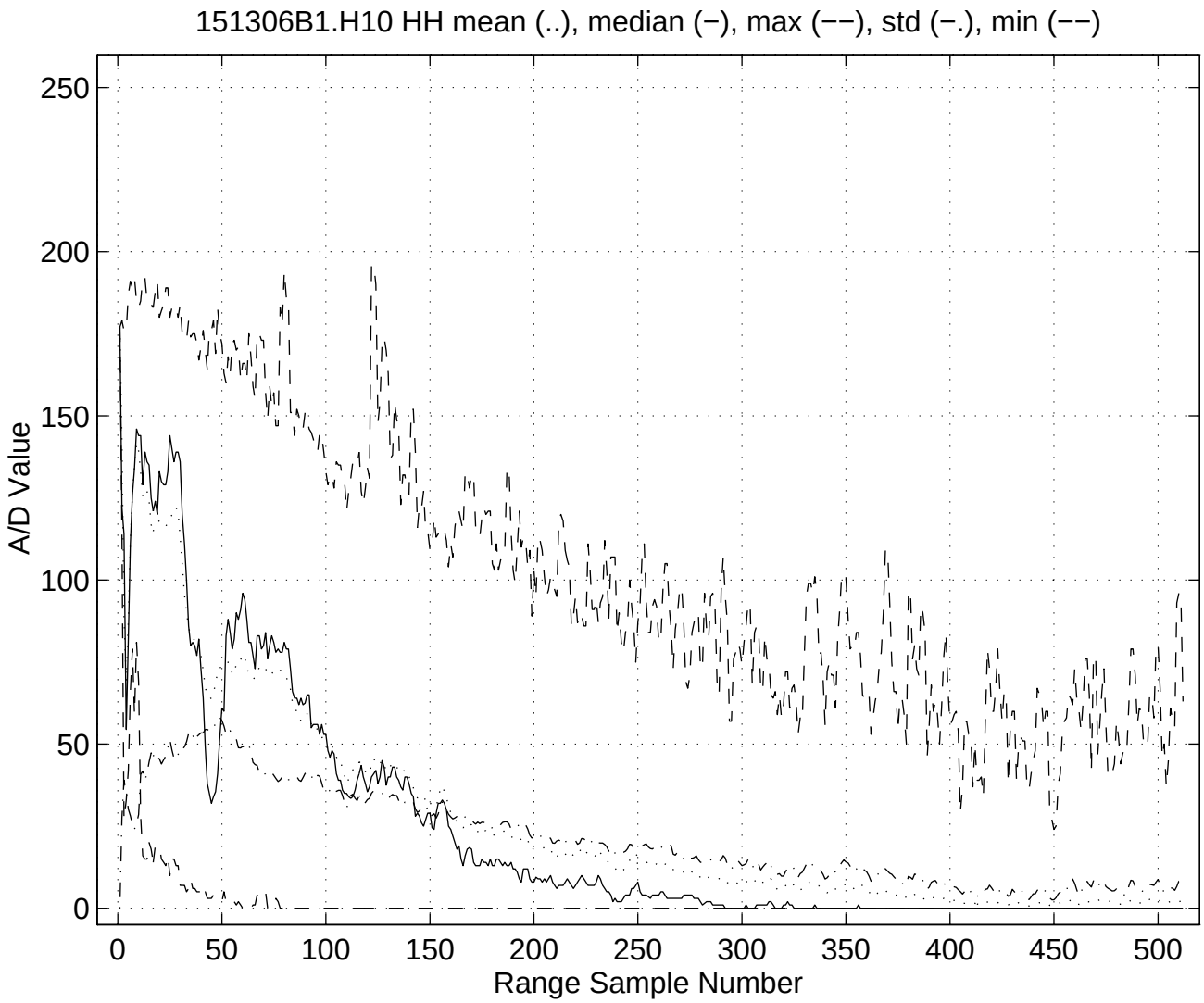

Figure 3-37 Plot of minimum, maximum, mean, median, and standard deviation vs. range for the HH B-scan data from file 151306S1.H10

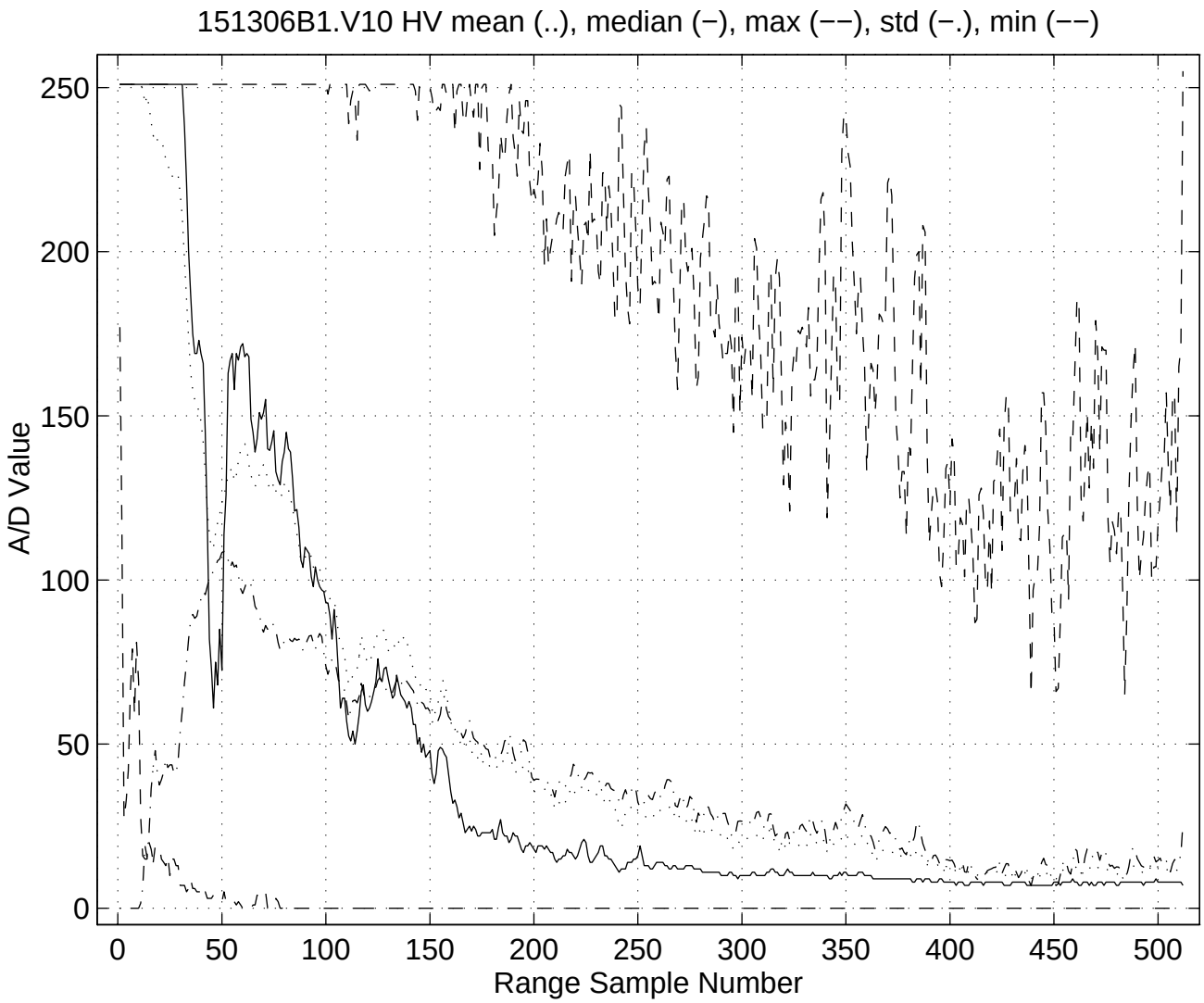

Figure 3-38 Plot of minimum, maximum, mean, median, and standard deviation vs. range for the HV B-scan data from file 151306S1.V10

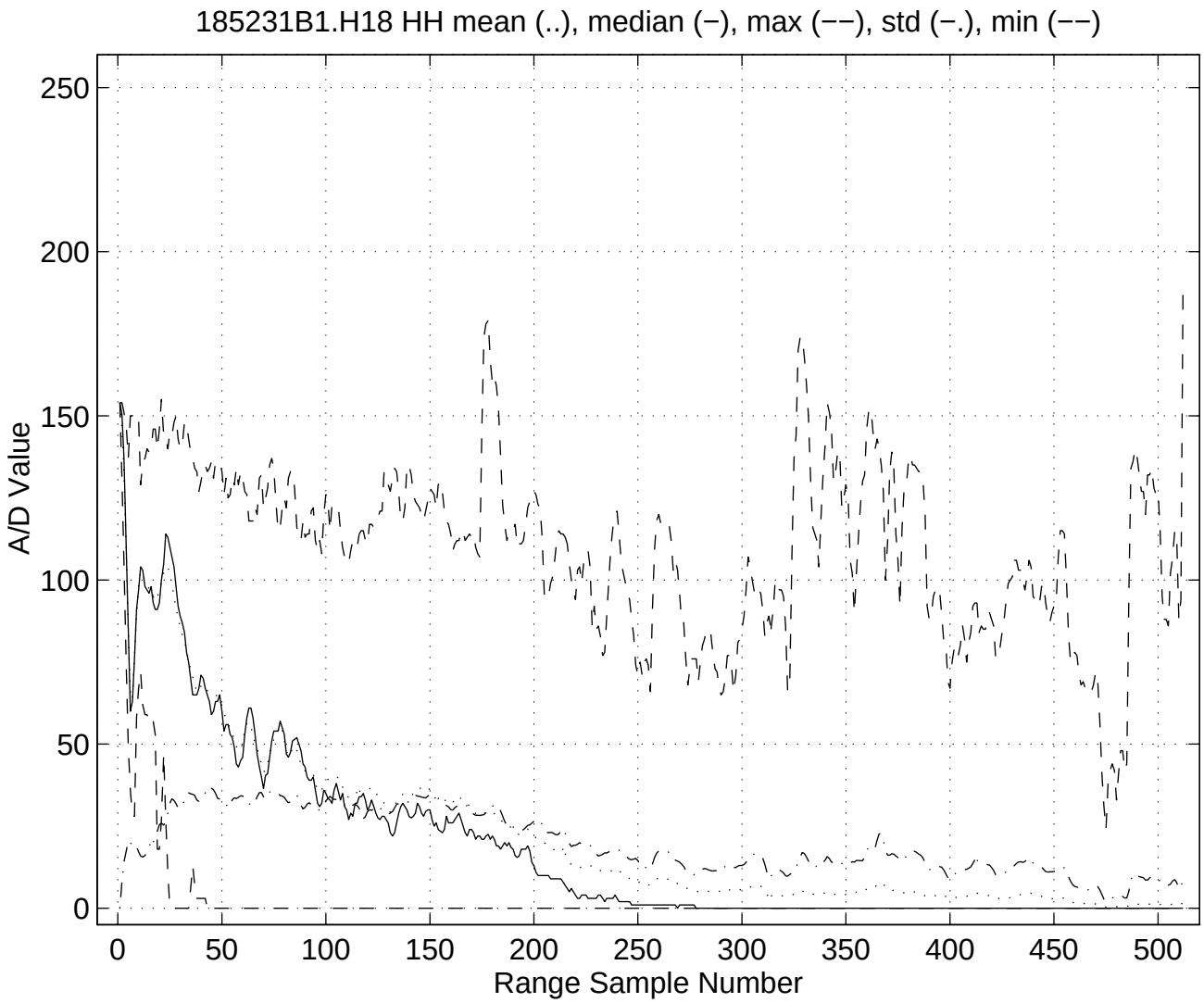

Figure 3-39 Plot of minimum, maximum, mean, median, and standard deviation vs. range for the HH B-scan data from file 185231S1.H18

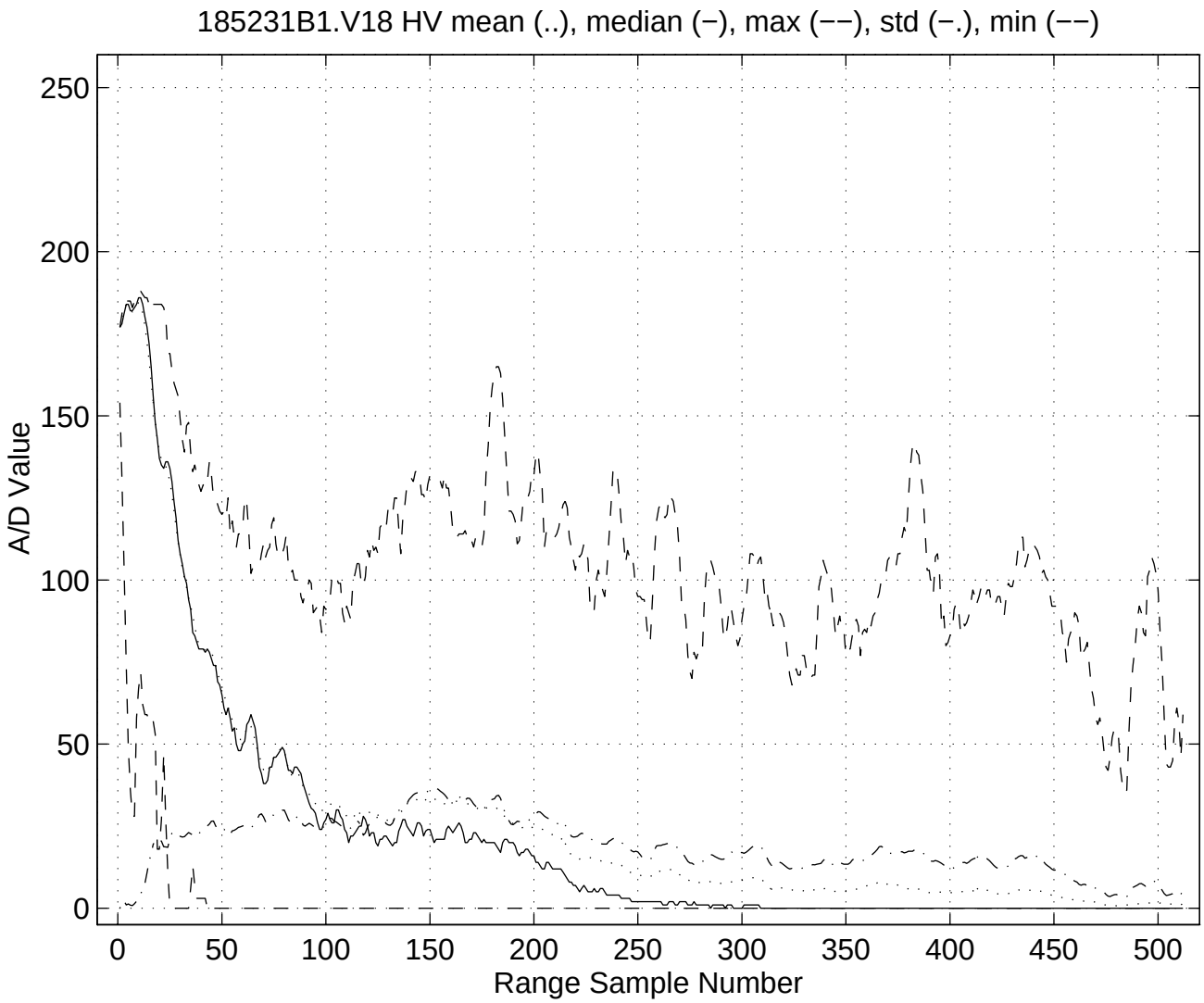

Figure 3-40 Plot of minimum, maximum, mean, median, and standard deviation vs. range for the HV B-scan data from file 185231S1.V18

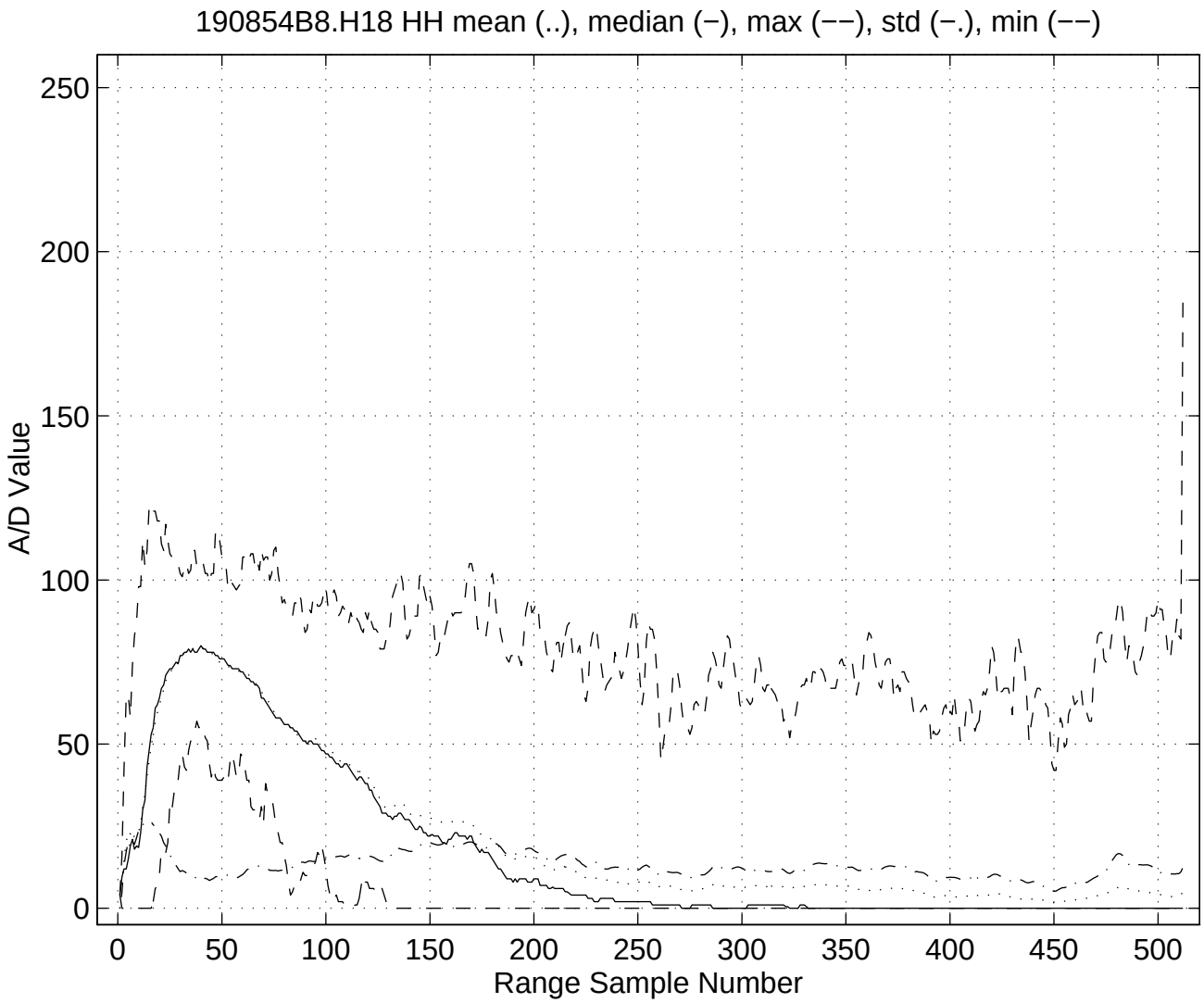

Figure 3-41 Plot of minimum, maximum, mean, median, and standard deviation vs. range for the HH B-scan data from file 190854S8.H18

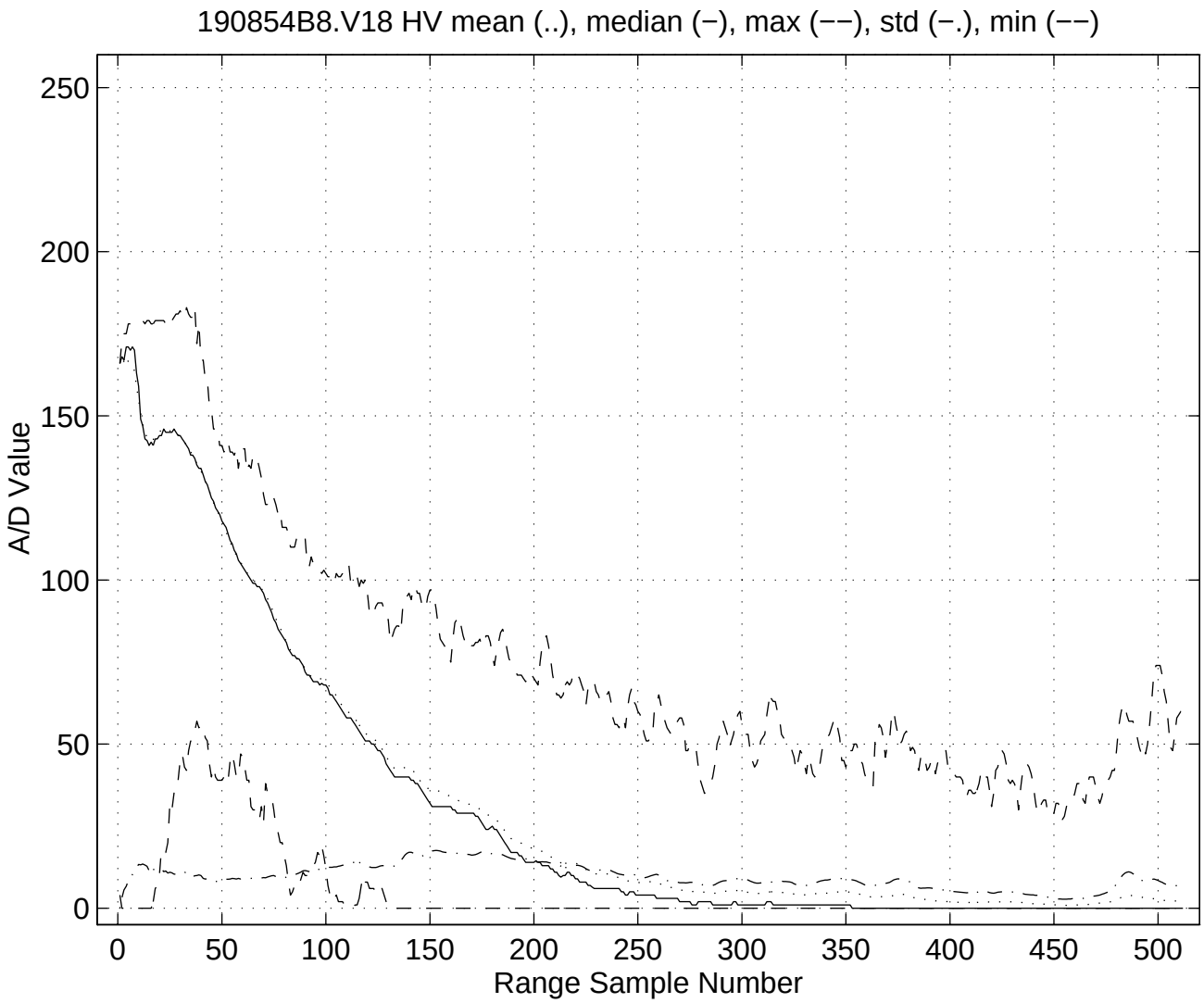

Figure 3-42 Plot of minimum, maximum, mean, median, and standard deviation vs. range for the HV B-scan data from file 190854S8.V18

Smoothed curves were then fit to the median. Figure 3-43 to Figure 3-50 show plots of the calculated median and the fitted curves, which were written to the 'M' files for use in the range normalization process.

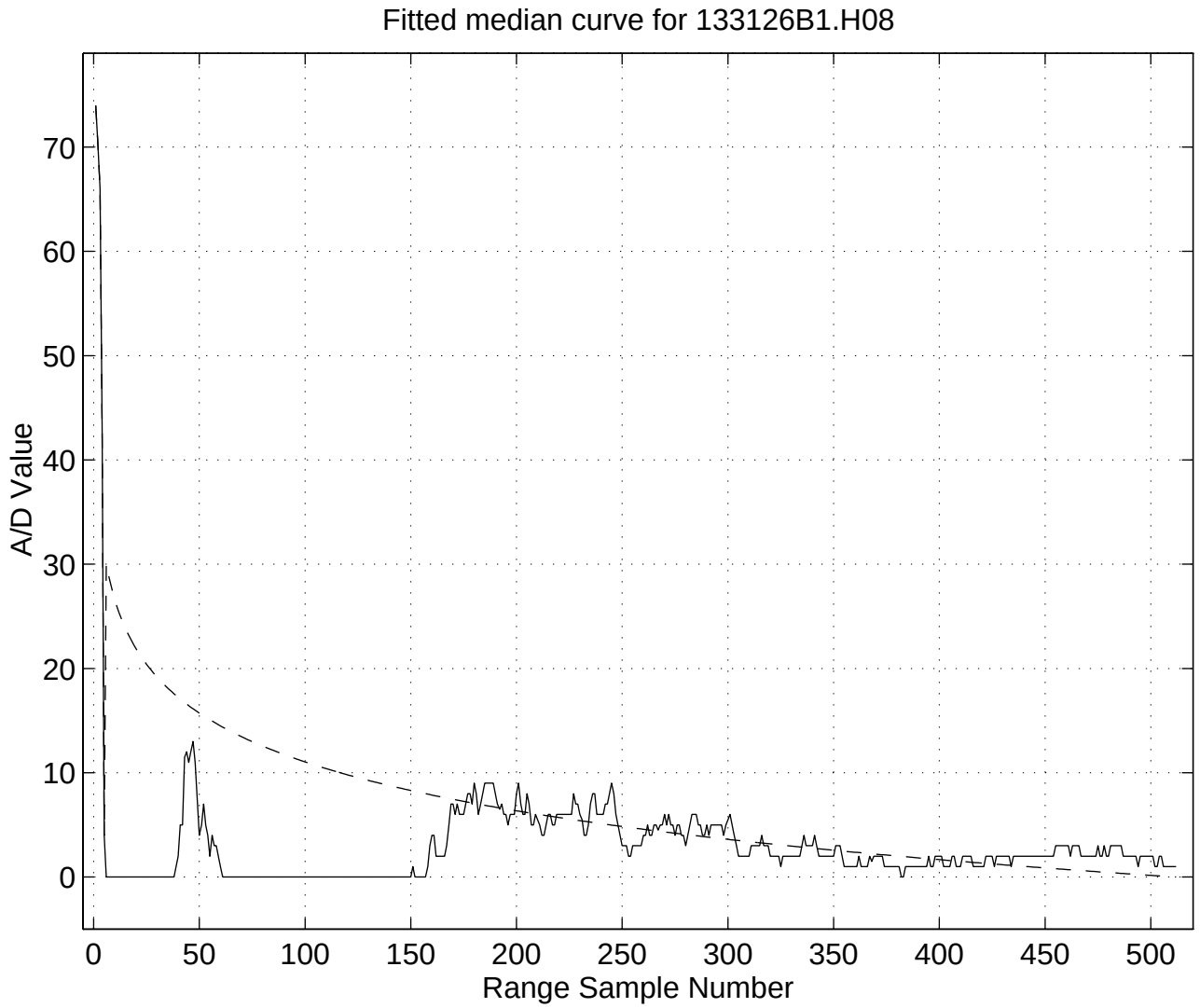

Figure 3-43 Plot of median and fitted curve vs. range for the HH B-scan data from file 133126S1.H08

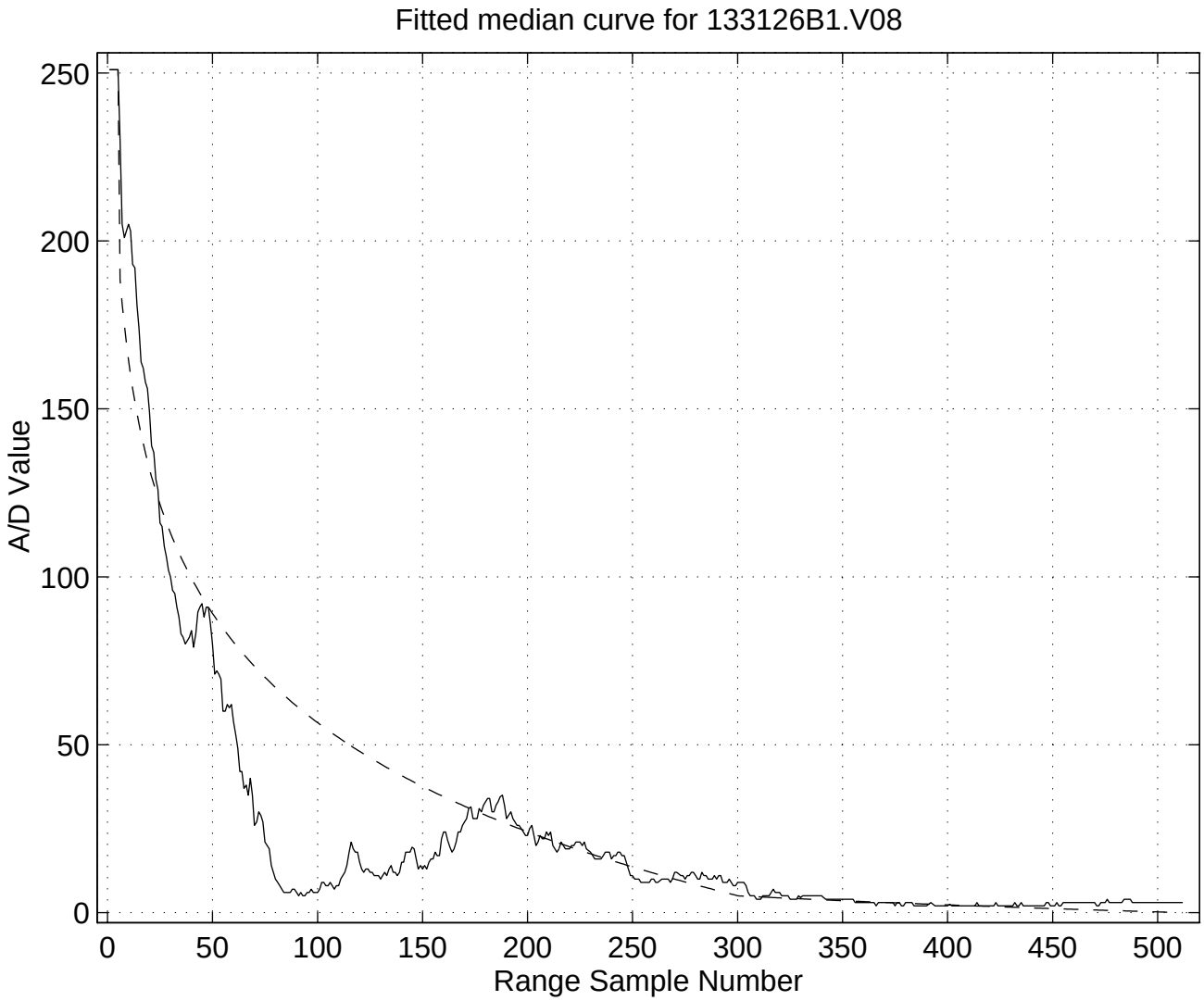

Figure 3-44 Plot of median and fitted curve vs. range for the HV B-scan data from file 133126S1.V08

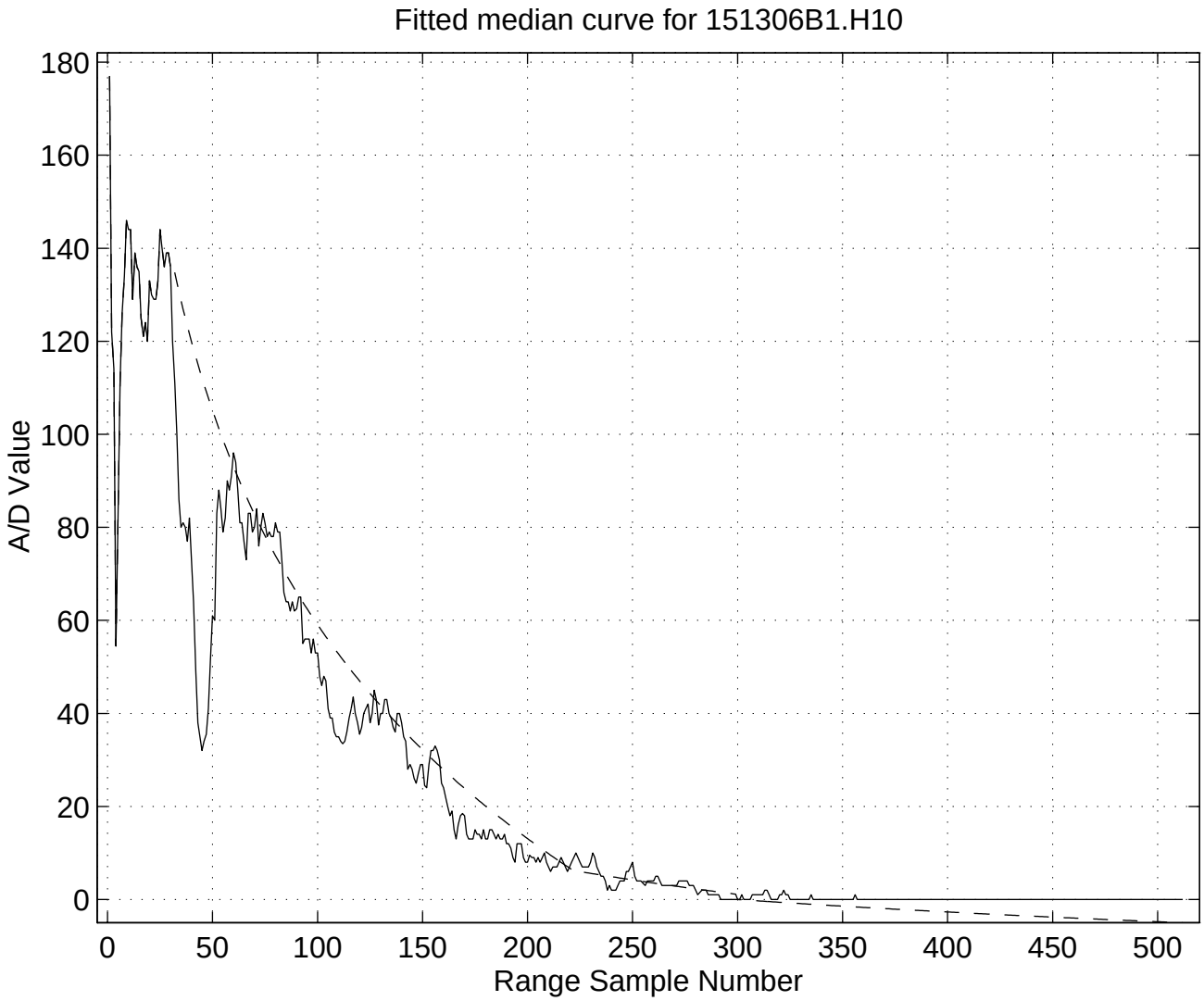

Figure 3-45 Plot of median and fitted curve vs. range for the HH B-scan data from file 151306S1.H10

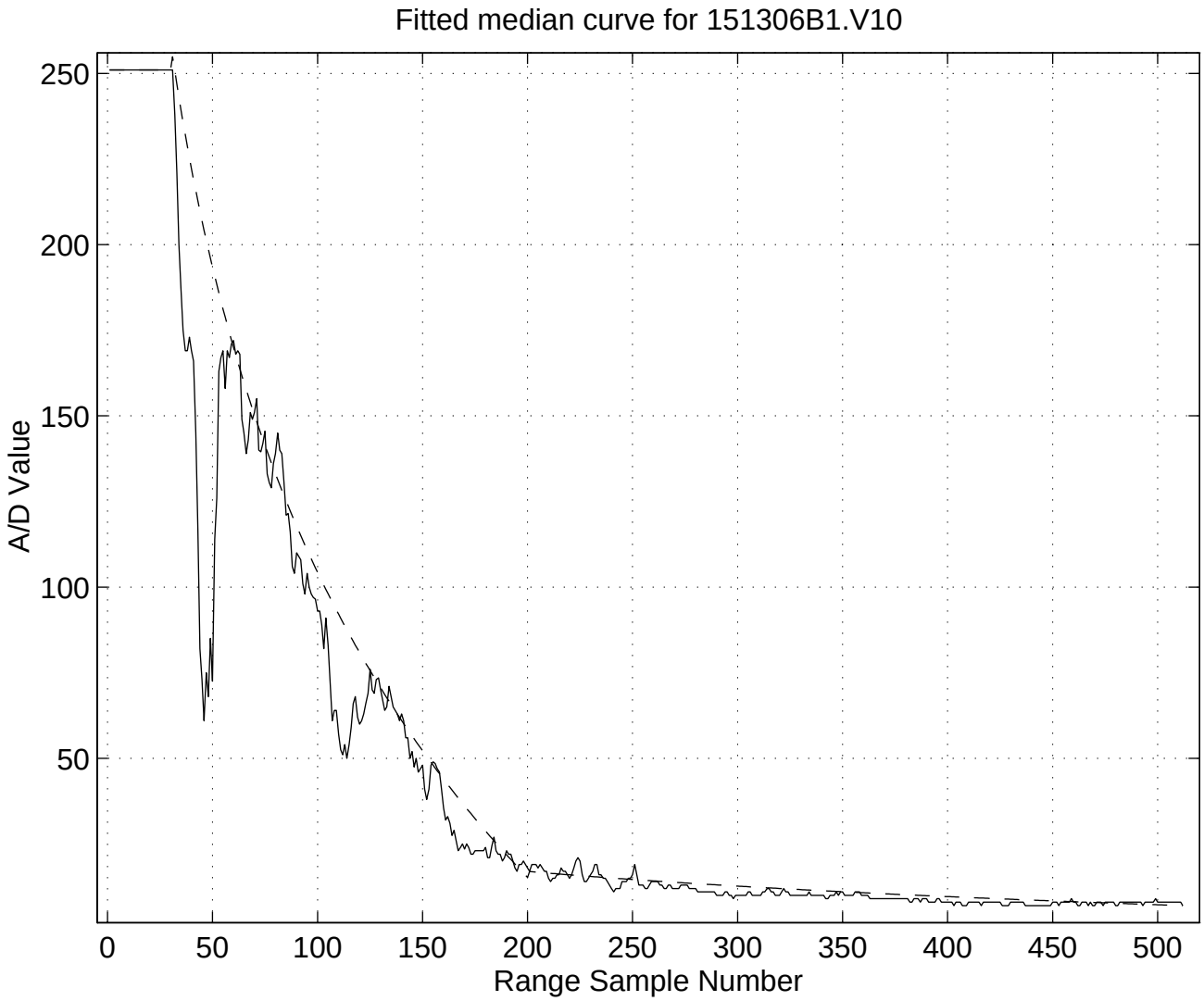

Figure 3-46 Plot of median and fitted curve vs. range for the HV B-scan data from file 151306S1.V10

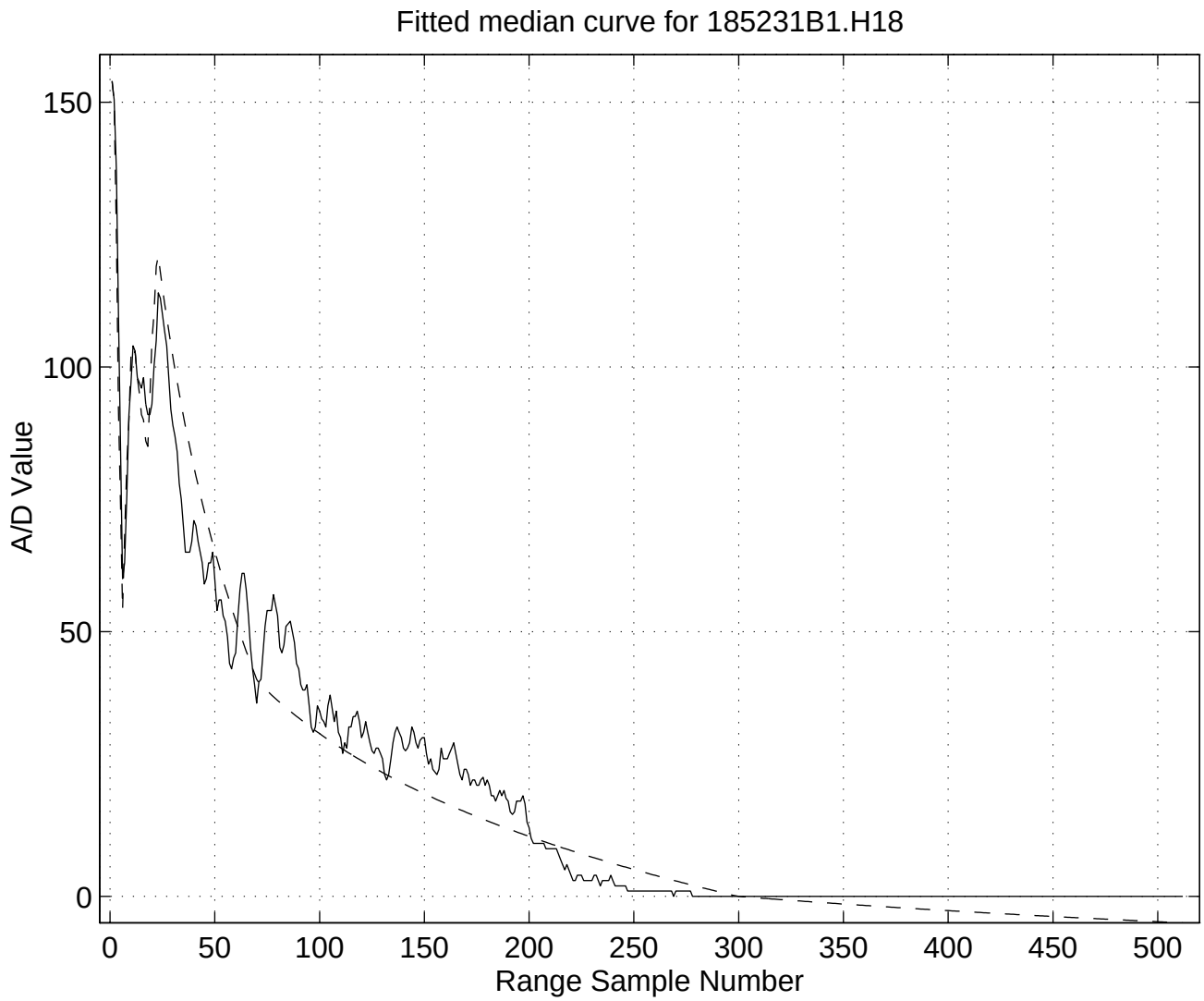

Figure 3-47 Plot of median and fitted curve vs. range for the HH B-scan data from file 185231S1.H18

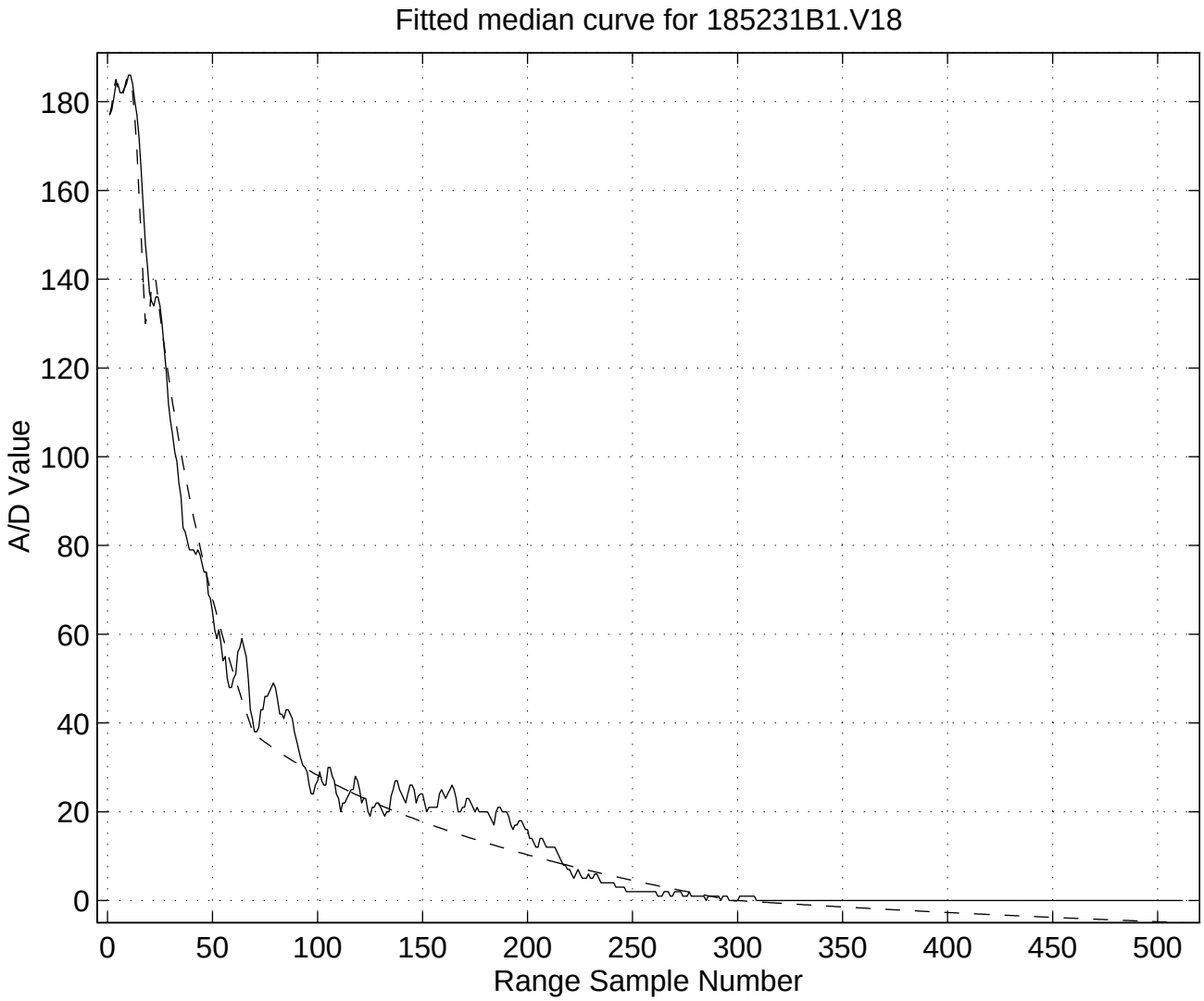

Figure 3-48 Plot of median and fitted curve vs. range for the HV B-scan data from file 185231S1.V18

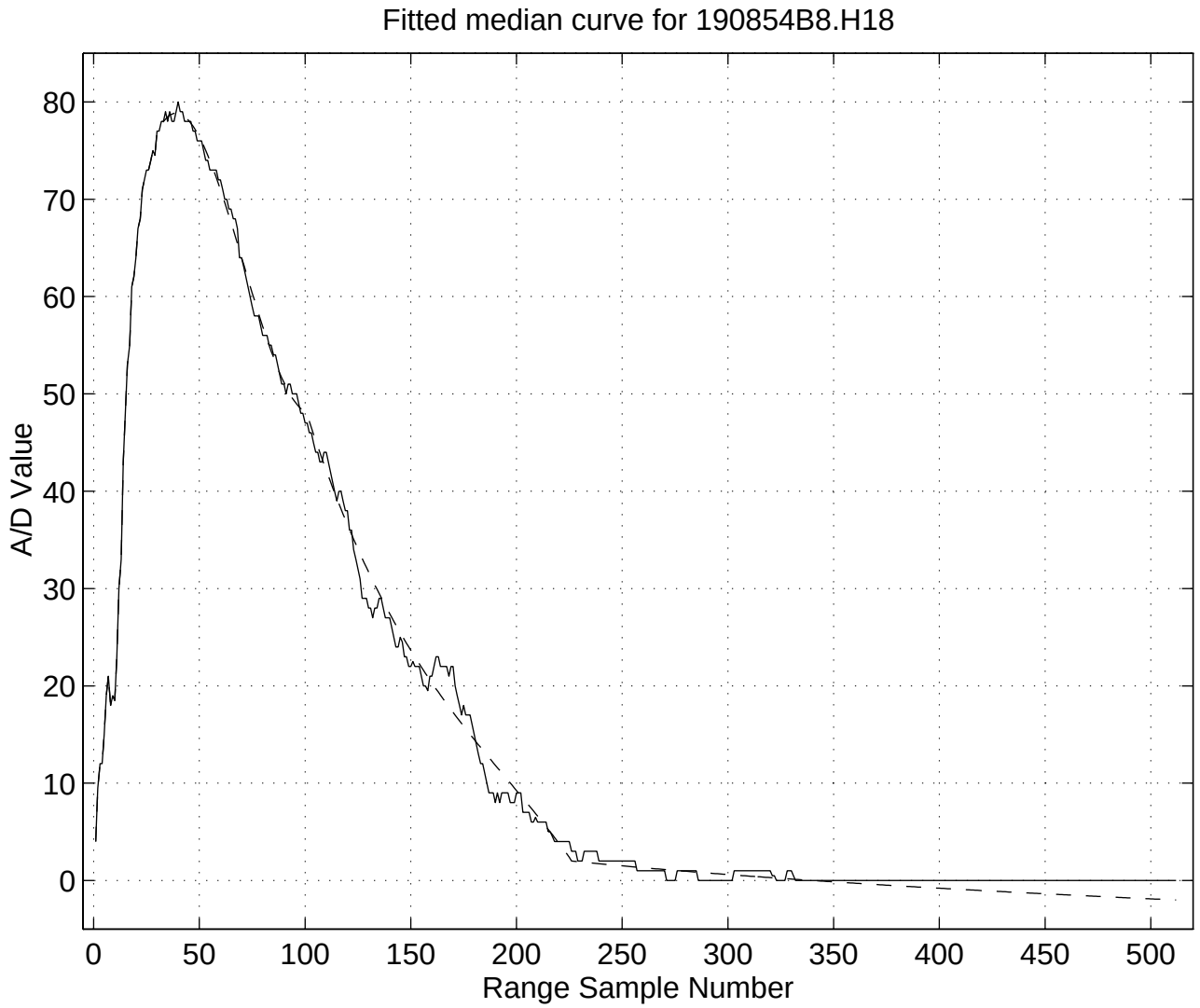

Figure 3-49 Plot of median and fitted curve vs. range for the HH B-scan data from file 190854S8.H18

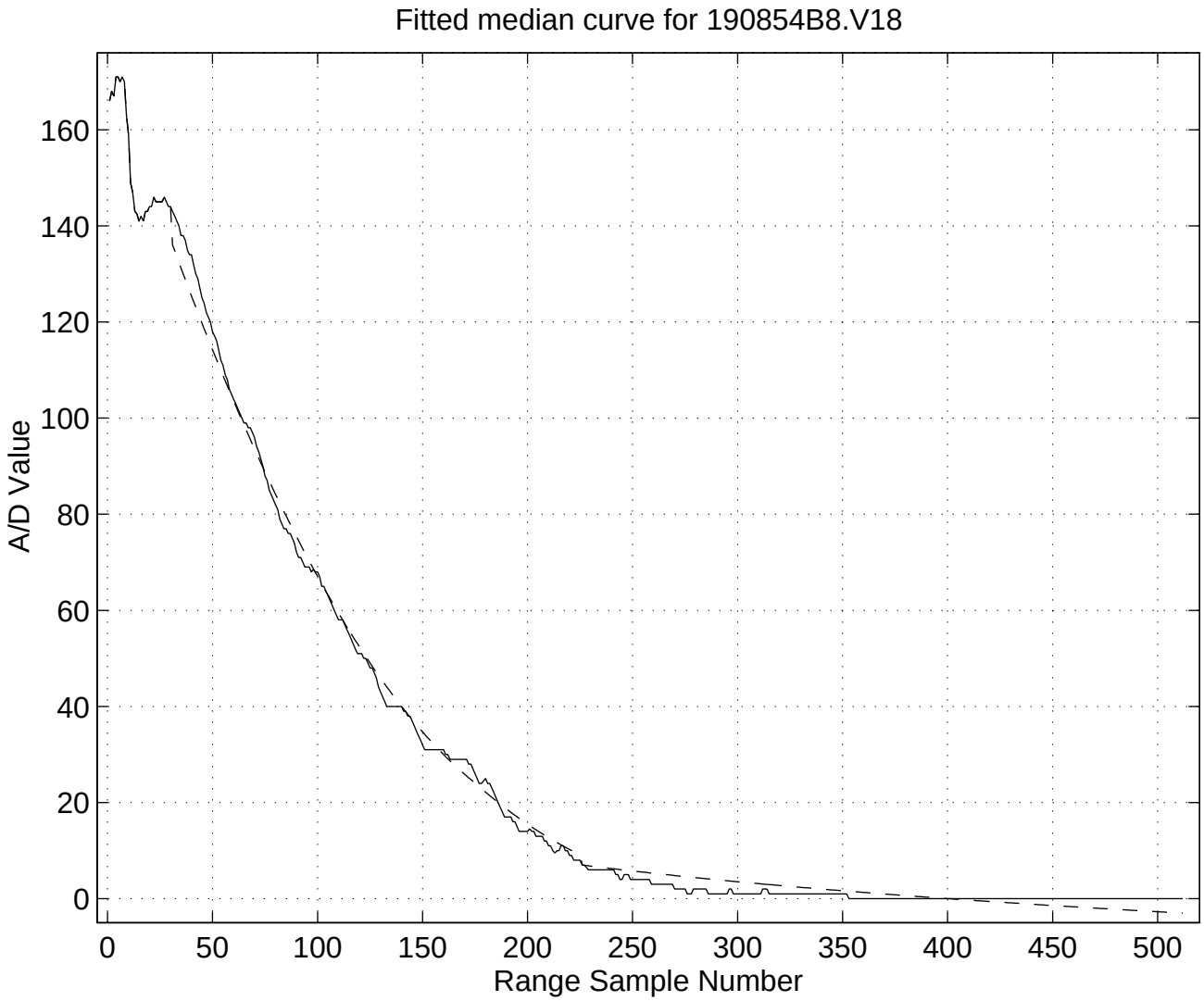

Figure 3-50 Plot of median and fitted curve vs. range for the HV B-scan data from file 190854S8.V18.

Figure 3-51 and Figure 3-52 show a sample histogram of regions containing ice known to be first year ice and multi year ice respectively. The darkness of the region indicates large density values. It is apparent that multi-year ice has much more samples at higher values of average intensity and (HV-HH). This is a significant difference as can be observed by the fact that though samples do exist in the first year ice at higher average densities, they do not have a corresponding higher (HV-HH) value. This fact was observed to be quite consistent in all the sample images which were part of the initial data analysis.

The resulting polarimetric images are shown in Figures 3-53 to 3-57. With the adopted colour tables, multi-year ice should show up in red (large HH-HV) while first-year ice should show up blue (small HH-HV). Green is in between. This statement may initially be seen to be in contradiction to the research described in Section 2, which showed multi-year ice have smaller HH-HV difference (equivalent to the cross-pol ratio for linear receivers) than first-year ice. The reason multi-year ice now shows up with a larger HH-HV difference is because of the range normalization algorithm used to balance the HH & HV images. The images are balanced to provide nominally equal gain from the same scatterers. Since most of the scatterers pertain to first-year ice, the HH and HV images will result in first-year ice being nominally matched in power (instead of HV returns being smaller). Therefore, multi-year ice will show up with the larger HH-HV difference.

To obtain a final colour coded image which map the data items correctly, the centre point and the span of the colour table must be derived from the histogram. However, this may lead to different colour mapping for each image. Although, this is not a significant problem, can still be easily automated, and is directly linked to image matching method, it is highly desirable to have a colour mapping which does not change very rapidly. This was tested by deriving the colour table from a single image and using the same for all the five image pairs which were combined. The results indicate that such an approach indeed works and thus points to simplified implementation.

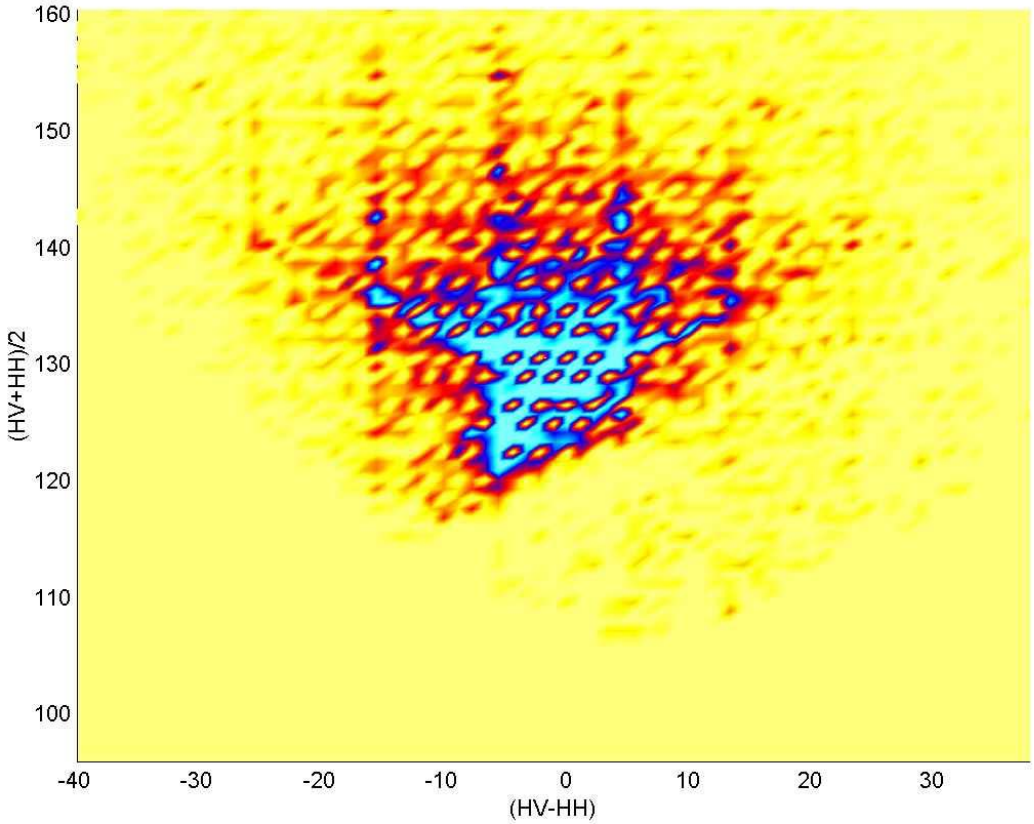

Figure 3-51 Sample histogram from regions containing first-year ice

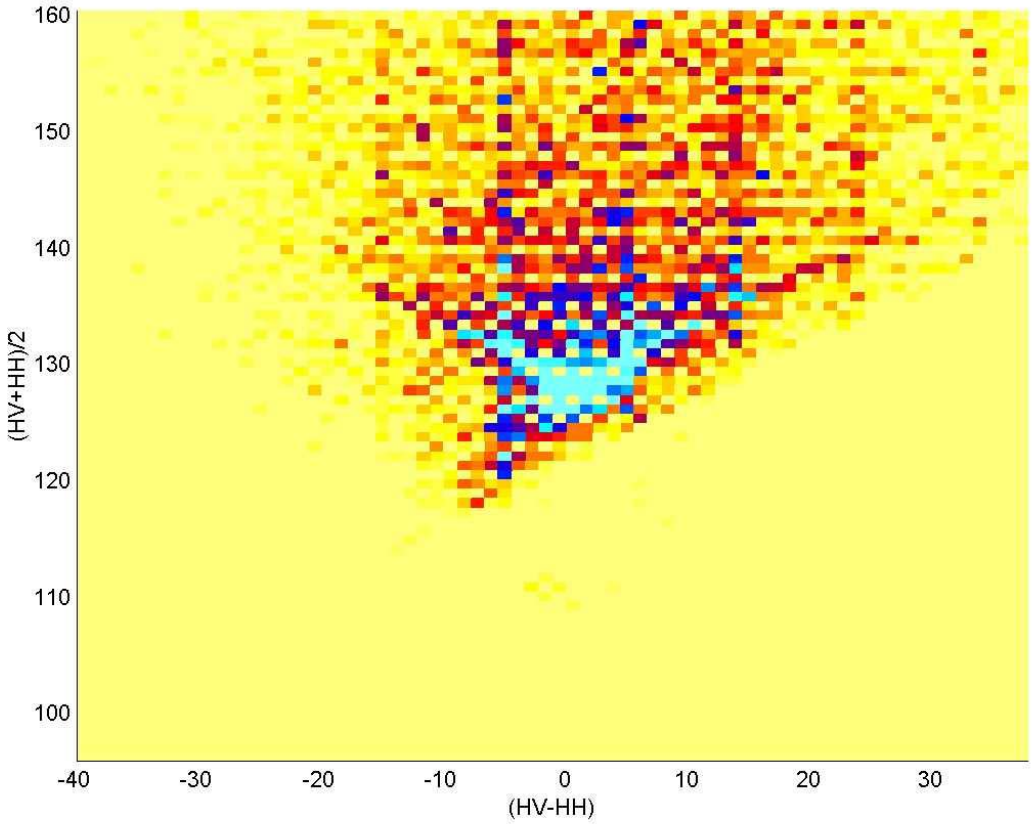

Figure 3-52 Sample histogram from regions containing multi-year ice

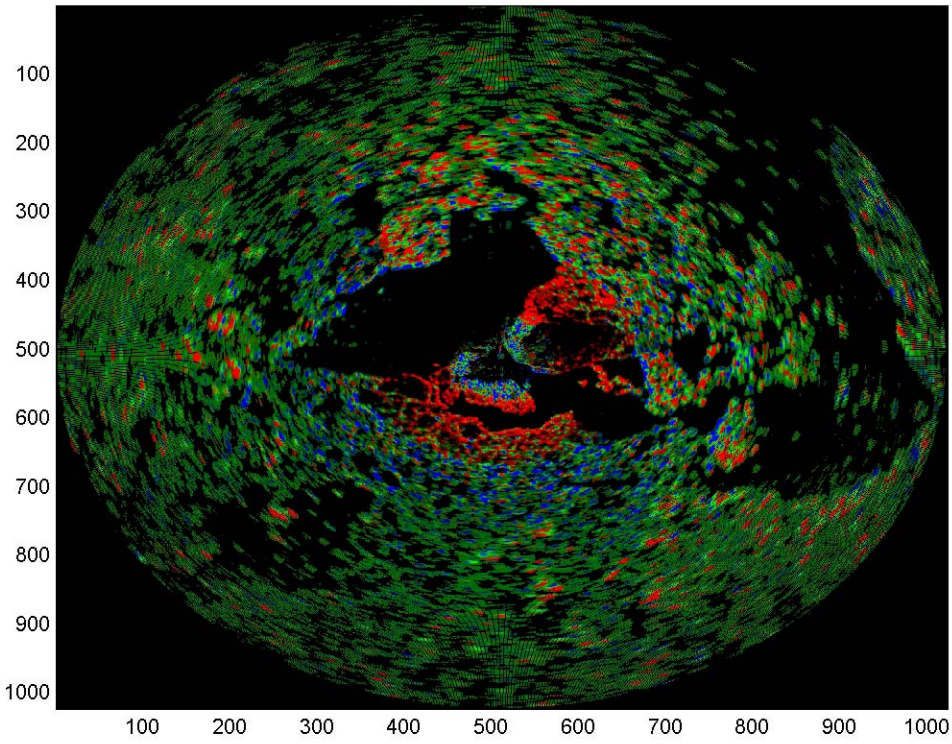

Figure 3-53 HSV colour-coded final image of data sequence 133126S1

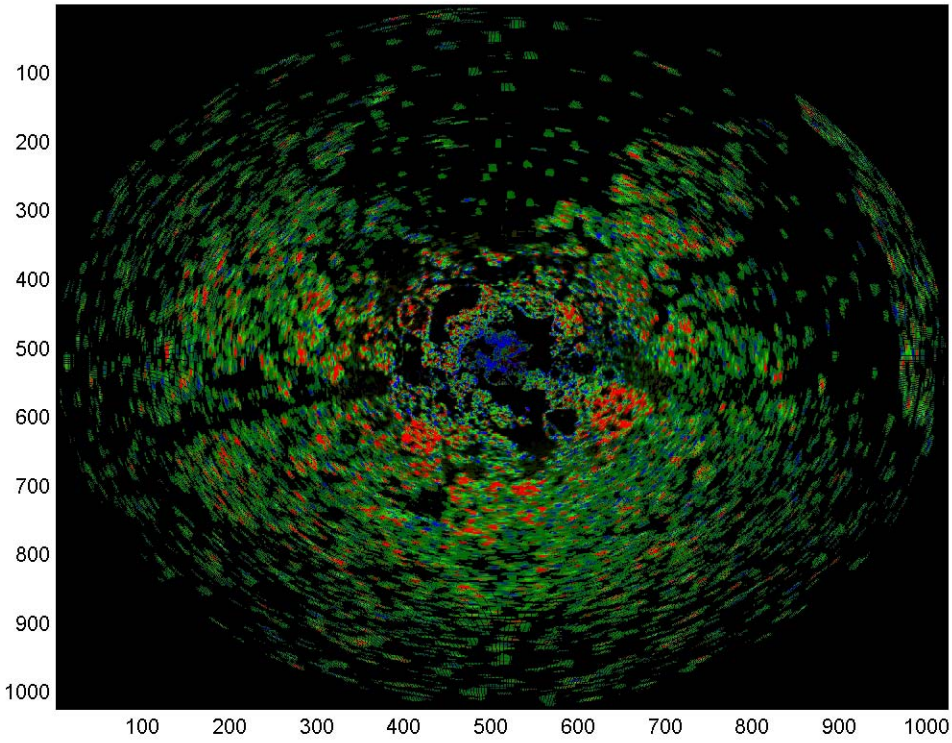

Figure 3-54 HSV colour-coded final image of data sequence 151306S1

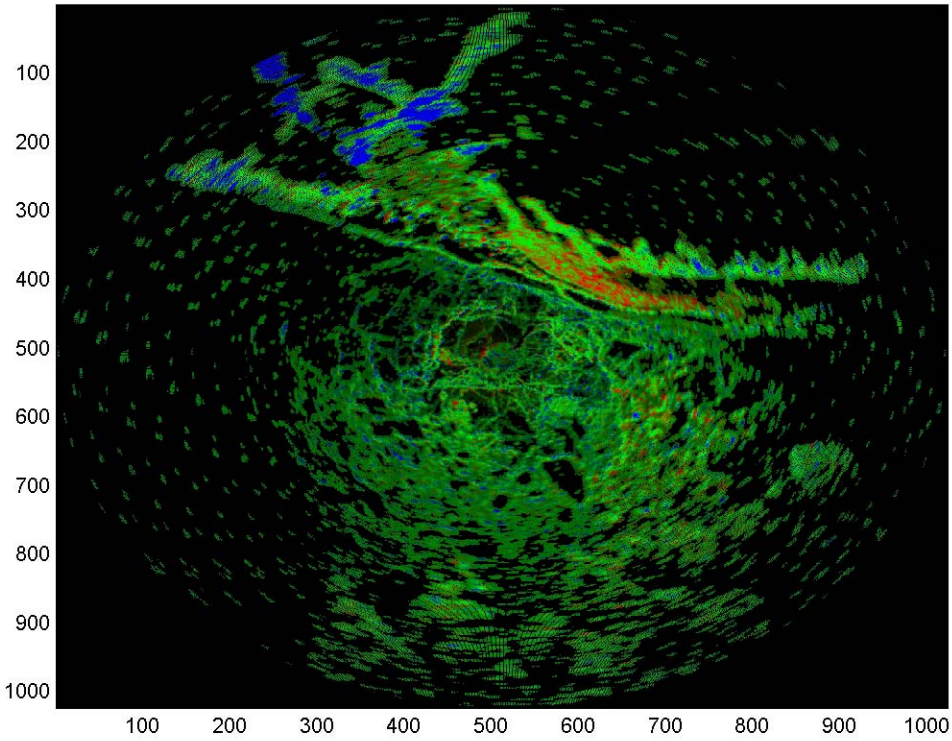

Figure 3-55 HSV colour-coded final image of data sequence 185231S1

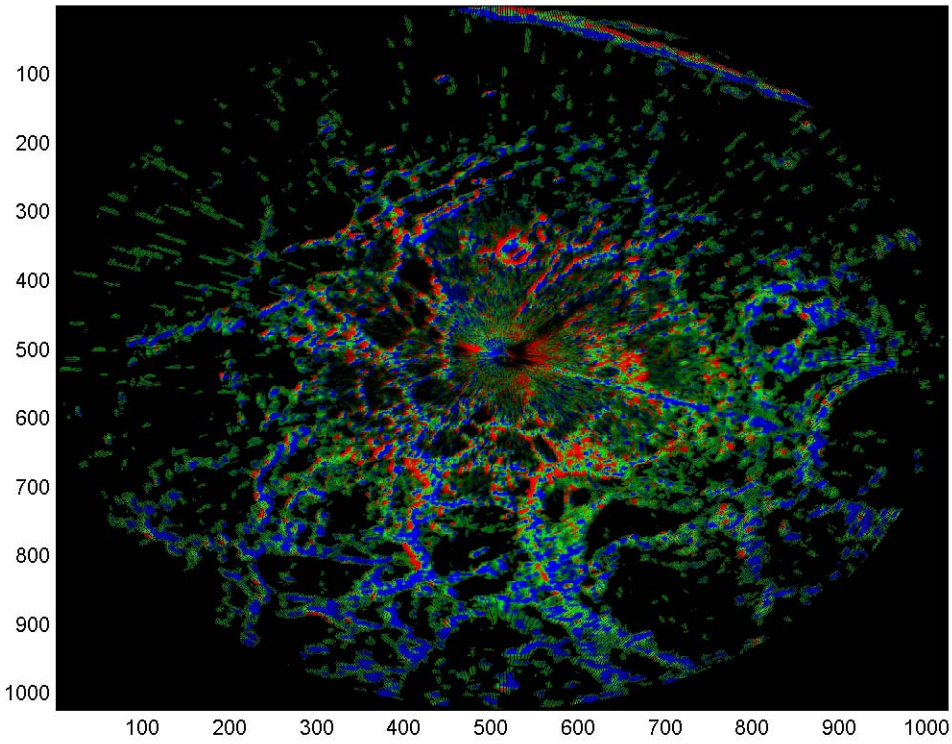

Figure 3-56 HSV colour-coded final image of data sequence 190854S8

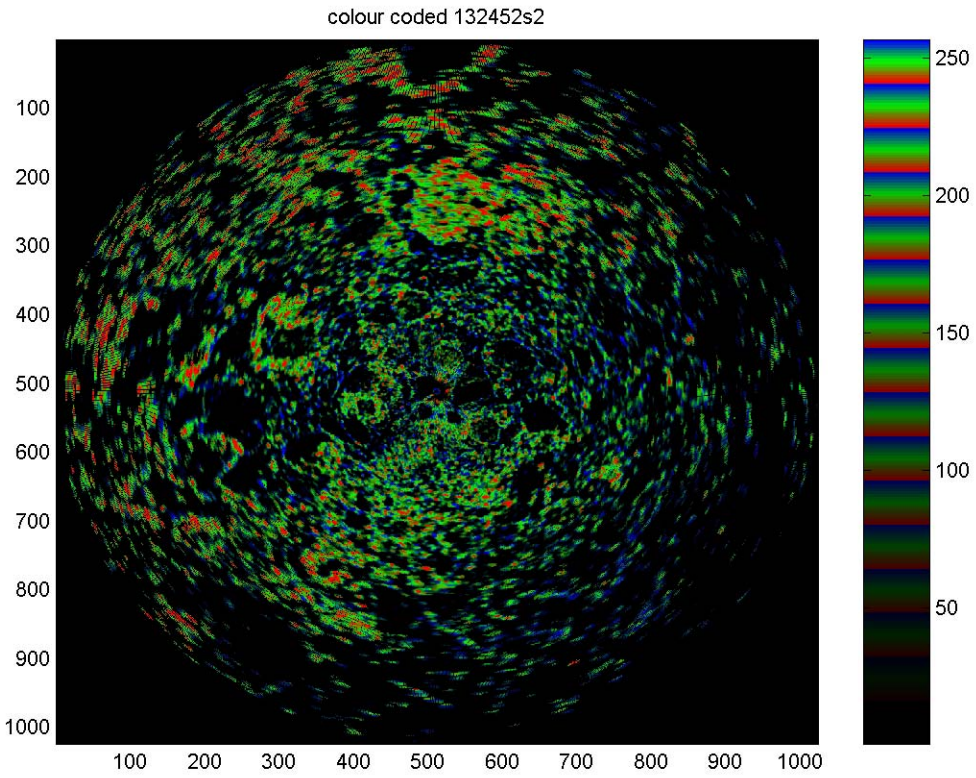

Figure 3-57 HSV colour-coded final image of data sequence 132452S2

These five image pairs were also analysed by Bob Gorman of Enfotech Technical Services Inc. and Mr. Charles Gautier of the Transportation Development Centre (TDC), well known experts in the field of ice recognition and the corresponding multi-year ice regions were marked. These images, which are presented in Figures 3.58 to Figure 3-62 formed the basis of our analysis in the sense that these results were used as ground truthing to deduce the differences in their respective histograms. It should be pointed out that the experts also indicated that there may be other unmarked regions of multi-year ice in these figures. As a result, it is possible that the histogram in Figure 3-51 is biased somewhat by the presence of multi-year ice. It is difficult, at this stage, to quantify the improvement of the combined image over the single channel HV or HH image. This would require strict ground-truth data and currently this avenue is being explored through the use of airborne SAR data. Notwithstanding this, it is possible to make the following qualitative assessments:

There is a very close match between the regions picked up by the experts as multi-year ice and the results indicated by combining the two channel data (indicated by red colour for multi-year ice)

There are other areas that are indicated as being multi-year ice than has been corroborated by the experts.

It is not necessarily the case that all the multi-year ice has large average brightness; neither is it true that all first-year ice has relatively small returns.

Although these results would have to be matched against proper ground-truthed data and the improvements quantified in a more rigorous manner, the image balancing and polarimetric processing results are very encouraging. The methods developed herein show promise and have the potential to lead to a significantly improved ice navigation radar system.

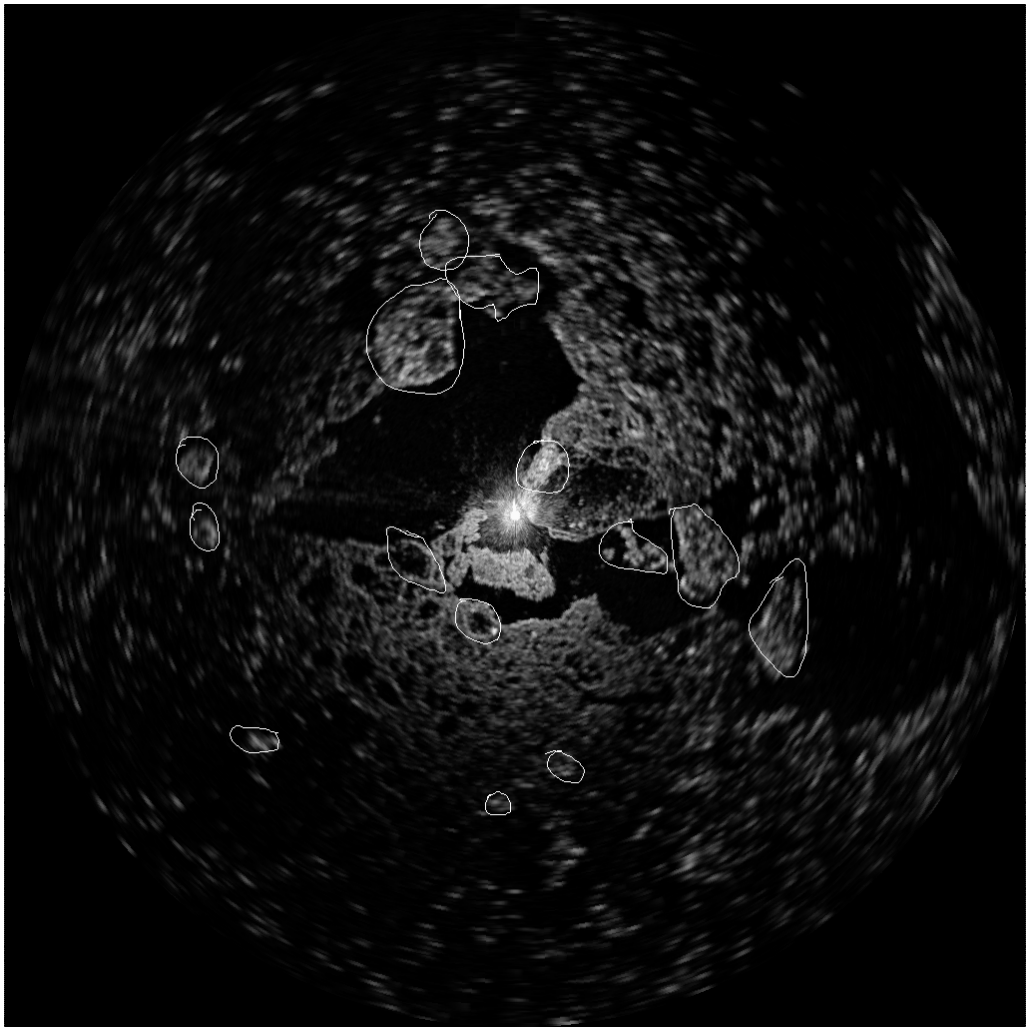

Figure 3-58: HV ppi image from sequence 133126S1, with multi-year ice marked by independent experts (the final combined image is shown in Figure 3-53)

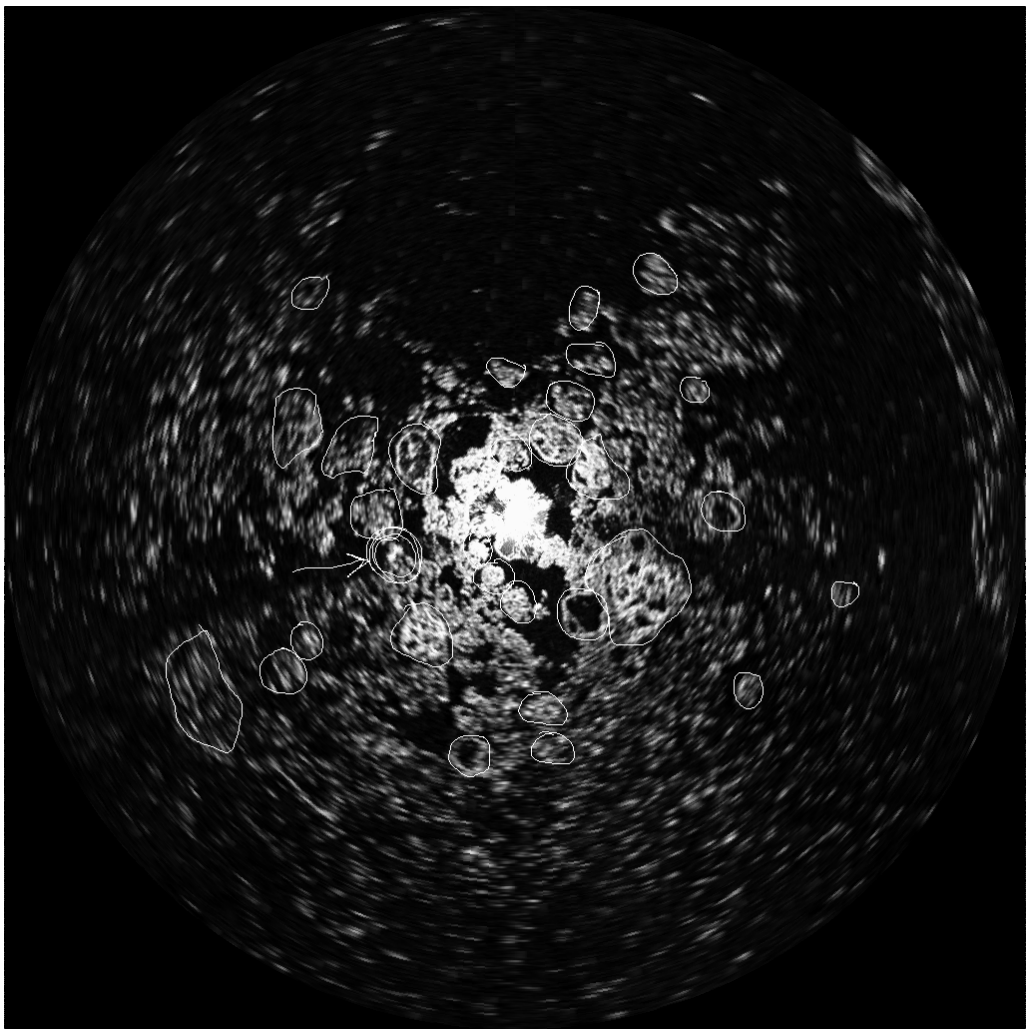

Figure 3-59 HV ppi image from sequence 151306S1, with multi-year ice marked by independent experts (the final combined image is shown in Figure 3-54)

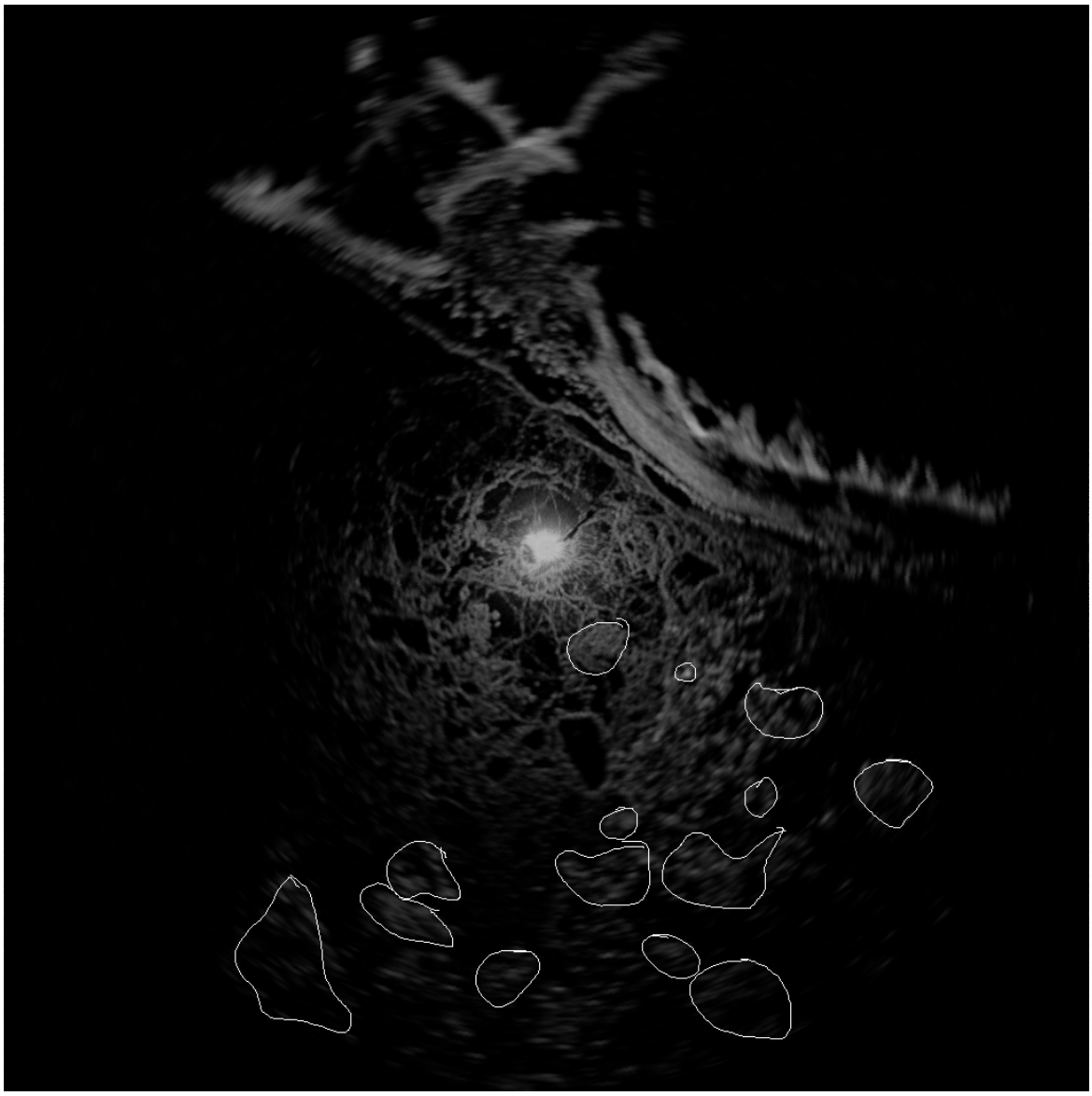

Figure 3-60 HV ppi image from sequence 185231S1, with multi-year ice marked by independent experts (the final combined image is shown in Figure 3-55)

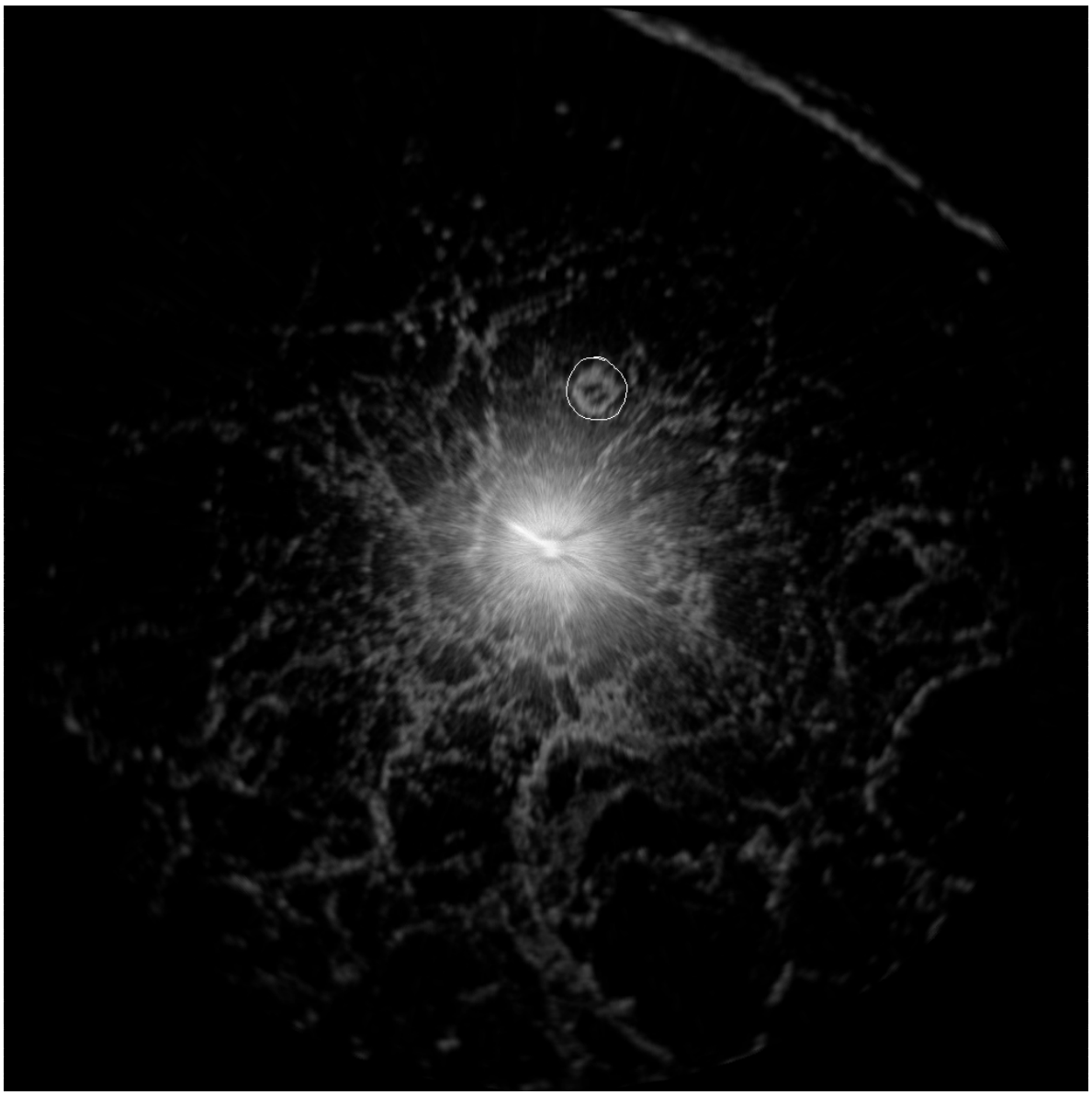

Figure 3-61 HV ppi image from sequence 190854S8, with multi-year ice marked by independent experts (the final combined image is shown in Figure 3-56)

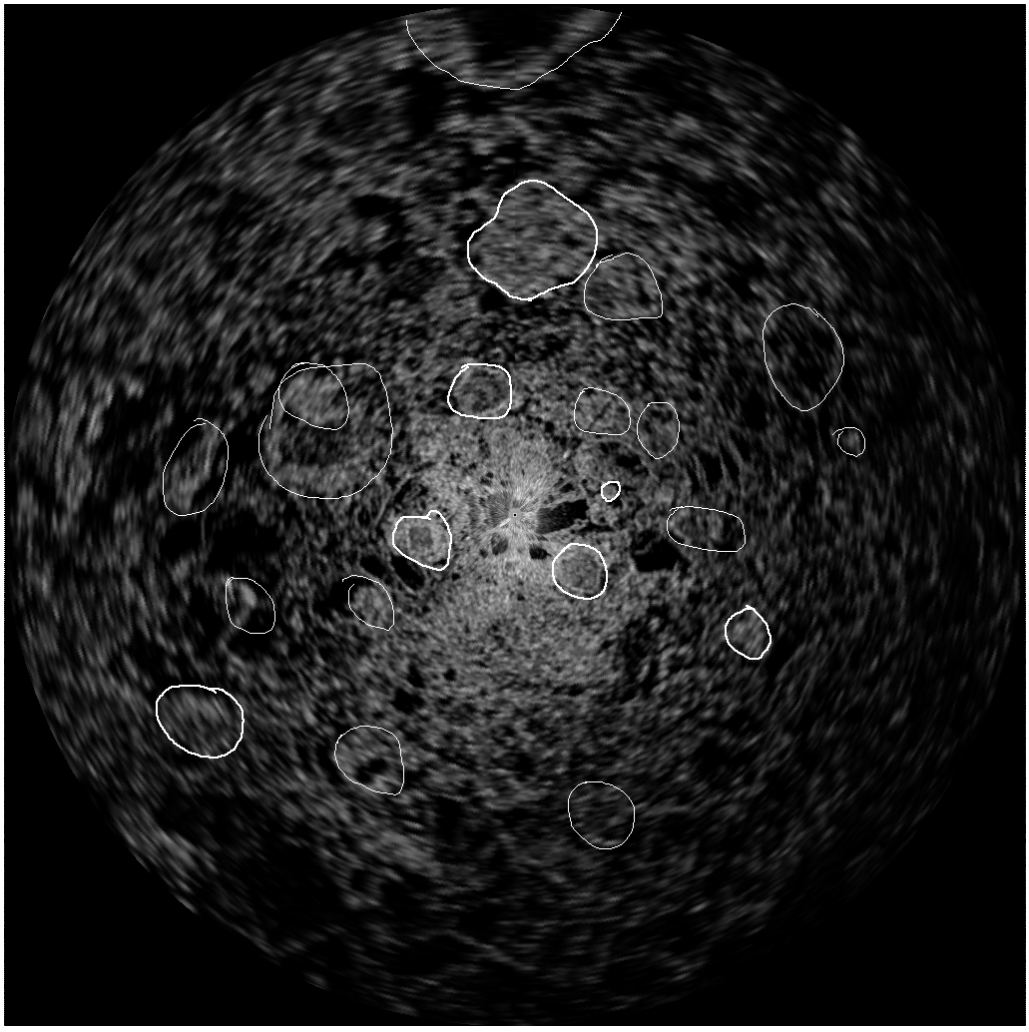

Figure 3-62 HV ppi image from sequence 132452S2, with multi-year ice marked by independent experts (the final combined image is shown in Figure 3-57)

4 FUTURE ENHANCEMENTS

4.1 Distinct Antennas

It is proposed to provide cross-polarization using two distinct antennas. The transmit antenna would be the ships existing antenna and is assumed to be horizontally polarized. A vertically polarized receive antenna would be installed on the ship in the vicinity of the existing antenna. The following sections provide an analysis and discussion of the technical issues related to this configuration.

The configuration is essentially a mono-static for the like polarization and bistatic for the cross polarization. The scattering cross section of ice features for mono-static and bistatic may be different and increasing with increasing displacement of the antennas. It is expected that the displacement between antennas can be kept to a minimum and this effect will be small.

4.1.1 Antenna Alignment

The bistatic vs. mono-static configuration also gives rise to the different look directions for the receive antenna resulting in alignment errors that change with bearing. When both antennas are looking in the direction colinear with the axis running through the two antenna centres, there is only a range displacement error; and that error is maximum over that from any other look direction. When both antennas are looking in the perpendicular direction, the range error will be negligible and the angular error will be maximum (and

will decrease with increasing range). Figure 4-1 provides an overview of the system geometry.

Figure 4-1 Antenna alignment geometry

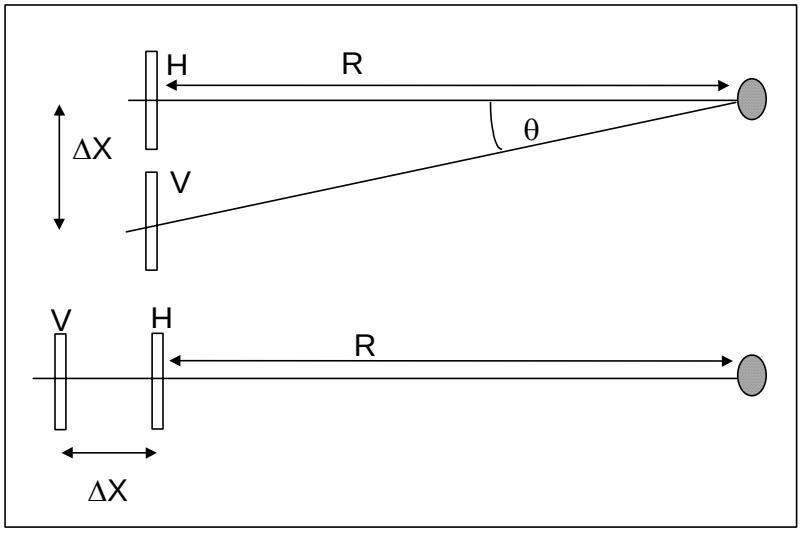

In Figure 4-1 it may be seen that the maximum angular error may be calculated from the arctan (ΔX/R). Table 4-1 presents a summary of the maximum angular error due to vertical polarization antenna displacement as a function of range.

Table 4-1 Maximum angular error

Angle Error (degrees)		Range (m)					
		250	500	1000	2000	3000	5000
ΔX(m)	2	0.46	0.23	0.11	0.06	0.04	0.02
	4	0.92	0.46	0.23	0.11	0.06	0.04
	8	1.84	0.92	0.46	0.23	0.11	0.06
	10	2.29	1.15	0.57	0.27	0.19	0.11

In Table 4-1 it may be seen that the near range error may be substantial even for small antenna displacements. Assuming practical limitations restrict the siting to the 2 to 4 m displacement range, the error at ranges greater that 1000 m is not significant for antennas having a 3 dB beamwidth of 1.0 degrees. Many existing X-band radars have 9 foot scanners having beamwidths on the order of 0.8 degrees and in this case the error of 0.23 degrees may just be tolerable.

If a specific range is of interest the antennas may be synchronized such that they are always focused on the desired range. This will reduce the azimuth error at the desired range to zero and increase the azimuth error at other ranges. As the transmit antenna can only illuminate one beamwidth at a time it will not be possible to focus the data from

other ranges. In bistatic radars where this type of operation is used the transmit antenna may remain stationary while the receive antenna scans from near to far range as desired. This type of operation is not considered feasible for retrofit to installed radars and scan time would be considerable unless a phased array receive antenna could be used.

In order to allow for possible angle errors, a wider vertical polarization antenna may be used. If a 2.0 degree antenna is used then even with a displacement of 4 m at least a half beamwidth overlap would be achieved at ranges of 250 m and greater. Table 4-2 provides some example antenna lengths and associated beamwidths available from a particular radar manufacturer. Other radar manufacturers offer a similar range of antennas.

Table 4-2 Example antenna lengths and beamwidths

Manufacturer	Length	Beamwidth	Gain	Sidelobes	
Racal Marine	800 mm	2.7°	25 dB	<21 dB(< 20°)	<26 dB(>20°)
	1200 mm	2.0°	27 dB	<23 dB(< 10°)	<28 dB(>10°)
	1800 mm	1.3°	31 dB	<23 dB(< 10°)	<30 dB(>10°)
	2400 mm	1.0 °	32 dB	<23 dB(< 10°)	<30 dB(>10°)

If this approach is taken and the vertical polarization antenna is slaved to the horizontal polarization antenna then the degree of alignment will depend upon the accuracy with which the slave antenna's position can be made to match the main antenna. If for example the two antennas can be locked such that the slave antenna beamwidth always includes the beam of the hpol antenna then the azimuth data from the hpol antenna may be used for both hpol and vpol data. This implies that as long as the desired lock is maintained the illumination by the hpol antenna defines the look angle and azimuth resolution of the vpol antenna. In theory, there may be second-order scattering effects from scatterers within the hpol beam to regions outside the main beam but within the vpol beam, however, these effects are presently not quantifiable but will probably be non-zero for distributed targets like sea ice and sea clutter. Figure 4-2 looks at what might happen in a case with this type of scatter in the presence of two targets. In the top case we have the expected scatter from a direct path from the radar to the target and the path length should be the total distance traveled. In the case below a intermediate scatterer in the main beam scatters energy to a target in the vpol receive beam and the resultant echo will show up at a distance corresponding to the total path length. If the path lengths in the top and bottom cases are the same then the received vpol signal will be the vector sum of the signals from A and B. This is equivalent to multipath common in mono-static radar systems. It is expected that in the lower case the scatter, if it is from sea ice, will be substantially reduced and that the only time this scenario may present a problem would be when A is a small target and B is a large target.

Figure 4-2 Bistatic Multi-Path Scattering

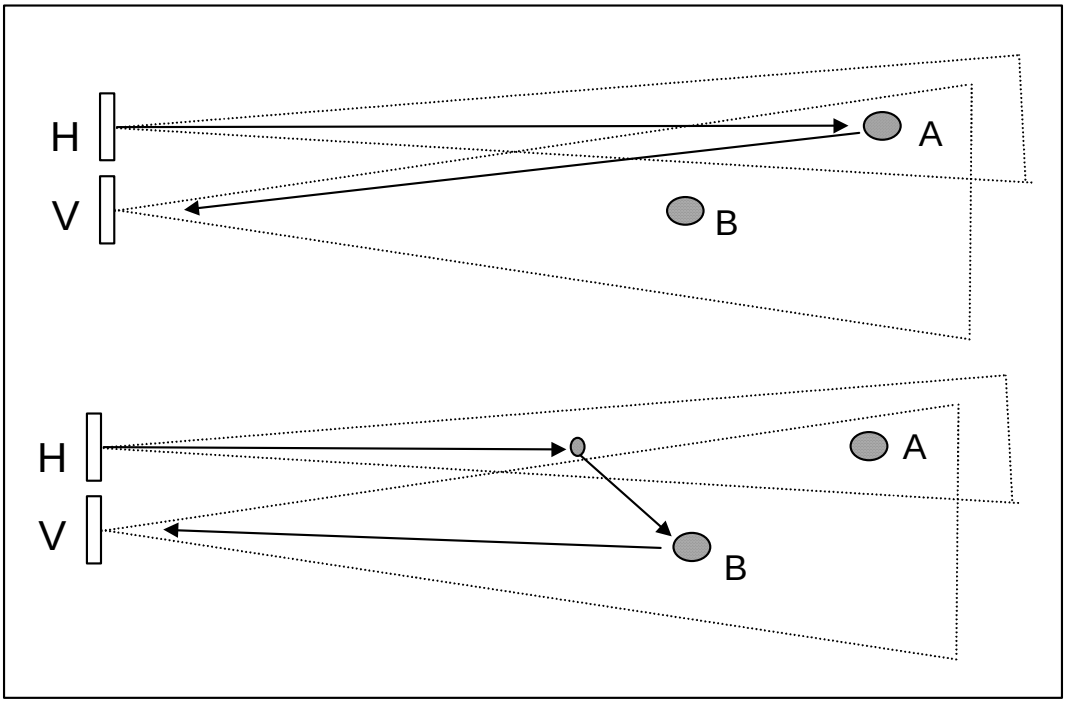

4.1.2 Tracking Accuracy

Given that the use of a broader beam for the vpol antenna will eliminate the need for angle compensation to accommodate antenna horizontal displacement it is necessary to define the required tracking accuracy necessary to maintain acceptable beam overlap. With a two degree vpol antenna and a one degree hpol antenna, a tracking accuracy of ±0.25° will be required to keep the beams overlapped(within 3 dB beamwidth) for all ranges greater than 250 m for a 2 m displacement(see Table 4-3). The range dependence in the tracking accuracy requirement is due to the horizontal antenna offset. If the antennas are located on top of each other, say on the same mast, then the tracking accuracy required will be constant with range and will be very close to that quoted for 5000 m in Table 4-3.

Table 4-3 Tracking Accuracy Required for a 2 m Antenna Offset

Tracking Accuracy (±degrees)		Range (m)					
		250	500	1000	2000	3000	5000
Vpol beam	2.0	0.27	0.39	0.45	0.47	0.48	0.49
	2.7	0.62	0.74	0.80	0.82	0.83	0.84

The slave vpol antenna will require an accurate bearing measurement system for use by the tracking control unit (motor controller). Figure 4-3 shows the type of configuration required for controlling the speed and position of the vpol antenna. It would be beneficial

if the antenna bearing information was absolute as this would permit static alignment of the antennas for calibration, however, most if not all newer radars use an Azimuth Count Pulse (ACP) and Heading Mark (or Azimuth Reset Pulse, ARP) to provide antenna angle data relative to the ARP. From a tracking perspective it will also be required that the control loop monitor the angle data from both antennas and generate a control signal based on the difference between the desired angle and the actual angle of the vpol antenna.

The controller will therefore consist of a counter or equivalent to convert the ACP data from each antenna into a bearing. The bearing resolution will be controlled by the antenna ACP count. Some antennas have ACP counts as low as 90 per scan resulting in a four degree resolution on angle data. This would probably not be acceptable for tracking purposes if tracking accuracy on the order of 0.5 degrees is required. One of the criteria in the selection of the vpol antenna should be the type and accuracy of its azimuth encoder. The hpol antenna will be an existing antenna so a method of dealing with varying resolution azimuth data will have to be developed. It will not be possible to modify the radar without affecting the radars type approval so external or manufacturer approved methods will be required. This comment also applies to other interfacing requirements. Several options are available. The radar manufacturer of the hpol antenna may provide for the fitting of optional higher resolution azimuth encoders or synchro units. This would not effect type approval. Another external method would be the use of the existing ACP data to generate a higher ACP count using a phase-lock-loop in a multiplier configuration. This is often done in radar systems and has the effect of interpolating new ACP counts between the actual counts and locking is achieved on the edges of the input ACP. This method would permit the increasing of low ACP count systems up to acceptable count and would provide the control loop with a predicted antenna position between actual antenna ACP counts and thereby providing better antenna position control.

4.1.3 Radar Image Alignment

It will be assumed for the following analysis that the radar angular information will be aligned using a slaved vertical polarization antenna and that the angle information from

Figure 4-3 Antenna control loop

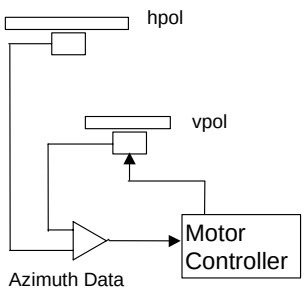

the hpol antenna will be used for both h and v polarizations. In this case the only adjustment required to the radar data will be to compensate for range displacement due to separate antennas. If the antennas are separated by less than half a radar resolution cell it will probably not be necessary to make any adjustments to range particularly as it applies to the longer range data.

Using Figure 4-1 as a reference in the worst case the total path length will be 2R for the hpol data and 2R+ΔX for the vpol data so the actual range error will be half the displacement between the antennas.

If the radar is operated on short pulse (50 ns) the radar resolution will be 7.5 m per radar resolution cell. If the radars are sited within 3.75 m of each other in the horizontal the worst range error would be 1.875 m or a quarter of a resolution cell. On medium pulse (250 ns) the radar resolution will be 37.5 m so a 3.75 m offset would be one twentieth of a resolution cell.

If the alignment of the short pulse data must be more precise then an angle based radar offset must be considered. The maximum error would be ΔX as defined in Figure 4-1 with antennas pointed in the vertical plane through their axes. If the antennas are 3.75 m apart a 1.875 m correction is required in the worst case. This equates to a ±12.5 ns correction to the data reducing to no correction when the antennas are pointed perpendicular to the plane through their axes (Figure 4-1). It is expected that this type of correction would not be feasible or necessary to implement.

4.1.4 Antenna Beam Patterns

As antennas are designed to operate at given frequencies and slotted waveguide antennas are frequency sensitive, it will be important to know the generated beam patterns of both the hpol and vpol antennas. The transmit/receive pattern of the hpol antenna is the same so it is self-compensating. The vpol antenna will have to be calibrated so that its look direction with respect to the hpol antenna is known. This will likely be accomplished using a fixed stationary target. The offset between the hpol bearing and vpol bearing should be measured so that the offset may be used in the antenna controller. This procedure would be facilitated if the antenna position encoders for the antennas provided absolute position. This would permit the use of static antenna measurements on stationary reference target.

4.1.5 Antenna Sidelobes

The hpol and vpol antennas will have sidelobes that may cause interference in the vpol channel. Using the data from Table 4-2, the worst case effect will be for the hpol antenna pointing into the back of the vpol antenna and will be typically greater than a lower gain vpol antenna pointing into the back of the hpol antenna. The worst case coupling will be given by,

Antenna Coupling = hpol gain + vpol sidelobe gain - isolation
= 32 + (-1) - 30
= 1 dB

and the best case will be given by,

Antenna Coupling = hpol sidelobe gain + vpol sidelobe gain - isolation
= 2 + (-1) - 30
= -29 dB

The isolation rejection of the orthogonal polarization is assumed to be 30 dB at a minimum. This figure will have to be confirmed with the manufacturers of the antennas for the vpol system.

The antenna coupling figures provided above represent the equivalent two way gain of the hpol/vpol antenna pair. Using the transmission equation the received power in the vpol system may be estimated. The received power will be,

$$P_r = (P_t G \lambda^2)/((4\pi)^2 L R^2) \quad (1)$$

Where P_r = Power received(watts)
P_t = Power transmitted(watts)= 25,000 W
G = Combined hpol/vpol Antenna Gain = 1, -29 dB
λ = Radar wavelength(m)=0.032 m
L = Radar Losses= 3.0 dB
R = Range between antennas(m)= 2 m

In the worst case the received power from the sidelobes will be -16 dB or +14 dBm and in the best case the received power from the sidelobes will be -45 dB or -15 dBm. If cross polarization isolation is greater than 30 dB or the sidelobe performance is better than that assumed the power received by the vpol receiver directly from the hpol transmitter will be less.

The received power will occur essentially at zero range as the two radar receivers will be synchronized using an external trigger feed to the vpol radar transceiver. This would have the effect of having the vpol receiver operate as if the power received from the hpol transmitter was from its own transmitter and could be used to tune the vpol receiver. Other than this effect it is not expected that the sidelobes will cause any detrimental problems with cross polarized operation.

4.1.6 Receiver Tuning

The use of magetrons as the source of the RF transmitted power permits the marine radar to be manufactured at low cost. The magnetron transmit frequency may vary from pulse to pulse and even within a transmitted pulse. The marine radar normally has a low noise front end with a mixer controlled by a local oscillator operating near the RF frequency. The local oscillator signal is used to mix the RF down to an IF frequency nominally centered at 60 MHz. Deviations in the transmit frequency show up as shifts in the IF frequency from the desired 60 MHz. The short term stability of the transmit frequency is

often compensated for by using an Automatic Frequency Control(AFC) circuit within the radar receiver. A review of how a Racal-Decca receiver operates reveals that the AFC is used to apply an error signal to the local oscillator to keep the IF centered at 60 MHz. A manual tuning control is normally provided and permits larger scale tuning of the local oscillator. A gating signal is used to permit the AFC circuit to operate only when the radar is transmitting. This prohibits the locking of the AFC circuit on interference from other radars.

The manual tuning of the radar for the best picture has often been used in the past as a way to ensure the radar is on tune. This has often been more effective than the use of the tuning indicator which normally presents a signal that is proportional to the power received from the transmitted pulse. This means that the tuning indicator will show larger deflections on long pulse than on short pulse.

There are a number of methods that may be used to maintain tuning of the vpol receiver on the hpol transmit frequency. The most direct way would be to supply a sample of the transmitted signal to the vpol receiver using a directional coupler on the hpol transmitter waveguide coupled to another directional coupler on the vpol waveguide. This method would provide a controlled sample of the transmitted pulse directly into to the front-end of the vpol receiver. If the hpol trigger is supplied to the vpol transceiver as an external trigger the tuning circuits of the vpol receiver may be made to operate normally, locking onto the transmit frequency of the hpol receiver. This type of installation would require access to the waveguide on the hpol radar which may be difficult in existing installations. Newer radars are often have upmast transceivers that permit no access to waveguide so this is not considered to be a generally applicable low cost solution.

As indicated in the previous section it is expected that a significant amount of the transmitted power is expected to be coupled into the vpol transceiver through the antenna sidelobes. If this power is sufficient to operate as the source of the tuning signal a simple connection of the radar trigger may accomplish what the more expensive directional coupler option provides.

This technique could be complemented by the use of the received signal amplitude as the source of how well the vpol receiver is tuned to the hpol transmit signal. With the radar trigger being supplied by the hpol transmitter a sampling device could be programmed to sample the average signal amplitude over the first few microseconds of the received signal. This could be averaged over the equivalent of one radar scan and used to supply a tuning indicator signal to the system operator. If a microcontroller is used for this operation the signal could be used to autotune the vpol receiver at a pre-programmed interval.

4.1.7 Conclusions

4.1.7.1 Antenna Positioning

The preferred configuration for positioning the two antennae will minimize the horizontal displacement. Ideally they should be mounted directly above one another. If this is not feasible, the horizontal displacement should not exceed 3.75 m. This would keep both

the range and angular errors below acceptable limits. There are no simple solutions to removing these errors once they have been introduced to the system.

4.1.7.2 Vpol Antenna

Providing a vertically polarized antenna with a wider beamwidth than the horizontally polarized antenna will address two problems:

1) The angular error introduced by a horizontal displacement of the two antennae will be reduced.
2) The tracking accuracy required for slaving the vpol antenna to the hpol antenna will be reduced.

4.1.7.3 Antenna Slaving

The vpol antenna must be slaved to the hpol antenna to provide the minimum angular error. This can be done by a custom antenna motor control unit. This unit will take in the current position of each antenna and adjust the vpol antenna to track the hpol.

The hpol unit may require modification in order to provide bearing data with a resolution high enough to meet the tracking requirements. Such modifications must not affect the hpol radar type approval.

4.1.7.4 System Calibration

The vpol antenna will have to be calibrated against the hpol antenna to accommodate differences in the antenna beam patterns.

4.1.7.5 Tuning

An external tuning unit may need to be developed to provide tuning information for the vpol unit. This unit would sample the received signal and use the result for tuning. The information could be sent to a display for an operator to manually tune the vpol unit, or generate a tuning signal to be applied directly. An external trigger connection should be used to connect the hpol transmitter to the vpol transceiver. This may require the modification of the vpol transceiver to accept an external trigger and to disable the transmitter.

4.2 Antenna Polarization Mechanics

Any polarization can be radiated by an antenna if two orthogonal field components can be adjusted in relative amplitude and phase. Polarizers can be employed for achieving this differential phase advance. A polarizer is a two port device that alters the polarization state in a controlled fashion. The two most common forms of polarizers are the 90 degrees and the 180 degrees polarizer. The former is used to convert an LP (Linearly Polarized) wave to CP and vice versa while the latter is used to rotate the plane of polarization of an LP wave (from HP to VP, for instance). The principle of operation of polarizer is presented in [1] and will not be repeated here. One way to approach this

problem is to employ an antenna which can transmit/receive two orthogonally polarized waves; and the phase and amplitude adjustment can be achieved at the feed port of the antenna using a ferrite phase shifter. Such an approach is described in [2], which uses three slotted waveguides in a symmetric configuration, and generates two orthogonal polarizations in a parallel plate region. Two arrays with matched inclined/displaced slots are used to generate the longitudinal component while one array with matched edged slots is used to generate the transversal component. The innovative use of two arrays for the longitudinal component leads to a very robust design by eliminating fragile wire grids or plates and is certainly capable of any polarization. However, the weight of the antenna as reported is rather high (~ 100 kg). This technology is used in the CHL antennas referred to later.

Another possible implementation is described in [3] which employs a pair of crossed slots in the sidewalls of a bifurcated rectangular waveguide that couple to even and odd waveguide modes. One linear polarization is excited by the even or sum mode and the orthogonal component is excited by the odd or difference mode. Expermental results presented indicate that for linear polarization, the cross-polarization component was on the order of –25 dB.

The two references cited above have been included to show it is technically feasible to build a marine radar antenna with vertical or circular polarization. The technology exists and experimental results do indicate satisfactory performance. Inspite of this, after extensive search, no manufacturer of civilian marine radars with vertically polarized antenna was located. However, there are a number of companies which have quite similar antennas used mainly for other applications such as ASDE (Airport Surface Detection Equipment) and VTS. Once again it was generally found that the polarization of choice is either Horizontal or circular. Though it is certainly technically feasible to have a slotted waveguide array with vertical polarization, lack of applications have generally restricted its commercial availability.

The most promising company is CHL in the Netherlands which specializes in multiple polarization capable slotted waveguide array antennas. Some of the products available are listed in Figure 4-4.

Radar Antennas CHL

	Beamwidth	*Beam shape*	*Polarisation*
X-band			
S-family	0.27° - 0.43°	Quasi inv. cosec²	V
SN-family *	0.43°	Fanbeam	V/H/C fixed
SHV	0.33° - 0.43°	Fanbeam Quasi inv. cosec²	V/H/C switchable
S-band			
SV107	1.1°	Fan beam	V
Ku-band			
ASDE	0.26°	Quasi inv. cosec²	C

* Also available in economic Silverline version

Figure 4-4 Types of antennas available from CHL, the Netherlands (from http://www.chl.nl/radar.html).

After consultation with the company it appears that the turning unit which can be used onboard a ship can support antenna up to 440 cm long, giving a horizontal beamwidth of 0.55 degrees. They can provide the antenna with a vertical, horizontal or circular fixed polarization.

The other details of the antenna are:

- sidelobe level <-27 dB
- gain >34 dB
- vswr , 1.3
- rpm 20 ± 10%
- price Between 165,000-185,000 NLG (1 NLG ~ 0.733 C$).

The preceeding discussion deals with methods where the polarization is altered by inserting a half-wave phase shifter in the signal transmission path. Another approach is to use an external polarizer in front of the antenna's radiating aperture. The advantages of using such an approach is that no hardware component needs to be replaced and the polarizer can be detached or replaced. Using this approach, therefore, it is possible to retrofit an existing marine radar antenna to transmit/receive vertical/circular polarization. Most of the literature on this topic deals with 90 degrees polarizer, but as indicated earlier, an application that used a 180 degree polarizer was not found. A commercial application of an external polarizer is in the antenna provided by Sperry for its Seatrack marine radar shown in Figure 4-5 ([4] page 31-11) which has two horizontally polarized linear arrays mounted back-to-back, each lying within the usual horizontal sectoral horn.

A 90 degrees polarizer (parallel plates) is placed across one of the horn end to convert it to a CP antenna.

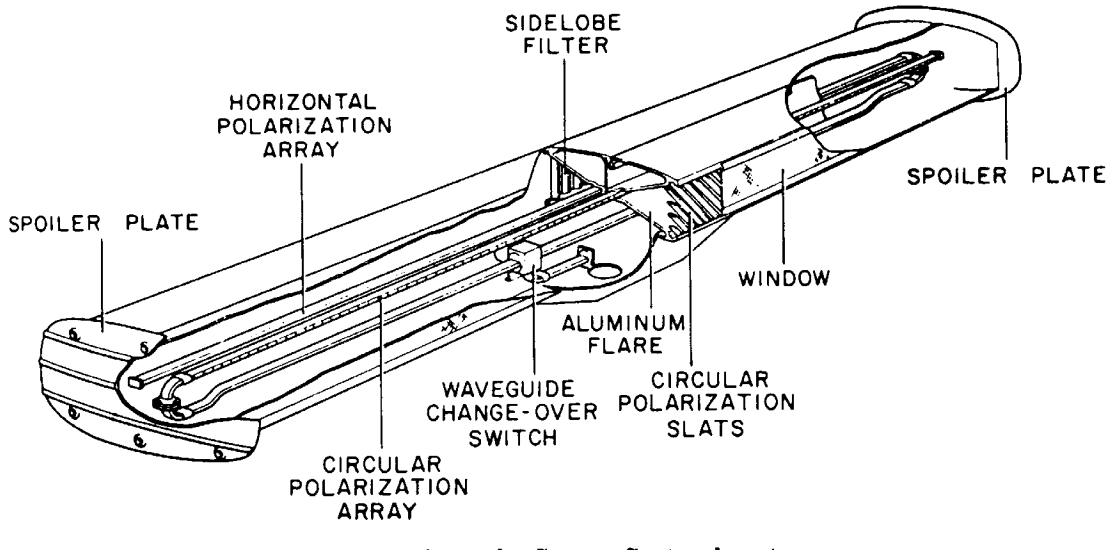

Figure 4-5 Sperry Marine Seatrack Antenna showing the use of external polarizer to convert linear to circular polarization ([4] page 31-11)

Technically therefore, replacing this polarizer with an appropriate 180 degrees polarizer is what is need to achieve an VP operation. Alternately the polarizer can be designed as an external radome. This is described in [5] and is straightforward.

Two of the most popular structures for external polarizers are the parallel plate polarizer [6], [7] and meanderline polarizer [8], [11], [9] and [10]. The parallel plate polarizer is the simpler of the two to engineer and has been known for over 40 years now. The idea is to incline an array of parallel plate waveguides relative to the electric vector of a normally incident linearly polarized plane wave. The wave propagating in each parallel plate guide can be decomposed into the TEM mode polarized normal to the plate and the TE_{10} mode polarized parallel to the plate. These modes propagate with different phase velocities, thus appropriate choice of plate separation and length can twist the polarization of the input wave to any desired polarization. The biggest disadvantage of this design is its rather flexible nature and its very narrow band of operation.

A meanderline polarizer (MLP) consists of several similar, thin, metallic conductors which literally meander back and forth in the manner of a periodic rectangular waveform. The conductors are spaced periodically, so that the composite device is doubly periodic structure. The basic approach is to make an array of structures which appear to be predominantly inductive to one polarization and capacitive to the orthogonal polarization. Instead of trying to achive a complete phase reversal with one sheet (each structure must be matched to free space to minimize reflections), a plurality of sheets spaced together is used to achieve this. Accurate spacing between the sheets can be achieved in a number of ways, such as using low-loss polyfoam or honeycomb material of desired thickness. Most of the references listed above deal with a 90 degrees polarizer. The only reference

for 180 degrees polarizer is [10] which employs 8 sheets to obtain the required phase shift. An attractive feature this design is that by simply rotating the meander lines, any desired linear polarization can be obtained.

Particularly important features of the MLP are that it simultaneously serves as a mechanically strong radome, and its bandwidth capability is much broader than that of parallel plate polarizer. Furthermore, it is possible to employ the meanderlines advantageously for other applications such as for radome deicing; this feature has been achieved on several occasions by simply connecting a low frequency AC source across some of the meanderlines to generate sufficient heat for the deicing process.

Several other external polarizer approaches are described in [12] to [17], and further support this concept.

4.2.1 Conclusions

Although we were unable to find an inexpensive, commercially available, vertically polarized antenna, an expensive vertically polarized slotted waveguide antenna was found; and a number of technically feasible solutions were found in the literature to convert the polarization of an existing antenna to vertical, using external polarizers. Though, the use of polarizers to convert from Hpol to Vpol has been rather limited, the literature suggests that it is certainly possible both technically and from an engineering point of view. A detailed study is required to perform engineering, manufacturing and performance trade-offs for such antennas, in order to confirm the feasibility of developing low-cost, vertically polarized antennas.

4.3 References

[1] Stutzman, W. L.; 'Polarization in Electromagnetic Systems', Artech House, 1992.

[2] Blommendaal, R. and Westerman, B.E., 'A Slotted Waveguide Antenna with Polarisation', IEE Electromagn Waves Ser 20, Adv in Radar Tech. Publ by Peter Peregrinus Ltd, London, Engl, 1985, pp. 411-416.

[3] Ajioka, J. S.; Joe, D. M.; Tang, R. and Wong, N. S., 'Arbitrarily Polarized Slot Radiators in Bifurcated Waveguide Arrays', IEEE Trans. Antennas and Propagation, AP-22, No. 2, March 1974, pp. 196-200.

[4] Skolnik, M. I., 'Radar Handbook', McGraw-Hill, 1970.

[5] Smith, K. C., 'Lens/Polarizer Radome', U.S. Patent No. 4901086, Feb 13, 1990.

[6] Cloete, J. H., 'Interaction Between a parallel plate polarizer and a linear slotted waveguide array', Proc. of Fourth International conference on Antennas and Propagation (ICAP'85), 1985, pp. 40-43.

[7] Sangster, A.J., 'Scattering Analysis of awaveguide slot radiator enclosed in a parallel plate polariser', IEE Proceedings-H, Vol. 139, No. 5, Oct. 1992, pp. 414-420.

[8] Epis, J. J., 'Meanderline array radome Polarizer for practical applications', IEE Electromagn Waves Ser 20, Adv in Radar Tech. Publ by Peter Peregrinus Ltd, London, Engl, 1985, pp. 411-416.

[9] Young, L.; Robinson, L. A. and Hacking, C. A., 'Meander-Line Polarizer', ibid, AP-21, No. 3, March 1973, pp. 376-378.

[10] Wu, T.K., 'Meander-Line Polarizer for Arbitrary Rotation of Linear Polarization', IEEE microwave and guided wave letters, Vol. 4, No. 6, June 1994, pp. 199-201.

[11] Collier, D.; Greenspan, M.; MacFadyen, D. and Orwig, L., 'RF Propagation from a flatplate array with Polarizing Lenses', Proc. of IEEE 1995 International Radar Conference, May 1995.

[12] Monser, G. J., 'Radio Frequency Antenna with Polarization Changer and Filter', U.S. Patent No. 4342034, July 27, 1982.

[13] Brunner, A. and Rieskamp, K., 'Radome for generating circular polarized electromagnetic waves' , U.S. Patent No. 4477815, Oct. 16, 1984.

[14] Wu, T. K. and Helms, D., 'Meanderline Polarization Twister', U.S. Patent No. 4786914, Nov. 22, 1988.

[15] Kisliuk, M and Axelrod, A., 'Build a Circularly Polarized Waveguide Slot Antenna', Microwaves & RF, Vol. 26, No. 6, Jun 1987, pp. 139-146.

[16] Min, K. S.; Hirokawa, J. and Goto, N., 'Single-layer dipole array for linear-to-circular polarisation conversion of slotted waveguide array', IEE proceedings-H, Vol. 143, No. 3, June 1996, pp. 211.

[17] Shafai, L. and Ittipiboon, A., 'Dual Polarized Ice Surveillance Radar Antenna', IEEE ELECTRONICOM '85 - Conference Proceedings, 1985, pp. 216.

THIS PAGE IS INTENTIONALLY LEFT BLANK

5 RECORDED DATA ANALYSIS

5.1 Analysis of Complete Sequences

Having considered how to balance a single pair of images for intercomparison, a subsequent question is how this balancing compares from one scan pair to the next within a given sequence, for which the radar settings remain unchanged, and the ice environment presented to the radar changes only due to ship motion.

The first step was to examine the change in the median profile vs. range over the sequence. The profile for each of the N scans in the sequence was calculated, then used to create a greyscale image of the median profile vs. successive scans. Figure 5-1 shows the HH median over the 26 scans of segment 2, tape 16, and Figure 5-2 shows the HV image. The median changes only very slightly from one scan to the next, with somewhat larger overall changes due to ship motion.

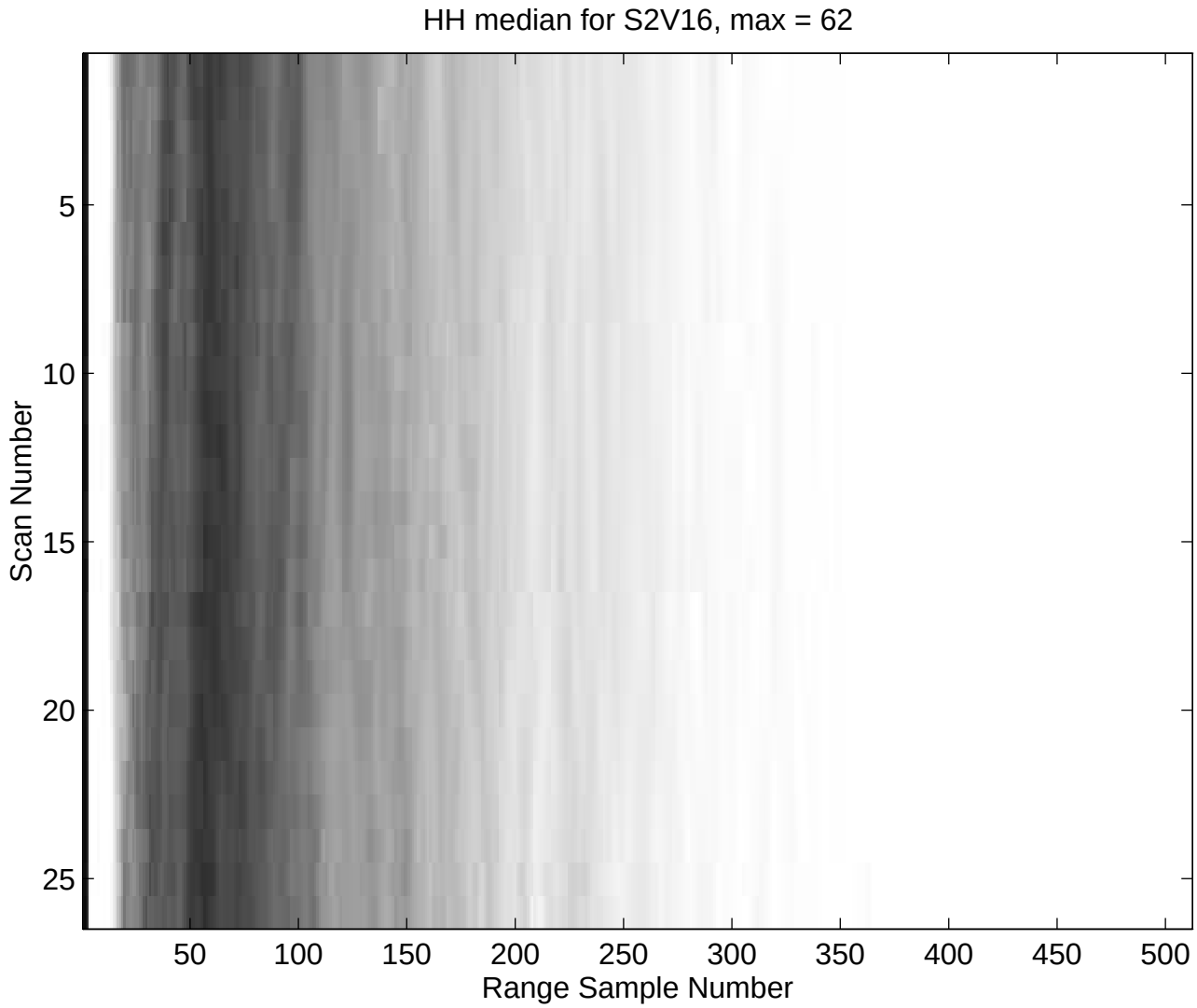

Figure 5-1 Median range profile vs. scan number for the data sequence S2H16

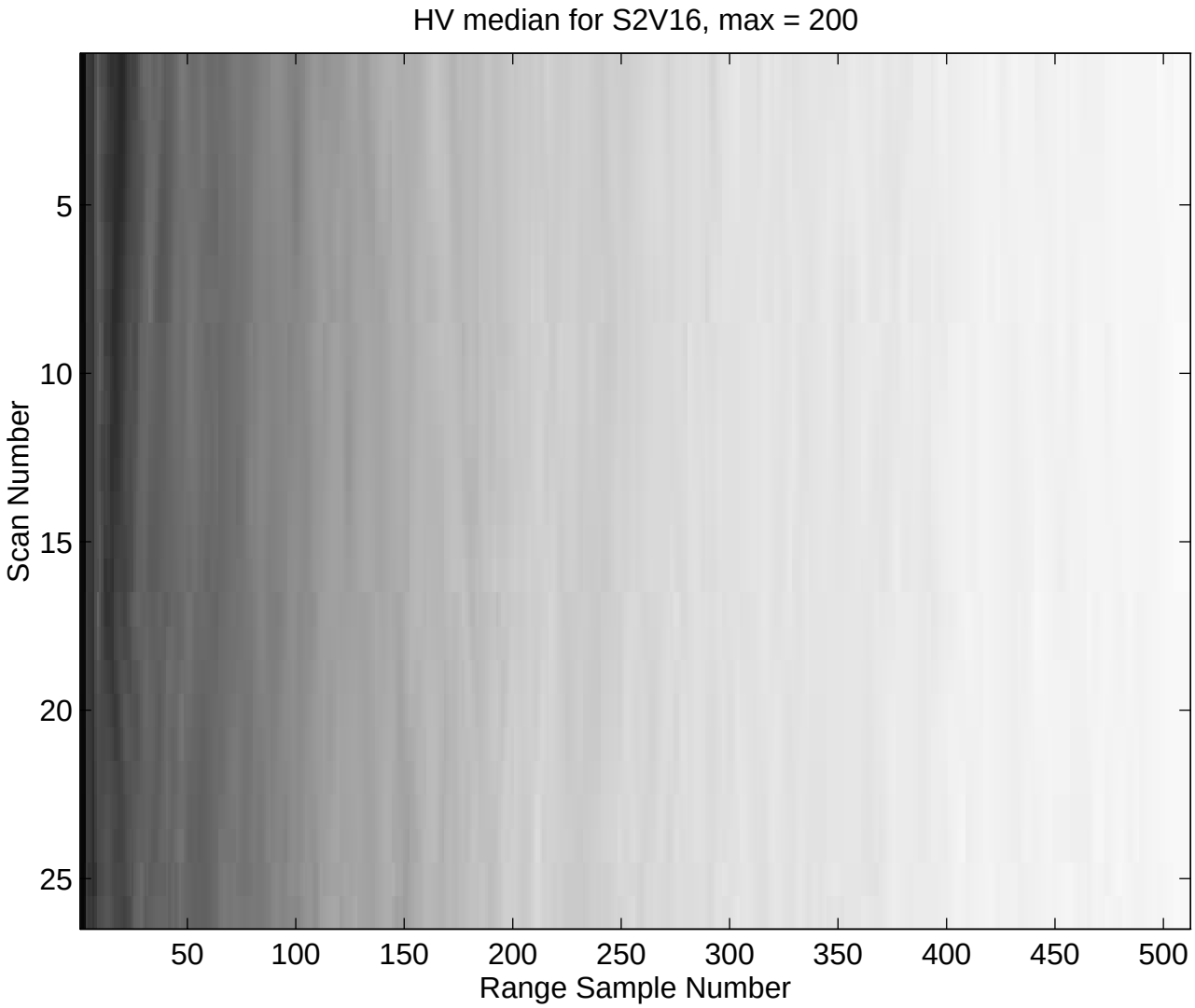

Figure 5-2 Median range profile vs. scan number for the data sequence S2V16

To indicate the variation over the N scans, the average median profile was calculated from the image, together with the standard deviation. Figure 5-3 and Figure 5-4 show the plots of the average median curve and the average plus one standard deviation for the HH and HV data respectively. It can be observed that the variation in the median curve is reasonably small, evidenced by the small standard deviation. Note that the average and standard deviations were calculated using only those points for which the data were non-zero. The plots for the other data sets are shown in Figure 5-5 to Figure 5-12.

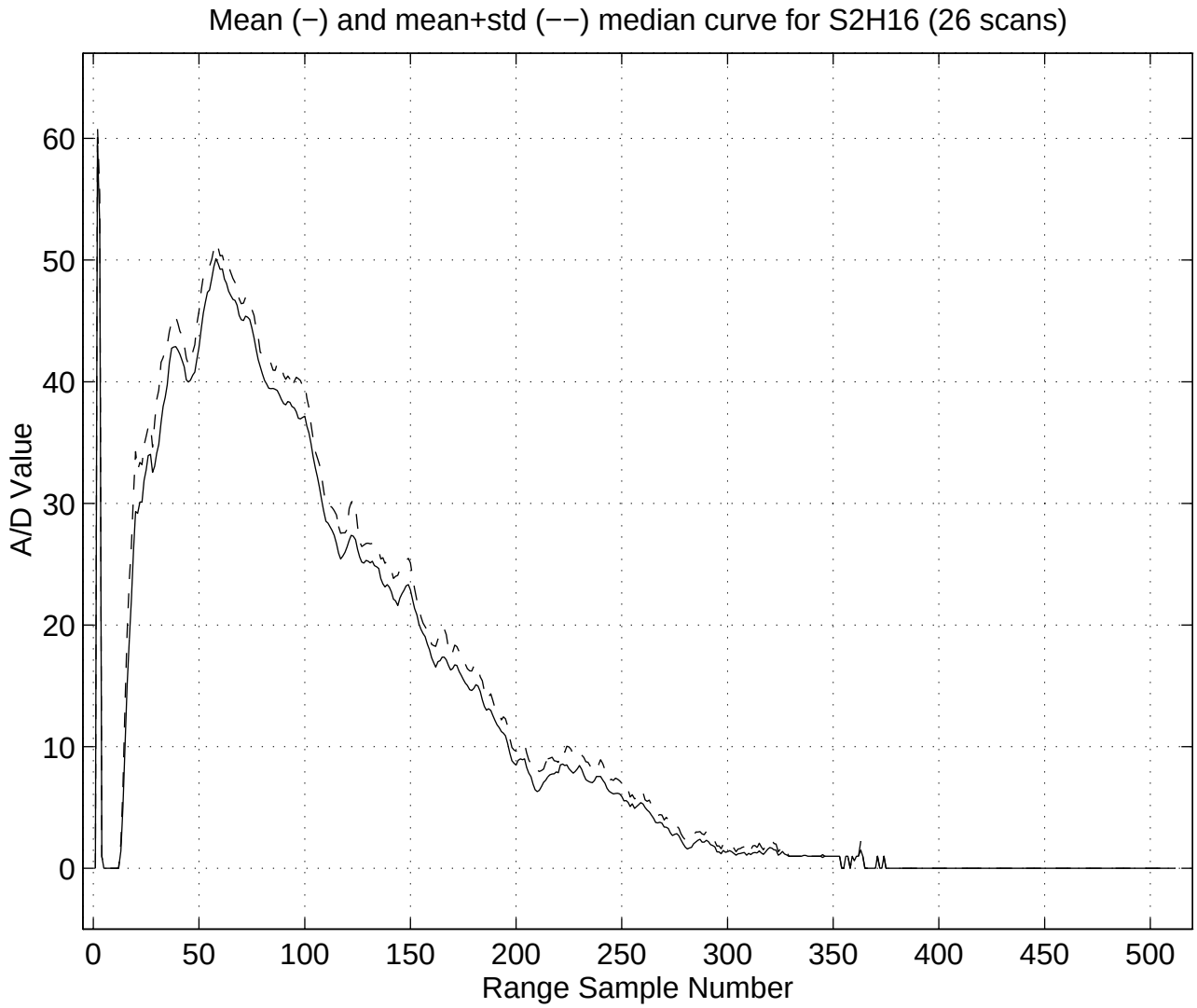

Figure 5-3 Average median curve, and average plus one standard deviation, for the data sequence S2H16

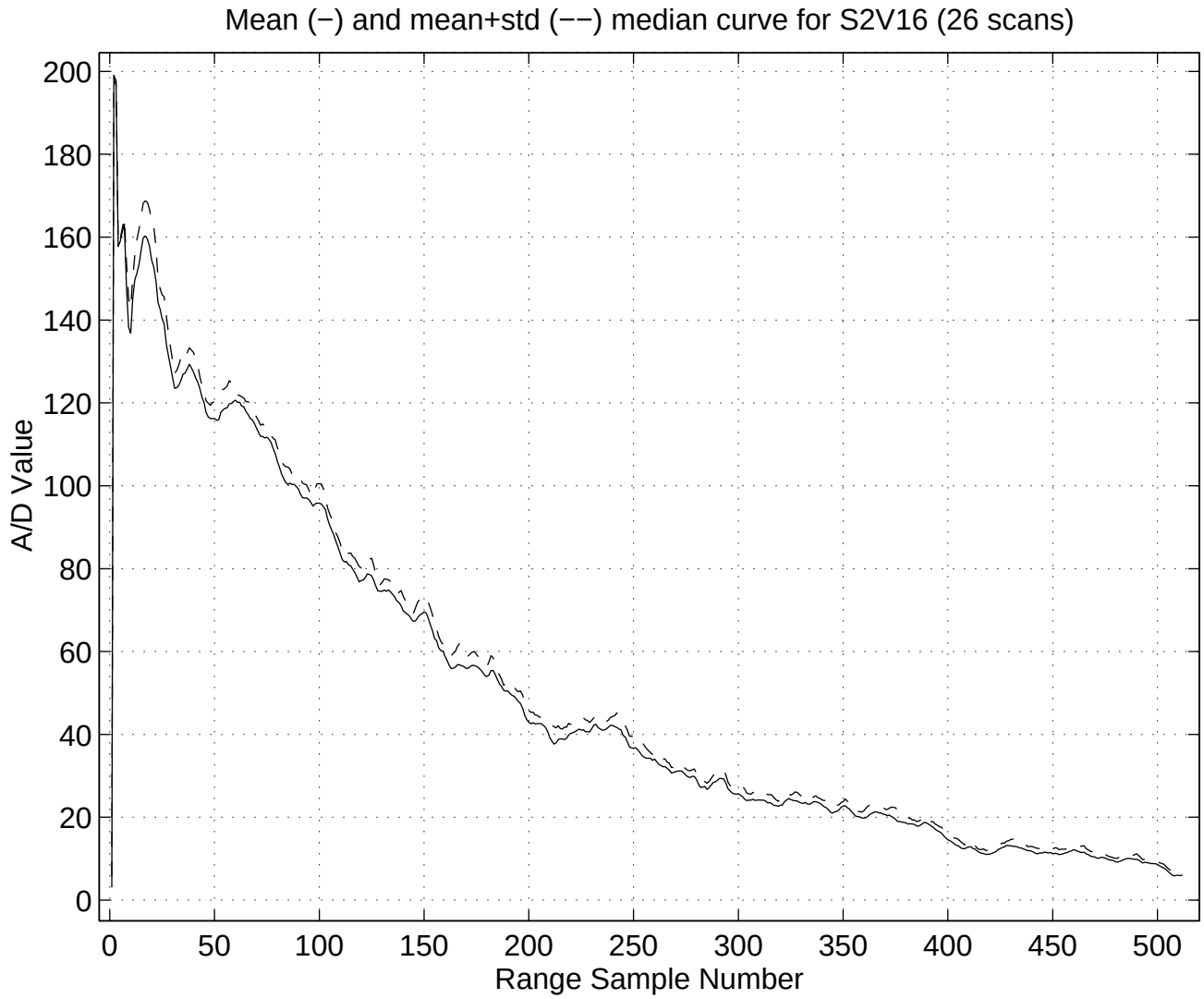

Figure 5-4 Average median curve, and average plus one standard deviation, for the data sequence S2V16

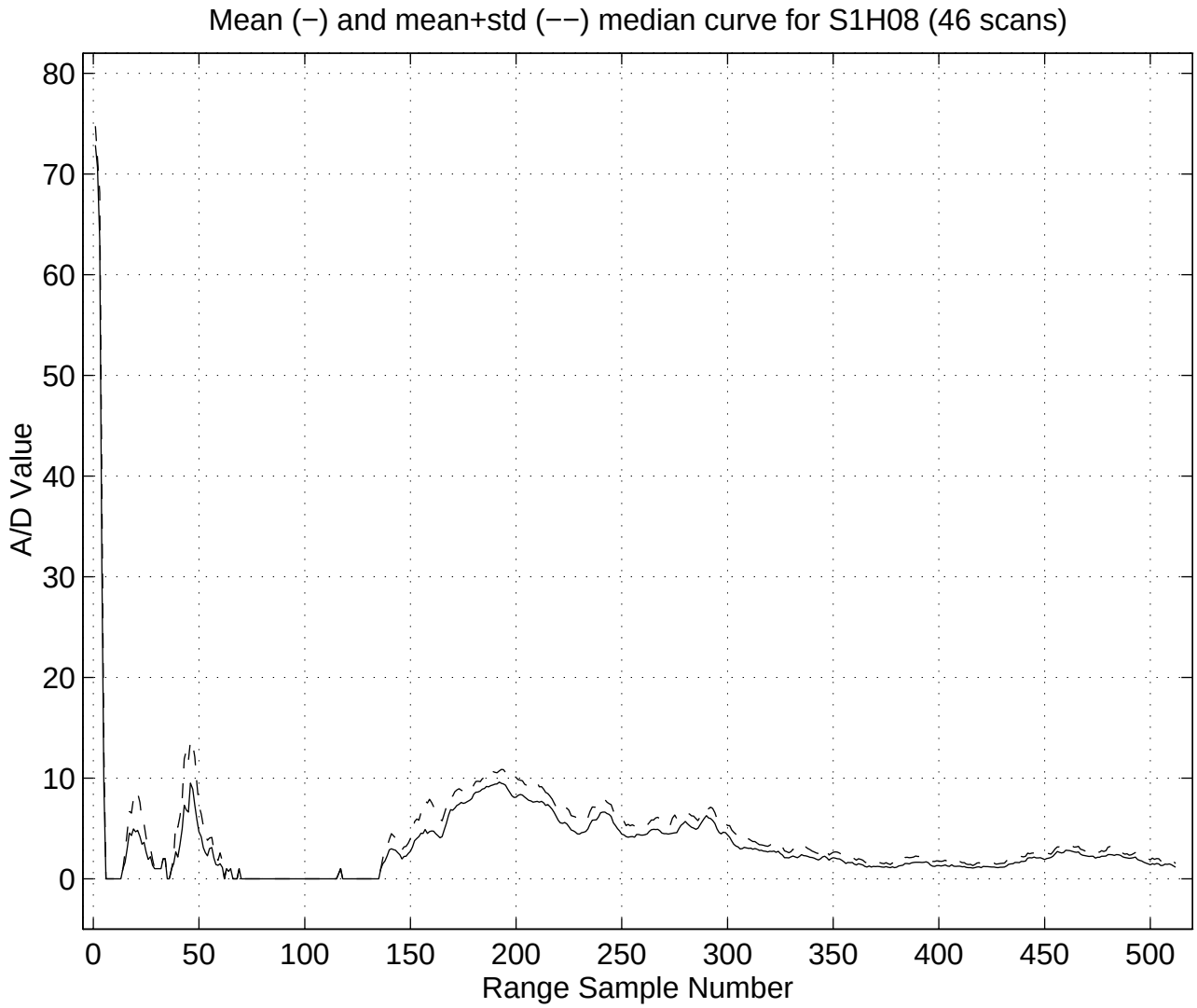

Figure 5-5 Average median curve, and average plus one standard deviation, for the data sequence S1H08

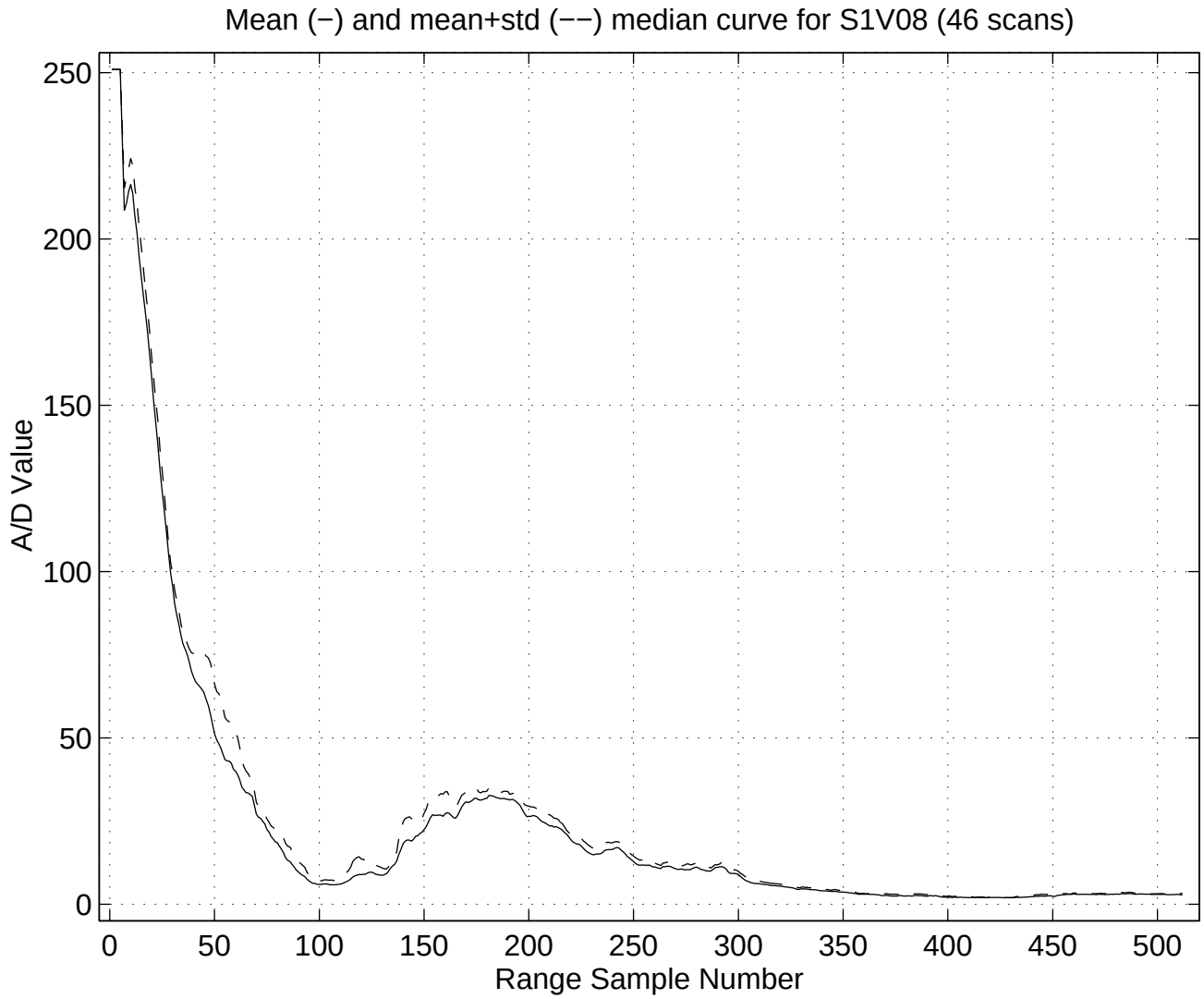

Figure 5-6 Average median curve, and average plus one standard deviation, for the data sequence S1V08

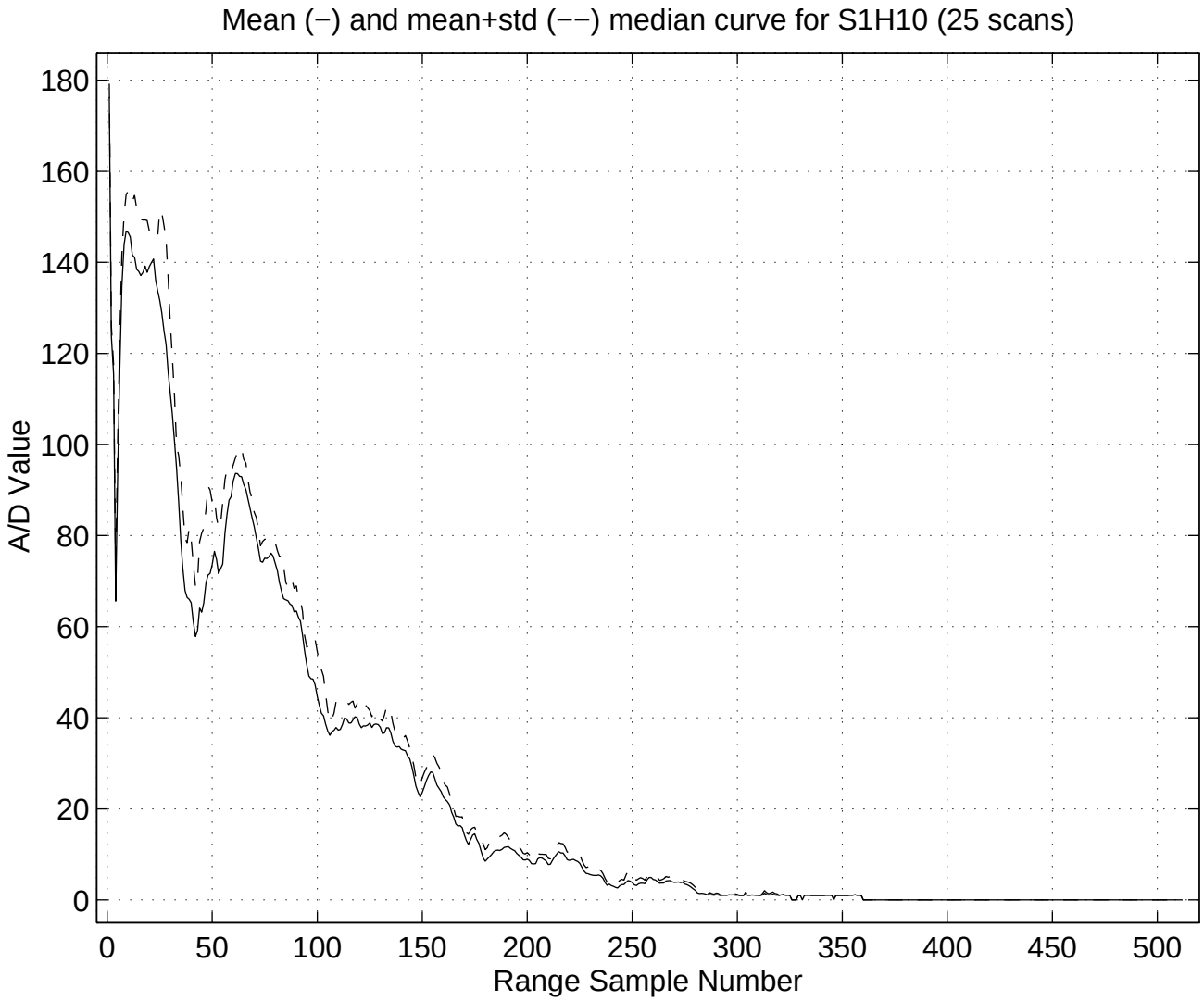

Figure 5-7 Average median curve, and average plus one standard deviation, for the data sequence S1H10

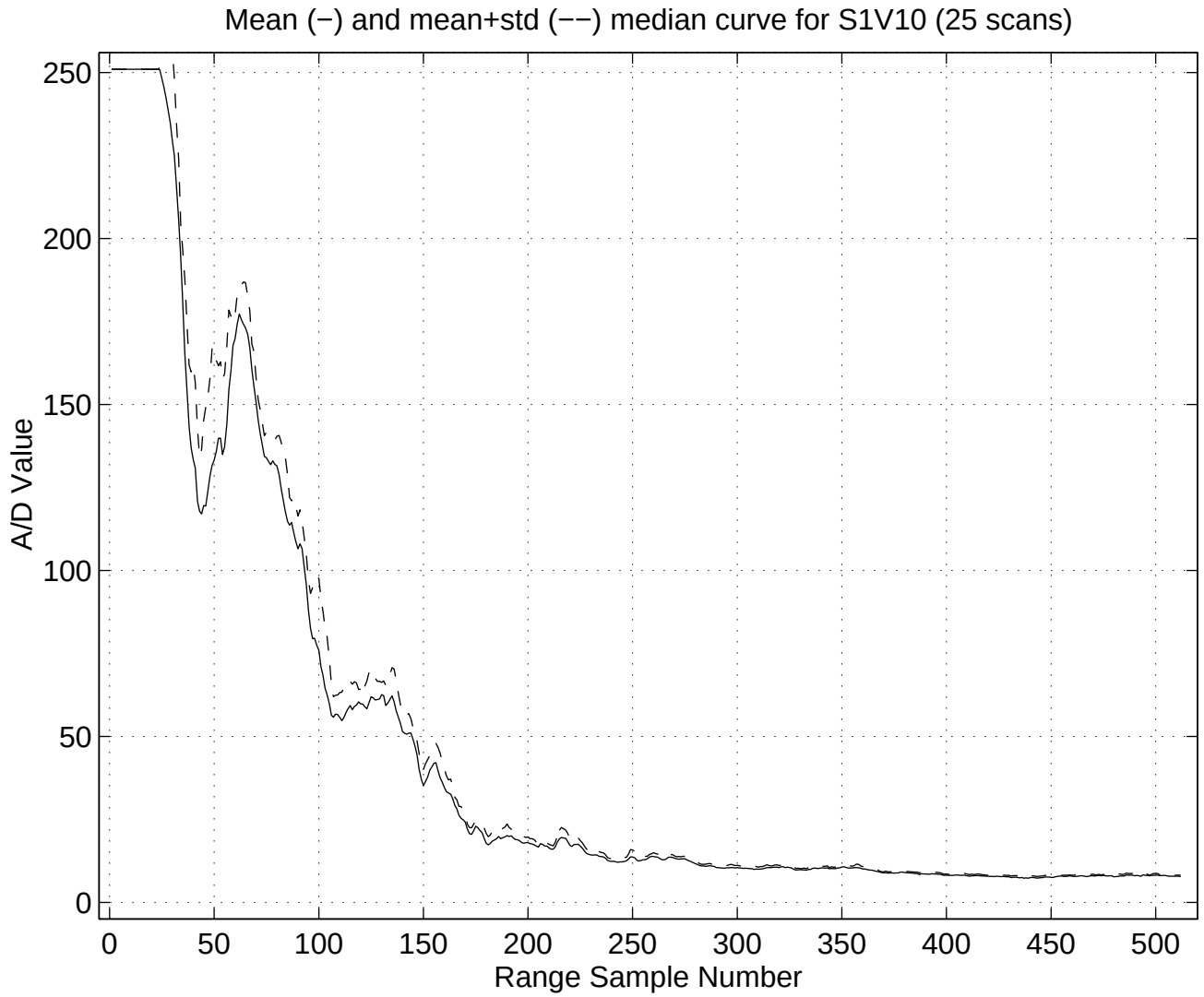

Figure 5-8 Average median curve, and average plus one standard deviation, for the data sequence S1V10

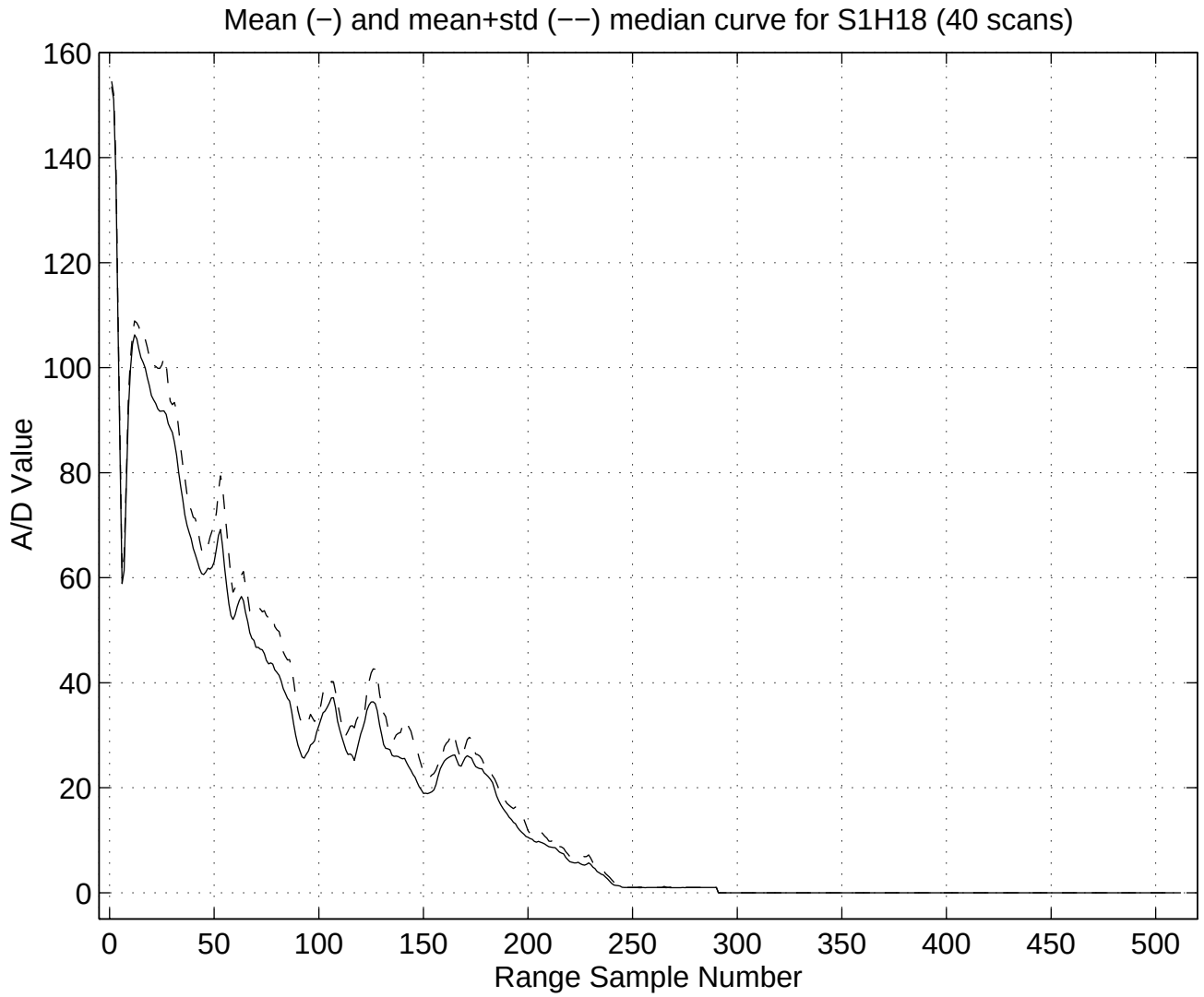

Figure 5-9 Average median curve, and average plus one standard deviation, for the data sequence S1H18

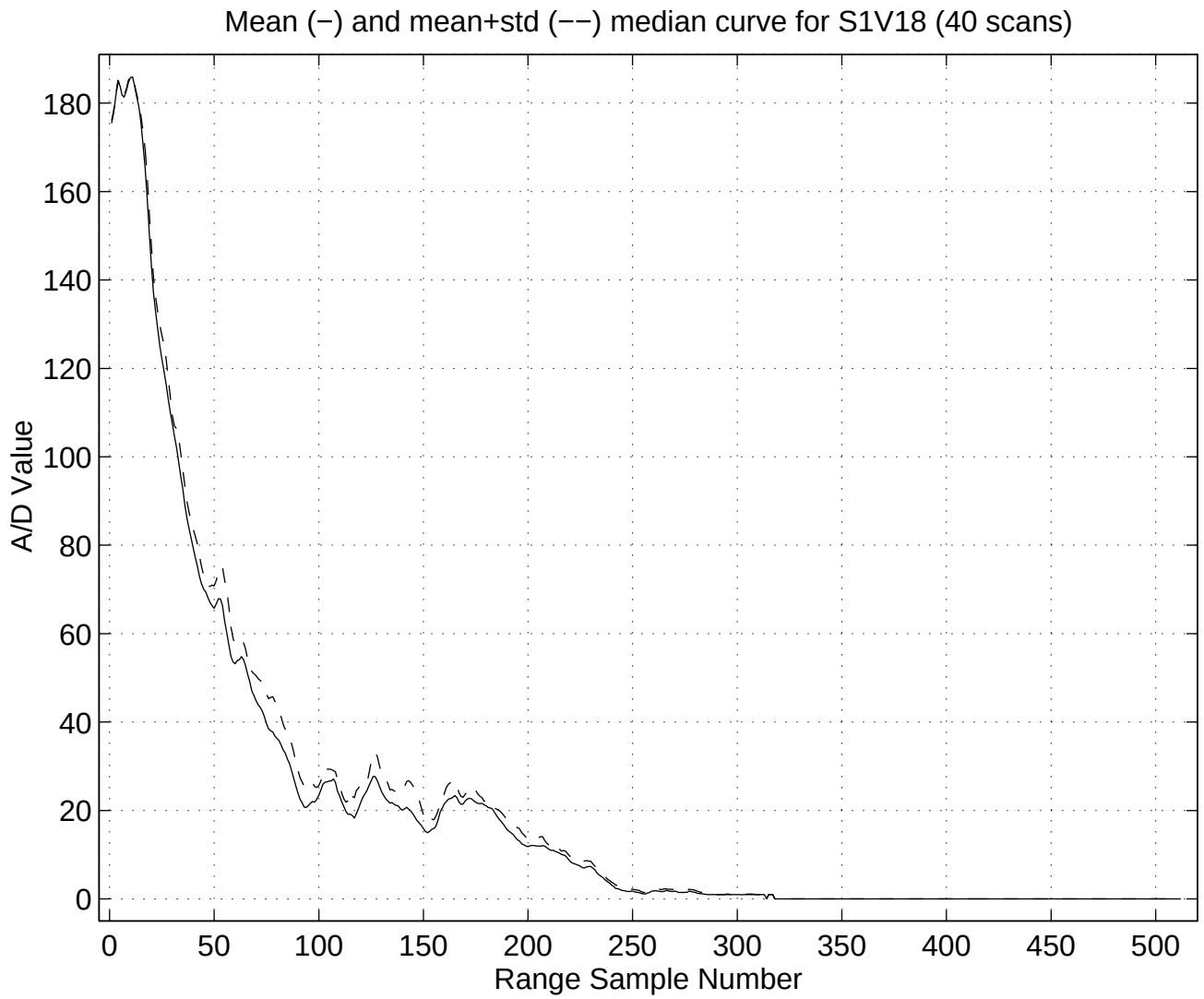

Figure 5-10 Average median curve, and average plus one standard deviation, for the data sequence S1V18

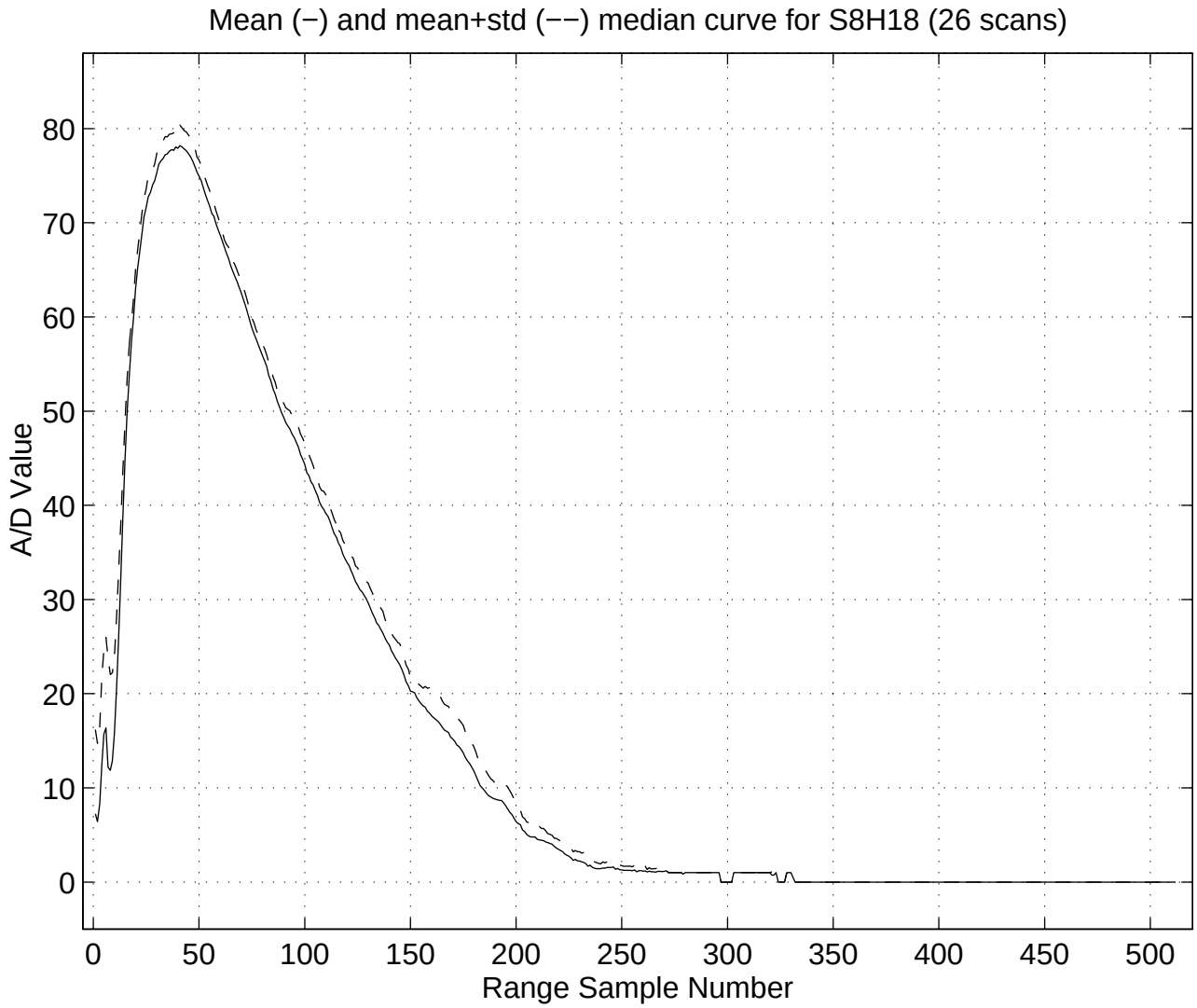

Figure 5-11 Average median curve, and average plus one standard deviation, for the data sequence S8H18

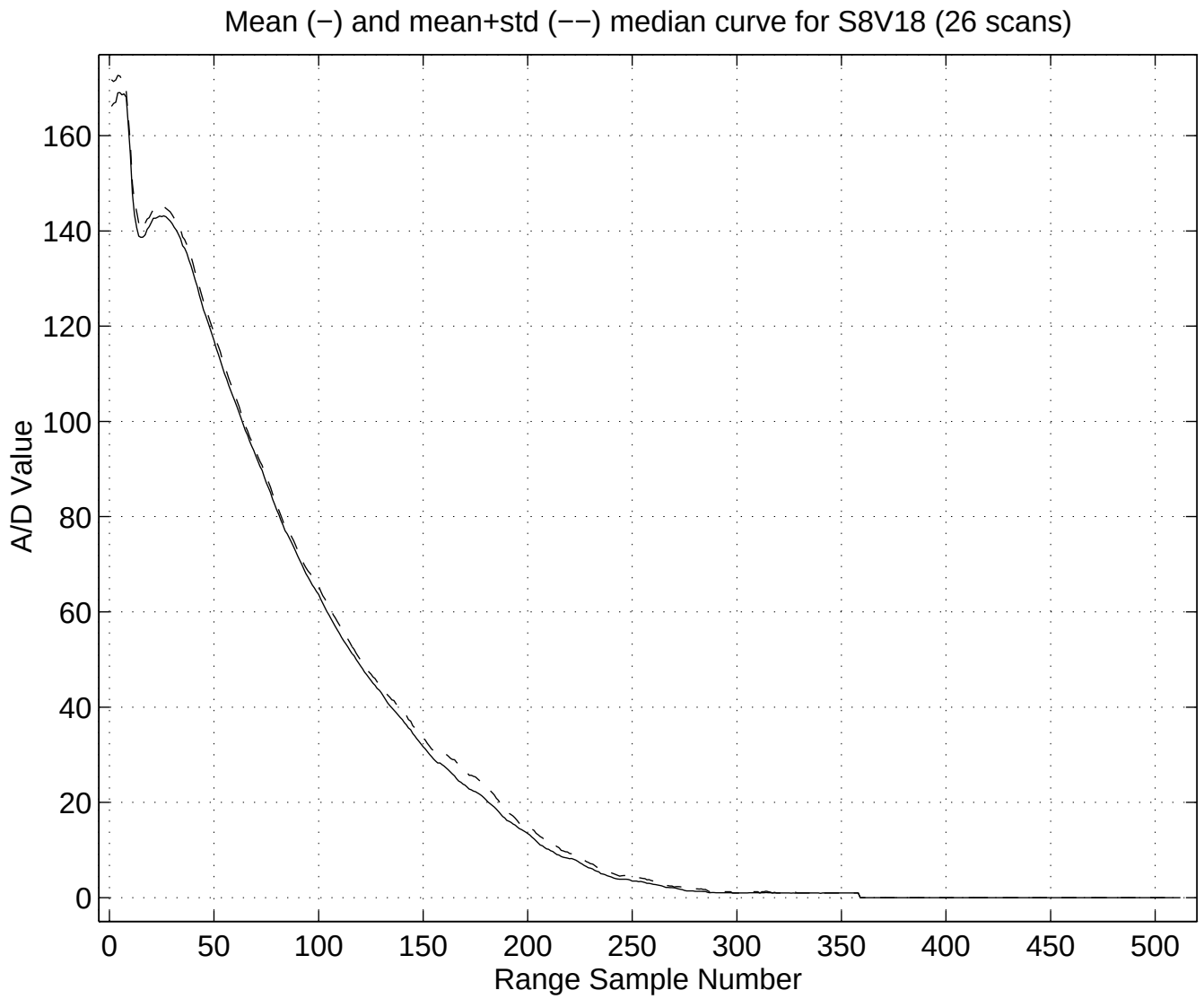

Figure 5-12 Average median curve, and average plus one standard deviation, for the data sequence S8V18

In a similar manner, the change in the estimated gain factor from scan to scan was examined. Using the techniques described earlier, the gain factor at 5 CDF levels was estimated for each pair of scans in the sequence. Figure 5-13 shows an example of the resulting gain factor (CDF 0.5) image for S2H16. Although the gain factor shows modest variation at the central ranges, the edges (particularly long range) are ragged. Figure 5-3 showed that the HH median is near zero for ranges 300 and larger. The gain factor is not calculated if the HH or HV median is zero. Therefore from scan to scan the median at these ranges may vary from zero, resulting in no estimated gain factor, to slightly non-zero, for which the gain factor is calculated. This factor is confirmed by Figure 5-14,

which shows, for each range, the percentage of the number of scans for which the gain factor was non-zero. As the range increases beyond sample 300, the number of scans having non-zero gain factors decreases.

The average gain factor for each cdf level was calculated from the corresponding gain image. Figure 5-15 shows a plot of the average gain factors for S2H16. The various CDF level gain factors agree fairly well, except at short and longer range. Part of the variation is due to the calculation of the average being based on an increasingly smaller number of scans. Therefore, in trying to estimate the behaviour of the gain factor with range, the number of scans used in the calculation should be kept in mind. Figure 5-16 to Figure 5-23 show the corresponding curves for the other 4 data sets.

Originally, 41 matched scan pairs were extracted from tape for data sequence S1H18. In developing the initial gain factor image for the sequence, an anomaly appeared in the gain factor for the first scan pair. Closer inspection revealed that one quadrant of the HV image was incorrectly recorded. This scan pair was removed from the sequence, leaving 40 pairs.

It should also be noted that the calculation of the return statistics vs. range, and subsequently the gain factors, is based on using complete range rings. The method is insensitive to any azimuth offset between the HH and HV images.

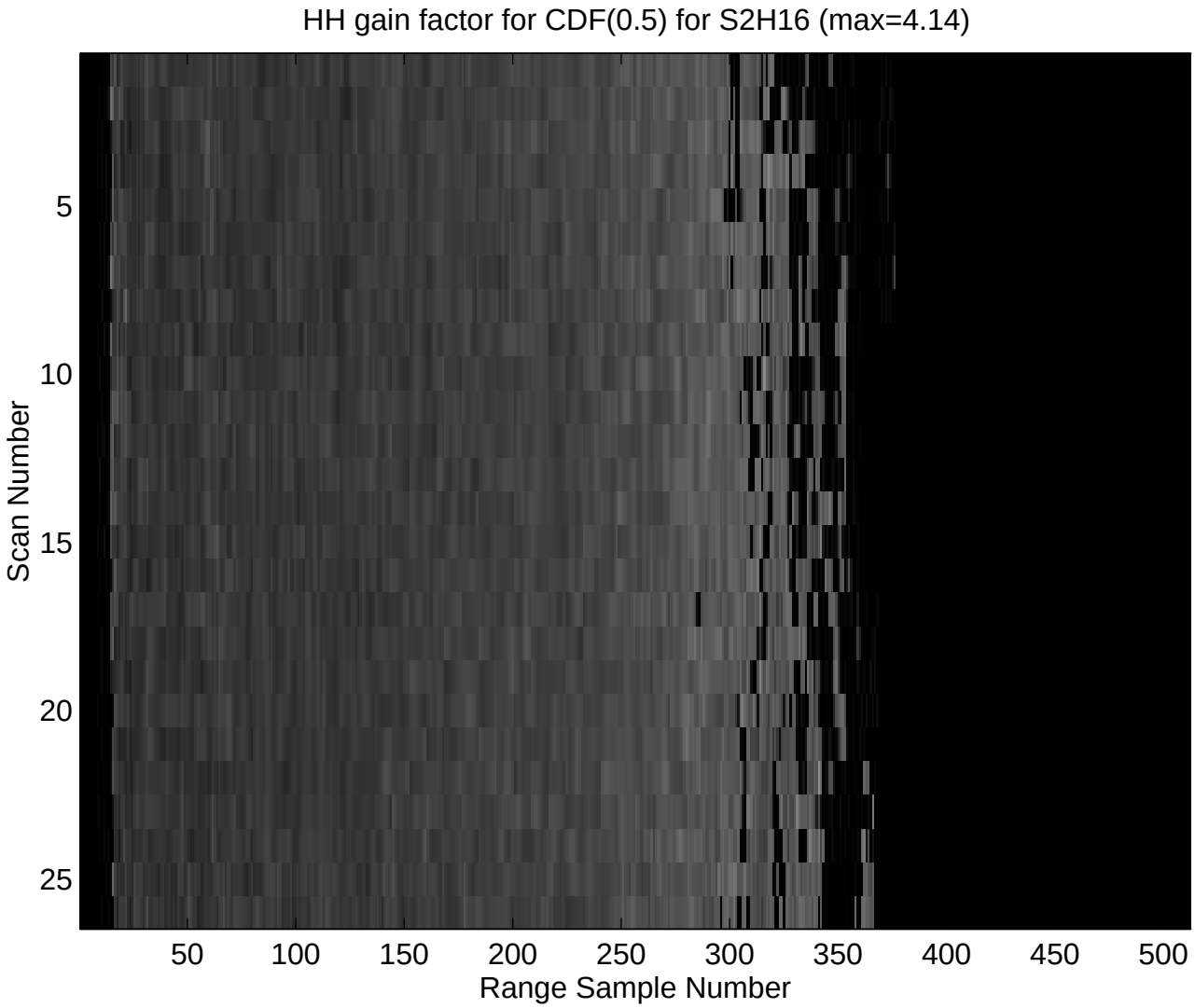

Figure 5-13 Gain factor at CDF level 50% vs. scan number for the data sequence S2H16

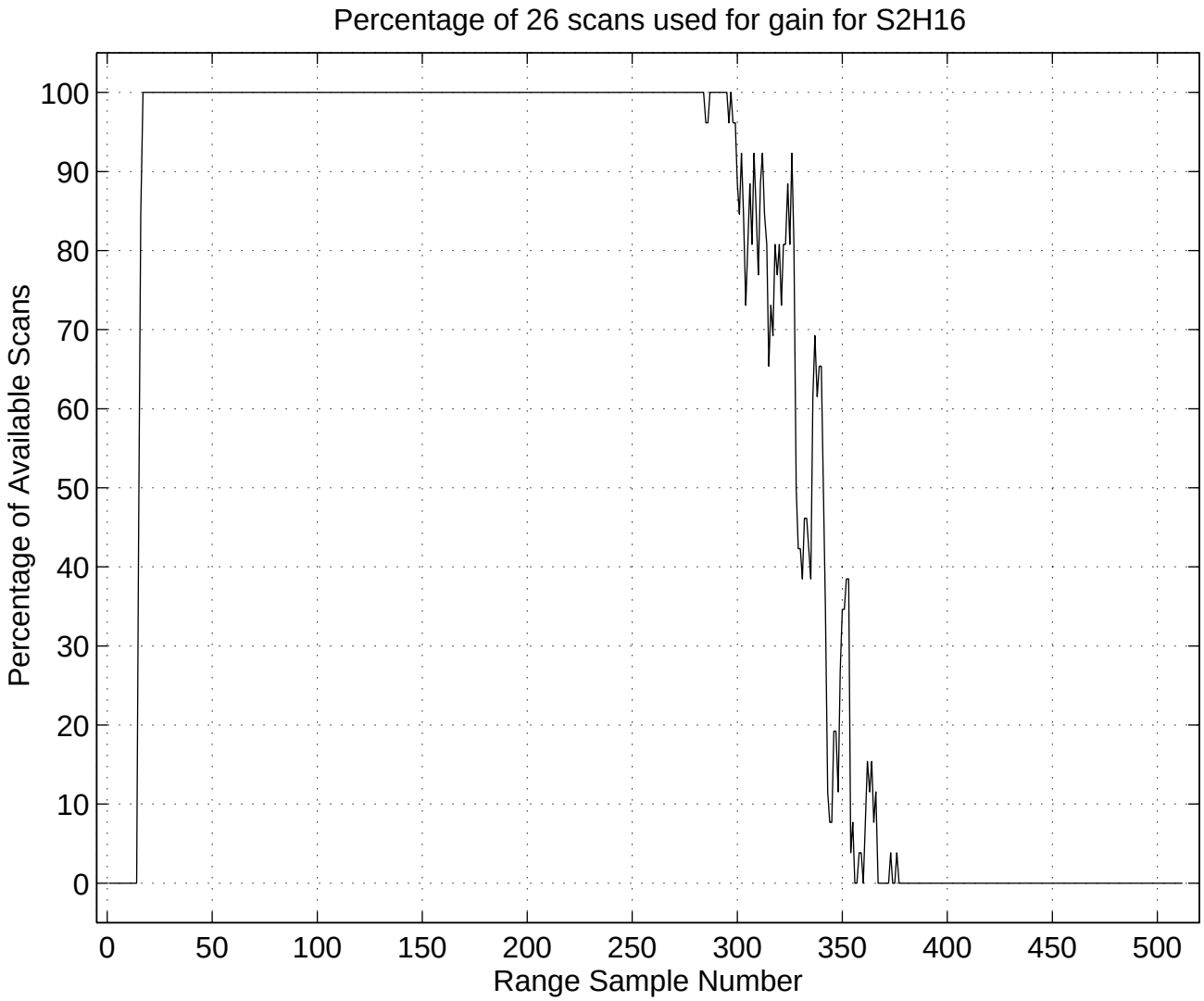

Figure 5-14 Percentage of scans available used in calculating the gain factor for data sequence S2H16

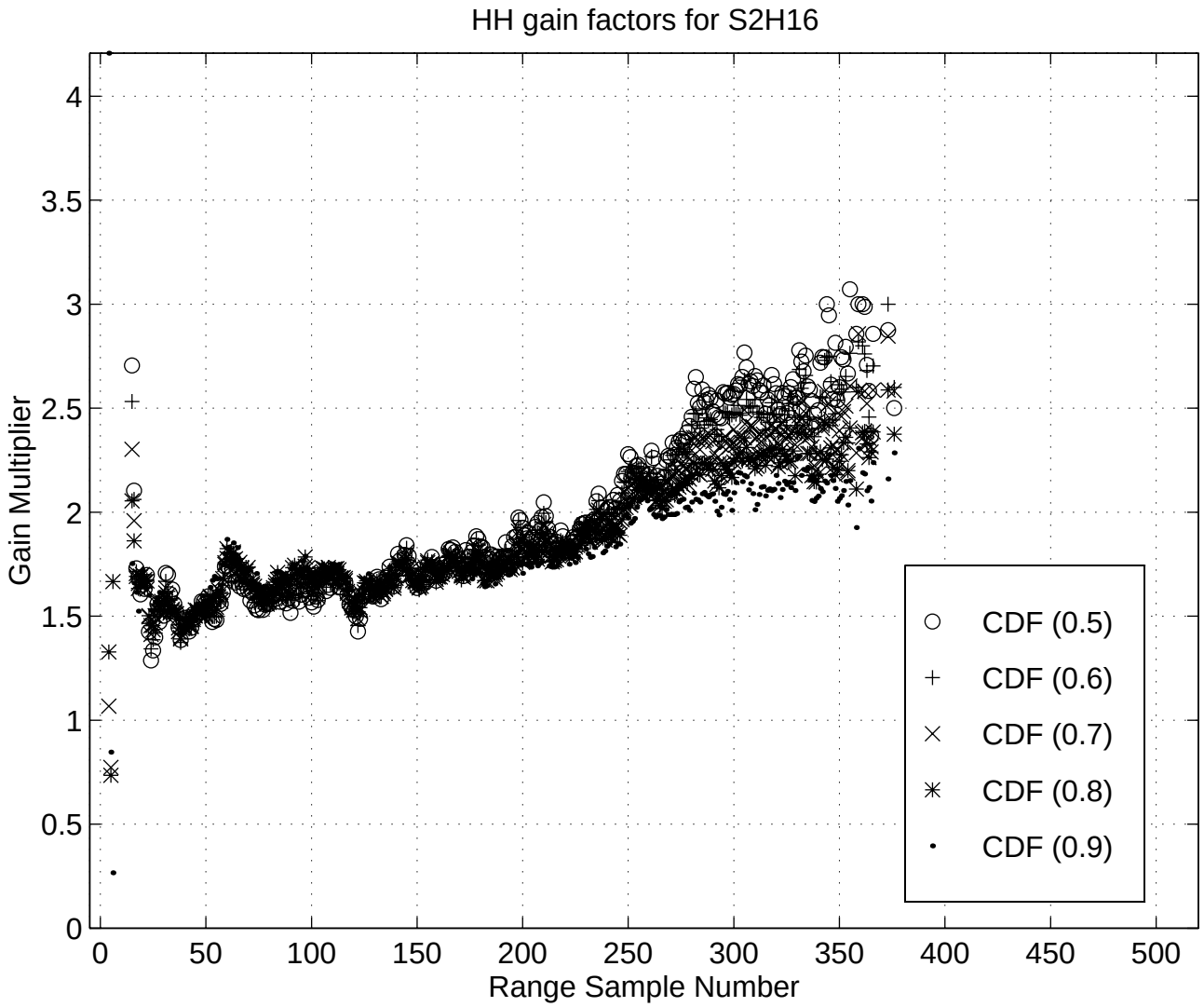

Figure 5-15 Average gain factor at various CDF levels for data sequence S2H16

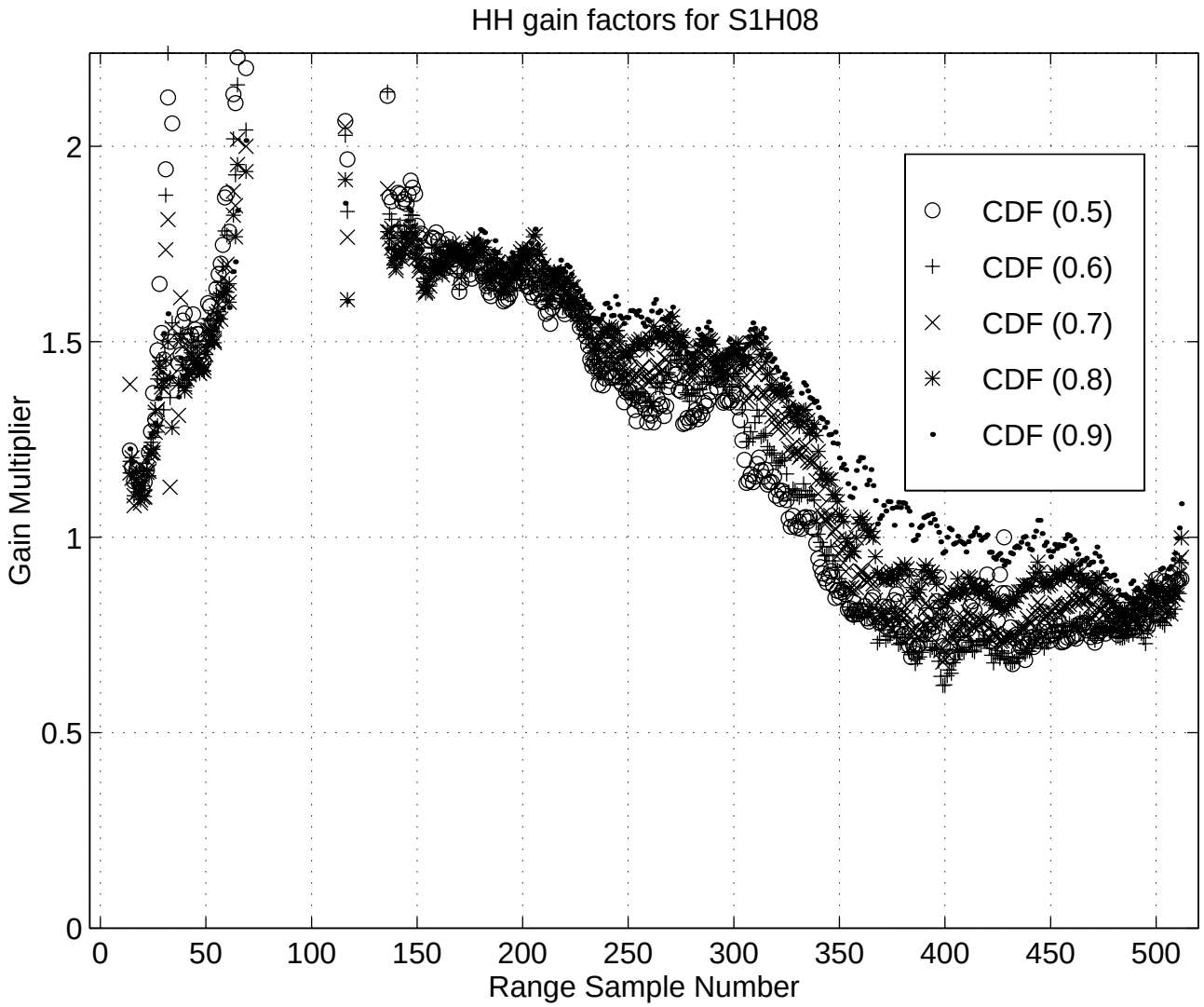

Figure 5-16 Average gain factor at various CDF levels for data sequence S1H08

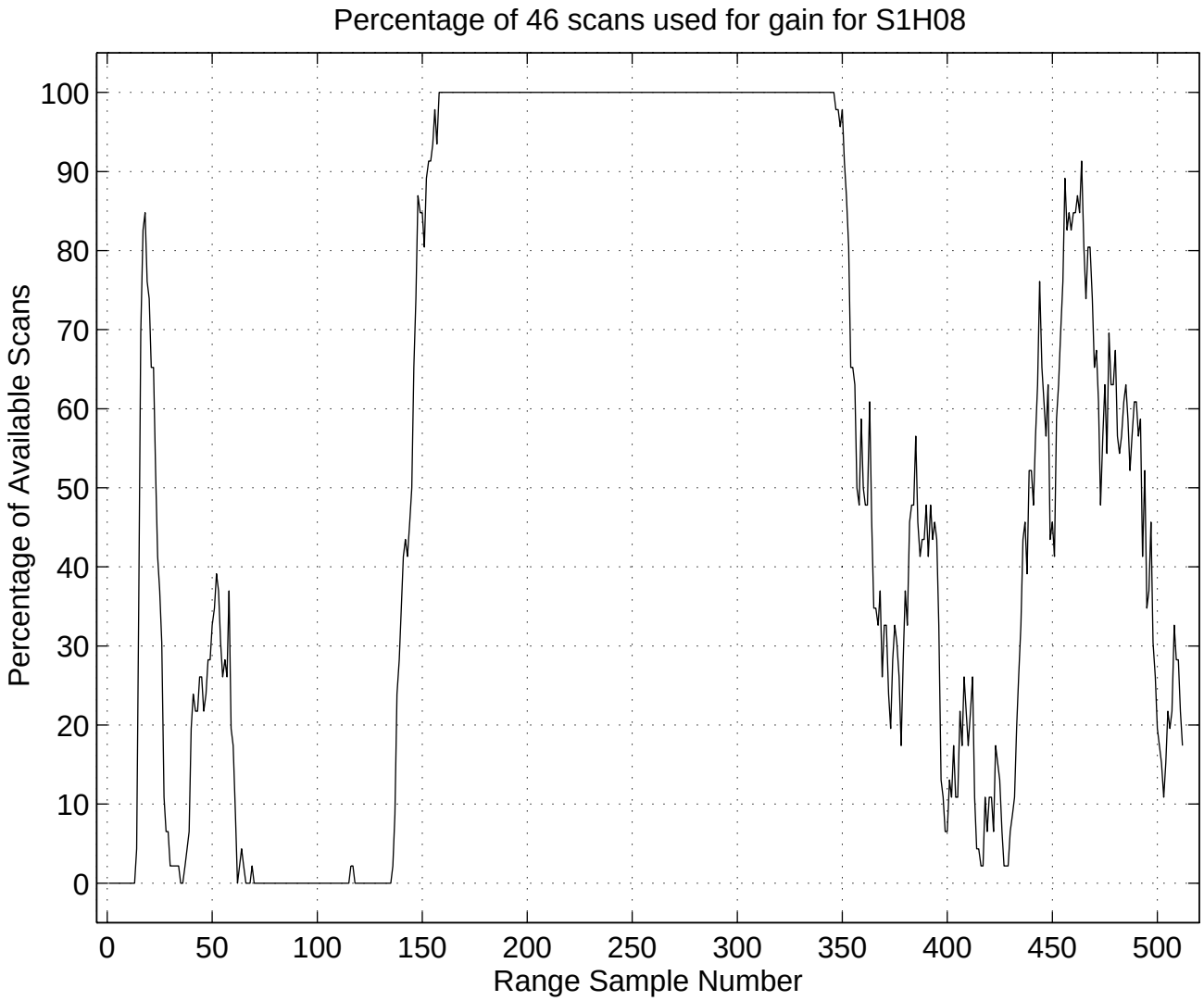

Figure 5-17 Percentage of scans available used in calculating the gain factor for data sequence S1H08

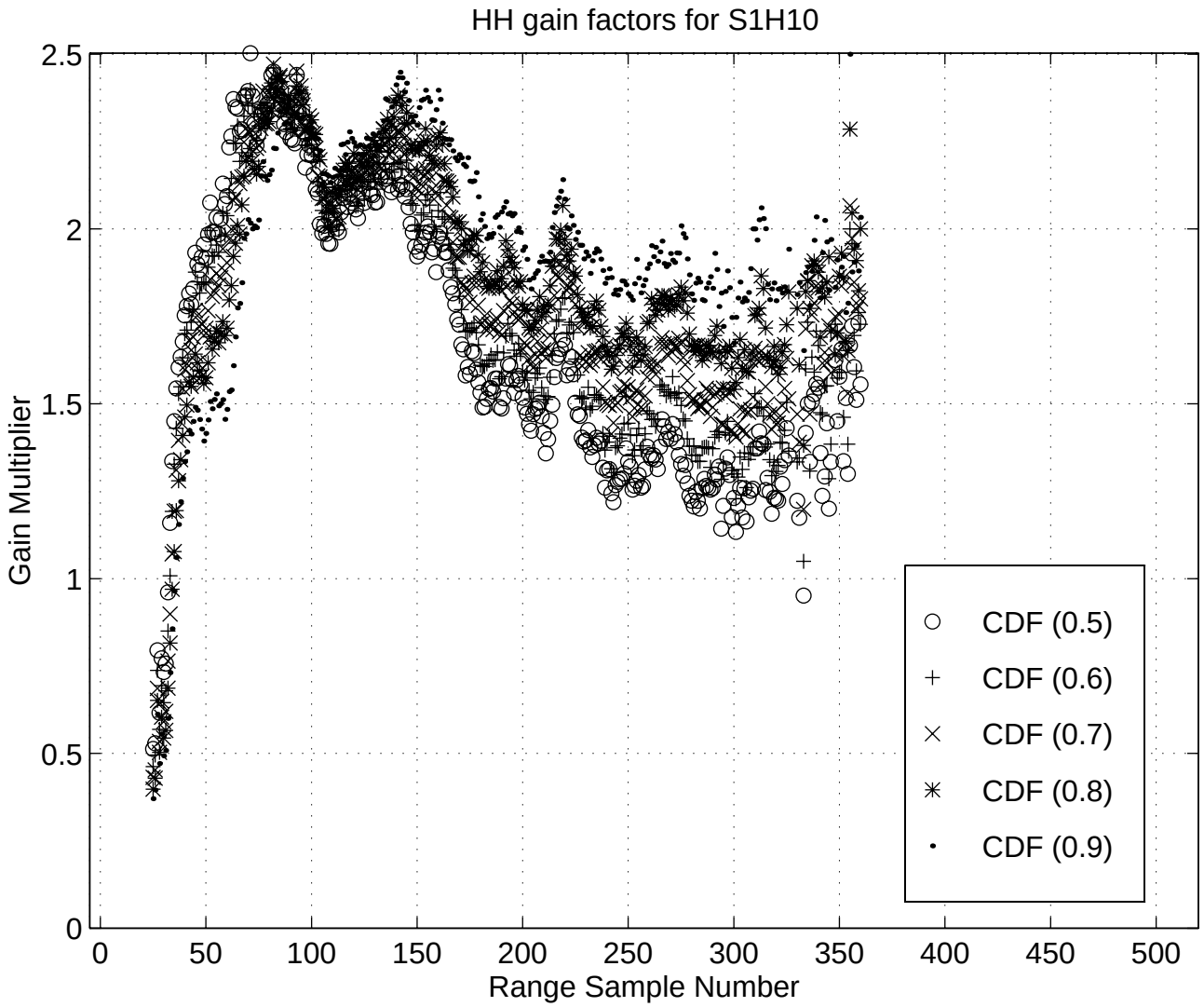

Figure 5-18 Average gain factor at various CDF levels for data sequence S1H10

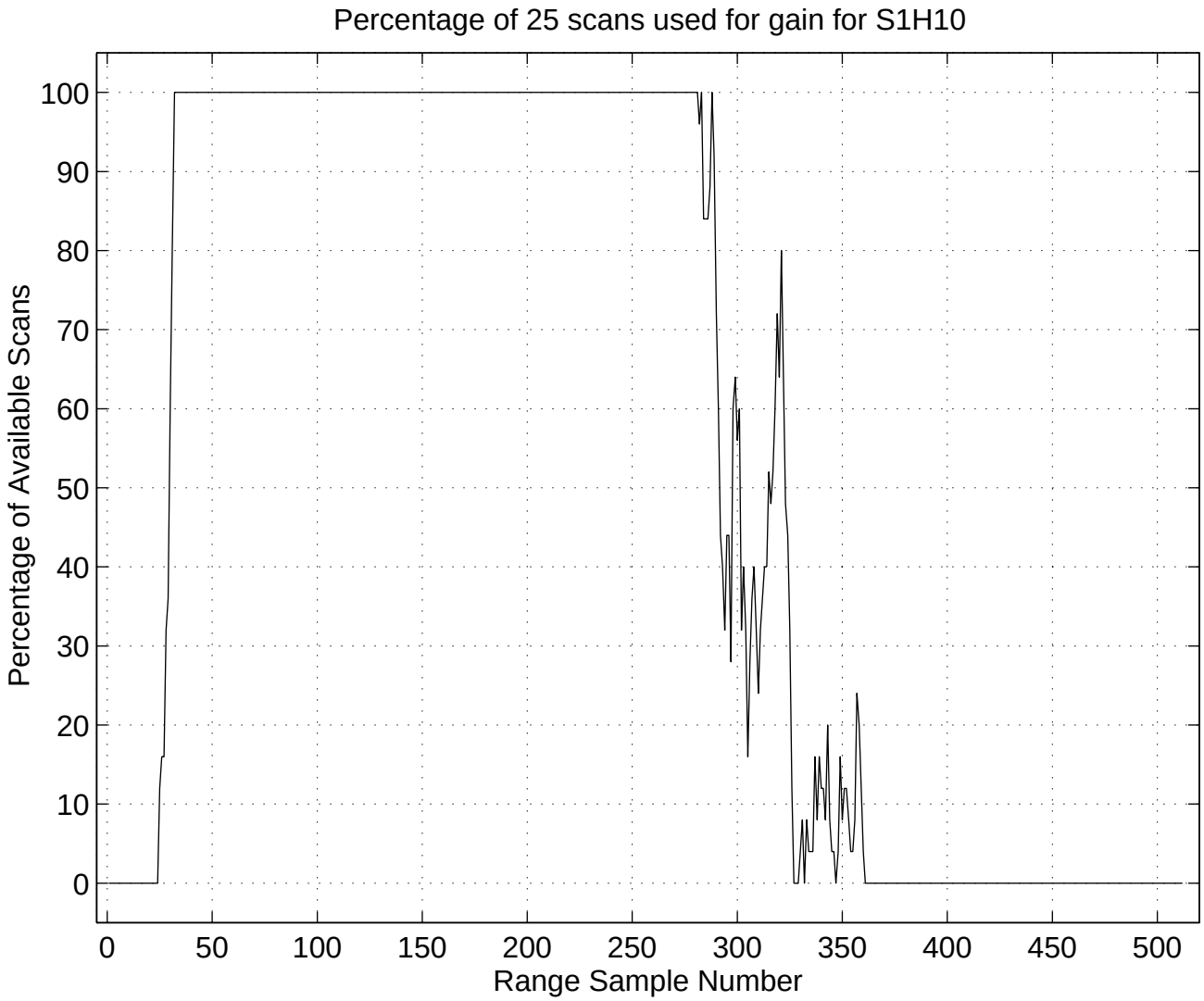

Figure 5-19 Percentage of scans used in calculating the gain factor for data sequence S1H10

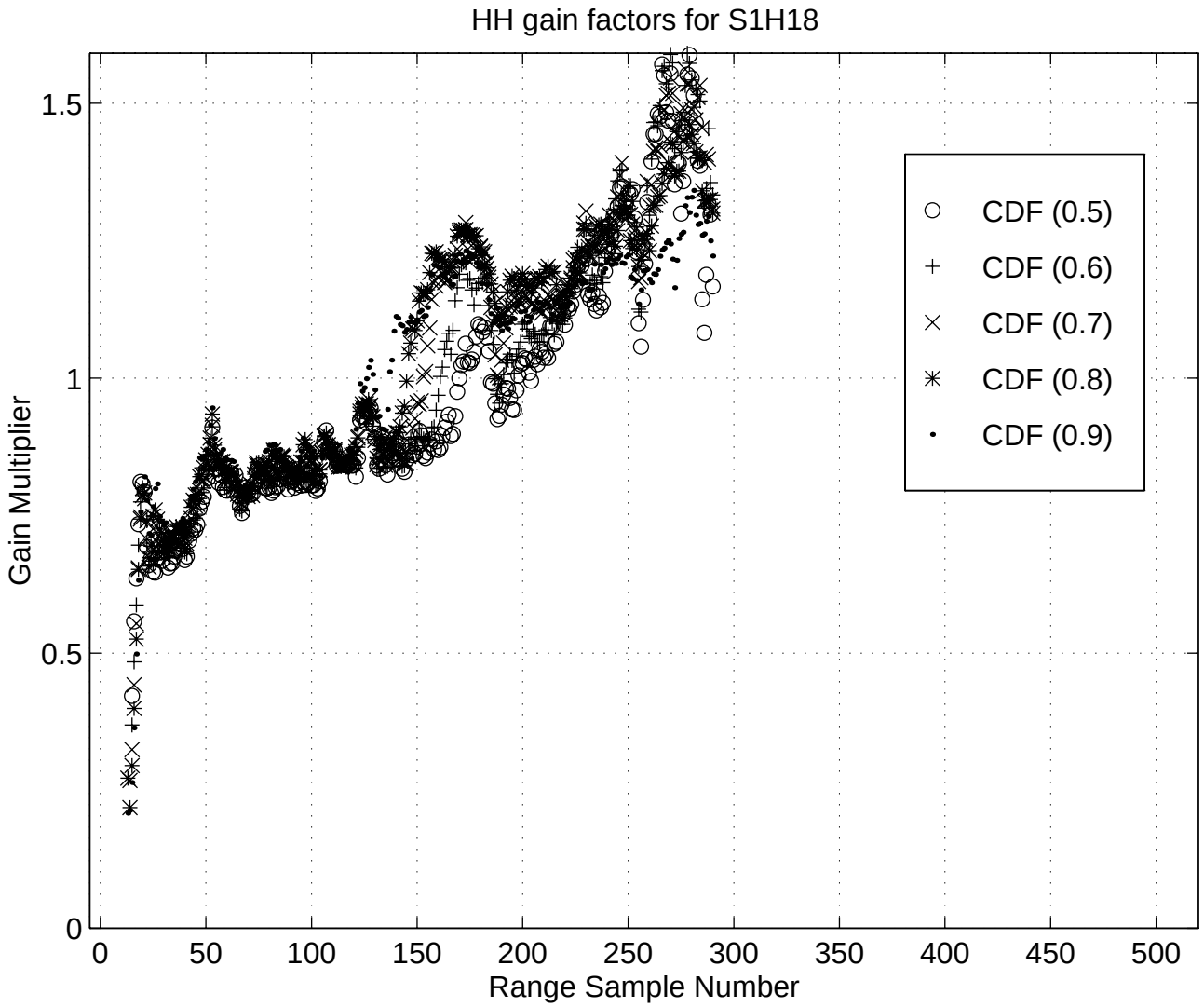

Figure 5-20 Average gain factor at various CDF levels for data sequence S1H18

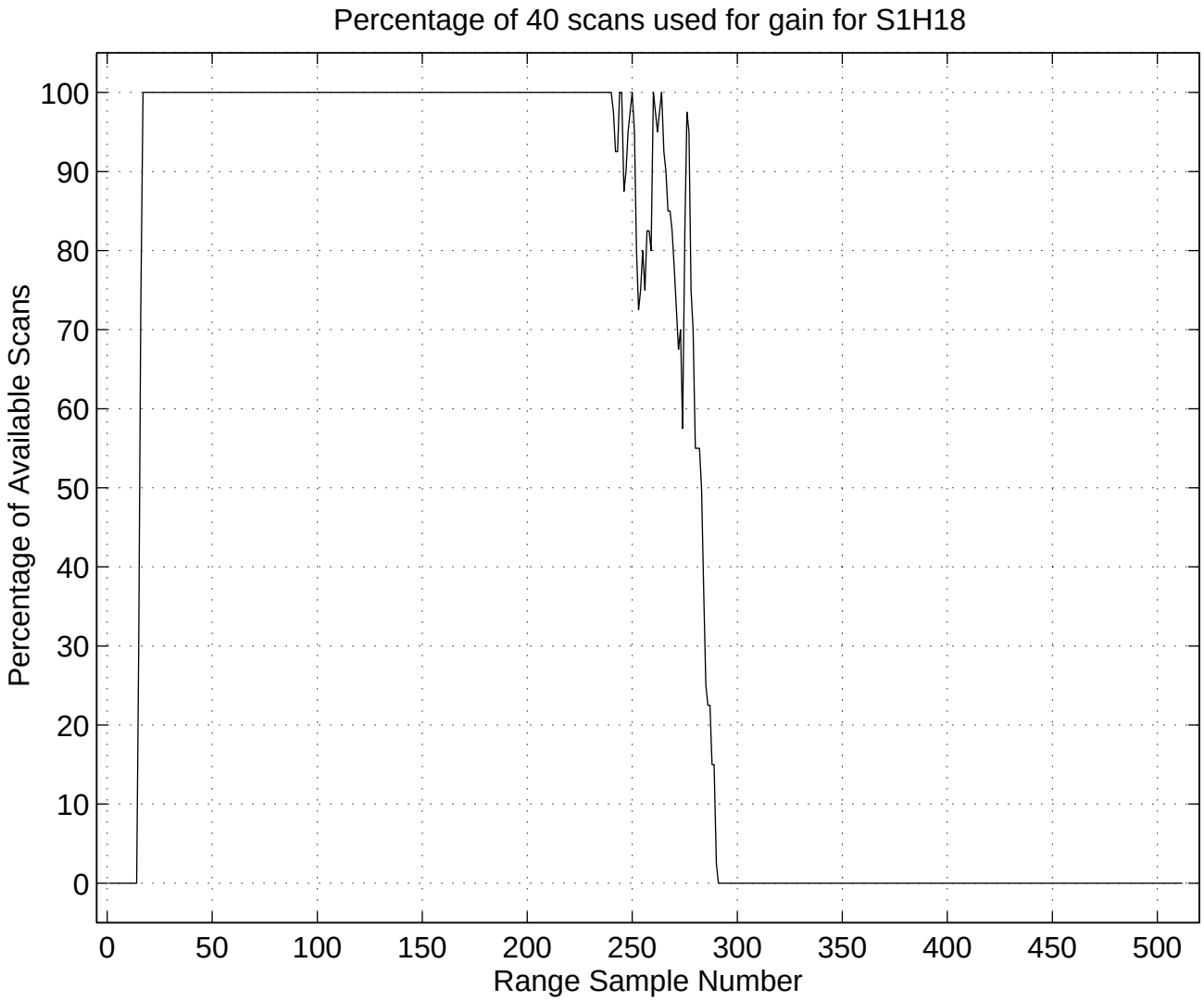

Figure 5-21 Percentage of scans available used in calculating the gain factor for data sequence S1H18

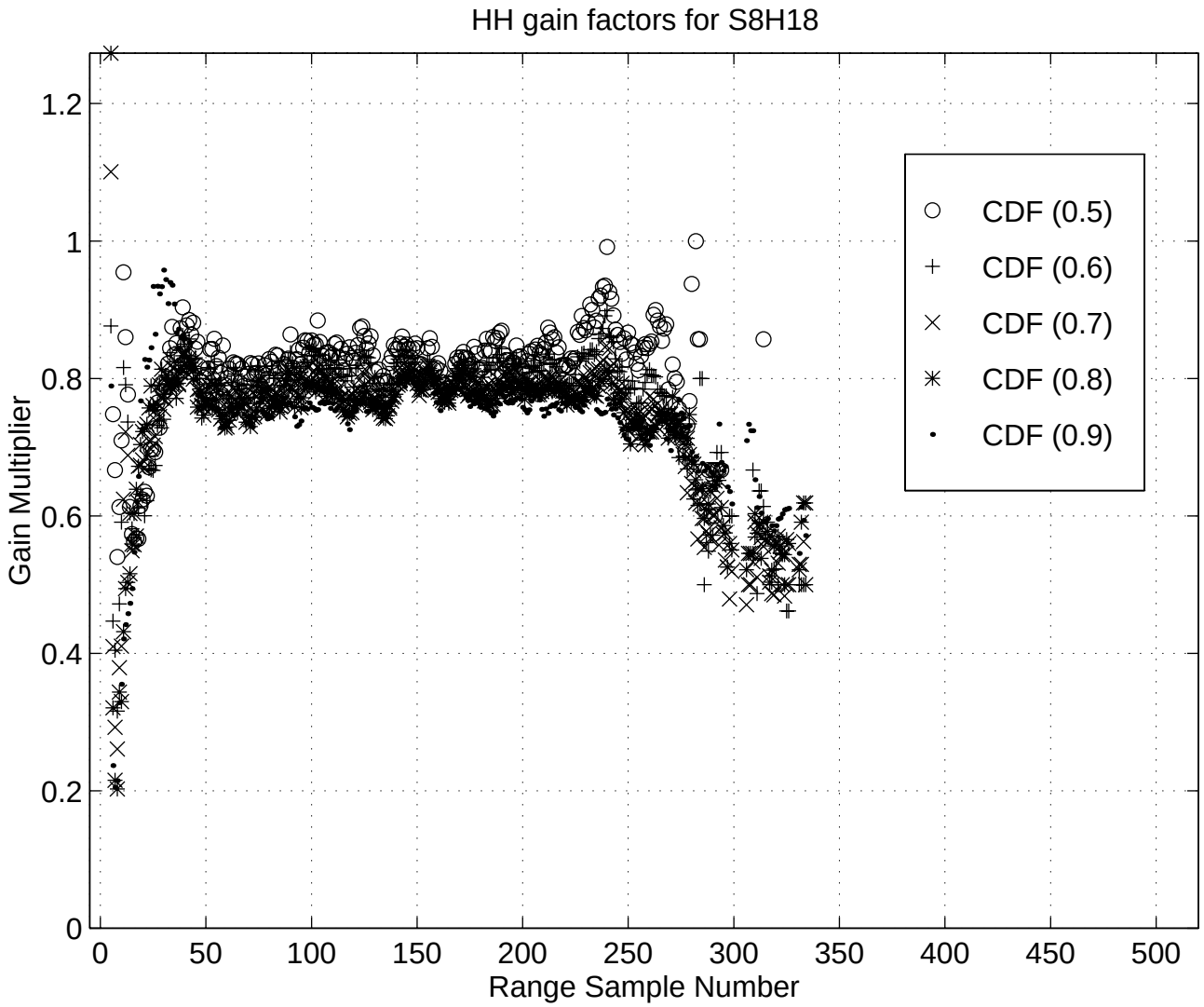

Figure 5-22 Average gain factor at various CDF levels for data sequence S8H18

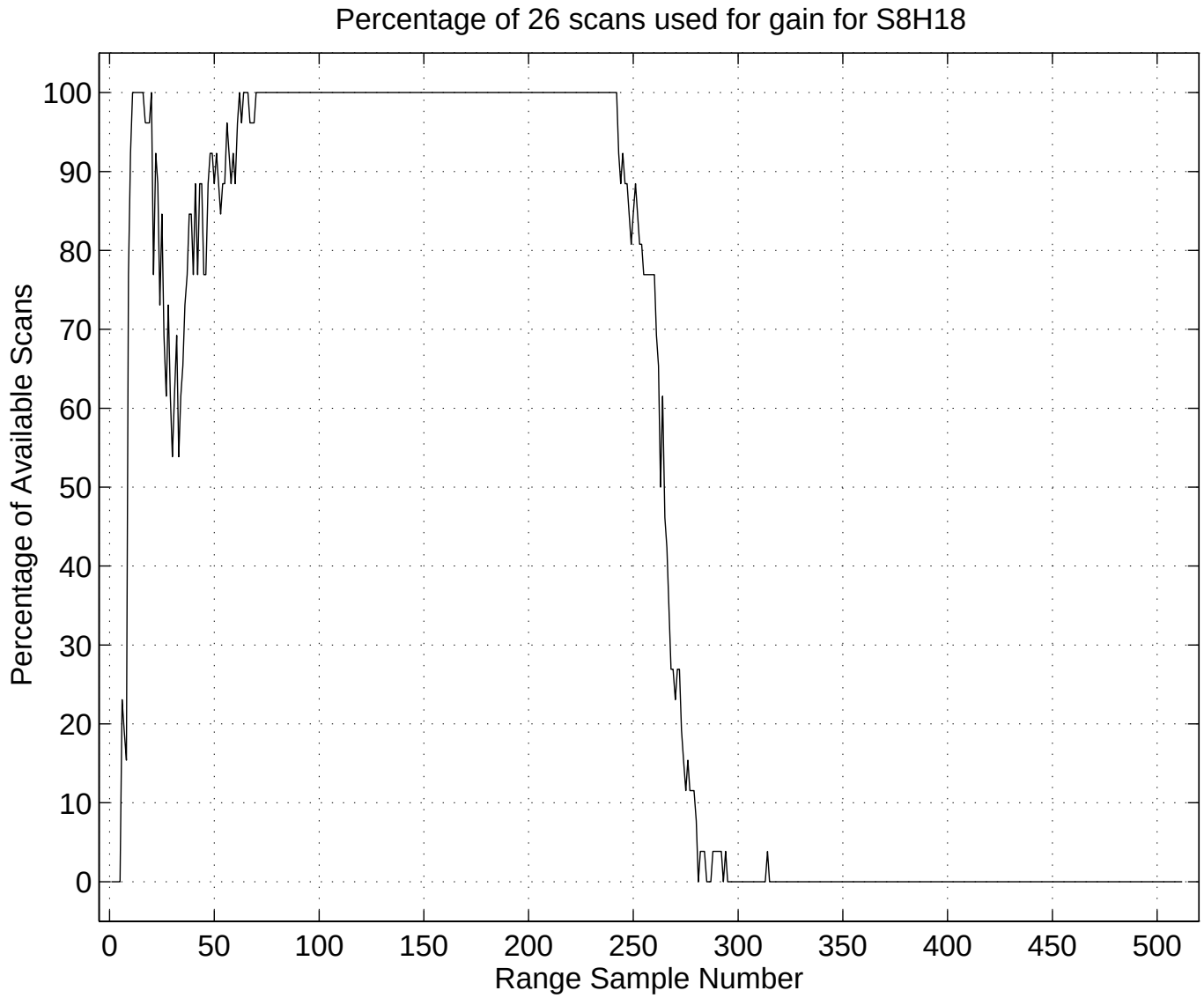

Figure 5-23 Percentage of scans used in calculating the gain factor for data sequence S8H18

Finally, one can visually estimate a gain curve, comprised of linear segments, to be used for the complete data sequence. At ranges for which few or no scans of data are available, the most prudent course seems to be to extend the gain factor from the neighbouring ranges at which better estimates are available. At short and long ranges, constant values are extrapolated. The final estimated gain curves are shown in Figure 5-24 to Figure 5-28. There is some question as to how quickly to let the gain curves vary with range. For example, for S1H10 (Figure 5-18), there is a large but consistent dip in all the gain factors around range 110. Since the spread of the curves was fairly tight, it was felt appropriate to permit the gain to vary to follow this dip. There is not enough data in this

example to know if the change in gain is real, or simply an artifact produced by the nature of the ice environment in that particular data set.

Figure 5-26 shows the gain curve estimated using the complete data sequence S2H16. This curve can be compared to the gain curve estimated earlier using only a single scan pair, shown in Figure 3-26. The curves are essentially the same.

For data set S8H18, the gain factor curves in Figure 5-22 only deviate from 0.8 when fewer than 100% of the scans contribute to the estimate. It was felt most prudent to simply make the gain curve a constant.

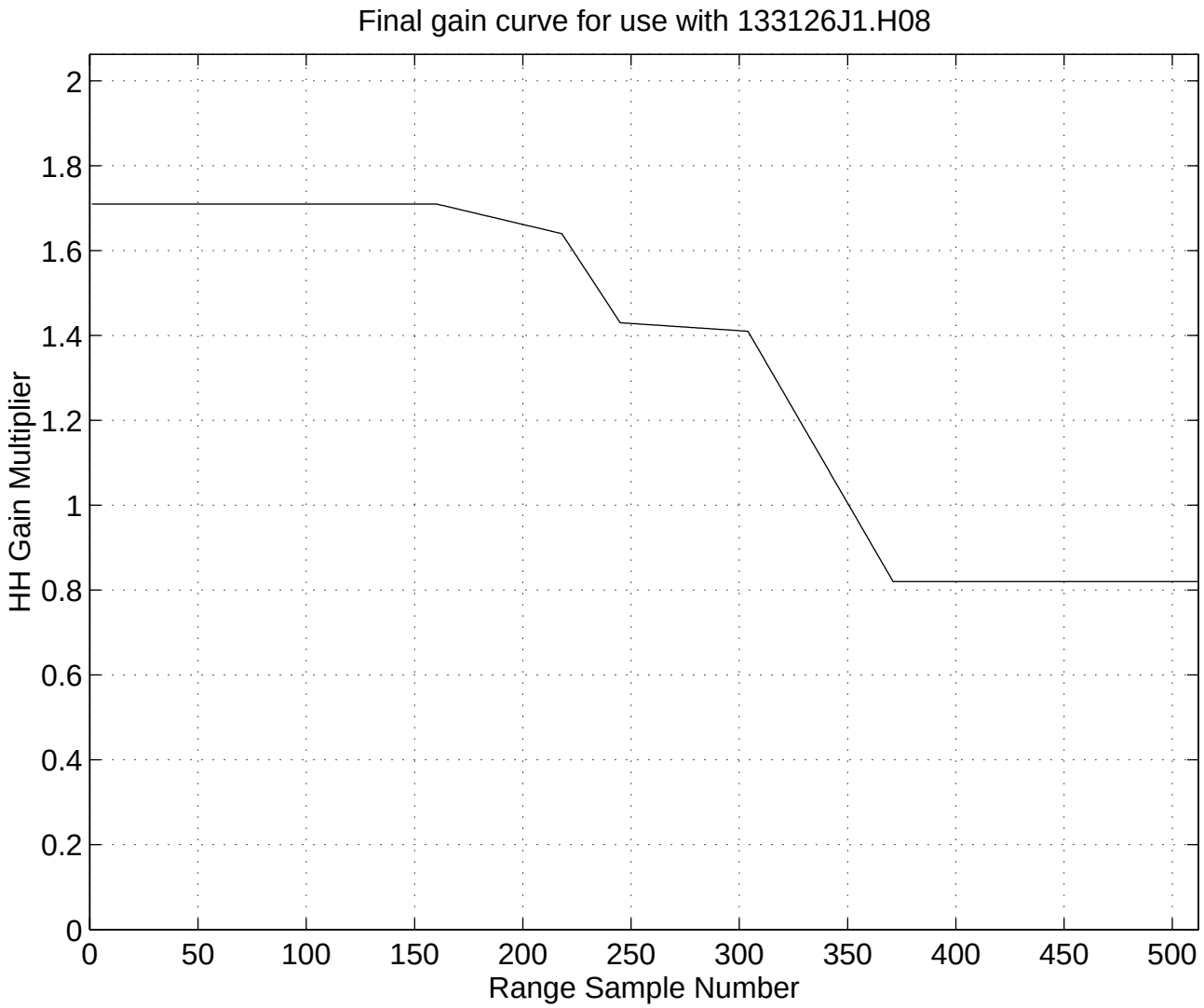

Figure 5-24 Gain factor for use with data sequence S1H08

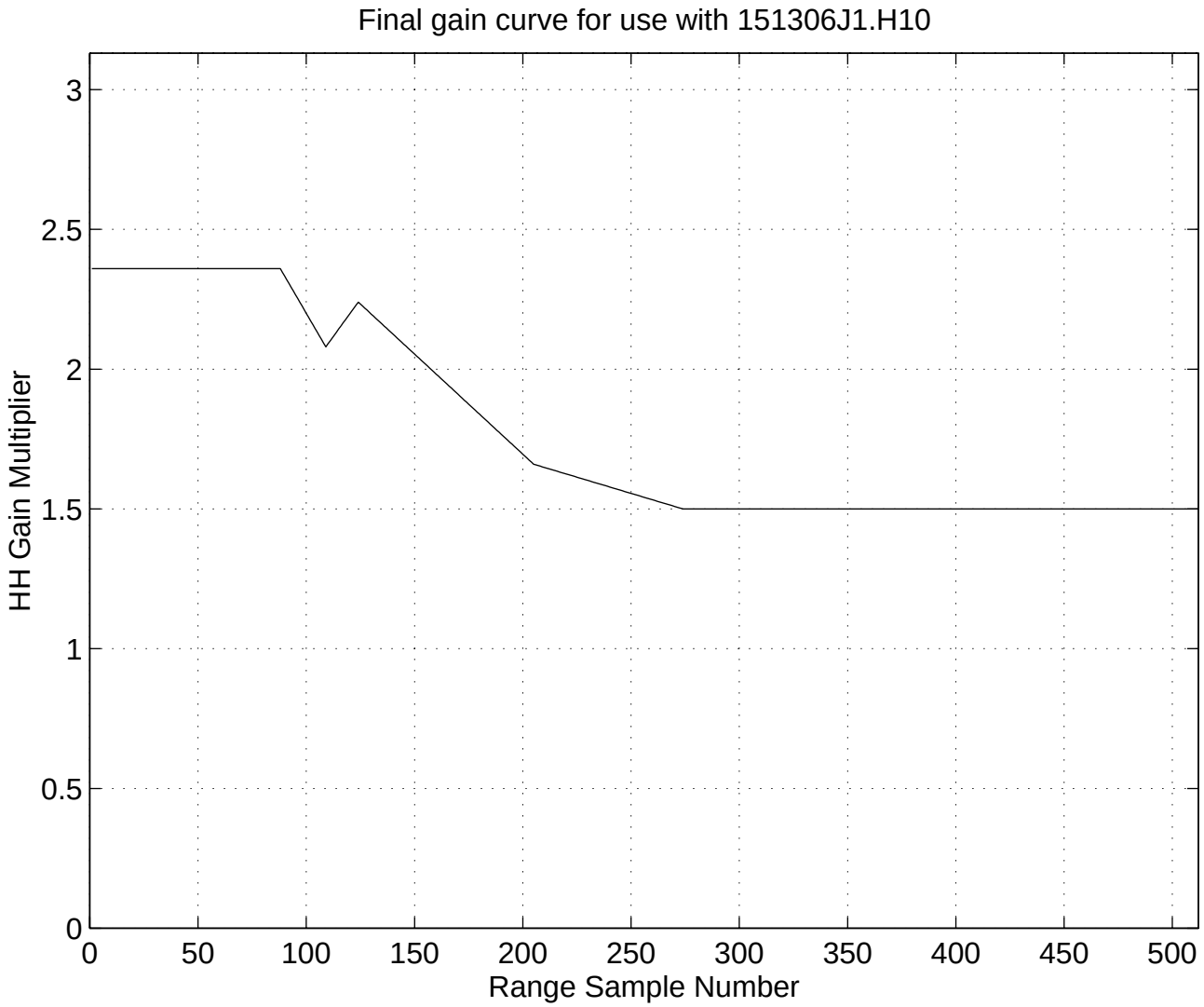

Figure 5-25 Gain factor for use with data sequence S1H10

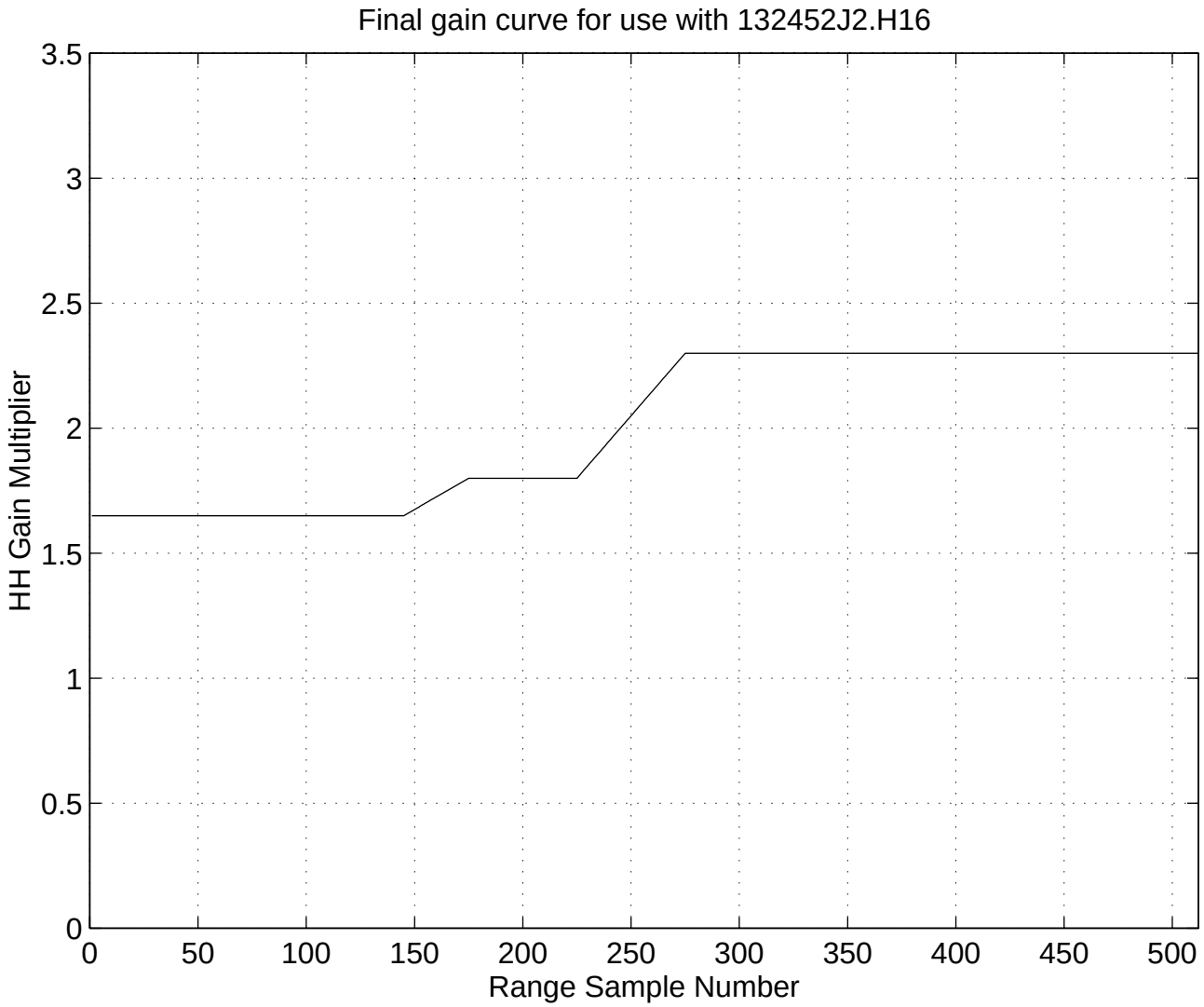

Figure 5-26 Gain factor for use with data sequence S2H16

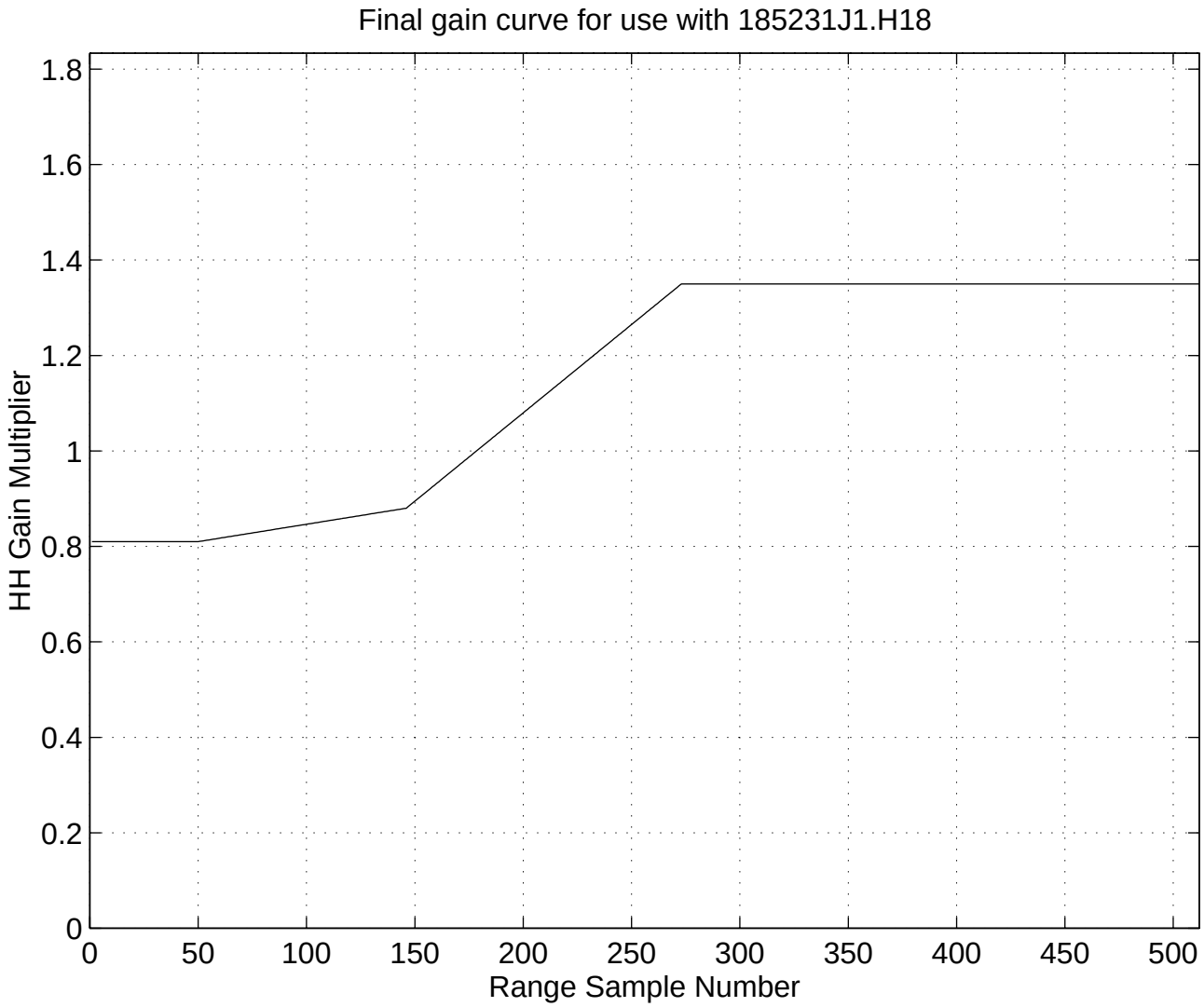

Figure 5-27 Gain factor for use with data sequence S1H18

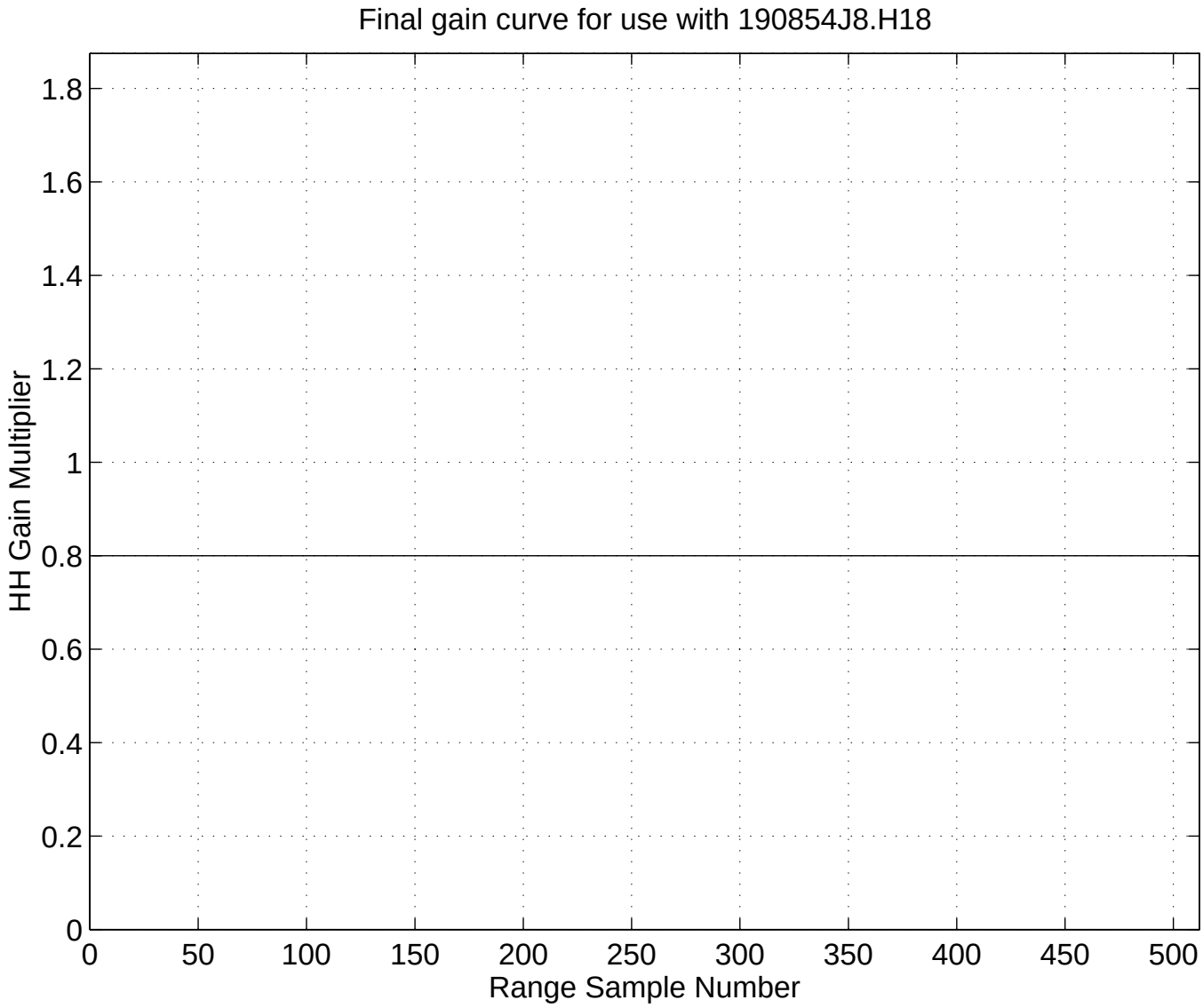

Figure 5-28 Gain factor for use with data sequence S8H18

5.1.1 Effect of Ship Motion

The format of the MRI PPI images is 'north-up', with the radar (i.e. ship) located at the centre. Therefore as the ship makes forward progress, the content of the radar image from scan to scan appears to be shifting past the image centre, in the opposite direction to the ship's heading. To estimate the ship's motion from a series of scan images, portions of the image were compared over a number of scans to estimate the displacement. More specifically, four image portions were chosen, each 100 pixels in X by 100 pixels in Y, one located in each of the four quadrants of the image. All portions were centred at a

range of 127 pixels, and bearings of 45^o (quadrant 1), 135^o (quadrant 2), 225^o (quadrant 3), and 315^o (quadrant 4). Using a series of N HH scans in a sequence, a pair of images numbered n and n+d were compared in each quadrant, then image pair n+d and n+2d, etc. The shift in X and Y between each pair of images was estimated by performing a two-dimensional correlation, and locating the peak. Initially, a separation d=1 was used. Often, however, the shift appeared to be a fraction of a pixel, which was then quantized to 0 or 1, leading to under or overestimating the shift. By changing to a value of d=8, more stable and accurate estimates were obtained. In the case of S1H08, a value of d=2 was better because of the small range scale.

By plotting the successive offsets in X and Y calculated over the series of scans, an estimate of the ship's heading can be made. For example, Figure 5-29 shows a plot of the cumulative X and Y offsets as compared to the first scan in the data set S2H16. Since the data points suggest a constant heading, fitting a line to the data can provide an estimate of the ship's heading. In this case the ship is heading toward the lower left. Therefore a time lapse of the scans in the sequence shows the image content appearing to shift upward to the upper right as the ship (image centre) moves downward to the lower left. The heading estimated from the fitted line is about 230^o. The data collection log kept during the voyage noted the heading as 231^o.

The cumulative offsets can also be used to estimate the distance traveled by the ship. The range, relative to the first scan of the sequence, can be estimated in pixels as $\text{sqrt}(\Delta X^2+\Delta Y^2)$. The header associated with each 'S' data file contains a 'range' variable, which gives the distance in nautical miles represented by each sample (pixel) in the image. Multiplying the range in pixels by this scale factor gives the distance travelled in nmi. Each image is time stamped (in its file name), so that the range travelled between images can plotted vs. time. Figure 5-30 shows the plot for data set S2H16. Here again the data points suggest a fairly constant speed, permitting the fitting of a linear line. The slope of the line gives the distance (in pixels) travelled per second. Multiplying by the range scale factor, and 3600 sec/hour, provides an estimate of the ship's speed in knots. The experimental log did not record a specific speed for S2H16. The ship was breaking ice and the speed was variable.

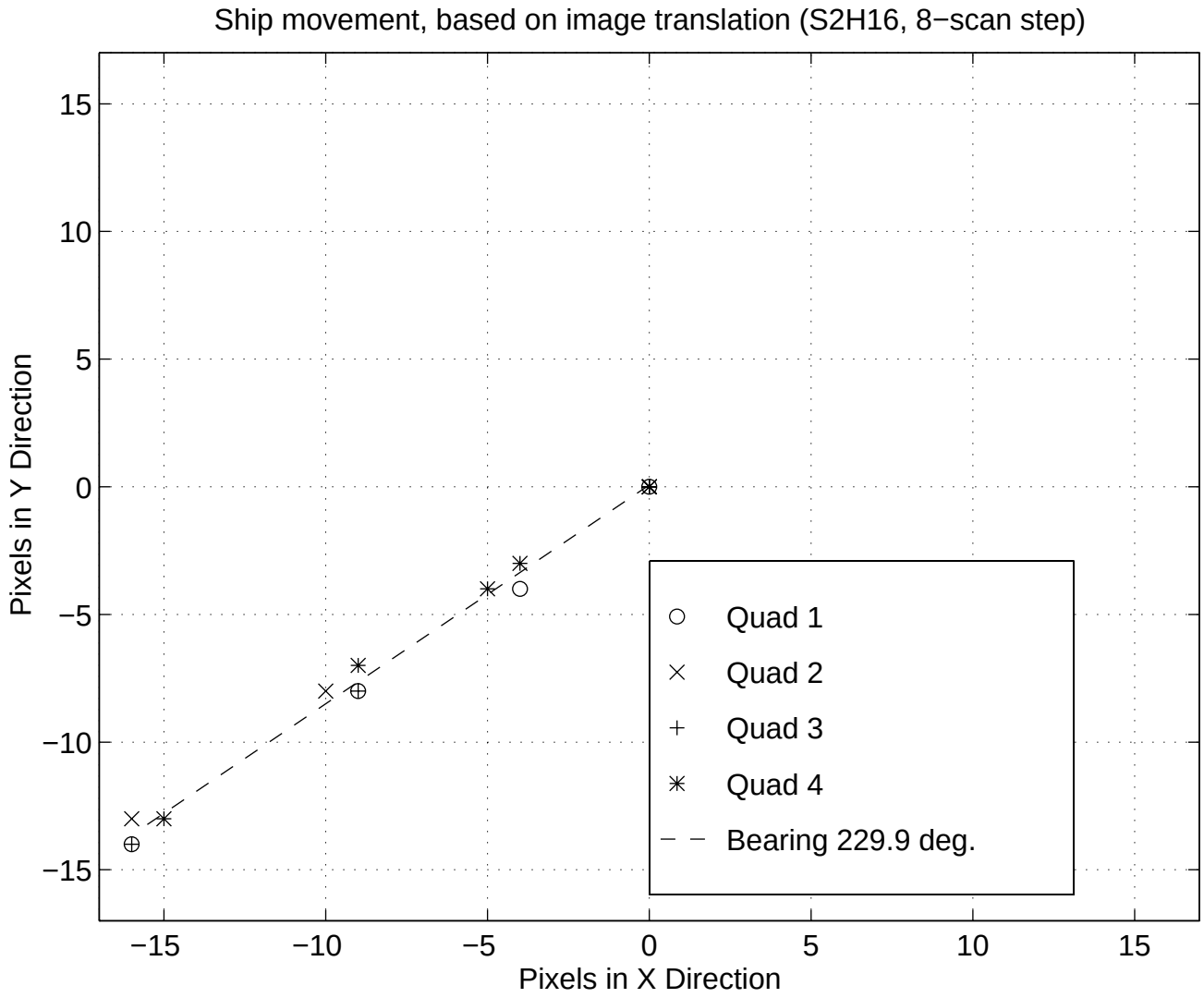

Figure 5-29 Cumulative X and Y offsets for data sequence S2H16. Fitted line provides an estimate of the ship's heading.

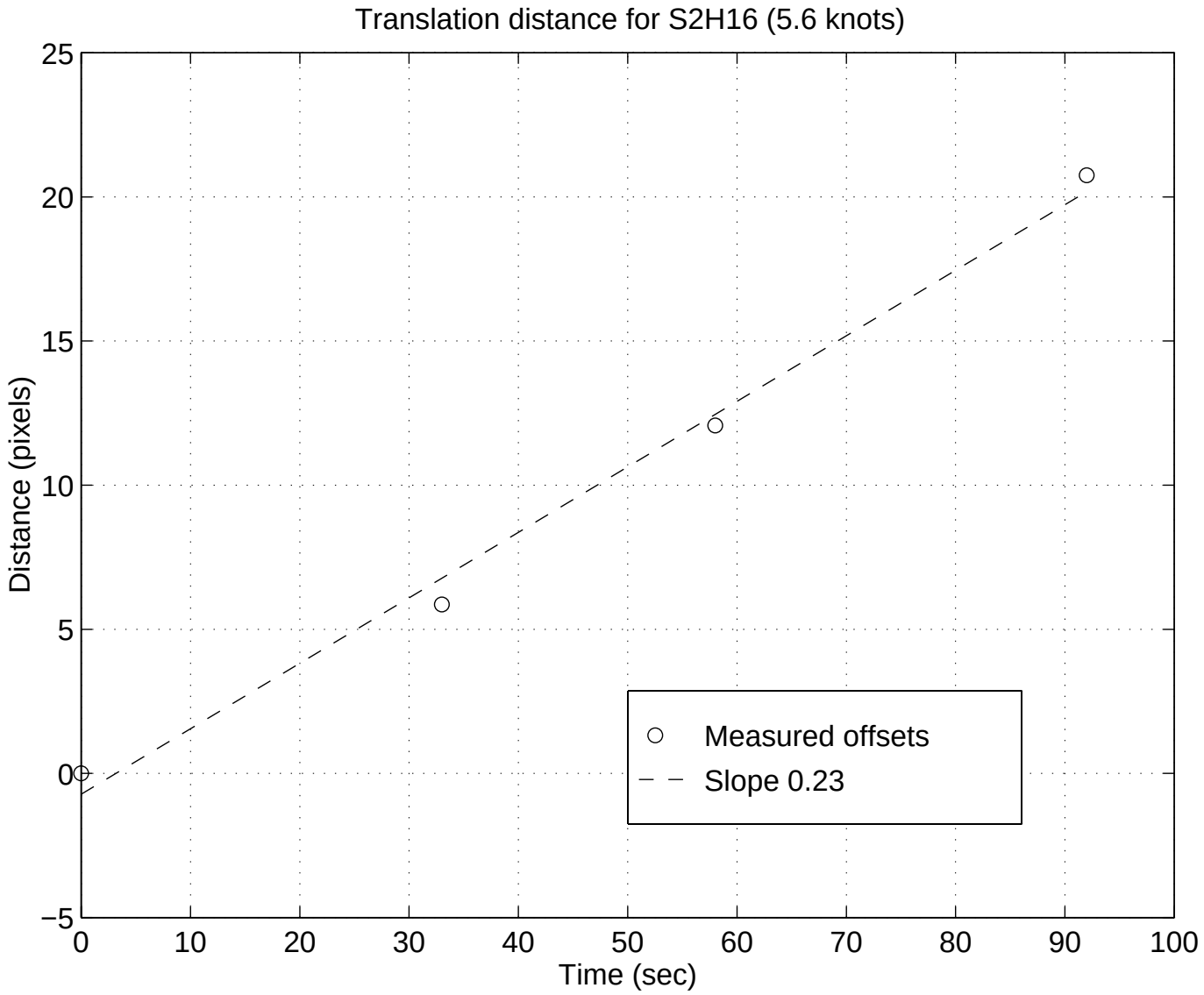

Figure 5-30 Cumulative distance, in pixels, traveled in data sequence S2H16 vs. elapsed time, taken from the timestamps. Fitted line estimates speed in pixels per second, which is then scaled to knots using the PPI range parameter.

Figure 5-31 to Figure 5-38 shows similar results for the other 4 data sequences. The resulting estimates of ship speed and heading are summarized in Table 5-1. The results agree well with data obtained from the experimental log.

All of the above estimates of ship speed and heading were derived from the HH data sequences. The fact that the headings agreed well with the logs suggests that the images were correctly north-up oriented. Visual inspection showed that HH and HV images for S1H08, S1H10, and S2H16 were similarly oriented. However, in data sequences S1H18 and S8H18, the HV images are rotated in azimuth with respect to the HH images. Using

two-dimensional correlation, this offset was determined to be approximately 68 digital azimuths, about (68/2048)*360 = 12^{o}. The cause of this offset has not been determined. It may be related to the gyro signal fed to the HV MRI. Before comparing the images for S1H18 and S8H18, the HV images must be appropriately rotated in azimuth.

From a visual inspection of the S8H18 images during the image correlation process, it appeared that the HV images exhibited some azimuthal smearing as compared to the HH images. This data set was for a scan integration setting of 4. It appears as if the registration of the multiple HV images prior to scan integration was not as good as it was for the HH channel. Again this could be gyro related.

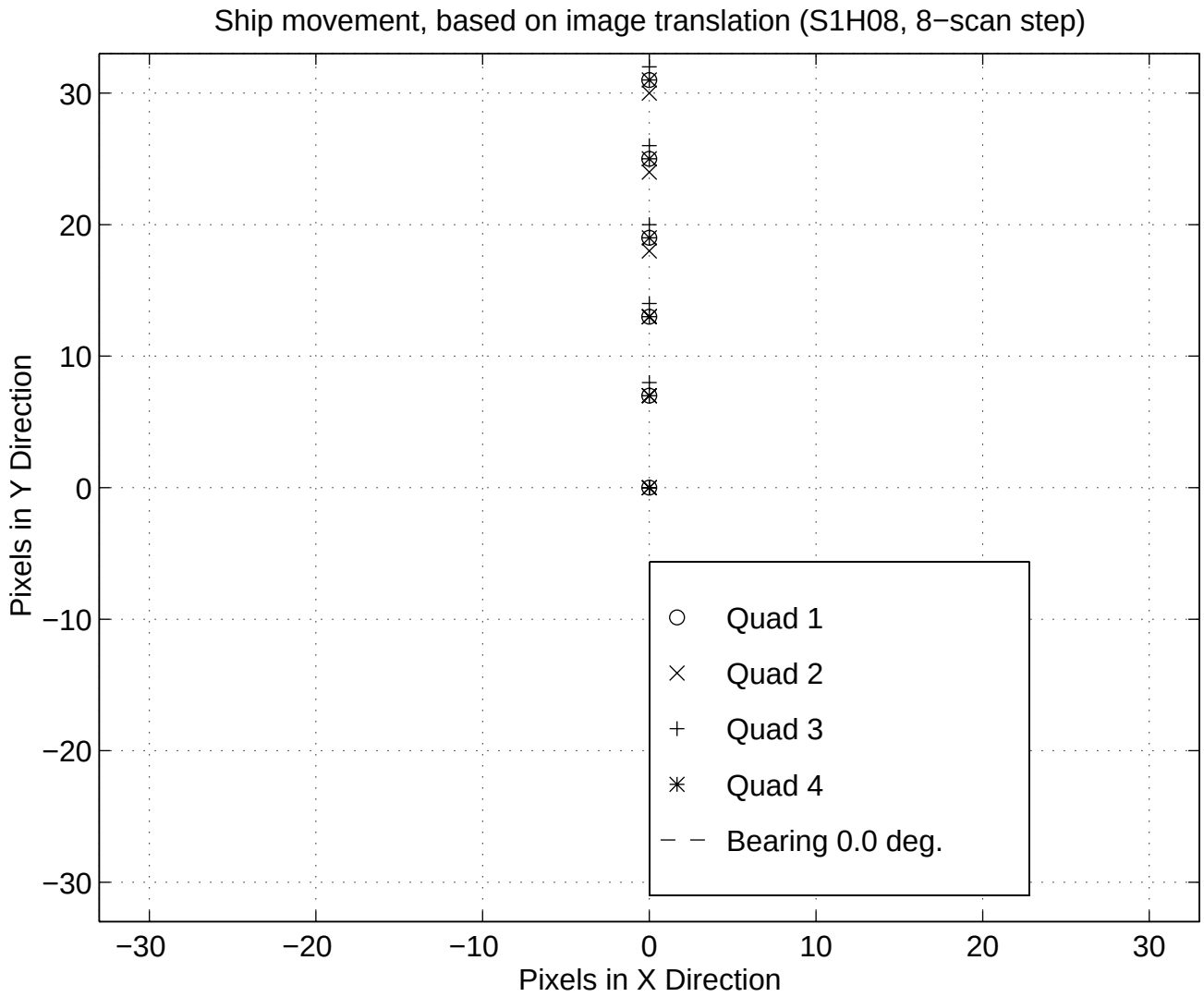

Figure 5-31 Cumulative X and Y offsets for data sequence S1H08. Fitted line provides an estimate of the ship's heading.

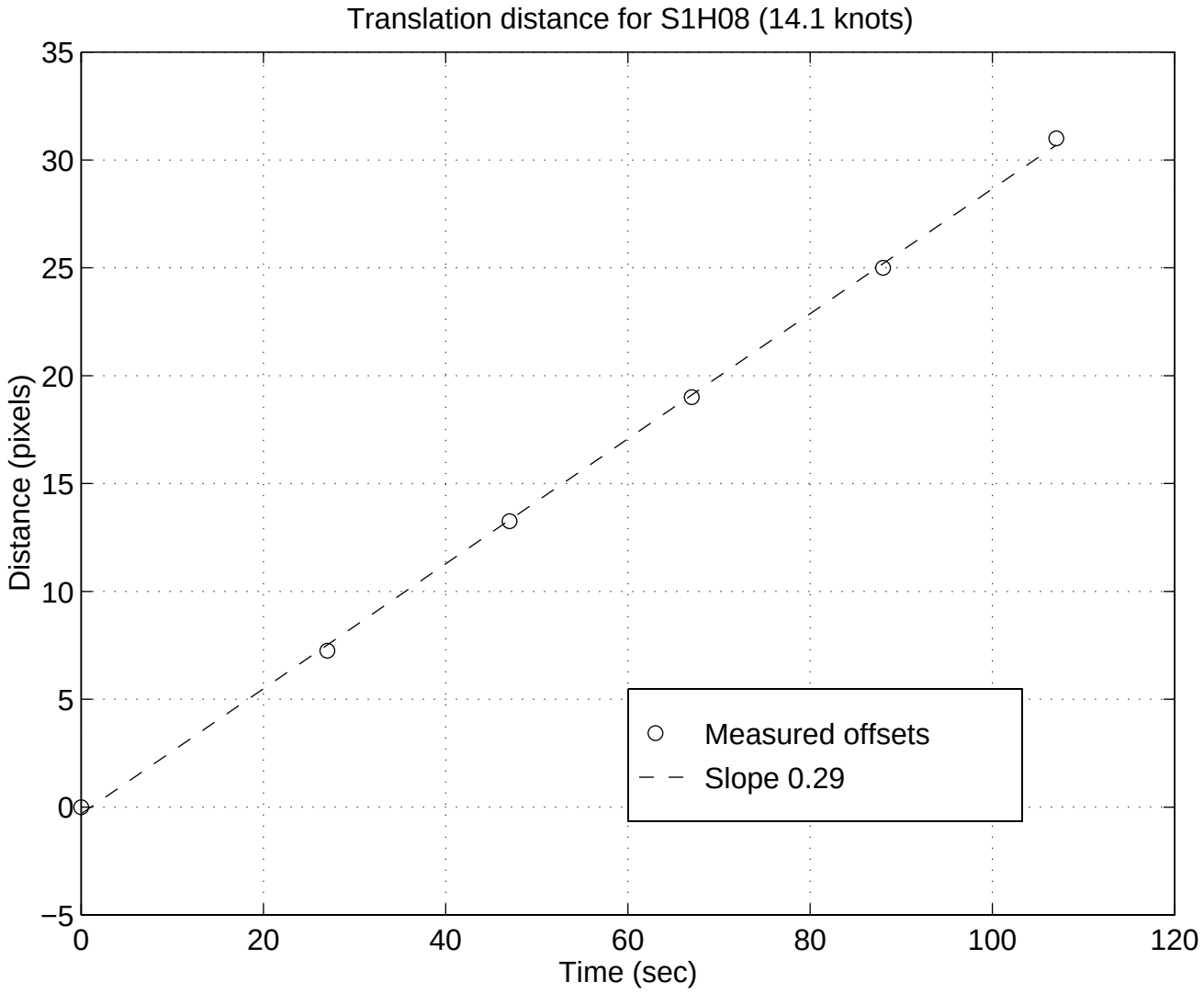

Figure 5-32 Cumulative distance, in pixels, travelled in data sequence S1H08 vs. elapsed time, taken from the timestamps. Fitted line estimates speed in pixels per second, which is then scaled to knots using the PPI range parameter.

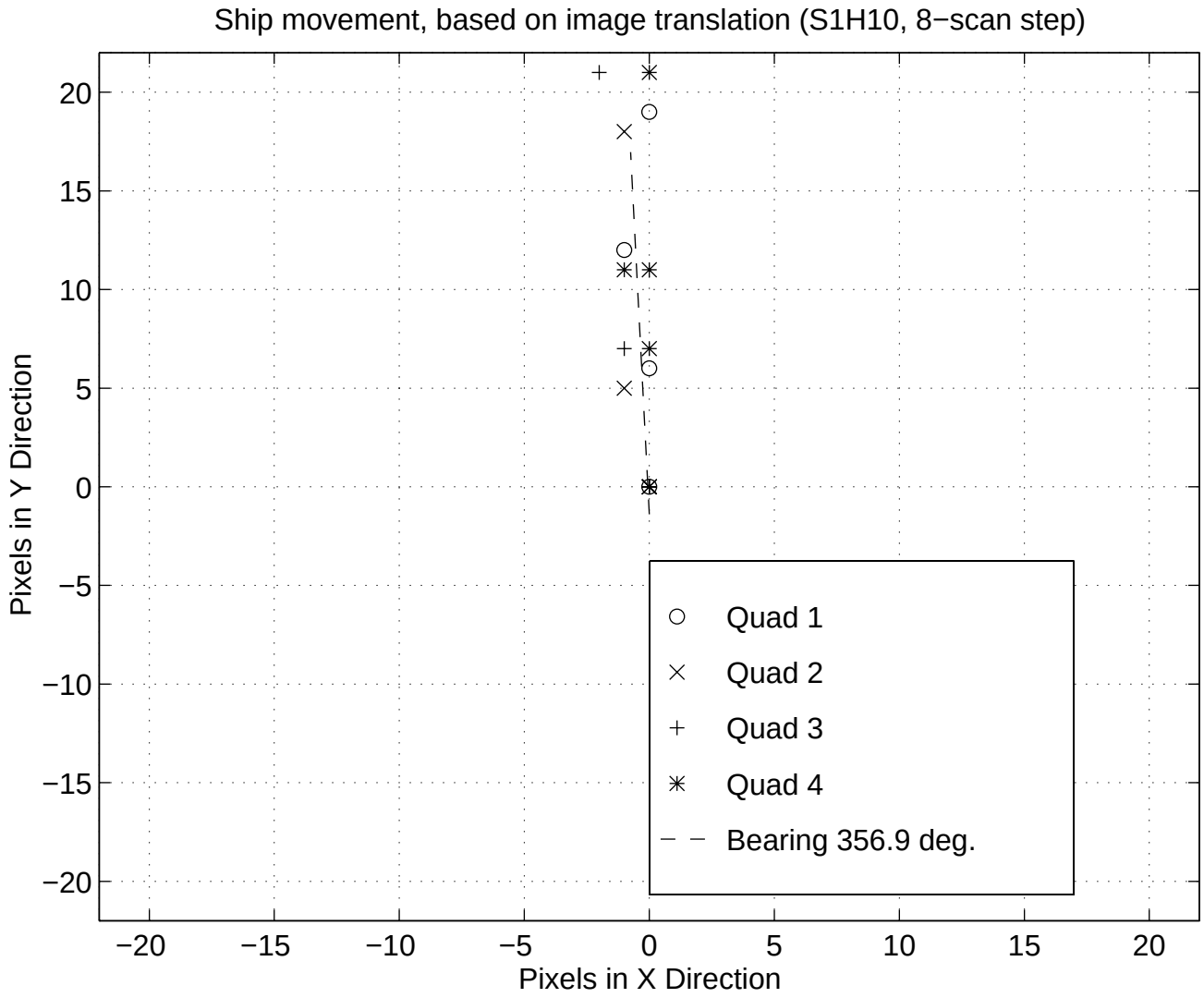

Figure 5-33 Cumulative X and Y offsets for data sequence S1H10. Fitted line provides an estimate of the ship's heading.

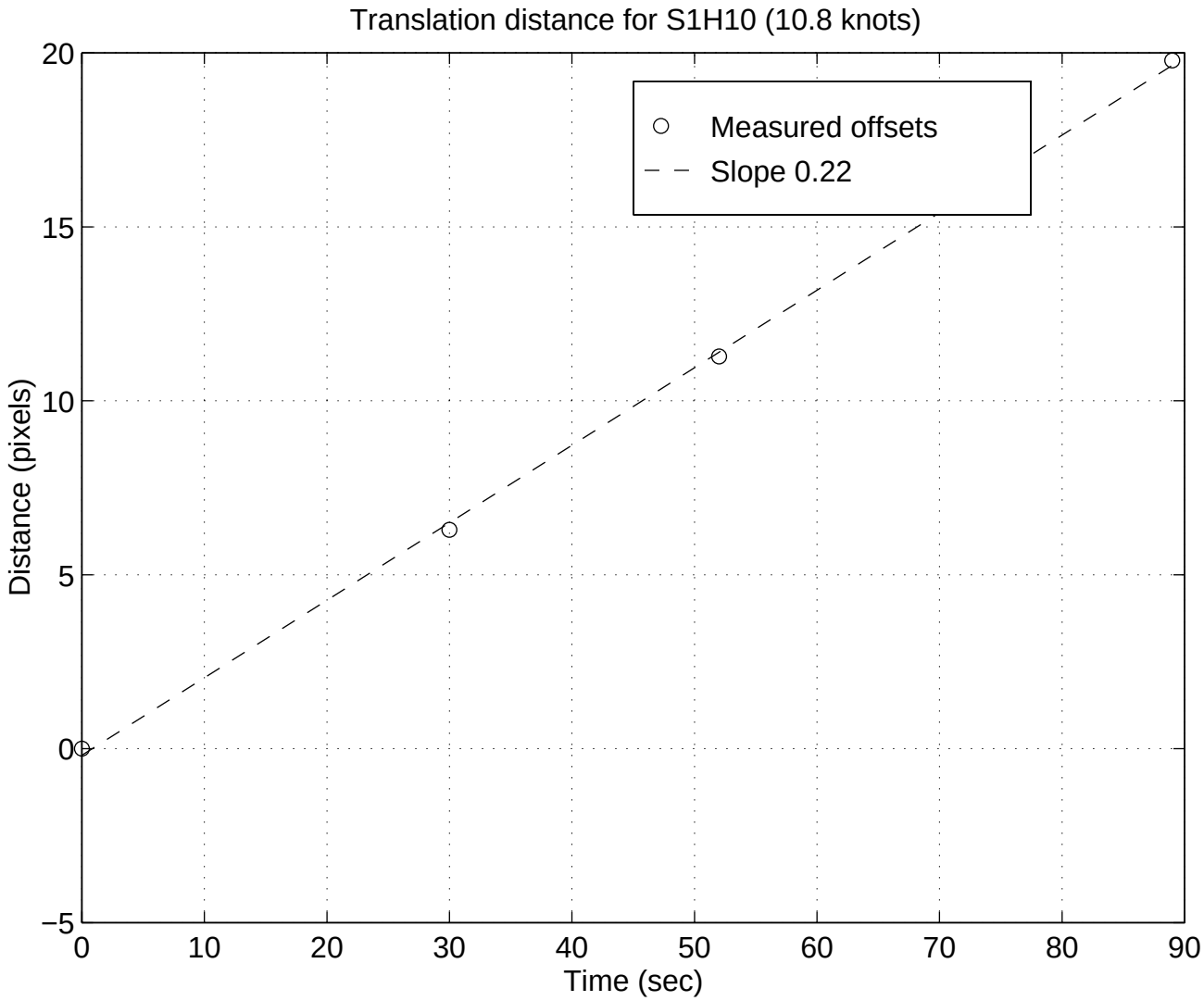

Figure 5-34 Cumulative distance, in pixels, travelled in data sequence S1H10 vs. elapsed time, taken from the timestamps. Fitted line estimates speed in pixels per second, which is then scaled to knots using the PPI range parameter.

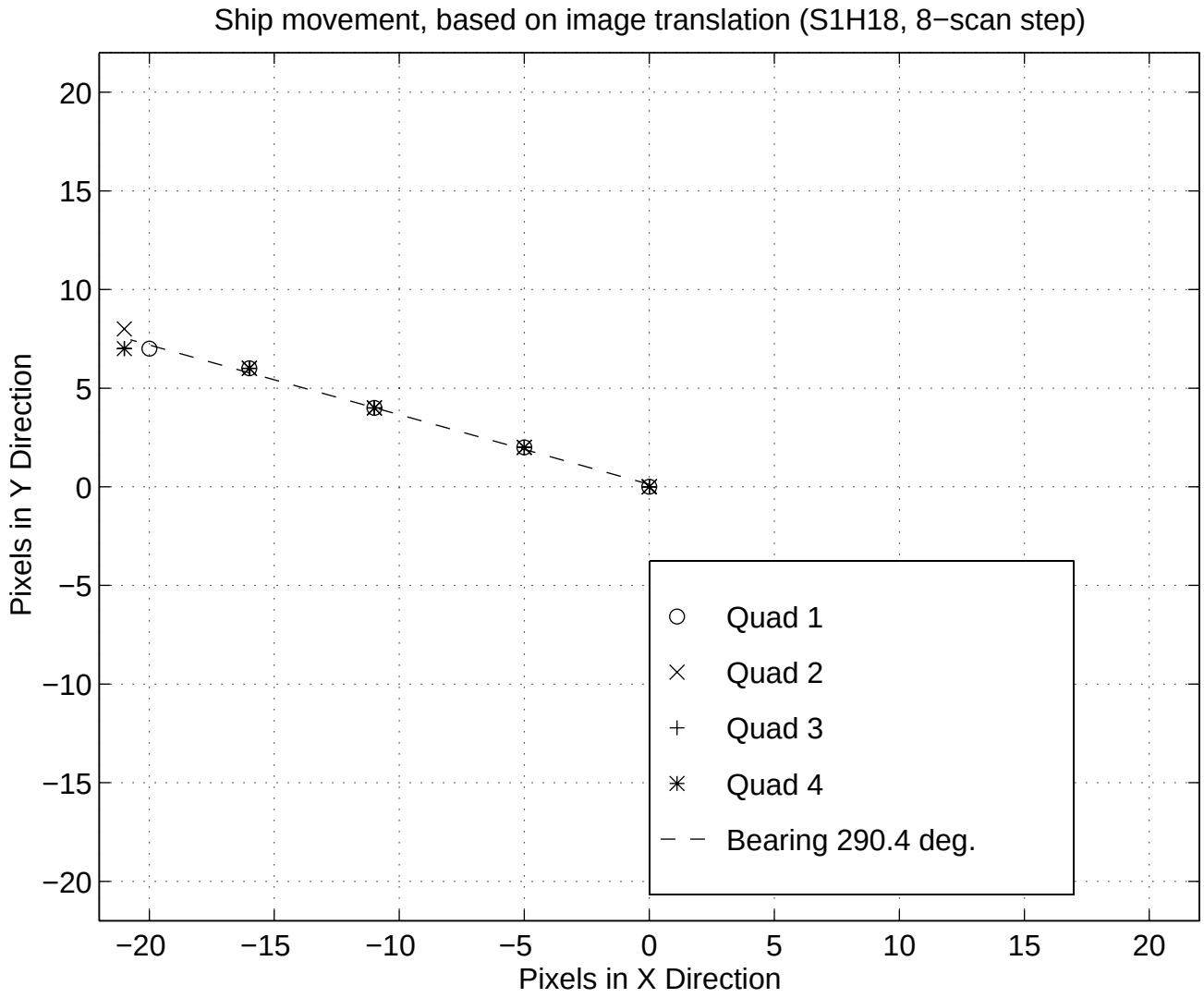

Figure 5-35 Cumulative X and Y offsets for data sequence S1H18. Fitted line provides an estimate of the ship's heading.

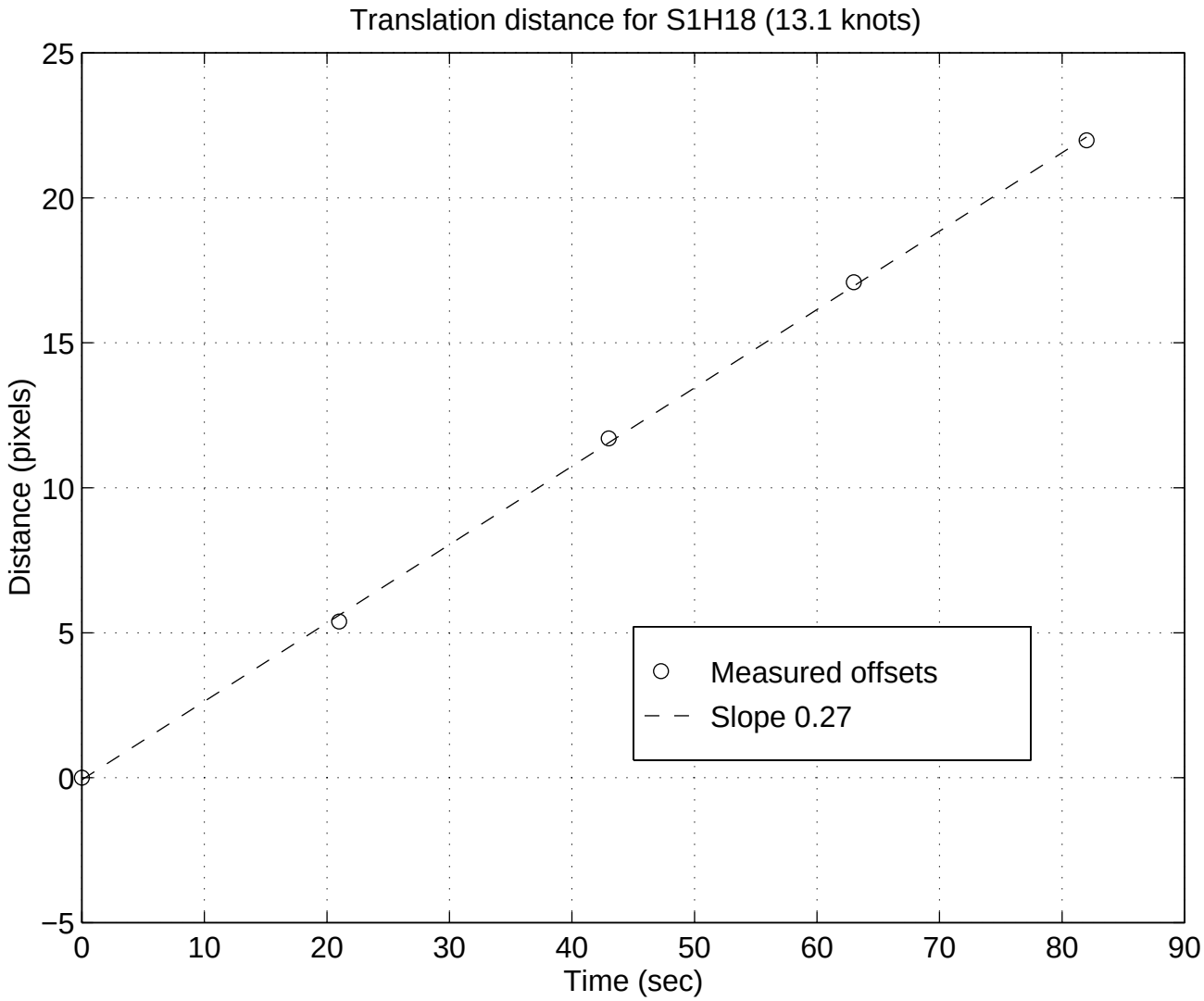

Figure 5-36 Cumulative distance, in pixels, travelled in data sequence S1H18 vs. elapsed time, taken from the timestamps. Fitted line estimates speed in pixels per second, which is then scaled to knots using the PPI range parameter.

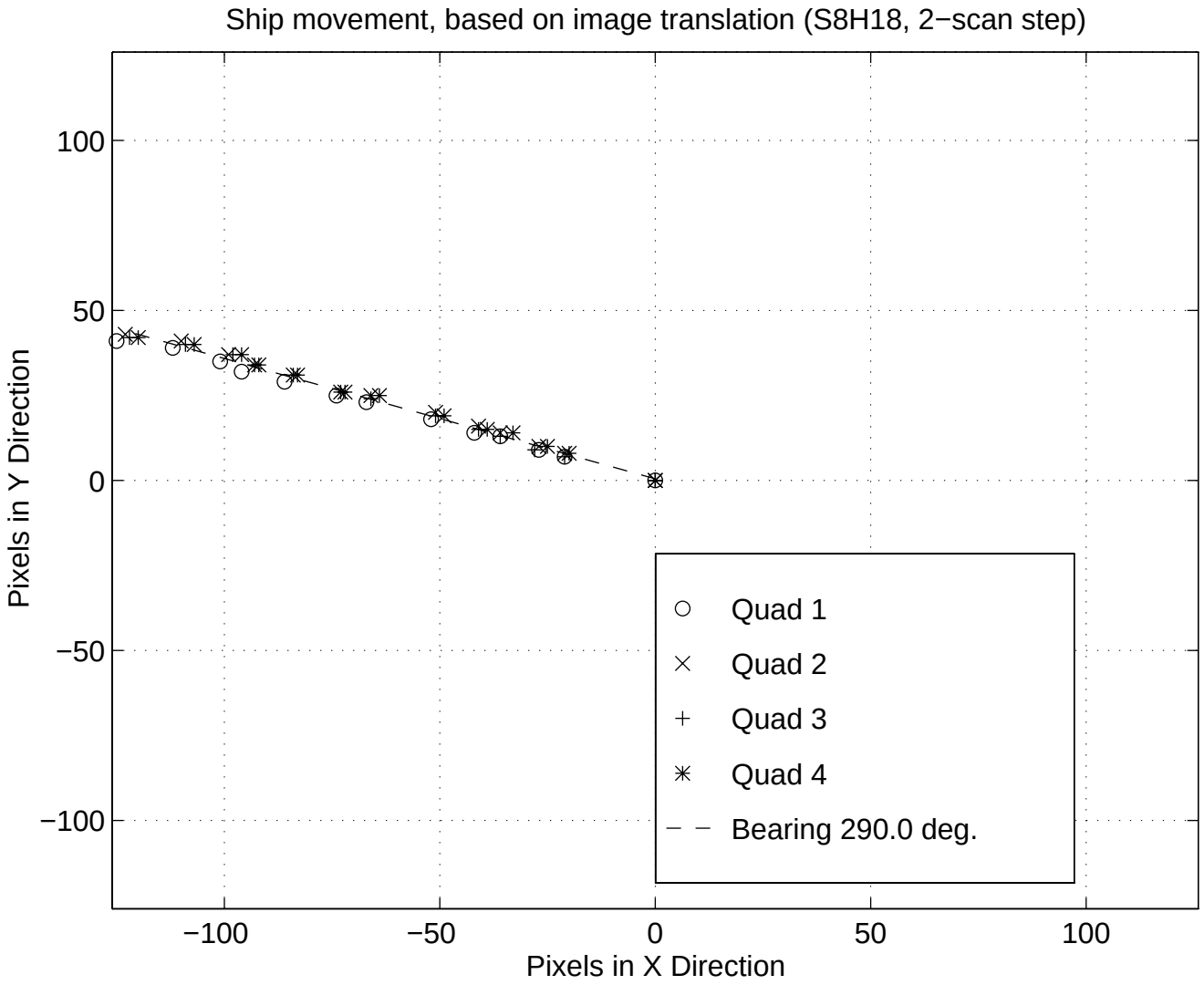

Figure 5-37 Cumulative X and Y offsets for data sequence S8H18. Fitted line provides an estimate of the ship's heading.

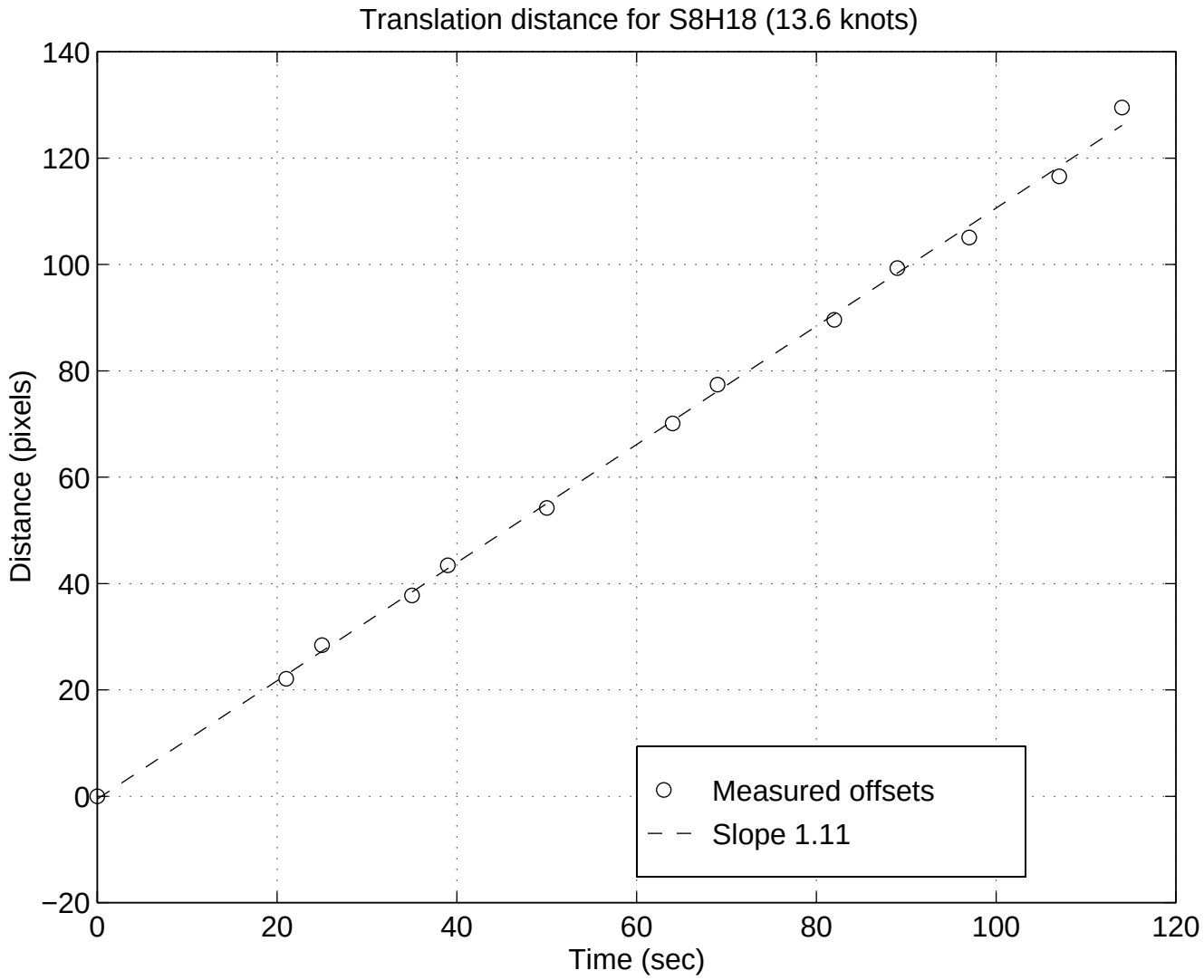

Figure 5-38 Cumulative distance, in pixels, travelled in data sequence S8H18 vs. elapsed time, taken from the timestamps. Fitted line estimates speed in pixels per second, which is then scaled to knots using the PPI range parameter.

Data Sequence	Heading	Heading (log)	Speed (pixels/sec)	Speed (knots)	Speed (log)
S1H08	0.0°	var	0.29	14.1	14
S1H10	356.9°	var	0.22	10.8	10
S2H16	229.9°	231 °	0.23	5.6	var
S1H18	290.4°	292 °	0.27	13.1	13
S8H18	290.0°	292 °	1.11	13.6	13

Table 5-1 Estimated ship motion parameters, and entries from experimental log. (var = variable)

5.1.2 Scan-to-scan Variation

One question of interest is how the radar return from a given ice target varies from scan to scan, as its aspect angle, range, and bearing vary due to ship motion. The ship motion statistics estimated in the previous section can be used to shift a range-bearing reference point from scan to scan so that the return from a fixed point on the surface can be extracted from successive scan images.

Using the first PPI scan in a data sequence, the X,Y location of an ice target of interest was noted. A 100x100 pixel image sub-area centred on this location was then extracted and copied to a file. The same procedure was then applied to all subsequent scans in the sequence, with the centre of each sub-image shifted to cancel the effects of ship motion. The original 'S' files, as stored on CD, were used.

For example, Figure 5-39 shows the 25 sub-images taken from 25 scans in data set S1H10. The image centre moves from a range (in pixels) of 117, bearing 152.1°, to range 135, bearing 156.5 °. The image appears very similar from scan to scan. As an indication of the alignment, Figure 5-40 shows the integration (average) of the 25 scans. Although the image is 'smoother' in texture, it is not significantly blurred, indicating little or no relative motion.

As further confirmation, close study of the 25 sub-images shows a small point echo (dark spot) in the upper left of each sub-image, that shifts location toward the upper left in subsequent scans. This radar return is, in fact, from the Louis St. Laurent, the icebreaker that accompanied the MV Arctic on the voyage. In the integrated sub-image, the ship return appears as a linear streak, revealing its motion relative to the 'ground stabilized' ice image. Figure 5-41 shows the corresponding integrated HV image. Note that each average scan image has been separately scaled to use the complete greyscale range for

display. Therefore one cannot make greyscale comparisons between the images to determine the relative HH and HV strengths.

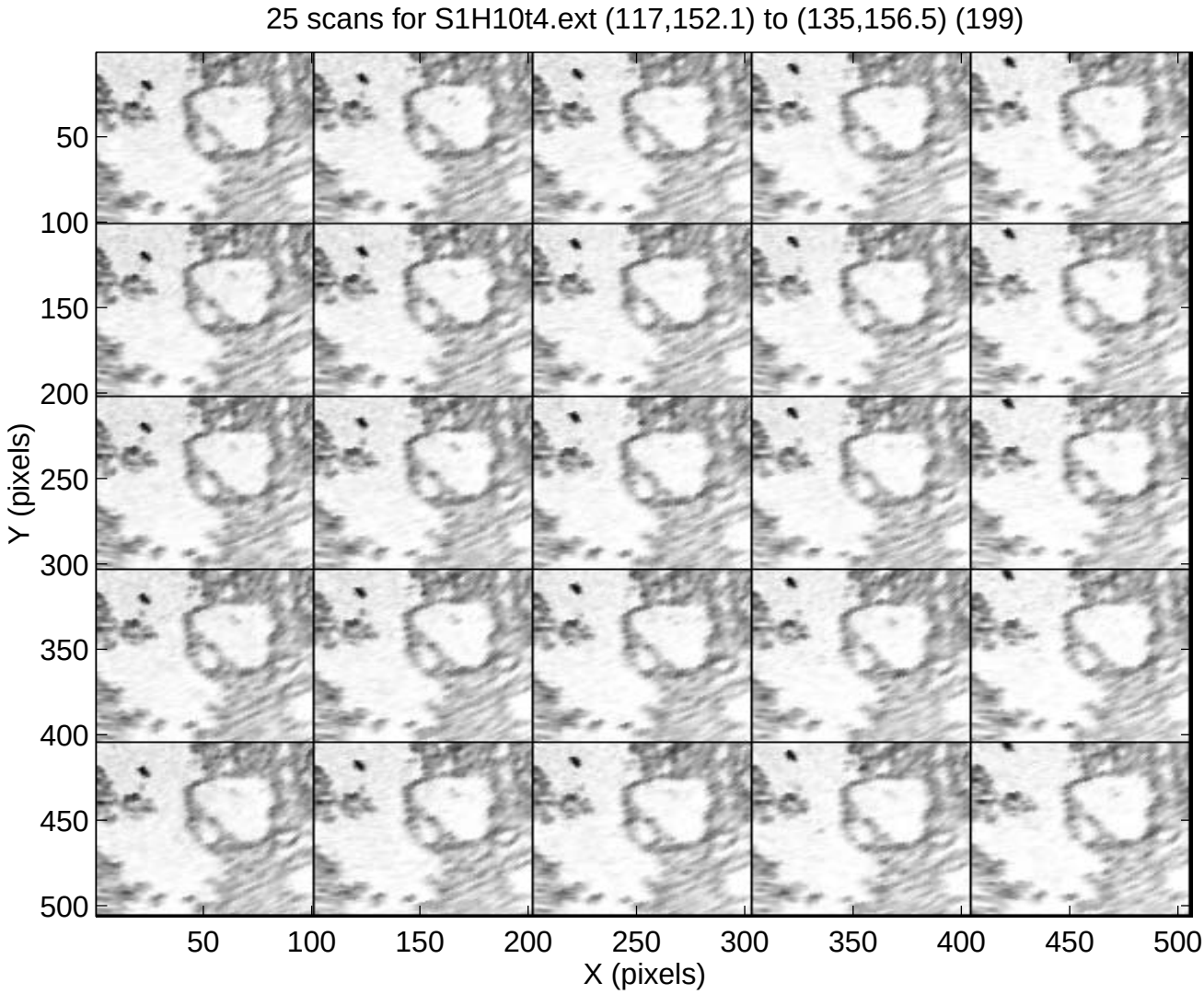

Figure 5-39 Sub-images from the 25 scans of sequence S1H10, after motion correction. Successive scans are shown top to bottom, left to right.

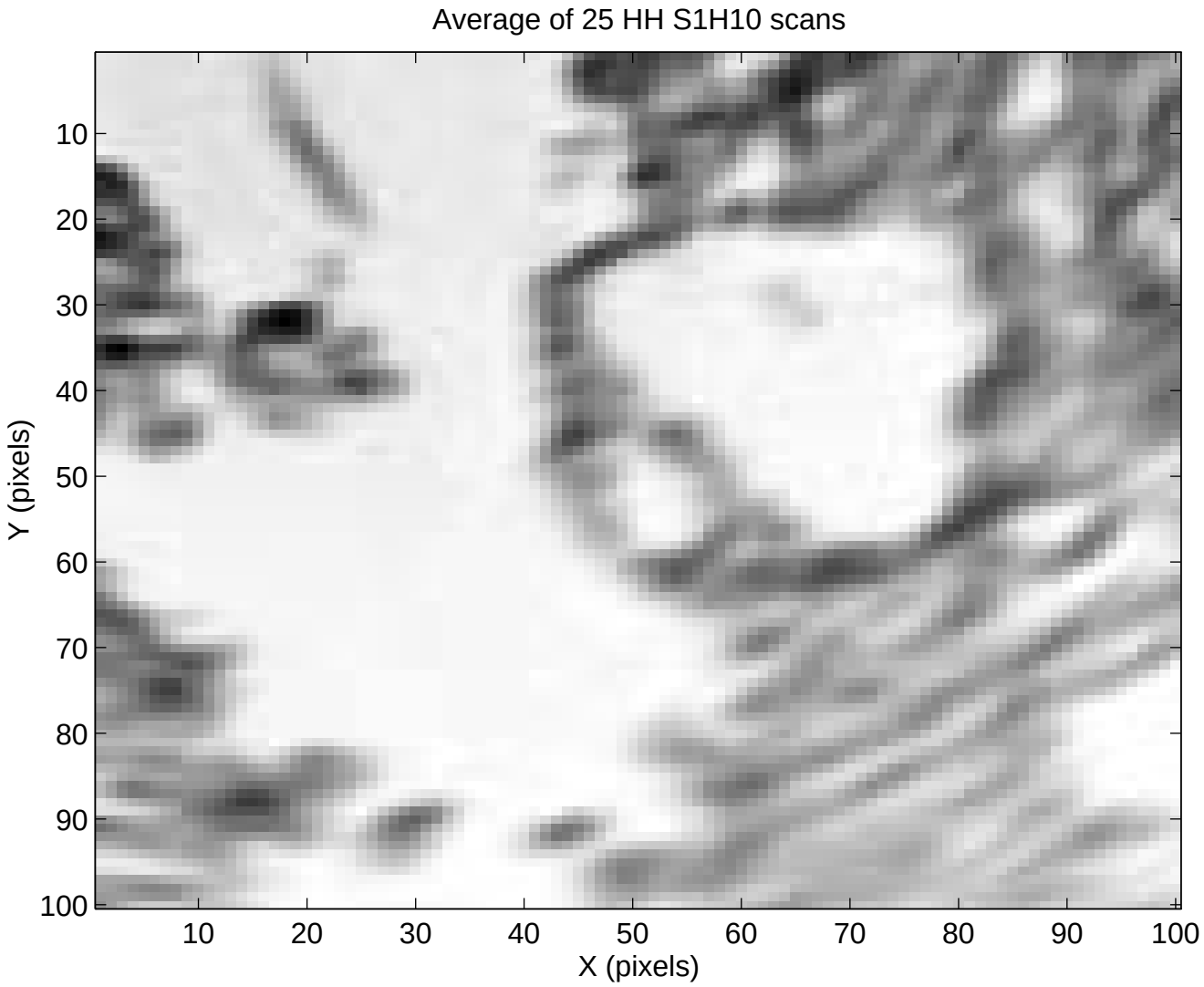

Figure 5-40 Integration of the 25 HH sub-images from S1H10, shown in Figure 5-39

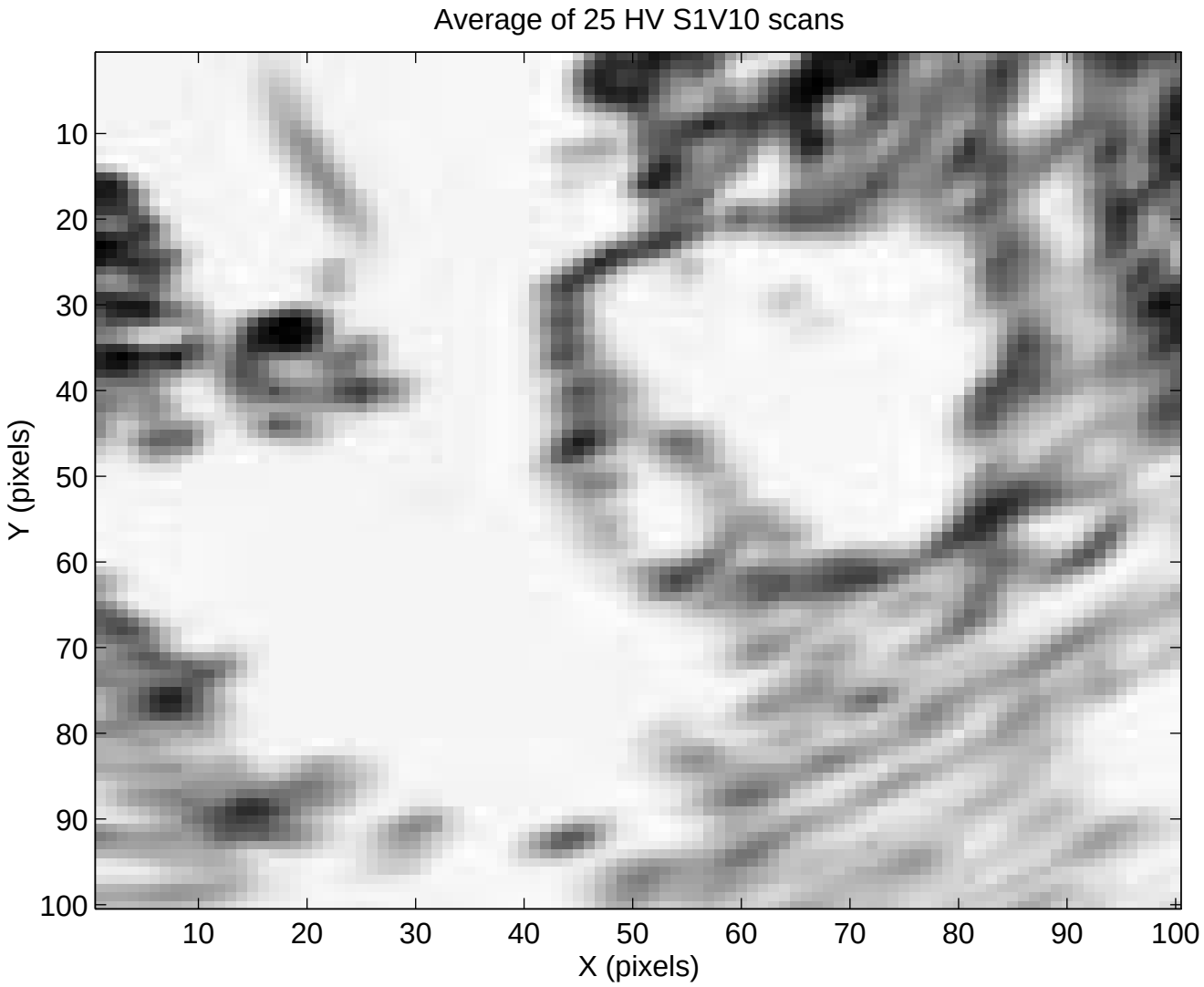

Figure 5-41 Integration of the 25 HV sub-images from S1V10

Having created this sequence of motion-corrected sub-images, the time history of the return from a given location (i.e. ice target) can be constructed. To try to accommodate minor errors in the image position correction, the following approach was used. The desired X,Y location was selected interactively using the cursor on the HH integrated image. A 3x3 pixel block, centred on that X,Y location, was then extracted from each of the N available scans in the HH and HV sequences. To indicate the variability in the 3x3 block, the maximum, median, centre, and minimum values were plotted vs. elapsed time as determined from the scan time-stamps. Figure 5-42 and Figure 5-43 show example HH and HV data from S1H10, taken at location (14,88) in Figure 5-40. It was felt that the median was the most robust measure to use for further study.

Noting the range (in pixels) of the chosen X,Y location, the appropriate median ('M') file and gain ('E') values were used to balance the HH and HV data. It is the combined strength of the HH and HV data, together with the HH-HV difference, that is used in an attempt to discriminate ice type.

Figure 5-44 shows a plot of the balanced HH and HV medians, and their difference, for the chosen X,Y location. There is often considerable variation in the return from one scan to the next. To help to provide smoothing, a 3-point median filter was applied to the HH and HV median curves. The results are shown Figure 5-45.

From visual inspection of a number of HH and HV time histories, including the use of balancing, the HV return shows more scan-to-scan variation than does the HH return. It is not clear how much of this variation is due to the nature of the ice echo itself, and how much is simply a function of the data itself, its recording and analysis. Without a proper radar calibration, the extent of the variation in A/D level in terms of actual received power variations in dBm is unknown. Therefore, one should not attempt to draw quantitative conclusions about any one particular location in the radar image. Instead, one relies on the ice types of interest occupying large enough areas of the radar image that local variations 'average out', revealing an overall impression of the HH-HV behaviour, hence the ice type.

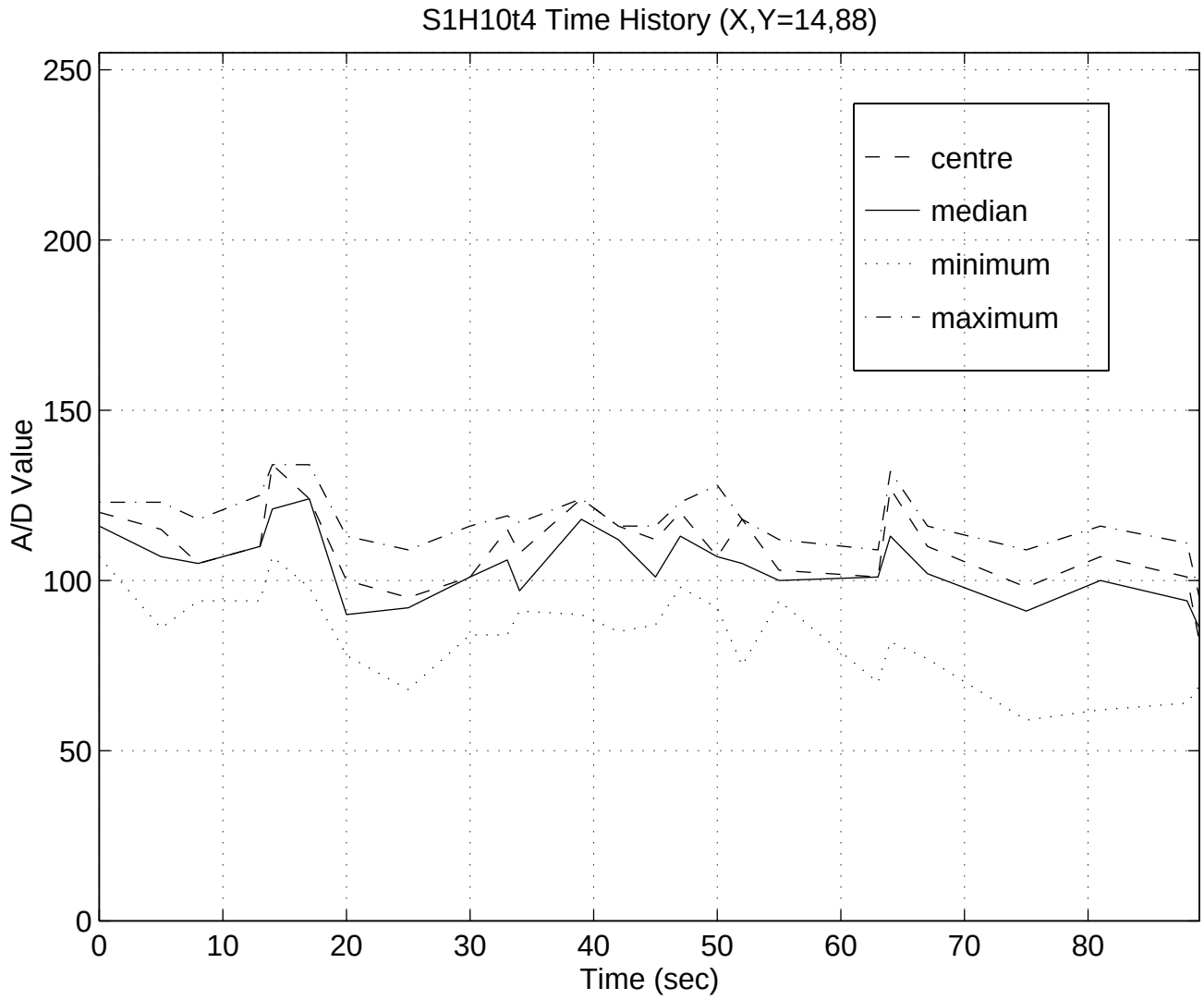

Figure 5-42 Time history for HH data from S1H10 at location (14,88) in Figure 5-40

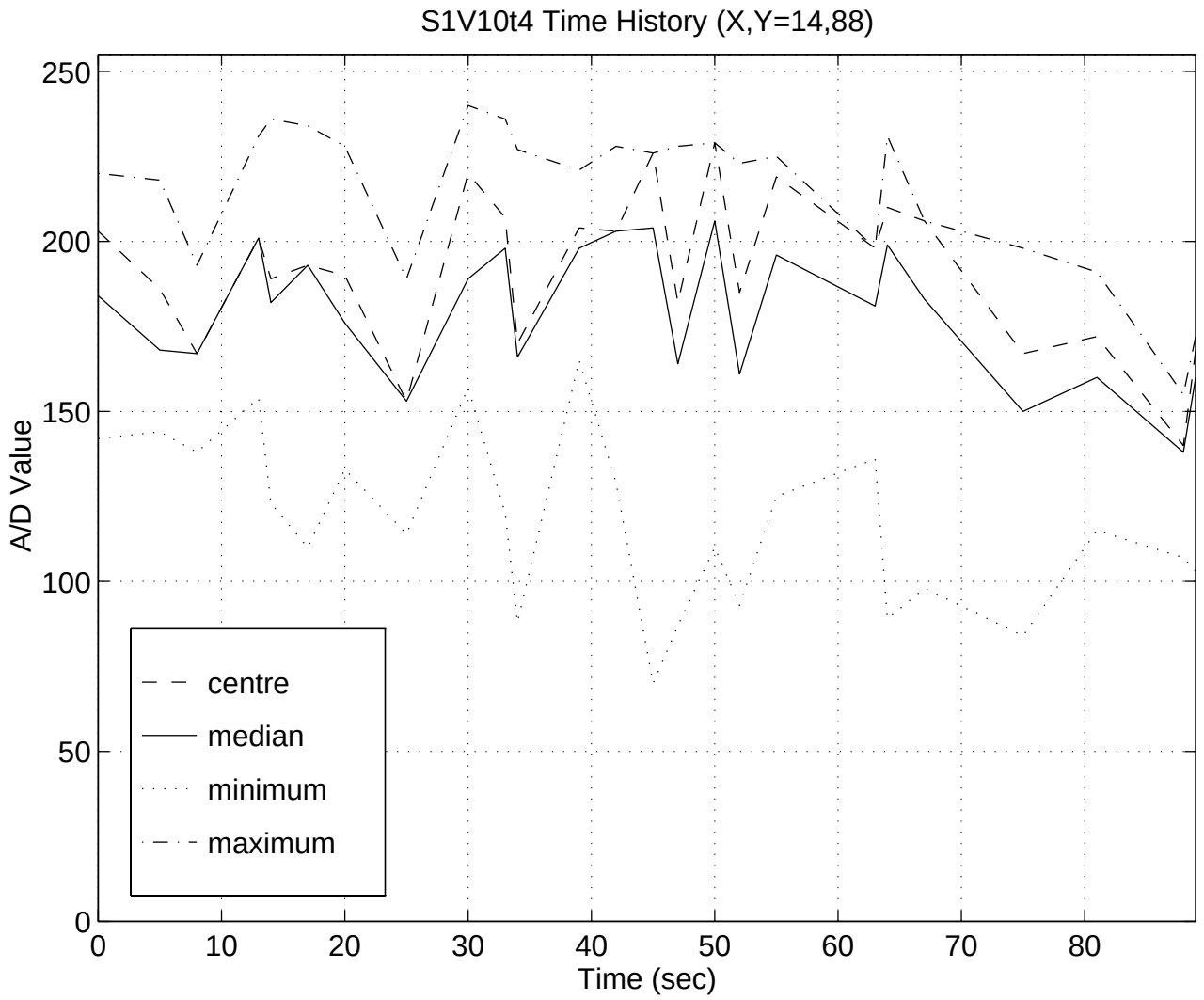

Figure 5-43 Time history for HV data from S1V10 at location (14,88) in Figure 5-40

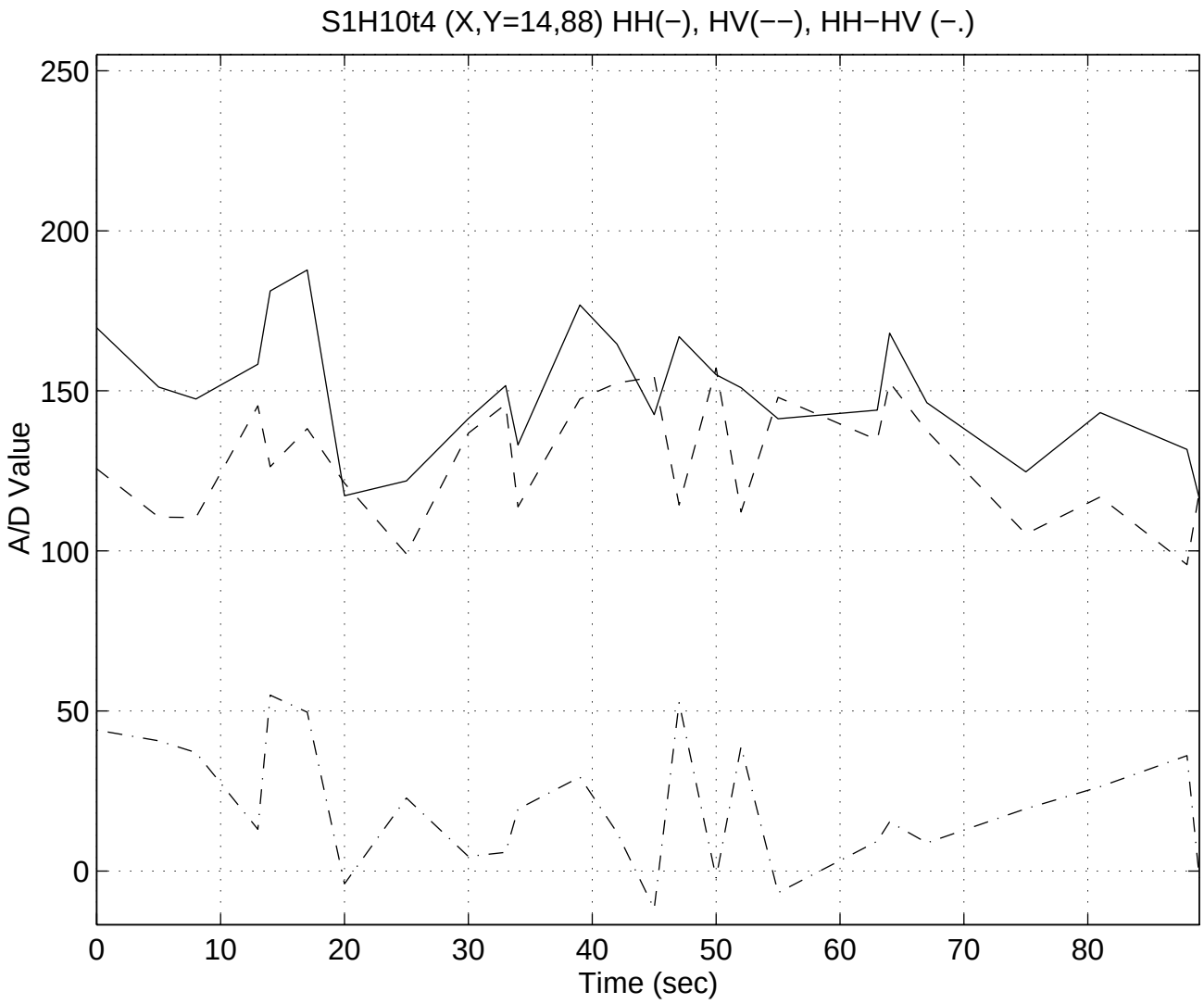

Figure 5-44 Time history for HH, HV, and HH-HV median data from S1H10 at location (14,88) in Figure 5-40. The HH data was balanced to match the HV data.

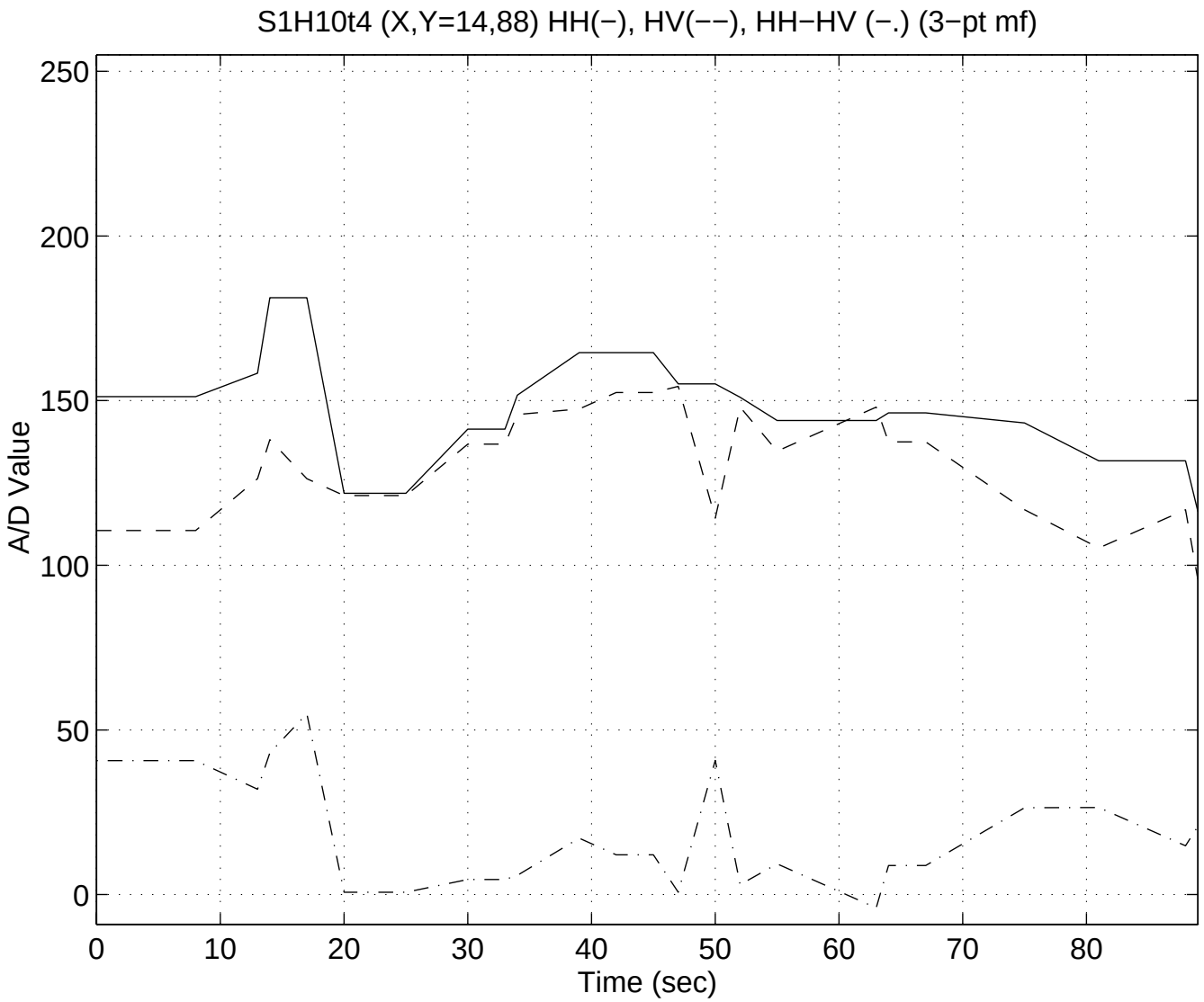

Figure 5-45 Time history for HH, HV, and HH-HV data from S1H10 at location (14,88) in Figure 5-40. Curves have been smoothed using a 3-point median filter.

Use of Non-collocated Radars

The data being analysed in this report was collected using a dual-polarized antenna, so that the HH and HV images are exactly collocated, in both time and space. An option to be considered is the use of two separate radars, each with its own antenna, with one radar being the master and transmitting/receiving the co-polar signal (e.g. HH), and the second radar being slaved to the first, receiving (no transmit) the cross-polar return (e.g. HV) by having its antenna footprint follow that of the master radar. Two such radar antennas typically will be offset in the horizontal and vertical directions. The large vertical

beamwidth of the marine antennas will mitigate vertical offset. The horizontal offset could be expected to be on the order of 20 m or less.

From the data base available for this study, one can simulate the effect of having HH and HV scans collected from spatially separated antennas. As a result of ship motion, successive scans are separated in space, that is, by the distance traversed by the ship during the time interval between the scans. For a ship speed of 13 knots, the ship is moving 13 nmi/hr * 1852 m/nmi / 3600 sec/hr = 6.7 m/s. For an antenna scanning rate of 20 rpm (i.e., 3 sec per scan), successive scans will be offset by about 20 m.

To test the feasibility of using non-collocated antennas, the following procedure was used. Previously we used the HH and HV time histories over N scans to plot the time history of the instantaneous HH-HV difference. This was the value using collocated (in time and space) data. To simulate non-collocated antennas, the HV was slipped by one scan. That is, the HH data for scan n was combined with the HV data for scan n+1. Thus the HH and HV data were spatially offset by the order of 20 m, and the scans were also offset in time by the scanning interval. Therefore this should represent a near worst-case.

Figure 5-46 shows the HH, HV, and instantaneous HH-HV data as was previously given in Figure 5-45, with the additional of the HH-HV (delayed) difference. Although the HH-HV and HH-HV(delayed) curves vary in detail in certain cases, certainly the overall trend is maintained, with the major variations still captured.

Further examples of time histories, also showing the HH-HV and HH-HV(delayed) data comparison, are given. All the locations are with reference to the integrated scan image of Figure 5-40. Figure 5-47, location 45,26 is on the upper left edge of the rounded floe. Locations 82,54 (Figure 5-48) and 83,41 (Figure 5-49) are on the right edge of the rounded floe. Location 73,85 (Figure 5-50) is in the area of ice in the lower right part of the image. Location 55,12 (Figure 5-51) is in the area of ice above the rounded floe. In most places, the HH-HV difference is positive. However, for the locations on the right edge of the floe, the differences are negative, or near zero. By setting a suitable threshold, and setting of the colour tables, one can use the differences in the HH-HV quantities to suggest delineation of different types of ice or ice features. Note that these threshold settings are dependent on the image content, and the scene-specific balancing parameters.

As discussed elsewhere, it is not on the basis of a single pixel that the ice type indication is based; it is formed by a consensus of pixels over a reasonably sized area of the image. Thus, it is felt (at least for the data available to this work) that HH and HV data taken from spatially separated radars can be successfully used to provide the wider area sense of the nature of the ice type.

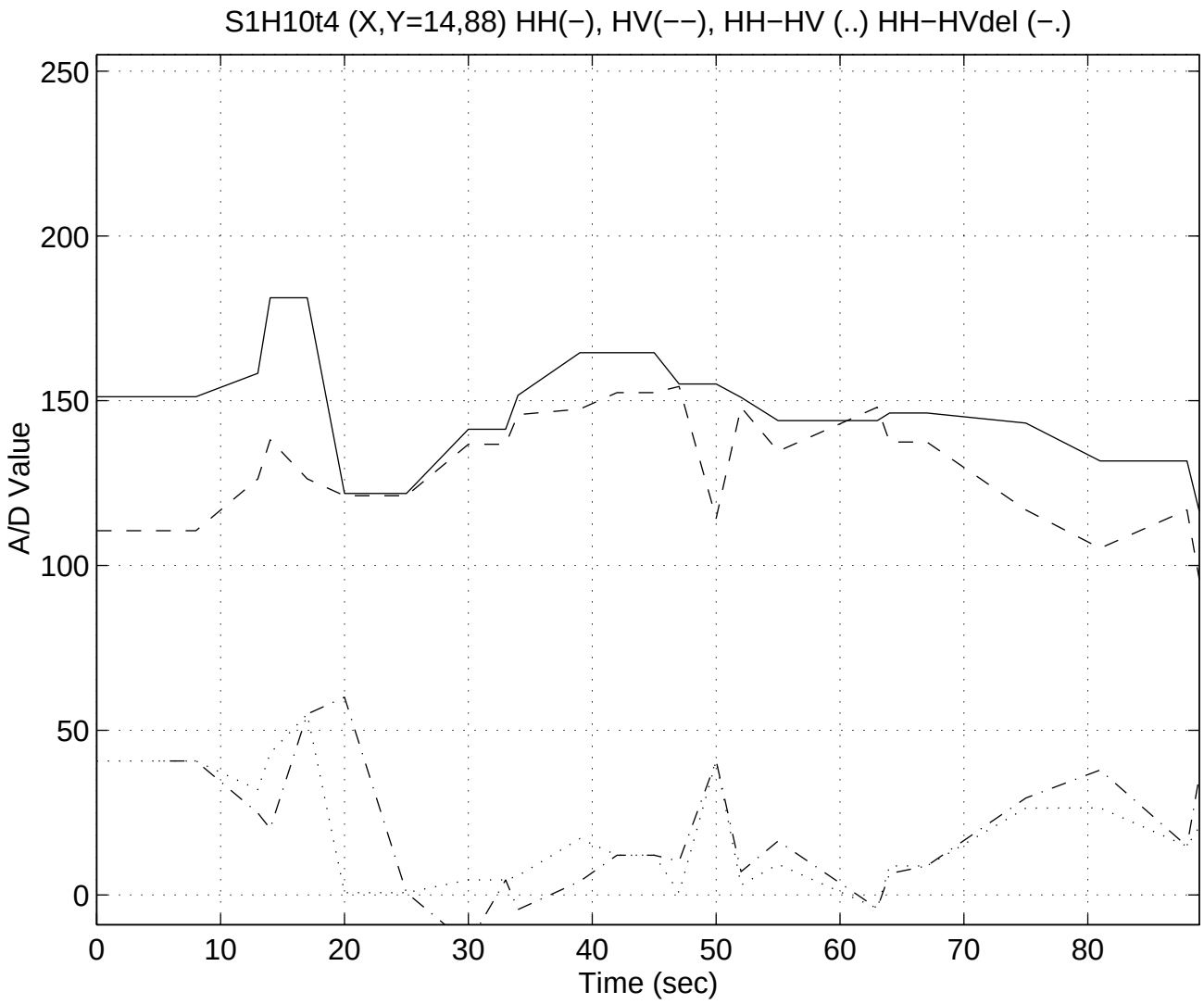

Figure 5-46 Time history for HH, HV, HH-HV coincident, and HH-HV (delayed) data from S1H10 at location (14,88) in Figure 5-40

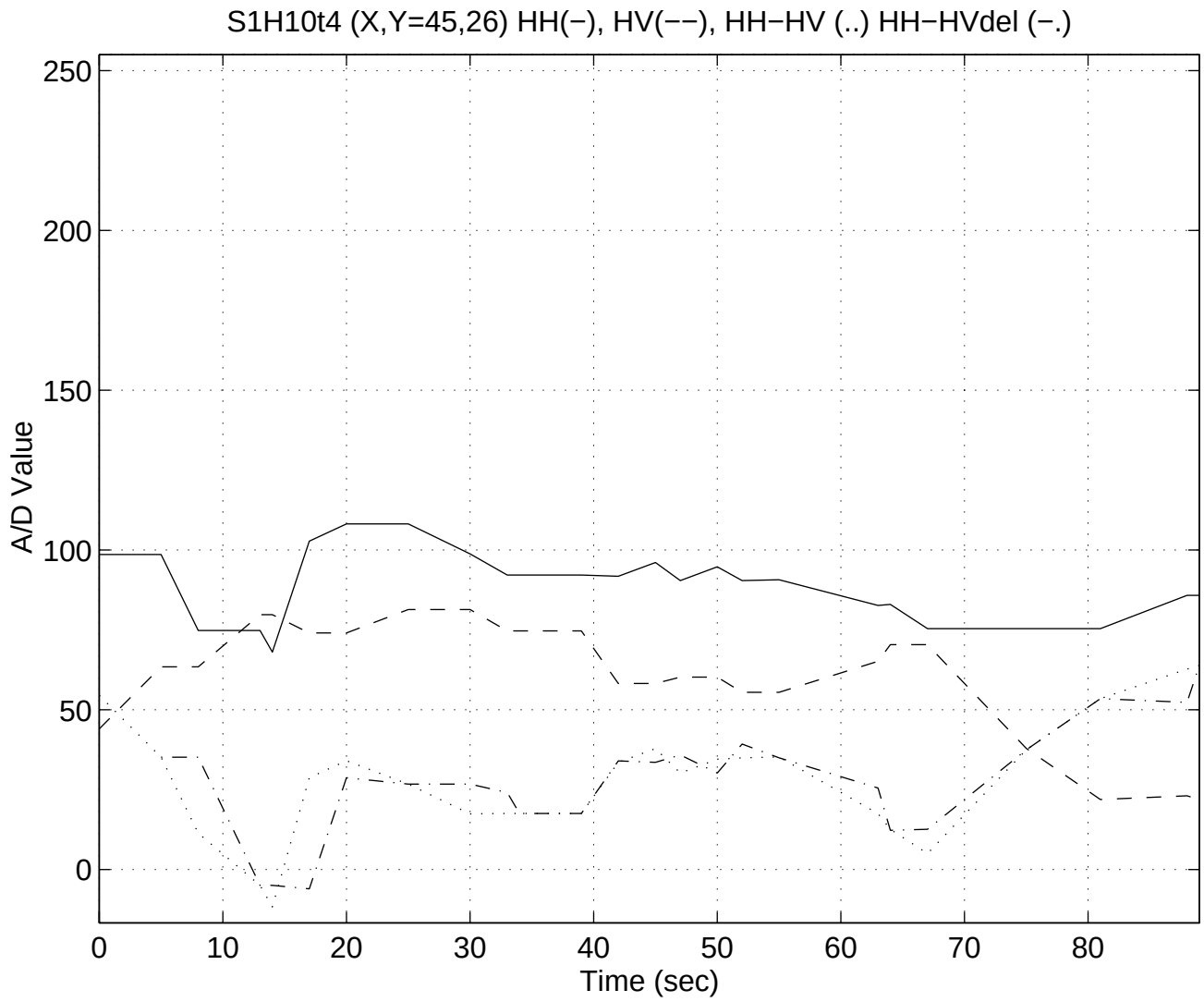

Figure 5-47 Time history for HH, HV, HH-HV coincident, and HH-HV (delayed) data from S1H10 at location (45,26) in Figure 5-40

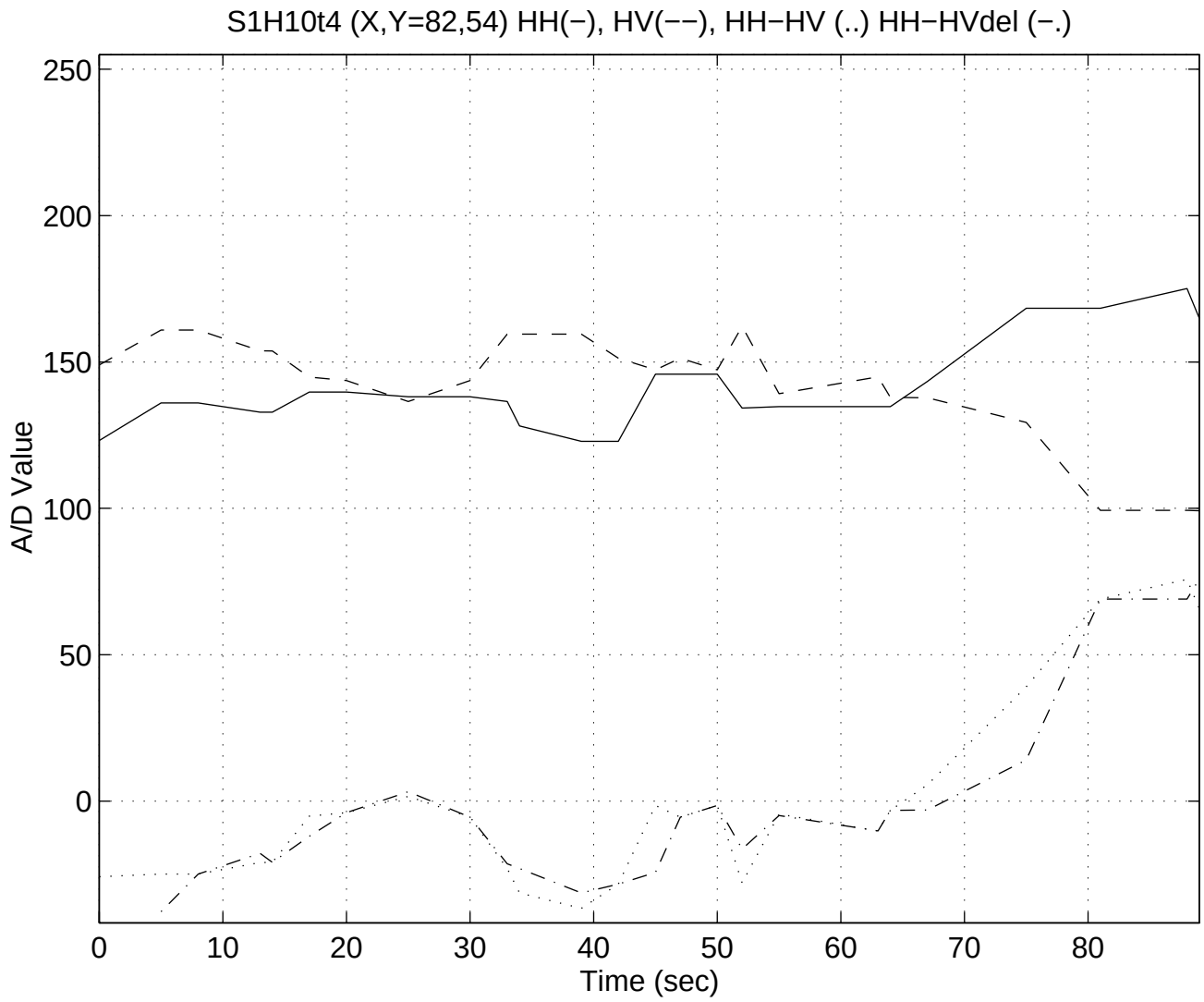

Figure 5-48 Time history for HH, HV, HH-HV coincident, and HH-HV (delayed) data from S1H10 at location (82,54) in Figure 5-40

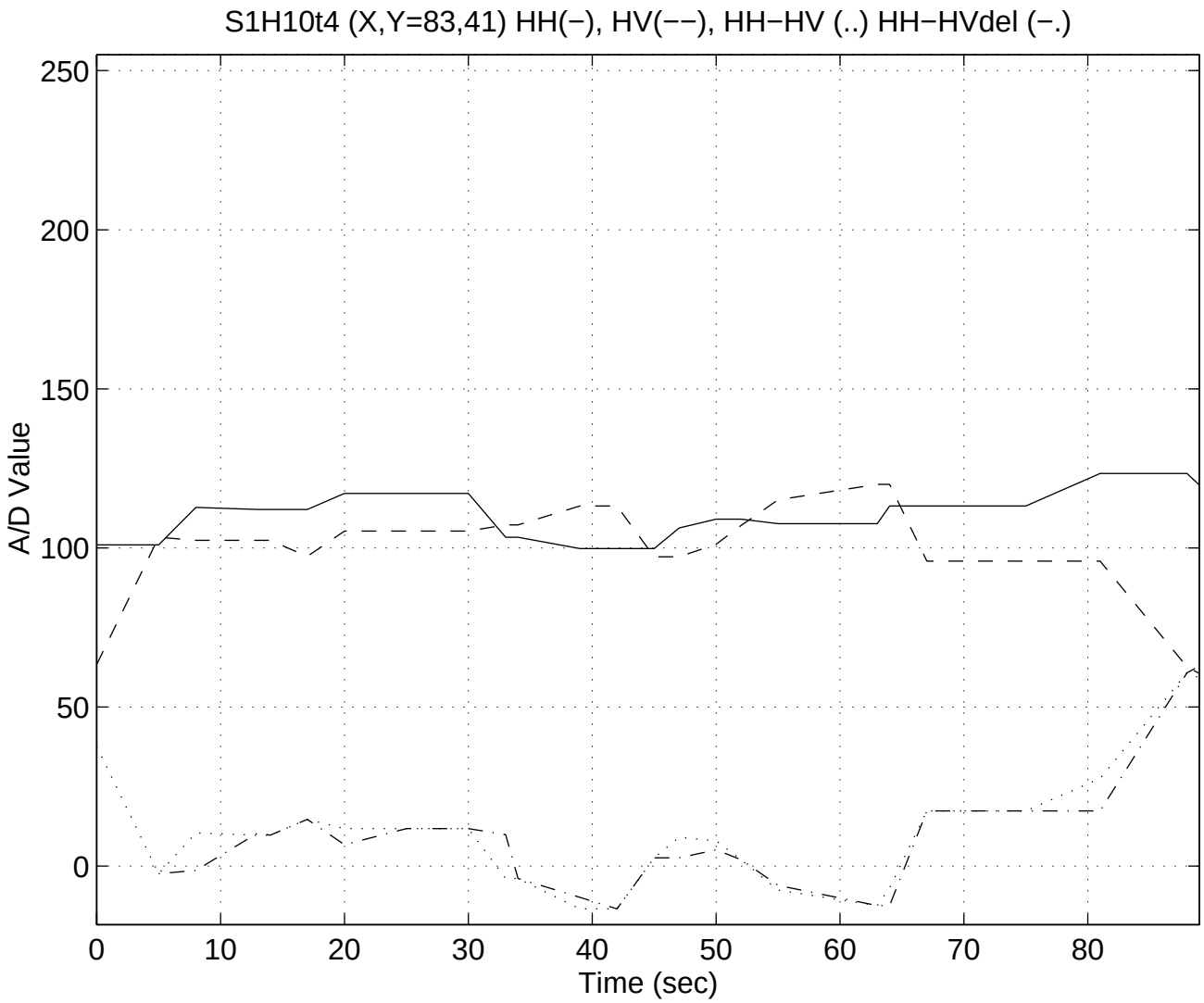

Figure 5-49 Time history for HH, HV, HH-HV coincident, and HH-HV (delayed) data from S1H10 at location (83,41) in Figure 5-40

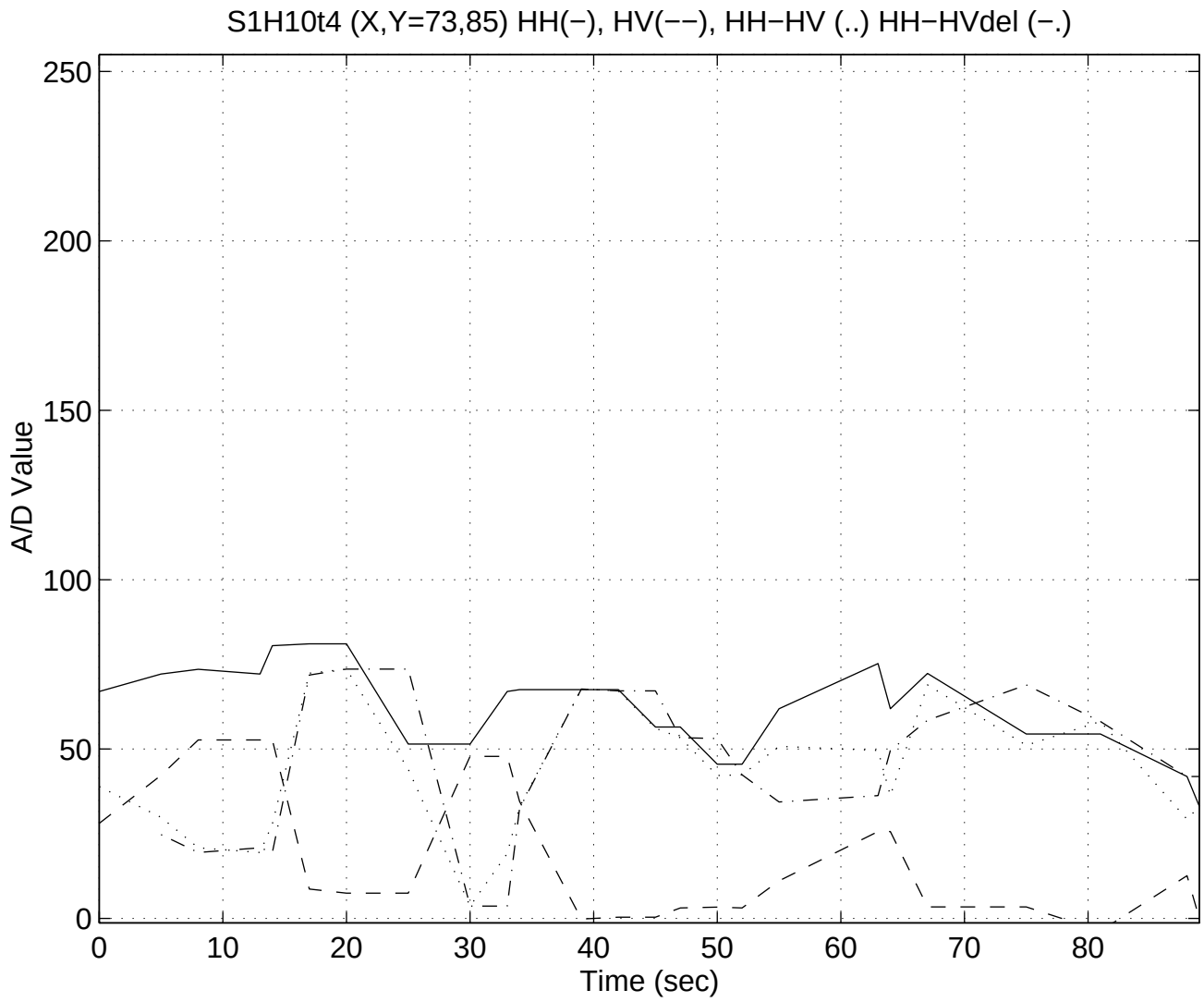

Figure 5-50 Time history for HH, HV, HH-HV coincident, and HH-HV (delayed) data from S1H10 at location (73,85) in Figure 5-40

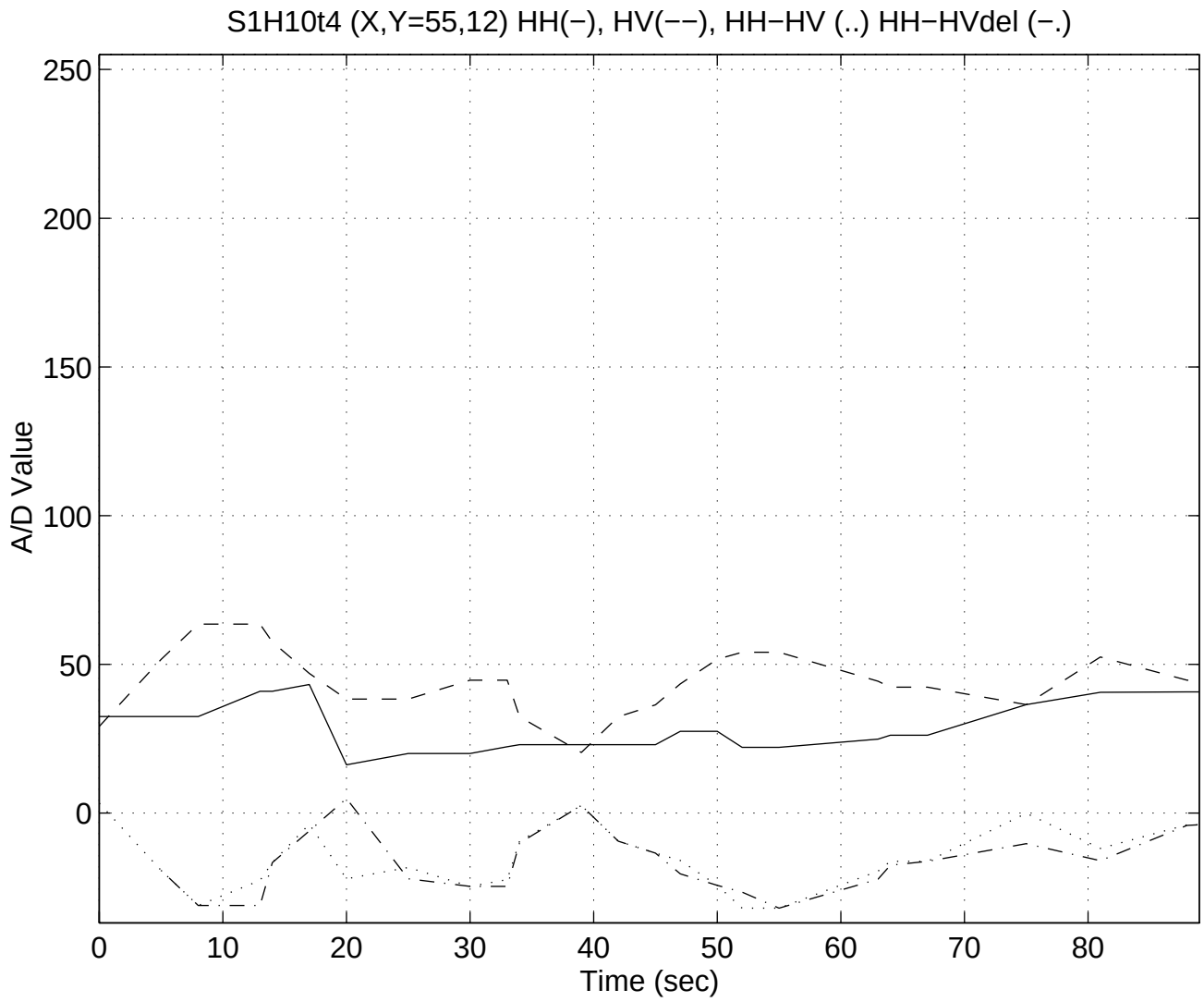

Figure 5-51 Time history for HH, HV, HH-HV coincident, and HH-HV (delayed) data from S1H10 at location (55,12) in Figure 5-40

THIS PAGE IS INTENTIONALLY LEFT BLANK

6 GROUND TRUTHING WITH STAR-1 SAR DATA

6.1 STAR-1 SAR Data

During the 1995 MV Arctic field trials, Canarctic (now Enfotec Technical Services Inc.) engaged the services of a STAR-1 synthetic aperture radar (SAR) to map the area of Lancaster Sound just prior to the MV Arctic's arrival. The STAR-1 SAR radar mapped the areas on the south and eastern shore of Devon Island, and Lancaster Sound as far as Griffith Island, on 01 November 1995 and 05 November 1995. These SAR data have been digitized by Enfotec onto CD-ROM and provided to Sicom to analyse, for the purpose of ground truthing the scenes of polarimetrically processed in Section 3.

The CD-ROM provided by Enfotec contains two directories corresponding to 01 November and 05 November 1995, respectively. Five SAR image files, corresponding to five flight lines are found in each of the two directories. The image files are in a binary format that can be read by ImageMate (by DataQuest), a remote sensing software package. The SAR imagery is 15 m resolution, and is coded as 8-bit (0 to 255) intensity, which is easily mapped onto 8-bit gray-scale by ImageMate. ImageMate allows one to open a flight line, and to pan around the image. If a region of interest is identified, it can be extracted as a TIFF cookie, i.e. a .tif file that can be imported into other packages. The original intent of our review was to identify and extract cookies from the SAR imagery that pertained to the five shipboard PPI radar displays examined and processed in Section 3. Both the November 1st and November 5th flight lines were analysed, and two cookies were extracted that are believed to correspond to files 151306S1.v10 and 133126S1.v08.

File parameters associated with the 01 November 1995 are listed in Table 6.1 .

Table 6.1: 01 November 1995 SAR data parameters

FILENAME	SIZE (KB)	NO. OF LINES	PIXELS/LINE
A101-In	41,184	20,592	2,048
B101-In	29,844	14,922	2,048
C101-In	33,688	16,844	2,048
D101-In	40,532	20,266	2,048
E101-In	23,782	11,891	2,048

File parameters associated with the 05 November 1995 are listed in Table 6.2 .

Table 6.2: 05 November 1995 SAR data parameters

FILENAME	SIZE (KB)	NO. OF LINES	PIXELS/LINE
A101-In	46,782	23,391	2,048
B101-In	48,844	24,422	2,048
C101-In	15,938	7,969	2,048
D101-In	25,656	12,828	2,048
E101-In	28,656	14,328	2,048

Each of the flight lines varies according to the number of lines collected. The longest flight lines are believed to represent approximately 366 km in length. The width of each flight line is approximately 18.5 km (i.e. only 1230 pixels in each line is valid data). After analysing all of the SAR data, Sicom determined that a good part of the MV Arctic's voyage was not covered by the SAR data. This assertion caused a review at Enfotec to occur, and it was determined by Enfotec that approximately 800 pixels were mistakenly not written to CD in each flight line. With this additional 800 pixels, the MV Arctic's voyage should indeed covered by the SAR data. Unfortunately, the analysis of these additional data will have to wait for a follow-on contract.

In Table 6.3, parameters of the five shipboard radar images are listed for comparison.

Table 6.3: Parameters of selected shipboard radar images

FILENAME	SHIP LATITUDE (deg)	SHIP LONGITUDE (deg)	FULL DISPLAY RANGE (nmi)	DATE
133126s1.v08	74.50	-80.03	13.5	Nov02
151306s1.v10	74.45	-80.93	13.5	Nov02
132452s2.v16	74.59	-92.83	6.8	Nov03
185231s1.v18	74.62	-94.77	13.5	Nov03
190854s8.v18	74.64	-94.98	3.4	Nov03

While Table 6.3 provides the position (latitude, longitude) where each image was taken, no georeference data was available for the SAR data. This made it quite difficult to find any SAR cookies that corresponded to the shipboard radar imagery. After panning through the SAR imagery trying to identify features that matched any of the shipboard radar images, it became clear that a different approach was required.

Since the shipboard radar imagery occurred on 02 to 03 November, it was decided to focus first on the November 1st SAR imagery. It was first assumed that all flight lines were parallel. The SAR imagery was subsampled by a factor of 4 in the flight direction and printed onto paper to try to form a mosaic of the five flight lines. The hope was that if a mosaic could be formed and geographic land features could be identified (like the south shore of Devon Island) then an atlas could be used to georeference the SAR data; then it would be straight forward to find the cookies we were after. Unfortunately, only two of the flight lines seemed to align well. We assumed the difficulty in aligning the flight lines was caused by either incorrect image scaling (each flight line was independently histogram-equalized to print well with 8-bit gray-scale, when a common feature between the flight lines should in fact be used to maintain equalization across flight lines) and / or non-parallel flight lines.

To resolve this problem, all five SAR flight lines were printed at full resolution (no subsampling), for both November 1st and 5th , and can be found in Appendix A. Once the printing was complete (took half a day print time), the long flight lines (up to 9 feet long) were pieced together like a puzzle. Fortunately, this task was successful, and with the help of detailed geographic maps, key SAR features were geo-referenced.

The next step was matching the five radar images listed in Table 6.3 to the SAR data. Each of the five radar images were printed to scale to match the SAR data, and located on the SAR mosaic using the radar latitude and longitude. Only two of the five radar images (133126 and 151306) overlapped with the SAR data. (Note: it is possible that the other three radar images will overlap with the SAR data when the 800 missing pixels are included in the data.)

It should be noted that a perfect match should not be expected for several reasons. First, two different radars are used at two very different viewing aspects. Secondly, the SAR images and shipboard radar images were collected at different times. The 133126 shipboard radar data was collected on November 2nd, and the corresponding SAR imagery was taken 3 days later on November 5th. The 151306 shipboard radar data was collected on November 2nd, while its corresponding SAR data was collected a day earlier on November 1st. We are told that ice in Lancaster sound moves eastwardly, while ice on the eastern shore of Devon Island moves southernly.

Notwithstanding the differences in time, we were able to get a good match for the 151306 shipboard radar data, and a *possible* match for the 133126 shipboard radar data.

The shipboard radar and SAR imagery are shown in Figures 6.1 and 6.2.

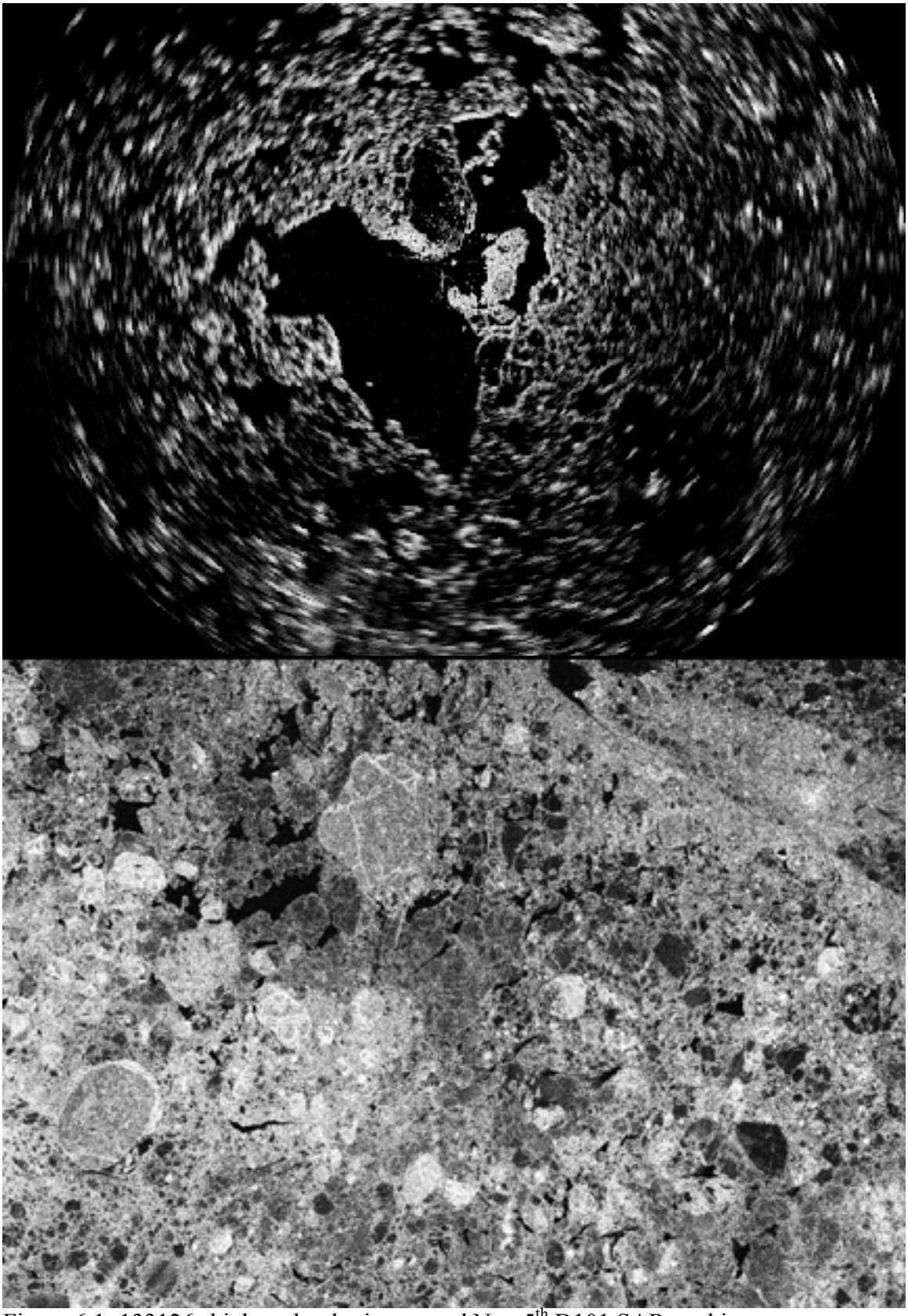

Figure 6.1: 133126 shipboard radar image and Nov 5th D101 SAR cookie

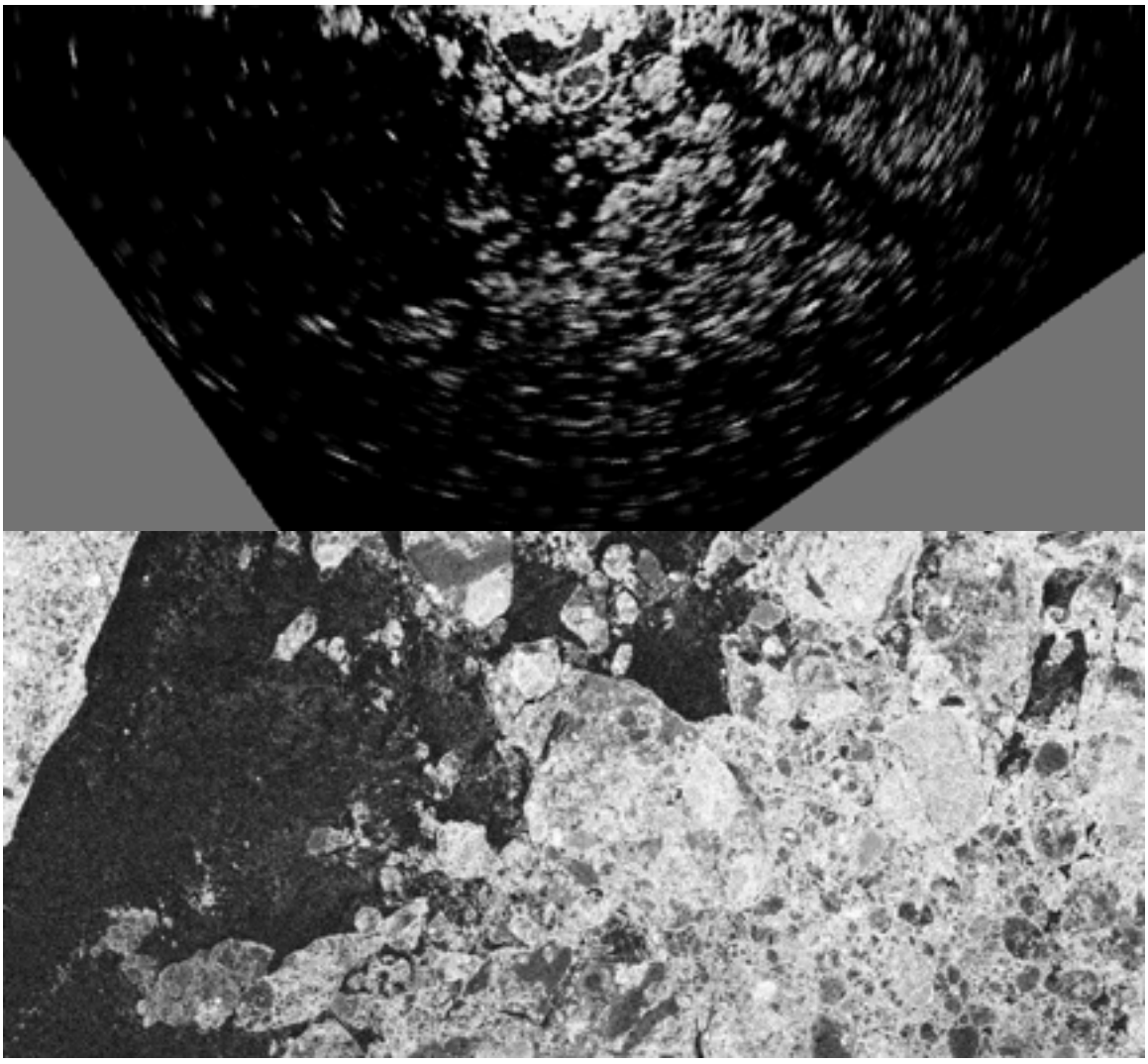

Figure 6.2: 151306 shipboard radar image and Nov 1st B101 SAR cookie

Consider now Figure 6.1. This match is deemed a possible match because the shipboard radar image and the SAR data are co-located geographically; i.e. they share the same latitude/longitude, and they share features that are *somewhat* similar. The all-black regions in the centre of the radar image are low-reflectivity returns believed to be from water, in the vicinity of the ship (which is at the centre). The SAR imagery shows a similar, low-reflectivity region which may correspond to wet or submerged ice. In addition, the radar image and the SAR image share a large, almost circular feature just north-northwest of the ship's location (i.e. approximately half-way across and two-thirds up the image). The SAR imagery suggests this ice to be a multiyear flow of diameter approximately equal to 3 km. This observation is consistent with the polarimetrically processed image in Figure 3.53. Notwithstanding these arguable similarities, the two images are quite different overall, and indeed, may not match at all due to the 3 days that has transpired between the shipboard radar and SAR collections.

Consider next Figure 6.2. This match is far more certain than in the previous case as the images are much more similar. Again, the shipboard radar image and the SAR data are co-located geographically. Large regions of low reflectivity match (water). However, the most convincing feature is an upside down, whale-shaped feature that occurs half across and near the top of the radar image. This whale-shaped feature is also found in the same location on the SAR image. Furthermore, just beneath this feature is a circular feature that was determined by our ice experts in Figure 3.58 to be multi-year ice, and which shows up in Figure 3.54 as red. Indeed, the corresponding SAR feature in Figure 6.2 confirms this. It is unfortunate that the additional 800 SAR pixels were not available at the time of processing; as they would have allowed the entire radar image to be compared to the SAR imagery.

Note: by comparing the radar images in Figures 6.1 and 6.2 to Figures 3.57 and Figure 3.58, one can see that the images in Figures 6.1 and 6.2 have been rotated counter-clockwise by 90°. This rotation was necessary so that the images are north-up, which matches the orientation of the SAR imagery.

As a final note, it should be emphasized that when this project started, it was not believed that SAR data would be available for ground truthing. As a result, the five selected PPI images were selected without consideration to where they were located. With SAR data now available, future radar data sets should selected by *first* consulting the SAR strip maps for features of interest, and then by selecting the corresponding shipboard radar data for processing.

7 CONCLUSIONS AND FUTURE DIRECTIONS

Previous research indicates that multi-year ice returns a larger cross-polarization ratio (HH/HV) than first-year ice, at X-band, thereby providing the basis for discriminating between hazardous and nonhazardous ice (to shipping). The current study is intended demonstrate the feasibility of developing an affordable, ice hazard detection system which would be of great importance to arctic navigation. The polarimetric algorithms developed during this project were motivated by, and tested on polarimetric data collected during the 1995 MV Arctic Field Trials during the first week in November 1995. HH and HV marine radar PPI data were captured as the vessel navigated through Lancaster Sound, along the south shore of Devon Island. Both hazardous and non-hazardous ice were present. This study is the first that has examined in detail the radar data collected during the aforementioned field trial.

Two key issues were investigated during this project are:

1. Can polarimetric information be retained and exploited when using uncalibrated radars for polarimetric processing, and

2. Can non-specialized, non-collocated radars provide the polarimetric information.

Conventional marine radars are not absolutely calibrated and therefore estimating absolute signal strengths (and consequently the like- to cross-polarized ratios) is not directly feasible. Data-dependent processing offers one possible way to self-calibrate the

signals so that meaningful ratios between the like- and cross-polarized returns could be obtained.

Having a specialized cross-polarized radar antenna is an expensive proposition. Dual-channel rotary joints and and dual waveguide runs can add to the cost. A possible alternative would be to use two distinct radars with orthogonal polarizations. The second radar would be set to receive-only and synchronized to the transmitting radar in rotation, frequency, and pulse timing. The ability to economically modify conventional marine antennas to achieve vertical polarization has been examined.

The next section provides some of the conclusions reached during this project.

7.1 Main Findings

The polarimetric algorithms developed herein work basically as follows: first, they attempt to match the gain versus range function of the two uncalibrated radars. This matching process uses a median versus range profile, and histograms calculated at each range ring to equalize the two channels. The hope is that once the two channels are equalized, then any resulting gain differences would be due to the polarimetric properties of the ice itself. A polarimetric algorithm was developed that computes the polarimetric difference (actually a ratio but logarithmic receivers were used) and the absolute power at every resolution cell, and uses these two parameters to drive a colour-coded polarimetric display. Five selected PPI images were marked up by ice-recognition experts (i.e. multi-year ice was identified in these data files) and used as the basis for testing the developed algorithms. Qualitatively, the polarimetric algorithms did quite well detecting the expert-identified, multi-year ice features.

The polarimetric data analysed in this report were collected from a collocated, dual-polarized radar. Since it is of commercial interest to consider the polarimetric performance when using two, non-collocated, orthogonally-polarized marine radars, some preliminary investigations were conducted using the MV Arctic HH data and HV data at different times. Since the ship moves in time, time can be used to emulate a non-collocated radar. Overall, it was determined that the image matching quantities (median vs. range and gain) and the polarimetric difference (HH-HV) were reasonably stable in time, indicating that non-collocated radars have the potential of delivering the same kind of polarimetric discrimination observed using the collocated radars.

A brief review of the range and angle accuracy requirements on the slaved radar (used as part of the non-collocated radar concept) suggests that if the displacement of the slaved V radar from the transmitting H radar is less than 3.75 m, and the slaved V radar has a beamwidth larger than the H radar, then it would be practical to slave the two radars properly. A one-degree beamwidth H radar and a two-degree beamwidth V radar are suitable.

Finally, since most conventional marine radars use horizontally-polarized antennas, inexpensive, vertically-polarized antennas were investigated to be used with the slaved radar. Although very expensive, V-pol antennas were found (similar to that used on the MV Arctic for the field trials), an inexpensive, commercially available V-pol antenna was not found. Notwithstanding this shortcoming, the literature describes the use of an external polarizer that theoretically could be fitted onto an existing H-antenna to convert to vertical polarization. It would appear that such an approach could be used to develop a low-cost, vertically polarized antenna.

In conclusion, the results presented in this report do show potential and can be used to develop a better ice navigation system that descriminates between hazardous and non-hazardous ice. Such a system is believed to be both technically feasible and economically viable. As this project was only a feasibility study, a number of issues still need to be investigated in greater detail, to better characterize the possible improvements, and to demonstrate the technical and economic viability of a cross-polarized ice hazard radar. Later in this section, these issues are presented as suggestions for future directions.

A large literature database has been collected that specifically deals with detection and classification of sea ice using cross-polarization. This literature, itself is quite valuable for any future studies.

7.2 Summary of Detailed Results

HH /HV Matching

The video level settings used for the data recordings taken during the 1995 voyage of the MV Arctic were set by the radar operator to produce a 'reasonable looking' radar image. Since the A/D has a limited dynamic range, most of the recordings show clipping of either large or small signals or both. Clipping, of course, is a nonlinear operation which impedes the HH/HV matching operation. Histograms of data samples versus range, presented in this report, give a quick and concise view of the quality of the recorded data. **It is suggested that some variation of histogramming be incorporated into the MRI, on a dynamic basis, so that the MRI can automatically adjust its gain and bias levels in response changes in the radar settings. It is recognized that the MRI may not be able to fully compensate for some radar settings. In these cases, the MRI should provide an appropriate indication to the radar operator, with prompts to return the radar to a more satisfactory setting.**

Variations in the gain factors calculated using different percentile ranking levels in the cumulative distribution curves were observed, although similar trends versus range resulted. In this study, the histograms at a given range cell were based on the 2048 samples around each range ring. Thus the shape of the histogram was often poorly quantized, leading to variations in the matching process. **In a future system, it may be possible to accumulate and maintain these histograms versus range using many**

more samples, by including multiple scans. It is expected that the gain factor produced by the matching process will then be more stable.

This study has sought to develop image balancing procedures that can operate with essentially no knowledge (or control) of the properties of the digitized radar video. This approach obviously has its limitations. It may be possible to acquire at least some rudimentary 'calibration' information at the time of the MRI installation on a given radar system. For example, a receiver noise-only signal, obtained either with the radar in stand-by or in the sweep deadtime, can be digitized by the MRI to determine its DC level and dynamic variation. The radar's gain and STC controls can be stepped through a number of settings, and a table of MRI gain and offset settings accumulated. Assuming the MRI is installed while the radar is stationary (i.e., the vessel is in port), one can use stationary (ground) clutter signals as a test signal, and again vary the radar gain and offset controls to 'bracket' the radar video's levels, particularly versus range. All of this information can be stored on disk in the MRI, and used thereafter to guide in the setting of the gain and offset of the MRI, and in the calculation of the balancing parameters.

Despite the shortcomings of the recorded data, the HH to HV matching process that was developed in this study worked reasonably well. It is expected with the inclusion of MRI-controlled gain and bias adjustments, the problems related to the current data base will be largely mitigated, and the algorithms should work well. Additional studies should be performed to refine the matching process, under a broader set of environmental conditions.

Polarimetric Algorithms

Once the HH and HV channels were matched, polarimetric algorithms were developed and applied to the matched channel data. In order to test the ability of these algorithms to discriminate between hazardous and non-hazardous ice, several data files were selected and multi-year ice features were identified by ice recognition experts who manually compared the HH and HV radar images. The automatic, polarimetric algorithms were tested on these images, and performed well in discriminating these identified, hazardous ice features. These results are very encouraging as they suggest sufficient polarimetric information survived the image matching process. Additional data sets should be prepared, ground-truthed using the now-available SAR data, and analysed, to validate performance results over a broader data set. Refinements to the polarimetric algorithms should also be made.

Note: SAR data that should be very useful for ground truthing the marine radar data only became available near the end of the contract. In follow-on studies, the SAR data should be reviewed for particular ice features of interest, and then, the corresponding PPI radar data should be selected for polarimetric processing. In this way, PPI radar data sets will be selected for processing, with advance knowledge that good ground truthing is available.

The statistics of the recorded data were analysed, more specifically the median return versus range, and appeared quite stable over the 1-2 minute sequences examined herein. The calculation of the relative gain to balance the HH channel (with respect to the HV) was also reasonably stable over the data sequences, at ranges for which unclipped data was available. These stability results suggest that similar polarimetric performance should be achievable for non-collocated radars, as for the collocated radars used herein. Further analysis should be performed, however, to simulate full polarimetric displays from non-collocated radars, and to compare them to the corresponding collocated polarimetric images.

As witnessed in the process of manually trying to 'ground-truth' the PPI images after the fact, it is not simply pixel level differences that are used in defining iceberg and multiyear ice areas, but rather certain spatial features are recognized. For icebergs, there is a bright spot of return, usually with a radial radar shadow behind (revealing significant vertical relief). Multi-year ice appears mostly as floes, often roughly circular, with ridging around their perimeter, and a change of grayscale inside the floes compared to outside. This study has concentrated on essentially pixel level balancing of the HH and HV images, leaving any spatial feature interpretation to the operator. Future studies should consider trying to incorporate some machine-assisted spatial feature detection and enhancement procedures to improve performance.

The approach developed in this study is based entirely on relative differences; there is no absolute calibration information available. The expectation for ice type discrimination is based on the property that the HH-HV difference in cross-sections for iceberg and multiyear ice is smaller than that for first-year ice (logarithmic receivers are used). In lieu of an absolute reference level, the procedures developed herein attempt to 'match' the gain and STC of the HH and HV images as closely as possible. Then the images are combined using HV-HH and HH+HV to highlight their relative differences. An *optimized* color table is required in order to *maximize* the visual separation of iceberg/multiyear ice features and first-year ice areas, on the polarimetric radar display. In this study, a color table threshold parameter was determined using histograms of designated multiyear and first-year ice (i.e., ground-truthing) from one of the five data sets, in order to generate a suitable color table. This color table was held fixed for the processing of the other four data sets. In practice, control of this color table threshold may need to be given to the operator, much like a contrast or brightness control on existing monochrome displays. Alternatively, other means can be investigated to completely automate the process.

Radar Configuration

The preferred configuration for positioning the two antennas will minimize the horizontal displacement. Ideally they should be mounted directly above one another. If this is not feasible, the horizontal displacement should not exceed 3.75 m. This would keep both the range and angular errors below acceptable limits. There are no simple solutions to removing these errors once they have been introduced to the system.

Apart from the vertically polarized slotted waveguide antennas that are commercially available, a number of technically feasible solutions were found in the literature to convert the polarization of an existing antenna using external polarizers. Though, the use of polarizers to convert from horizontal to vertical polarization has been rather limited, it is possible to do so, both technically and from an engineering point of view.

Providing a vertically polarized antenna with a wider beamwidth than the horizontally polarized antenna addresses two problems:

1. The angular error introduced by a horizontal displacement of the two antennas is reduced.

2. The tracking accuracy required for slaving the vpol antenna to the hpol antenna is reduced.

The vpol antenna must be slaved to the hpol antenna to provide the minimum angular error. This can be done by a custom antenna motor control unit. This unit will take in the current position of each antenna and adjust the vpol antenna to track the hpol.

The hpol unit may require modification in order to provide bearing data with a resolution high enough to meet the tracking requirements. Such modifications must not affect the hpol radar type approval.

The vpol antenna will have to be calibrated against the hpol antenna to accommodate differences in the antenna beam patterns.

An external tuning unit may need to be developed to provide tuning information for the vpol unit. This unit would sample the received signal and use the result for tuning. The information could be sent to a display for an operator to manually tune the vpol unit, or generate a tuning signal to be applied directly. An external trigger connection should be used to connect th hpol transmitter to the vpol transceiver. This may require the modification of the vpol transceiver to accept an external trigger and to disable the transmitter.

A separate development study should be undertaken to confirm the feasibility of developing a low-cost, cross-polarized radar. Slaving issues should be revisited and confirmed, as well as the use of external polarizers to create a low-cost, vertically polarized antenna. These development efforts should ideally be undertaken only after the matching algorithms and polarimetric processing algorithms have been validated more thoroughly, as described earlier.

7.3 Summary of Future Work

This section summarizes the next phase of work that would build upon the results of this project. The main objective of the next phase of work is to improve and validate the concepts and algorithms developed herein by analysing additional MV Arctic Fall 1995 data, and by performing additional studies. Suggestions made to MRI hardware/software as described in the previous section are not required at this time, as the existing MV Arctic Fall 1995 data will be used.

1. Review MV Arctic Fall 1995 database and identify additional data sets to be used for further refinements and validation of matching and polarimetric algorithms.

2. Review the STAR-1 SAR data in order to correlate with MV Arctic data, so that ground-truthing can be assured before finalizing radar data selection from 1.

3. Refine and validate HH and HV matching algorithms using the selected data in 1.

4. Refine and validate polarimetric display algorithms using the selected data in 1. Consider the use of spatial and temporal discriminants, rather than simply pixel discriminants for a given scan.

5. Perform a complete, non-collocated, slaved-radar simulation by using the selected data in 1. This will involve the generation of full polarimetric displays (from HH and HV data at different scan times, and hence spatially displaced) that can be compared to the corresponding, collocated polarimetric displays.

6. Further investigate the feasibility of developing a low-cost, vertically-polarized antenna. Consider the use of simulations and/or prototype development to demonstrate the external polarizer concept, and to determine key engineering issues.

7. Further investigate the control aspects necessary to slave a vpol, receive-only, non-collocated radar with an hpol, primary radar. Inexpensive, commercial marine radars could be used to demonstrate the concept, if item 6 is successful.

THIS PAGE IS INTENTIONALLY LEFT BLANK

APPENDIX A : STAR –1 SAR IMAGERY

(Not available in electronic format/
Non disponible en format électronique)